2017

Theoretical Investigation of the Catalytic Hydrodeoxygenation of Levulinic Acid Over Ru (0001) Catalyst Surface

Osman Mamun
University of South Carolina

THEORETICAL INVESTIGATION OF THE CATALYTIC HYDRODEOXYGENATION OF LEVULINIC ACID OVER RU (0001) CATALYST SURFACE

by

Osman Mamun

Bachelor of Science
Bangladesh University of Engineering and Technology, 2012

Submitted in Partial Fulfillment of the Requirements

For the Degree of Doctor of Philosophy in

Chemical Engineering

College of Engineering and Computing

University of South Carolina

2017

Accepted by:

Andreas Heyden, Major Professor

John R. Regalbuto, Committee Member

John R. Monnier, Committee Member

Mark J. Uline, Committee Member

Gabriel A. Terejanu, Committee Member

John W. Weidner, Committee Member

Cheryl L. Addy, Vice Provost and Dean of the Graduate School

ACKNOWLEDGEMENTS

I want to begin by thanking Prof. Andreas Heyden for being such a good advisor and a true role model of a good scientists. He knows how to motivate graduate students without being a micromanager. Importantly for me, he knows how to reassure his graduate students when things do not go in the right direction. His knowledge and continuous acquisition of new ideas are a tremendous source of inspiration. I am thankful, particularly, for giving me the scope to discover my own path as a researcher.

I am grateful to my committee members, Drs. John R. Regalbuto, John R. Monnier, Mark J. Uline, Gabriel A. Terejanu, and John W. Weidner, for their guidance, time, and help. Also, I would like to thank Heyden group members, Dr. Salai Ammal, Dr. Jianmin Lu, Dr. Muhammad Faheem, Dr. Sina Behtash, and Mohammad Saleheen, who contributed to my thesis with their knowledge, work, and constructive criticisms. I also extend my thanks to Dr. Yongjie Xi, Dr. Supriya Saha, Wenqiang Yang, Charles Fricke, Kyung-Eun You, Adam Yonge, Elizabeth grace, and Subrata Kundu, for their support.

I am grateful to the Chemical Engineering Department staffs, Marcia Rowen, Loretta Hardcastle, Vernon Dorrell, and Brian Loggans, for assisting me with administrative and technical issues.

To all my USC friends, you made my life much more fun and exciting.

Finally, on a personal note, I would like to thank my parents for always giving me love, advice, and enrichment. I also want to thank my siblings for their support and love.

ABSTRACT

Due to the rapidly declining fossil fuel reserves and the onset of global climate change, the development of active, selective, and stable catalytic materials for the efficient production of biomass derived platform chemicals, i.e., levulinic acid (LA), succinic acid (SA), γ-valerolactone (GVL) etc., is receiving considerable attention in order to produce second generation biofuels and commodity chemicals. Though solid lignocellulosic biomass is significantly cheaper than petroleum; however, the available technology is the significant barrier for large scale utilization of biomass for the production of biofuels. The development of biomass conversion technology requires, 1) identification of potential biomass chemicals that can selectively be transformed into targeted molecules, 2) understanding fundamental bond breaking/formation mechanism (i.e. C-H, O-H, C-C bond cleavage and formation) at solid/gas and solid/liquid interface, and 3) identification of active site.

Among the 'top 10' platform biomass chemicals identified by the Department of Energy (DOE), GVL is of particular interest because of its widespread application as a gasoline blender and in the production of bio based polymers. Understanding the reaction kinetics governing the aqueous phase hydrodeoxygenation (HDO) of levulinic acid (LA) to γ-Valerolactone (GVL) over Ru surfaces will expedite the design of better catalysts for this conversion process considering that Ru/C catalyst is the most used catalysts for the HDO of LA. In this dissertation, we report a computational investigation of the reaction

mechanism of LA to GVL using DFT calculations and mean-field microkinetic modeling in both vapor and liquid phase reaction conditions.

In vapor phase calculations, our model predicts a dominant reaction route that propagates through the alkoxy formation step leading to the formation of a five member ring structure which is subsequently followed by a C-OH cleavage to form GVL. This pathway deviates from the previously proposed mechanism that involves formation of 4-hydroxypentanoic acid (HPA). At low temperature region (T<373 K), our model identifies that at a vapor phase condition Ru(0001) is not the experimentally observed active sites, while at high reaction temperatures (T > 423 K), Ru(0001) constitutes the majority of the active site. At high temperatures (T> 473 K), our model also confirms the experimental observation that α-angelica lactone (AGL) formation pathway is responsible for mild reversible catalysts deactivation. Next, our liquid phase results indicate that polar solvents (i.e. water) have a beneficial effect on the reaction kinetics of the hydrodeoxygenation of LA. Specifically, in an aqueous phase condition and 323 K reaction temperature, reaction rate is 4-5 order of magnitude higher in comparison to the rate at gaseous phase condition which explains the low temperature activity found in experimental studies. In contrast, non-polar solvents (1,4-dioxane) have a detrimental effect on the reaction kinetics, as also confirmed by several experimental studies, due to high solvent coverage on the Ru surface. In addition, our results also show that Ru (0001) is highly active for the hydrogenation of LA to its corresponding alcohol product, 4-Hydroxypentanoic acid (HPA), at a high reaction temperature above 373 K. However, at a low reaction temperature (T < 373 K), the hydrogenation rate is significantly slower than the measured experimental kinetics, even in the presence of an aqueous environment. Considering furthermore that the

hydrogenation of various short chain ketones (acetone, butanone-2, and pentanone-2) over Ru (0001) also lead to reaction rates much smaller than the rate predicted by experiments, we conclude that Ru (0001) is not the active site at low temperatures (T<373K) for HPA production, owing to the high activation barrier for the second C-H bond formation, i.e., alkoxy hydrogenation step. To identify the active Ru site for the experimentally observed low temperature activity for HPA formation, we performed a constrained thermodynamics study and identified surface oxygen species as a possible active site for the hydrogenation of LA. A computational investigation of the OH-assisted reaction pathway confirms the presence of a low energy pathway for the hydrogenation of LA to HPA in an aqueous environments.

TABLE OF CONTENTS

LIST OF TABLES

LIST OF FIGURES

CHAPTER 1 : INTRODUCTION

We follow the manuscript style format in this dissertation which means each chapter of this dissertation is an independent scientific publication. In chapter 2, we present the theoretical investigation of the hydrodeoxygenation (HDO) of levulinic acid (LA) to γ-valerolactone (GVL) over Ru (0001), this article has recently (January, 2017) been published in ACS Catalysis as a full length scientific article. In this work, we investigated the vapor phase kinetics for the HDO of LA via hydrogenation process and/or direct catalytic conversion process. In the hydrogenation pathway, hydrogenation of the ketone group in LA leads to the formation of 4-hydroxypentanoic acid (HPA). Subsequent dehydration and cyclization of HPA then leads to the formation of the desired product GVL. In the other catalytic route, i.e., direct catalytic conversion pathway, LA is directly converted to GVL without the formation of any intermediate product, such as HPA.

In chapter 3 (second publication), on the importance of angelica lactone (AGL) formation in the hydrodeoxygenation of levulinic acid to γ-valerolactone over Ru (0001) model surface: a density functional theory investigation, we follow the same research methodology as the first one to investigate the role of AGL formation pathway on the reaction kinetics by expanding the previous model to incorporate AGL derivatives and relevant reaction routes.

In chapter 4 (third publication), using implicit solvation method based on polarizable continuum approximation, we investigate the fluid phase kinetics for the LA conversion to GVL. These publications were supported by the National Science Foundation (NSF) grant (CBET-1159863), which was written as a collaborative undertaking between Dr. Andreas Heyden (computational part) and Dr. Jesse Bond (experimental part) to investigate the reaction kinetics governing the catalytic conversion of biomass molecule in order to identify activity and selectivity descriptor for designing of a better catalysts with higher reaction activity at typical reaction conditions.

CHAPTER 2 : THEORETICAL INVESTIGATION OF THE HYDRODEOXYGENATION OF LEVULINIC ACID TO γ-VALEROLACTONE OVER Ru (0001)

Mamun, O.; Walker, E.; Faheem, M.; Bond, J.Q..; Heyden, A. *ACS Catalysis*, **2016**, 7(1), 215-228.

Reprinted here with permission of the publisher

2.1 Abstract

The reaction mechanism of the hydrodeoxygenation (HDO) of levulinic acid (LA) to γ-valerolactone (GVL) has been investigated over a Ru(0001) model surface by a combination of plane-wave density functional theory (DFT) calculations and mean-field microkinetic modeling. Catalytic pathways involving the direct hydrogenation of LA to GVL with and without formation of the experimentally proposed 4-hydroxypentanoic acid (HPA) intermediate have been considered. In the low reaction temperature range of 323-373 K, the activity of the model Ru(0001) surface is low owing to a very small number of free sites available for catalysis. As a result, it is unlikely that Ru(0001) is the active site for the experimentally observed catalysis at low temperatures. In contrast, in the medium to high temperature range (423-523 K), the HDO of LA is facile over Ru(0001) and we predict at 423 K a turnover frequency, apparent activation barrier and forward reaction orders that are fairly close to prior experimental observations, leading us to suggest that Ru(0001) sites might constitute the active site for high temperature catalysis. Finally, our microkinetic analysis suggests that the HDO of LA occurs by LA adsorption, hydrogenation of LA to an alkoxy intermediate, surface ring closure, and –OH group removal, i.e., it does not occur via HPA production as previously suggested. The first hydrogenation step of LA towards the formation of an alkoxy intermediate is the most rate controlling step over Ru(0001).

Keywords: Ruthenium; Density functional theory; Hydrodeoxygenation; Microkinetic modeling; levulinic acid; γ-valerolactone (GVL)

2.2 Introduction

Our society relies heavily on fossil resources to meet its energy demand and to produce commodity and specialty chemicals (around 13% of petroleum is being used to produce non-fuel chemicals).[1-3] Depletion of fossil fuels and increased demand for second generation renewable fuels has stimulated research aimed at utilizing alternative energy and carbon sources based on biomass.[1] However, significant research challenges remain for implementation of a biorefinery that can economically compete with a petrochemical refinery, partially because of lack of fundamental understanding of the catalytic conversion processes.[4] Catalytic upgrading of targeted biomass-derived feedstocks can be achieved by hydro-treatment which often involves hydrodeoxygenation, decarboxylation, and hydrogenation/dehydration processes to reduce the oxygen content and to increase the energy density. Design of novel catalysts for the above mentioned hydro-treatment processes requires a better understanding of C-O, O-H, C-H, and C-C bond dissociations over transition metal catalysts. A number of experimental and computational studies have been published investigating various hydro-treatment processes;[5-7] however, a clear understanding of various bond cleavage processes on transition metal surfaces has not emerged yet. It is our hypothesis that more careful density functional theory (DFT) studies, tightly integrated with experimental data through microkinetic models, are needed to advance our understanding of various catalytic deoxygenation processes.

Levulinic acid (LA) has been identified as a potential platform chemical of a future biorefinery[4] that can be produced inexpensively and on a large scale from C_6 carbohydrates. Heeres and co-workers[8] identified a series of technologies to produce LA from both monomeric sugars and cellulose. Though it can be produced easily and with relatively high

yield from acid treatment, its isolation and purification is a complex process due to LA's high miscibility with liquid water. To facilitate the separation process, it has been proposed that unrefined LA be catalytically converted to γ-valerolactone (GVL),[9-10] which has comparable flexibility as a platform chemical as LA. GVL is sufficiently hydrophobic to allow an energy efficient separation from its aqueous reaction environment by extraction with a low-boiling acetate followed by facile distillation. GVL can be used as solvent,[11-12] fuel additive,[10, 13-15] and to produce nonfuel chemicals.[16] Horvath et al. have tested a mixture of conventional gasoline, ethanol and 10 vol% GVL and found improved combustion characteristics because of the lower vapor pressure of GVL as compared to other oxygenates, including methanol, ethanol, etc.[17] One proposed pathway to produce GVL involves the hydrogenation of LA to form 4-hydroxypentanoic acid (HPA) which then undergoes a ring closing reaction to produce GVL.[18] Manzer et al. screened the catalytic activity of carbon supported Ir, Rh, Pd, Ru, Pt, Re and Ni for the conversion of LA to HPA.[19] According to their study, Ru/C was found to be the most active and effective catalyst for the hydrogenation of LA. Luo et al.[20] also reported that supported Ru is the most active monometallic catalyst, though they found bimetallic random alloys such as Au-Pd/TiO_2 and Ru-Pd/TiO_2 to have better catalytic activity than monometallic Ru. However, performance of bimetallic alloys strongly depends on the preparation method, structural characteristics, and composition. Next, we highlight the scientific study by Cao et al.[21] who reported that Ru/C catalysts are more active than Ru/Al_2O_3 catalysts. They also reported a strong positive effect of potassium dopant on the catalyst activity and found that hydrogenation of LA is structure sensitive to the catalyst particle size. According to their discussion, they suggested a B5 type site (a site that consists of 5 surface atoms at the

interface of Ru(0001) and Ru(100)) as the likely active site for this reaction. However, Abdelrahman et al.[22] observed no particle size effect in the reaction kinetics of the HDO of LA to GVL in aqueous reaction environments, suggesting that the reaction is not structure sensitive and that Ru(0001) sites that constitute the majority of sites of the relatively large Ru nanoparticles on carbon supports should be equally active as B5 type sites.

It is the objective of this study to (1) identify the reaction mechanism of the HDO of LA to GVL over Ru(0001) and (2) to investigate if Ru(0001) sites are possibly the active site for catalysis at experimental low ($T < 373$ K) and high ($T > 473$ K) temperature reaction conditions. Specifically, Figure 2.1 illustrates two likely reaction pathways investigated for the HDO of LA to GVL. First, we investigated the hydrogenation of LA to form HPA which then undergoes a dehydration process to yield GVL (the previously proposed reaction pathway[22]) and second, we studied a direct conversion pathway which avoids the second hydrogenation of LA to HPA (a step often believed to be slow[23]) and which involves a combination of hydrogen addition and hydroxyl group elimination processes. We note that Sautet et al. previously investigated the hydrogenation of acetone[24] by a DFT study and found that addition of explicit water molecules significantly facilitates the hydrogenation over Ru(0001). However, considering the difficulty in accurately modeling a liquid phase environment from first principles (due to our inability to extensively sample solvent configurations), we focused in this investigation on DFT calculations in a vacuum environment and only considered the liquid phase in the chemical potentials of the reactants and products in our microkinetic model. In this way, our model is somewhat representative for a nonpolar (or weakly polar), aprotic reaction environment such as in liquid 1,4-dioxane although we are using the LA chemical potential of 0.45 M LA in liquid water for our

simulations (see below) [21]. To the best of our knowledge, no theoretical DFT and microkinetic modeling study has yet been published on the catalytic HDO of LA to GVL over transition metal catalysts.

2.3 Methods

All calculations have been performed using the Vienna Ab Initio Simulation Package (VASP) to perform plane-wave DFT calculations.[25] We used the projector augmented wave (PAW)[26] method to describe electron-ion interactions and the Perdew-Burke-Ernzerhof (PBE) functional with an energy cutoff for the plane waves of 400 eV in all calculations.[27-28] Dispersion interactions play a vital role in the accurate prediction of the energetics of adsorption and desorption processes of long chain hydrocarbon molecules.[29-30] Considering that the PBE functional is unable to describe these van der Waals interactions, we included them semi-empirically by using Grimme's DFT-D3 methodology.[30] In the appendix A, we illustrate that at least the gas phase energetics for the HDO of LA is reasonably well described by the PBE-D3 level of theory. To build a catalytic slab model, we first optimized the bulk hcp-Ru lattice constants which we computed to be $a = 2.704$ Å and $c/a = 1.577$. These lattice constants are in good agreement with the experimental values of $a = 2.705$ Å and $c/a = 1.582$.[31] Next, a Ru(0001) surface model was constructed as a periodic 4×4 slab with four metal layers that are separated by a vacuum of 15 Å to eliminate interactions between the slab and its periodic image along the direction perpendicular to its surface plane. The bottom two layers were fixed to bulk Ru positions and the upper two layers were relaxed in all optimizations. All adsorbate and transition state degrees of freedom were fully relaxed in

all calculations using a maximum force criterion of 0.01 eV/Å for all relaxed ionic degrees of freedom. Brillouin zone integration is done using a $4 \times 4 \times 1$ Monkhorst-Pack grid[32] and a 1st order Methfessel-Paxton smearing[33] of 0.1 eV.

Finally, the transition state of each elementary reaction step was determined by application of the NEB[34] method followed by the dimer method.[35-38] Each transition state was characterized by a unique imaginary frequency along the reaction coordinate computed by a numerical vibrational frequency calculation with a step length of 0.001 Å (the same step length is used for frequency calculations of all stable states).[39] In all vibrational frequency calculations all metal atoms were fixed in their relaxed optimized position and we only varied the hydrocarbon coordinates. Dimer calculations were performed with a force based criterion of 0.01 $^{eV}/_{\text{Å}}$ for all transition states except for four elementary reactions (r_{19}, r_{20}, r_{33} and r_{39}) for which we could not converge the dimer calculations to the desired convergence criterion. For these elementary reactions, we used a Brønsted-Evans-Polanyi (BEP)-type[40-41] relation described in the appendix A to estimate the activation barrier. Fortunately, a kinetic rate control analysis of our microkinetic model suggested that these four elementary reactions are not rate controlling such that our results are robust with regards to the higher uncertainty of the rate constants for these elementary steps.

2.3.1 Microkinetic modeling

Harmonic transition state theory (Eyring equation) was used to calculate elementary surface rate constants, $k_{forward}$.

$$k_{forward} = \frac{k_B T}{h} e^{-\frac{\Delta G^{\ddagger}}{k_B T}} \tag{2.1}$$

Here, k_B is the Boltzmann's constant, T is the reaction temperature, h is the Planck's constant, and $\Delta G^{\ddagger}$ is the free energy of activation. Free energies of reaction and activation are calculated as

$$\Delta G_{rxn} = \Delta E_{scf} + \Delta E_{zpe} - k_B T ln \frac{q_{vib}^{product}}{q_{vib}^{reactant}}, \tag{2.2}$$

$$\Delta G^{\ddagger} = \Delta E_{scf}^{\ddagger} + \Delta E_{zpe}^{\ddagger} - k_B T ln \frac{q_{vib}^{TS}}{q_{vib}^{reactant}} \tag{2.3}$$

$\Delta G_{rxn}\ (eV)$ is the free energy of reaction, q_{vib} represents the vibrational partition function of the adsorbates, E_{scf} is the self-consistent field energy, and ΔE_{zpe} is the zero-point energy correction which was calculated as $\frac{1}{2}\sum_i h\nu_i$ with ν_i being the vibrational frequencies. One well-known limitation of harmonic transition state theory (HTST) is that the motion described by low lying frequencies is not well described by the harmonic approximation which can lead to large over- or under-predictions of reaction rate constants. To reduce this potential error, we replaced all (real) frequencies below $100\ cm^{-1}$ by our cutoff value of $100\ cm^{-1}$. As a result, these low frequency modes cancel out in our calculation of rate constants.

For adsorption processes, the zero-point corrected adsorption energies are calculated as

$$\Delta E_{ads} = E_{slab+adsorbate} - E_{slab} - E_{adsorbate(gas)} + \Delta E_{zpe} \quad (2.4)$$

We used collision theory to calculate the forward rate constant of an adsorption process,

$$k_{forward,ads} = \frac{S_0}{N_0\sqrt{2\pi m k_B T}} \quad (2.5)$$

Here, N_0 is the number of sites per area (1.57×10^{19} $sites/_{m^2}$) and m denotes the molecular weight of the adsorbate. S_0 is the sticking coefficient and is assumed to be 1 in our model. The reverse rate constant, $k_{reverse}$, is calculated using

$$k_{reverse} = \frac{k_{forward}}{K_{equilibrium}} \quad (2.6)$$

where we used the harmonic oscillator and rigid rotor approximation (for fluid phase molecules) in the calculation of the equilibrium constant. Steady state mass balances are used to generate *N* differential equations for *N* adsorbed species. In addition, we used the overall site balance to build a microkinetic reactor model consisting of a set of differential and algebraic equations (DAE). To solve this full set of equations to its steady state solution and to obtain individual surface coverages and turnover frequencies (TOF), we used the BzzMath library.[42] No assumptions in regards to rate controlling steps, irreversibility, etc. have been made in the development of the microkinetic model.

2.4 Analysis of DFT results

Figure 2.2 illustrates the reaction pathways investigated for the HDO of LA over Ru(0001). Most stable adsorption geometries of all surface intermediates considered are shown in Figure A.3 in the appendix section at the end of this dissertation. Figure A.4 (see appendix A) illustrates all transition state geometries identified for various elementary

reactions (except for the four reactions for which we could not obtain a converged transition state geometry). The number of adsorption sites and the binding mode of the adsorption geometry are given in Table 2.1. We adopted for this paper the binding mode nomenclature $\eta_i\mu_j$ which designates that i atoms of the adsorbate are bound to j atoms of the metal surface. Table 2.2 lists the zero-point corrected reaction and transition state energy, imaginary frequency of the reaction coordinate in the transition state, and Gibb's free energy of reaction at various temperatures. In the following section, we will discuss the adsorbed intermediates and potential energy surface (PES). Then, we will discuss the results of our microkinetic reactor model which includes a sensitivity analysis of various parameters. Finally, we will discuss our computational findings in light of the experimental observations.

2.4.1 Potential energy surface and adsorption energies

The first step in the HDO of LA ($CH_3 - CO - CH_2 - CH_2 - COOH$) is the adsorption of the reactants, such as LA and H_2. LA adsorbs in $di - \sigma - \eta_2\mu_3(O,O)$ mode, which means it adsorbs through oxygen from both functional groups with an adsorption energy of -1.33 eV. When LA approaches the catalytic surface, the interaction between the metal surface and LA leads to the breaking of the π bond of the ketone and carboxyl group and those electrons tend to form σ bonds with the metal surface. Hydrogen adsorbs dissociatively on the Ru(0001) surface with an adsorption energy of -0.65 eV. We studied the atop, bridge, fcc and hcp adsorption sites for hydrogen adsorption and found the hcp site to be the most stable adsorption site for hydrogen adsorption. Next, the reaction proceeds either by hydrogenation or direct catalytic deoxygenation of LA. In the

hydrogenation pathway, the carbonyl group of LA is converted to the corresponding alcohol, 4-Hydroxypentanoic acid (HPA), which can undergo a surface dehydration mechanism along with a cyclization reaction to form GVL or which can desorb and form GVL by homogeneous, acid or base catalyzed esterification. In an alternative direct deoxygenation pathway, LA can go through at least three different catalytic reactions (removal of an –OH group, addition of an –H atom and ring closing reaction) to form the final GVL product.

2.4.1.1 LA hydrogenation to HPA ($LA* + 2H* \rightarrow HPA*$)

Hydrogenation of the carbonyl functional group leads to the formation of HPA. LA-derived hydrogenation can proceed either by initial C-H bond formation or O-H bond formation of the ketone group. This hydrogenation route has been well studied for various ketones by Neurock et al.[23] and Sautet et al.[24] In both studies, it was found that, at least for small ketones such as acetone, the C-H bond formation pathway, i.e., an alkoxy pathway, is favored over an O-H bond formation pathway, i.e., a hydroxy pathway. Here, scheme 2.1 shows all the reaction routes considered for hydrogenation of LA.

Scheme 2.1: LA hydrogenation to HPA pathways

Reaction Route	Name	Pathway
Reaction Route-1	Alkoxy pathway	$LA* + 2H* \rightarrow Al* + H* \rightarrow HPA*$ $(r_3 \rightarrow r_5)$
Reaction Route-2	Hydroxy pathway	$LA* + 2H* \rightarrow Hy* + H* \rightarrow HPA*$ $(r_4 \rightarrow r_6)$

In the alkoxy pathway, hydrogen binds to the carbon from the ketone group to form an alkoxy intermediate ($CH_3 - CH(\dot{O}) - CH_2 - CH_2 - COOH$), for which the preferred mode for adsorption is $\eta_2\mu_4(O,O)$. The reaction and activation energy for this reaction (r_3) are 0.06 and 0.67 eV, respectively, which indicates that this thermo-neutral reaction possesses only a moderate activation barrier. Then, the alkoxy intermediate is further hydrogenated to form HPA ($CH_3 - CH(OH) - CH_2 - CH_2 - COOH$) which is the corresponding alcohol product of LA. HPA is one of the stable products of this HDO process that can be collected as products. The most stable mode of HPA adsorption was found to be $\eta_3\mu_3(O,C,O)$ where the carbon and oxygen of the carboxyl group bind on two adjacent atop sites and the oxygen from the ketone group binds weakly on another atop site. This second hydrogenation step (r_5) has a reaction and activation energy of 0.76 eV and 1.29 eV, respectively. In the alkoxy pathway, the second hydrogenation to form HPA is the rate-limiting step as suggested by the high activation energy. For the hydroxy mechanism, the order of hydrogen addition is opposite to the alkoxy mechanism. The reaction and activation energy of LA hydrogenation to the hydroxy intermediate, r_4, ($CH_3 - \dot{C}(OH) - CH_2 - CH_2 - COOH$) are 0.88 eV and 1.36 eV, respectively, and the subsequent second hydrogenation to HPA, r_6, has a reaction and activation energy of -0.05 eV and 0.76 eV, respectively. From the energy profile of the alkoxy and hydroxyl pathway shown in Figure 2.3, we can conclude that the alkoxy pathway is favored over the hydroxy mechanism which agrees with previous computational studies on the hydrogenation of small ketone molecules.[23-24]

2.4.1.2 HPA dehydration to form GVL ($HPA* \rightarrow GVL* + H* + OH*$)

Dehydration of surface adsorbed HPA is a complex three step process that results in the formation of GVL and surface hydroxyl and hydrogen which can combine to produce water. This reaction mechanism includes three different types of reactions such as

- -OH removal, i.e., C-OH bond scission either from the alcohol or carboxylic acid group
- -H removal, i.e., O-H bond scission
- Ring closure and lactone formation

Since we found that direct ring formation from HPA leads to a high energy surface species, in scheme 2.2, we considered only the following pathways for GVL formation from HPA.

Scheme 2.2: HPA dehydration to GVL pathways

Reaction Route	**Name**	**Pathway**
Reaction Route-3	Hydrogenation of –COOH group of HPA with subsequent –OH elimination	$HPA* + H* \rightarrow I-02* \rightarrow I-04* + OH* \rightarrow I-07* + H* + OH* \rightarrow I-08* + H* + OH* \rightarrow GVL* + 2H* + OH*$ $(r_8 \rightarrow r_{13} \rightarrow r_{22} \rightarrow r_{24} \rightarrow r_{31})$
Reaction Route-4	Hydrogenation of –COOH group of HPA with subsequent –H removal	$HPA* + H* \rightarrow I-02* \rightarrow I-05* + H* \rightarrow I-07* + OH* + H* \rightarrow I-08* + H* + OH* \rightarrow GVL* + 2H* + OH*$ $(r_8 \rightarrow r_{15} \rightarrow r_{23} \rightarrow r_{24} \rightarrow r_{31})$

Reaction Route-5	-OH removal from –COOH group of HPA with subsequent –H deletion	$HPA* \rightarrow I-01* + OH*$ $\rightarrow I-06* + H* + OH*$ $\rightarrow GVL* + H* + OH*$ $(r_7 \rightarrow r_{11} \rightarrow r_{30})$
Reaction Route-6	-OH elimination from –COOH group from HPA with subsequent –H addition	$HPA* \rightarrow I-01* (+H*) + OH*$ $\rightarrow I-04* + OH*$ $\rightarrow I-07* + H* + OH*$ $\rightarrow I-08* + H* + OH*$ $\rightarrow GVL* + 2H* + OH*$ $(r_7 \rightarrow r_{12} \rightarrow r_{22} \rightarrow r_{24} \rightarrow r_{31})$
Reaction Route-7	-OH elimination from alcohol functional group of HPA with subsequent ring closing	$HPA* \rightarrow I-03* + OH*$ $\rightarrow I-08* + OH*$ $\rightarrow GVL* + H* + OH*$ $(r_{10} \rightarrow r_{20} \rightarrow r_{31})$
Reaction Route-8	-OH elimination from alcohol functional group with subsequent –H removal	$HPA* \rightarrow I-03* + OH*$ $\rightarrow I-09* + OH* + H*$ $\rightarrow GVL* + H* + OH*$ $(r_{10} \rightarrow r_{21} \rightarrow r_{33})$

Reaction Route-3

Hydrogenation of HPA at the carboxyl group produces I-02 ($CH_3 - CH(OH) - CH_2 - CH_2 - \dot{C}(OH)_2$) which we found to bind to the Ru(0001) surface with a binding energy of -1.94 eV, which is as expected significantly higher in energy than HPA. The reaction energy of this step, r_8, is 0.55 eV and the activation barrier is 1.02 eV. Subsequent removal of an -OH group from the terminal $-C(OH)_2$ leads to I-04 ($CH_3 - CH(OH) - CH_2 - CH_2 - \ddot{C} - OH$). This step, r_{13}, is thermodynamically downhill by -0.37 eV and possesses an activation barrier of 0.29 eV. Subsequent hydrogen removal of I-04, r_{22}, yields I-07 ($CH_3 - CH(\dot{O}) - CH_2 - CH_2 - \ddot{C} - OH$), which adsorbs strongly with a reaction and activation energy of -0.44 eV and 0.59 eV, respectively. Cyclization of I-07,

r_{24}, produces the desired five-member ring structure I-08 ($CH_3 - C_4OH_5 - OH$), which is an endothermic process with a reaction and activation energy of 0.21 eV and 1.28 eV, respectively. Final hydrogen removal from the terminal –OH group, r_{31}, produces the desired product GVL. This step possesses a reaction and activation energy of -0.72 eV and 0.75 eV, respectively. GVL binds to the surface through its carbonyl group with $\eta_2\mu_4(O,C)$ mode and desorption is endothermic by 0.72 eV. In this route, the first reaction step, r_8, is the rate limiting step as it is both thermodynamically and kinetically unfavorable with a highly endothermic heat of reaction and high activation energy.

Reaction Route-4

The fourth pathway is very similar to the third pathway except that hydrogen removal from intermediate I-02 occurs ahead of the dehydroxylation, i.e., I-02 first decomposes to hydrogen and I-05 ($CH_3 - CH(\dot{O}) - CH_2 - CH_2 - \dot{C}(OH)_2$), which then undergoes a C–OH bond scission at the terminal -$\dot{C}(OH)_2$ group to produce I-07 ($CH_3 - CH(\dot{O}) - CH_2 - CH_2 - \dot{C}(OH)$). The first step of this reaction pathway (r_{15}) possesses a reaction and activation energy of -0.25 eV and 0.64 eV, respectively, and the second step (r_{23}) has a reaction and activation energy of -0.56 eV and 0.75 eV, respectively. Finally, reaction pathways following production of surface intermediate I-07 have already been described above.

Reaction Routes-5 and 6

Hydroxyl group elimination from HPA (r_7) produces surface intermediate I-01 ($CH_3 - CH(OH) - CH_2 - CH_2 - \dot{C} = O$) which is an exothermic reaction (ΔE_0 = -0.66 eV) with a small activation barrier of 0.15 eV. I-01 can then follow an exothermic dehydrogenation step (r_{11}) from the alcohol group to produce I-06 ($CH_3 - CH(\dot{O}) -$

$CH_2 - CH_2 - \dot{C} = O$) ($\Delta E_0$ = -0.88 eV, $E_{a,0}$ = 0.36 eV). Next, I-06 can undergo an endothermic (ΔE_0 = 0.76 eV) ring closure reaction, r_{30}, with an energy barrier of 1.24 eV to produce GVL. The large activation barrier for this reaction is a consequence from intermediate I-06 strongly binding through 3 adsorption sites whereas GVL binds only moderately strong through two adsorption sites, $\Delta E_0(LA(g) + H_2(g) + 2 * \rightarrow GVL ** + H_2O(g))$ = -1.44 eV. Alternative to route-5, surface intermediate I-01 ($CH_3 - CH(OH) - CH_2 - CH_2 - \dot{C} = O$) can be hydrogenated to form I-04, r_{12}, ($CH_3 - CH(OH) - CH_2 - CH_2 - \ddot{C}(OH)$, which connects this pathway with reaction route-3 already discussed above. Considering that the hydrogenation reaction of I-01 to I-04, r_{12}, is highly endothermic with a high barrier (ΔE_0 = 0.83 eV, $E_{a,0}$ = 1.54 eV) this pathway is unlikely to occur.

*Reaction Route-*7

This reaction route starts by C-OH bond cleavage of the alcohol group of HPA to produce surface intermediate I-03, r_{10}, ($CH_3 - \dot{C}H - CH_2 - CH_2 - COOH$) ($\Delta E_0$ = -0.34 eV, $E_{a,0}$ = 0.99 eV). Ring closure in I-03 produces I-08 (r_{20}). While we could not clearly identify a transition state for this endothermic reaction (ΔE_0 = 0.28 eV), based on BEP correlations described below, we expect this step to possess a barrier of about 0.81 eV. Finally, hydrogen removal from I-08, r_{31}, leads to GVL (ΔE_0 = -0.72 eV, $E_{a,0}$ = 0.75 eV).

Reaction Route-8

Reversing the order of the dehydrogenation and ring closure steps of the previous pathway leads to reaction route-8. Dehydrogenation of the carboxyl group in I-03, r_{21}, leads to surface intermediate I-09 ($CH_3 - \dot{C}H - CH_2 - CH_2 - C(\dot{O}) = O$) ($\Delta E_0$ = -0.98 eV, $E_{a,0}$ = 0.34 eV). Again, we could not clearly identify a transition state for the

endothermic ring closure reaction to GVL (ΔE_0 = 0.54 eV); however, BEP correlations for this ring closure reaction (r_{33}) suggest an activation barrier of 1.04 eV.

Overall, we note that a slow step in all reaction routes involving HPA is the formation of HPA by hydrogenation of LA. Particularly, Figure 2.3A illustrates that the second hydrogenation step is relatively slow, questioning whether GVL production over Ru(0001) occurs via HPA.

2.4.1.3 Direct catalytic conversion of LA to GVL ($LA* \rightarrow GVL* + H* + OH*$)

An alternative pathway for the production of GVL from LA involves the direct deoxygenation of LA on the Ru(0001) surface without formation of HPA. Again, we found that direct ring formation from LA results in high energy species such that we rejected this possibility from our reaction mechanism. Instead, we considered only the following pathways for direct GVL formation from LA. Scheme-2.3 lists all the reaction routes considered for the direct catalytic conversion of LA.

Scheme 2.3: Direct catalytic conversion of LA

Reaction Route	**Name**	**Pathway**
Reaction Route-9	Alkoxy route with subsequent –OH elimination	$LA* + 2H* \rightarrow Al* + H* \rightarrow I-06* + OH* + H* \rightarrow GVL* + H* + OH*$ $(r_3 \rightarrow r_{14} \rightarrow r_{30})$
Reaction Route-10	Alkoxy route with subsequent ring closing	$LA* + 2H* \rightarrow Al* + H* \rightarrow I-18* + H* \rightarrow GVL* + H* + OH*$ $(r_3 \rightarrow r_{17} \rightarrow r_{25})$

Reaction Route-11	Alkoxy route with subsequent –H addition	$LA* + 2H* \rightarrow Al* + H* \rightarrow I-05* \rightarrow I-07* + OH* \rightarrow I-08* + OH* \rightarrow GVL* + H* + OH*$ $(r_3 \rightarrow r_{16} \rightarrow r_{23} \rightarrow r_{24} \rightarrow r_{31})$
Reaction Route-12	Hydroxy route with subsequent ring closing-1	$LA* + 2H* \rightarrow Hy* + H* \rightarrow I-13* + H* \rightarrow I-16* + H* + OH* \rightarrow I-15* + 2H* + OH* \rightarrow GVL* + H* + OH*$ $(r_4 \rightarrow r_{19} \rightarrow r_{27} \rightarrow r_{28} \rightarrow r_{32})$
Reaction Route-13	Hydroxy route with subsequent ring closing-2	$LA* + 2H* \rightarrow Hy* + H* \rightarrow I-13* + H* \rightarrow I-16* + H* + OH* \rightarrow I-08* + OH* \rightarrow GVL* + H* + OH*$ $(r_4 \rightarrow r_{19} \rightarrow r_{27} \rightarrow r_{29} \rightarrow r_{31})$
Reaction Route-14	Hydroxy route with subsequent –OH removal-1	$LA* + 2H* \rightarrow Hy* + H* \rightarrow I-14* + H* + OH* \rightarrow I-16* + H* + OH* \rightarrow I-15* + 2H* + OH* \rightarrow GVL* + H* + OH*$ $(r_4 \rightarrow r_{18} \rightarrow r_{26} \rightarrow r_{28} \rightarrow r_{32})$
Reaction Route-15	Hydroxy route with subsequent –OH removal-2	$LA* + 2H* \rightarrow Hy* + H* \rightarrow I-14* + H* + OH* \rightarrow I-16* + H* + OH* \rightarrow I-08* + OH* \rightarrow GVL* + H* + OH*$ $(r_4 \rightarrow r_{18} \rightarrow r_{26} \rightarrow r_{29} \rightarrow r_{31})$
Reaction Route-16	-H removal from –COOH group of LA	$LA* + 2H* \rightarrow I-11* + 3H* \rightarrow I-12* + 2H* \rightarrow I-17* + 2H* \rightarrow I-18* + H* \rightarrow GVL* + H* + OH*$ $(r_{35} \rightarrow r_{38} \rightarrow r_{39} \rightarrow r_9 \rightarrow r_{25})$
Reaction Route-17	-OH elimination from –COOH group of LA with subsequent ring closing	$LA* + 2H* \rightarrow I-10* + 2H* + OH* \rightarrow I-15* + 2H* + OH* \rightarrow GVL* + H* + OH*$ $(r_{34} \rightarrow r_{36} \rightarrow r_{32})$
Reaction Route-18	-OH elimination from –COOH group of LA with subsequent -H addition	$LA* + 2H* \rightarrow I-10* + 2H* + OH* \rightarrow I-06* + H* + OH* \rightarrow GVL* + H* + OH*$

	$(r_{34} \rightarrow r_{37} \rightarrow r_{30})$

Reaction Route-9

This reaction route proceeds via LA hydrogenation and formation of an alkoxy intermediate (r_3), followed by –OH group removal from the –COOH group of the alkoxy species (r_{14}) yielding intermediate I-06. This exothermic reaction step (ΔE_0 = -0.77 eV) possesses a very low activation barrier of only 0.12 eV. The ring closure of I-06, r_{30}, follows as in reaction route-5. Clearly, this reaction route is preferred to reaction route-5 as it avoids the energetically demanding second hydrogenation of LA to HPA.

Reaction Route-10

Alternatively, the alkoxy intermediate can directly undergo a ring closure reaction to form I-18 ($C_4OH_5(CH_3)(\dot{O})(OH)$), r_{17}, (ΔE_0 = 0.22 eV, $E_{a,0}$ = 0.33 eV) which binds to the metal surface in $\eta_2\mu_3(O,O)$ mode where both the oxygen from the carboxyl group bind on two adjacent atop sites. The adsorption energy of I-18 ($E_{ads,0}$ = -1.44 eV) suggests a weak interaction between the adsorbate and the metal surface. In the next step, the C-OH bond at the C_1 of the intermediate I-18 is cleaved, leading to the formation of the final reaction product GVL. This step, r_{25}, is accompanied by a very low activation energy and moderate heat of reaction (ΔE_0 = -0.24 eV, $E_{a,0}$ = 0.04 eV). Thermodynamically, this route is feasible as the first step is thermo-neutral (ΔE_0 = 0.06 eV), the second step is only moderately endothermic (ΔE_0 = 0.22 eV), and the third step is moderately exothermic (ΔE_0 = -0.24 eV). Also, kinetically this reaction route is facile as all activation barriers in this route are either only moderately high ($E_{a,0}$ = 0.67 eV for r_3) or low ($E_{a,0}$ = 0.33 eV for r_{17} and $E_{a,0}$ = 0.04 eV for r_{25}).

Reaction Route-11

A theoretically possible reaction pathway is the hydrogenation of the alkoxy intermediate at the terminal carboxyl group to form the reaction intermediates I-5 ($CH_3 - CH(\dot{O}) - CH_2 - CH_2 - \dot{C}(OH)_2$) which binds to the metal surface in $\eta_2\mu_5(O,C)$ mode. This reaction path, r_{16}, is highly endothermic with a high activation energy (ΔE_0 = 1.06 eV, $E_{a,0}$ = 1.41 eV) because the resulting intermediate has a $C(OH)_2$-group which we generally find to be quite unstable. This high reaction energy and activation energy make this reaction route both thermodynamically and kinetically unfavorable. After the formation of I-5 this routes follows the reaction path described in reaction route-4.

Reaction Routes-12, 13, 14 and 15

After formation of the kinetically demanding hydroxy intermediate from LA via O-H bond formation, the intermediate can either go through a ring closure reaction step to form I-13, r_{19}, ($CH_3(OH) - C_4OH_4 - OH$) (ΔE_0 = 0.04 eV, $E_{a,0}$ = 0.60 eV) or an –OH elimination step, r_{18}, to form I-14 ($CH_3 - \ddot{C} - CH_2 - CH_2 - COOH$) ($\Delta E_0$ = -0.50 eV, $E_{a,0}$ = 0.84 eV). Next, a C-OH bond scission at the C_1, r_{27}, leads to the formation of surface intermediate I-16 ($C_4OH_4(CH_3)(O)$) which is a ring species with two unsaturated carbon atoms. This reaction is exothermic with a heat of reaction value of -0.42 eV and a high activation energy of 0.86 eV. Alternatively, I-14 can undergo a cyclization process to produce I-16, this step (r_{26}) is slightly endothermic with a moderate activation energy (ΔE_0 = 0.16 eV, $E_{a,0}$ = 0.48 eV). Reaction steps from I-16 can then follow two different pathways to form GVL, in one pathway it is hydrogenated at the C_1 and then undergoes an O-H bond scission at the terminal OH group; in another pathway it goes through the same two elementary reaction steps but in an opposite order. Hydrogenation of I-16 at the C_1 (r_{29})

leads to the formation of I-8 ($C_4OH_5(CH_3)(OH)$), which binds to the surface with the unsaturated C_4 on the bridge site and with an adjacent ring oxygen on the atop site. The reaction energy of this step is moderately endothermic (0.35 eV) with a high activation energy of 0.87 eV. I-8 is then dehydrogenated (O-H bond scission) to form GVL (r_{31} - this step has already been discussed above). Alternatively, hydrogen removal from I-16, r_{28}, produces reaction intermediate I-15 ($C_4OH_4(CH_3)(O)$) which has two unsaturated atoms (C_1 and a branched oxygen atom) and binds to the surface via its carbon at a bridge site. This reaction step is exothermic (ΔE_0 = -0.50 eV) with a relatively high activation energy ($E_{a,0}$ = 0.73 eV). The next step is the hydrogenation of I-15 at C_1 to form GVL, this reaction step, r_{32}, is endothermic (ΔE_0 = 0.13 eV) with a very high activation energy ($E_{a,0}$ = 0.97 eV) which renders this route to be improbable.

Reaction Route-16

This reaction route starts with an O-H bond cleavage of the carboxyl group of LA that leads to the formation of I-11 ($CH_3 - CO - CH_2 - CH_2 - CO\dot{O}$). This reaction step is exothermic (ΔE_0 = -1.13 eV) with a very small activation barrier (0.06 eV). I-11 binds to the metal surface in its $\eta_3\mu_3(O,O,O)$ mode, i.e., all three oxygen atoms from both functional groups participate in the adsorption process and all of them bind on the atop sites with an adsorption energy of -1.82 eV. Next, hydrogenation of the carbonyl carbon yields I-12 ($CH_3 - CH(\dot{O}) - CH_2 - CH_2 - CO\dot{O}$) which also binds to the surface via its three oxygen atoms. This endothermic reaction step (ΔE_0 = 0.45 eV) possesses a moderate activation barrier of 0.68 eV. Intermediate I-12 can then undergo a cyclization process to form I-17 ($C_4OH_5(CH_3)(\dot{O})(\dot{O})$) which binds to the surface via its carboxyl oxygen atoms in $\eta_2\mu_3(O,O)$ mode. However, this reaction step is highly endothermic with a heat of

reaction 1.01 eV. Also, BEP correlations predict an activation energy of 1.49 eV for this reaction step that we could not converge with a dimer calculation to our desired accuracy. Adsorbed intermediate I-17 can be hydrogenated at its terminal carboxyl group to yield I-18 ($C_4OH_5(CH_3)(\dot{O})(OH)$) which is also a five-member ring structure that binds to the surface in $\eta_1\mu_1(O)$ mode. This thermo-neutral step (ΔE_0 = -0.04 eV) possesses a relatively moderate activation energy of 0.32 eV. Finally, I-18 is converted to GVL via a C-OH bond scission step which completes this route with a reaction energy of -0.24 eV and an activation energy of 0.04 eV. Although this last step is kinetically very facile, this route is highly unlikely to occur under practical reaction conditions considering the high endothermicity and reaction barrier for the ring closure reaction step r_{39}.

Reaction Route-17

In this reaction route, C-OH bond scission at the carboxyl functional group of LA produces intermediate I-10 ($CH_3 - CO - CH_2 - CH_2 - \dot{C}OO$) which binds to the metal surface through three atoms, $\eta_3\mu_3(O,C,O)$. The oxygen from the ketone group binds to a Ru atop site while the oxygen and carbon from the carboxylate group bind to two adjacent bridge sites. This exothermic reaction (ΔE_0 = -0.61 eV) possesses an activation energy of 0.71 eV. Next, a ring closing reaction occurs (ΔE_0 = 0.52 eV, $E_{a,0}$ = 0.87 eV) to produce I-15 ($C_4OH_4(CH_3)(O)$) which binds to the surface in $\eta_1\mu_1(C)$ mode. Further hydrogenation of I-15 leads to the formation of GVL. This endothermic reaction step (ΔE_0 = 0.13 eV) has a relatively high activation energy of 0.97 eV such that this reaction route is unlikely to occur under experimental reaction conditions.

Reaction Route-18

Alternatively, the intermediate I-10 produced in the previous reaction route can be hydrogenated at the C_1 carbon to produce intermediate I-6 ($CH_3 - CH(\dot{O}) - CH_2 - CH_2 - \dot{C}O$) which adsorbs on five metal atoms, $\eta_3\mu_5(O,C,O)$, with a reaction and activation energy of -0.10 eV and 0.70 eV, respectively. I-6 is then converted to GVL via reaction step r_{32} that has already been discussed above. Based on our analysis of the energetics of various intermediates and transition states, it is difficult to identify a preferred mechanism without development of a mean-field microkinetic model under realistic reaction conditions. As a result, we developed in the next section such a model based on parameters obtained from the DFT calculations and harmonic transition state theory.

2.4.2 Microkinetic modeling

To identify the intrinsic catalytic activity, dominant reaction mechanism, and rate controling steps for the conversion of LA to GVL over Ru(0001), we developed a mean-field microkinetic model based on the first principles data discussed above and the steady state species balances of various adsorbed intermediates. In the microkinetic models, we used a reaction temperature varying from 323 to 523 K and chemical potentials of the reactant and product species corresponding to a hydrogen partial pressure of 10 bar, a 0.45 M liquid solution of LA (see section A.4 of appendix A for a conversion to a hypothetical LA partial pressure), and a product chemical potential/partial pressure corresponding to 0.11% LA conversion which is somewhat charcteristic of experimental studies for the conversion of LA to GVL.[22] Next, we solved for the steady state solution of all adsorbed species and the free site coverage (site balance) using BZZMath.[42]

2.4.2.1 Adsorbate-adsorbate interactions

A limitation of conventional mean field models is that elementary rate constants are often coverage independent, although we frequently observe strong (repulsive) coverage dependent adsorption energies. Without considering lateral interactions, we observed a hydrogen covered surface and very small free site coverage which leads to an unrealistically small turnover frequency (the surface is poisoned by hydrogen). To at least approximately consider lateral interactions in our microkinetic models, we used the method proposed by Grabow et al.[43] for fitting coverage dependent differential adsorption energies, $\mathrm{E_a}^{differential}$, of hydrogen and oxygen (the oxygen coverage can become substantial at high water and low hydrogen chemical potential).

$$\mathrm{E_a}^{differential}(\theta_\mathrm{a},\theta_\mathrm{b}) = \begin{cases} E_0 + 2\varepsilon_{a-a}\left(\theta_\mathrm{a} - \theta_{\mathrm{a},0}\right) + \varepsilon_{0,a-b}\,\theta_\mathrm{b} \quad + \\ \frac{3}{2}\ \varepsilon_{0,a-b}\,\theta_\mathrm{b}\ \sqrt{\theta_\mathrm{a}\ \ \theta_\mathrm{b}} \quad if\ \left(\theta_\mathrm{a} - \theta_{\mathrm{a},0}\right) > 0 \\ E_0 + \varepsilon_{0,a-b}\,\theta_\mathrm{b} \quad + \\ \frac{3}{2}\ \varepsilon_{0,a-b}\,\theta_\mathrm{b}\ \sqrt{\theta_\mathrm{a}\ \ \theta_\mathrm{b}} \quad if\ \left(\theta_\mathrm{a} - \theta_{\mathrm{a},0}\right) \le 0 \end{cases} \tag{2.7}$$

where E_0 is the low coverage adsorption energy and ε_{a-a}, $\theta_{\mathrm{a},0}, and\ \varepsilon_{0,a-b}$ are fitting parameters. A detailed procedure for calculating the lateral interaction parameters is given in the appendix A. The functional form of the lateral interactions implemented in our model is (in units of eV)

$$E_H^{differential}(\theta_H, \theta_O)$$

$$= \begin{cases} -0.68 + 0.15(\theta_H - 0.12) + 0.31 \times \theta_O + \\ 3.99 \times \theta_O \sqrt{\theta_H \theta_O} \quad if\ (\theta_H - 0.12) > 0 \\ -0.68 + 0.31 \times \theta_O + \\ 3.99 \times \theta_O \sqrt{\theta_H \theta_O} \quad if\ (\theta_H - 0.12) \leq 0 \end{cases} \tag{2.8}$$

$$E_O^{differential}(\theta_O, \theta_H)$$

$$= \begin{cases} -2.994 + 2.014(\theta_O - 0.07) + 0.31 \times \theta_H + \\ 3.99 \times \theta_H \sqrt{\theta_O \theta_H} \quad if\ (\theta_O - 0.07) > 0 \\ -2.994 + 0.31 \times \theta_H + \\ 3.99 \times \theta_H \sqrt{\theta_O \theta_H} \quad if\ (\theta_O - 0.07) \leq 0 \end{cases} \tag{2.9}$$

In our microkinetic model, we used the lateral interaction in the hydrogen adsorption step and water dissociation step only, i.e., we assume that surface reactions are less sensitive to the lateral interaction effects due to the fact that lateral interactions will have a similar effect on the reactant and transition state. The negelect of most lateral interactions is furthermore justified as hydrogen is the dominant surface species and its lateral interaction with most hydrocarbon species is often found to be small and within the accuracy of our DFT calculations with empririal dispersion interaction.

2.4.2.2 Models and activity results

In our microkinetic modeling, we develop two different physical models, namely, a 1-site and a 2-site model. In the 1-site model, all surface species compete for adsorption sites, while in the 2-site model, we used two different sites, one site that is only accessible to hydrogen denoted as triangle (Δ) and another site that is only accessible to all other species but hydrogen denoted by asterisk (*). The rationale for using a two site model is

that (1) hydrogen is a very small atom that can potentially adsorb on interstitial adsorption sites of other large hydrocarbon molecules, thus making hydrogen adsorption a non-competitive process and (2) that the PBE-D3 functional likely overestimates the hydrogen adsorption energy such that a one site model might erroneously predict a too low TOF due to hydrogen poisoning. By using both models, our results should be less sensitive to the accuracy of the PBE-D3 functional and there is a higher chance that the activity of Ru(0001) is at least bracketed by these two models. Next, recent experimental observations from Abdelrahman et al.[22] suggested such a 2-site model based on a Langmuir-Hinshelwood interpretation of their experimental kinetic data. Unless otherwise specified, we will report results obtained from the conventional 1-site microkinetic model and list in square brackets [] the 2-site model results. The TOF reported for the 2-site model is based on the number of sites a non-hydrogen species can adsorb. In table 2.3, we tabulate the turnover frequency for both models at various temperatures along with the steady state coverage of the key surface intermediates. At low temperature (323K) we found the Ru(0001) surface to be fully covered by hydrogen (99.99% [100.00%]). 2-site model results show that the hydrocarbon adsorption site (*) is covered by I-11 ($CH_3 - CO - CH_2 - CH_2 - CO\dot{O}$) and I-6 ($CH_3 - CH(\dot{O}) - CH_2 - CH_2 - \dot{C}O$) with a surface coverage of 79.80% and 19.86% , respectively. The empty site coverage is only 1.47×10^{-4}% [3.97×10^{-3}%] which explains why the predicted TOF ($2.67 \times 10^{-9}\ s^{-1}$ [$1.94 \times 10^{-6}\ s^{-1}$]) is very low at 323 K. In our microkinetic model, LA adsorption is proportional to the square of the empty site coverage and hence a small change in empty site coverage has a significant effect on the activity of the model Ru(0001) surface. From the experimental study by Abdelrahman et al.,[22] the low temperature TOF of LA conversion to

GVL is reported to be $2.00 \times 10^{-3}\ s^{-1}$ which indicates that our model is underestimating the TOF by six [three] orders of magnitude. In other words, it suggests that Ru(0001) is likely not the active site at low temperatures (and vapor phase condition). The experiment by Abdelrahman et al. was conducted in a liquid water phase environment and water has possibly a positive effect on the catalytic performance of the Ru catalyst due to the polar nature of the adsorbates and the oxophillic nature of the metal surface.[23-24] At a slightly elevated temperature (373 K), the H coverage is found to be 99.10% [100.00%] and the empty site coverage is 2.05×10^{-3}% [9.95×10^{-3}%]. This improvement in empty site coverage increased the TOF by 4 orders of magnitude for the 1-site model and by 2 orders of magnitude for the 2-site model ($1.83 \times 10^{-5}\ s^{-1}$ [$4.33 \times 10^{-4}\ s^{-1}$]).

At moderately high temperatures (423-473 K), the coverage of all surface species including hydrogen decreases due to large entropic effects, i.e., the empty site coverage increases dramatically at those temperatures, and hence, a dramatic increase in TOF can be observed. At 423 K, the empty site coverage and TOF are 0.01% [0.02%] and $4.09 \times 10^{-3}\ s^{-1}$ [$1.94 \times 10^{-2}\ s^{-1}$], respectively. The experimental TOF at 423 K was reported to be $4.80 \times 10^{-1}\ s^{-1}$,[9] i.e., we are underestimating the TOF by about two [one] orders of magnitude which we consider to be within the error of microkinetic modeling results based on DFT data. Finally, in the high temperature range (473-523 K) where the free site coverage is substantial, the TOF varies from 0.11-0.90 s^{-1} [0.29-2.08 s^{-1}].

A careful examination of the individual TOFs of all elementary reaction steps at 423 K reveals valuable insights into the dominant reaction mechanism. After adsorption of LA and hydrogen on the catalytic surface, the reaction proceeds via four different routes; namely, r_3 (LA hydrogenation to form the Alkoxy intermediate), r_4 (LA hydrogenation to

form the Hydroxy intermediate), r_{34} (-OH group elimination from the acid group of LA to produce I-10), and r_{35} (O-H bond scission from the acid group of LA to produce I-11). In our earlier discussion of the PES, we found that the alkoxy pathway is thermodynamically favored over the hydroxy pathway and our microkinetic model also suggests that the alkoxy pathway is the preferred pathway of the four competitive routes. Then, the alkoxy intermediate can proceed through four different routes such as hydrogenation at the oxygen of the ketone group to form HPA, -OH group elimination at the acid group to form I-06, O-H bond formation at the acid group to produce an oversaturated intermediate I-05, or cyclization reaction to form a C-O bond between the oxygen of the ketone group and carbon from the acid group to produce a five-member ring structure I-18. Of these four routes, the dominant reaction pathway involves the cyclization reaction (r_{17}) to form I-18. Then, I-18 undergoes a C-OH bond scission step (r_{25}) to form the final desired product GVL. The dominant reaction mechanism of both our microkinetic models for LA conversion to GVL on Ru(0001) surface was found to be $LA \rightarrow Al \rightarrow I-18 \rightarrow GVL$ ($CH_3-CO-CH_2-CH_2-COOH\ ** \leftrightarrow CH_3-CH(\dot{O})-CH_2-CH_2-COOH\ ** \leftrightarrow C_4OH_5(CH_3)(\dot{O})(OH)\ * \leftrightarrow CH_3-C_4OH_5=O\ **$). We note that this observation questions the validity of prior DFT studies of the hydrogenation of LA to GVL over Ru(0001) that only focussed on the hydrogenation of LA to HPA. The second hydrogenation step in the formation of HPA possesses a significant barrier that is avoided in our proposed reaction mechanism over Ru(0001). Finally, to test the sensitive of our conclusions with regards to the reactant (LA and H_2) adsorption energetics of the PBE-D3 functional, we changed the rate and equilibrium constants for reactant adsorption and desorption processes in our microkinetic model to values obtained with the RPBE

functional [44] (which likely underestimates adsorption energies – all other rate constants are unchanged). Interestingly, our main conclusions of a low TOF at low temperatures and the reaction mechanism are robust with regards to such a change in the microkinetic model.

2.4.2.3 Apparent activation barriers and reaction orders

To further compare our microkinetic models for the HDO of LA to GVL over Ru(0001) to experimental data, we computed the apparent activation barrier and reaction orders illustrated in Figure 2.4. The apparent activation barrier was calculated in the temperature range of 423 to 523 K where reasonable TOFs are obtainable. We found it to be 1.10 eV [0.93 eV] which is somewhat larger than the experimentally observed barrier of 48 kJ/mol for the hydrogenation of LA and 70 kJ/mol for the esterification of HPA (the overall experimental activation barrier —which is likely more comparable— has been approximated to be in the range of 0.7-0.9 eV).[22] For the reaction orders, n_i, we used

$$n_i = \left(\frac{\partial ln(TOF)}{\partial ln(P_i)}\right)_{T,P_{j,j\neq i}} \tag{2.10}$$

where P_i is the effective partial pressure (see appendix A). We observe at 423 K a LA order of 0.66 [0.34] and a hydrogen order of -0.34 [0.34]. The corresponding experimental reaction orders (measured at 323 K) are -0.04±0.04 and 0.6±0.2, respectively. The calculated apparent activation barrier and reaction orders for our microkinetic model suggest that the 2-site model better describes the experimental reaction kinetics than the 1-site model. Overall, the TOF, apparent activation barrier, and reaction orders agree reasonably well for the 2-site model at moderate to high temperatures with experimental data such that it is feasible that Ru(0001) sites contribute significantly to the observed experimental reaction kinetics (we note that a widely accepted DFT uncertainty is at least

0.1-0.2 eV [45]). In contrast, the TOFs of all models deviate significantly from the experimental low temperature rate data such that it seems likely that Ru(0001) sites are *not* the active site for low temperature catalysis. Considering the high hydrogen coverage at low temperatures, we furthermore doubt that solvent effects, not considered in this study, could activate the Ru(0001) surface to result in the experimentally observed TOF.

2.4.2.4 Rate control analysis

To further characterize our microkinetic models for the Ru(0001) surface at 423 K, we used Campbell's degree of rate (KRC_i) and thermodynamic rate (TRC_n) control[46] of transition state *i* and intermediate state *n*, to perform a sensitivity analysis of our model with regards to the DFT energies.

$$KRC_i = \left(\frac{\partial \ln(TOF)}{\partial \ln(k_i)}\right)_{K_i, k_j \neq k_i} \tag{2.11}$$

here, k_j is the forward rate constant for step *j*, and K_i is the equillibrium constant of step i.

$$TRC_i = \left(\frac{\partial ln(TOF)}{\partial(-\frac{G_n^0}{k_B T})}\right)_{G_{m\neq n}^0, G_i^{0,TS}} \tag{2.12}$$

where, G_n^0 is the free energy of adsorbate *n*.

We observed that LA adsorption (r_1) has a KRC of 0.53 [0.26] and LA hydrogenation towards the alkoxy intermediate (r_3) has a KRC of 0.47 [0.73]. Other minor rate controlling steps are listed in the appendix A. A positive KRC means stabilization of the TS has a positive effect on the reaction kinetics or that the reaction step is partially rate

controlling. We note that LA adsorption does not possess a transition state but that this step becomes partially rate controlling due to the low free site coverage and the fact that LA adsorption requires two neighboring free sites. For the thermodynamic rate control, we compute the most negative TRC for adsorbed hydrogen, -1.11[-0.76] and for adsorbed intermediate I-11, -0.32 [-0.66]. All other surface species have a negligible TRC. A negative TRC means destabilization of that adsorbed intermediate has a postive effect on the reaction kinetics. The negative TRC for surface hydrogen and intermediate I-11 can be understood by their significant surface coverage. In the 2-site model, the TRC for adsorbed hydrogen originates from the lateral surface interactions with oxygen. To conclude, the sensitivity analysis suggests that strong hydrogen adsorption inhibits the reaction rate and that the first LA hydrogenation step ─ and not the second hydrogenation as previously suggested[24] ─ is the most rate controlling step in the HDO of LA to GVL over Ru(0001). In this way, the hydrogenation of LA to GVL deviates from the relatively straightforward ketone hydrogenation where no surface ring species can form.[23-24]

2.5 Conclusions

Catalytic hydrodeoxygenation of levulinic acid (LA) to γ-valerolactone (GVL) has been studied over Ru(0001) by DFT and microkinetic modeling. Two models have been developed: a 1-site model in which all surface species compete and a 2-site model in which adsorbed hydrogen does not compete with any other surface species. The LA and hydrogen chemical potentials in our models correspond to the experimental reaction condition from Abdelrahman et al.[22] In all models, the activity of Ru(0001) sites is very low at low reaction temperatures due to a very low free site coverage, suggesting that the Ru(0001) surface is

not active for the catalytic hydrodeoxygenation of levulinic acid at these low temperatures. Other, possibly minority sites that have for example been proposed to be active for nitrogen decomposition[47-48] might be responsible for the experimentally observed low temperature activity, which would suggest that the catalytic hydrodeoxygenation of levulinic acid is structure sensitive. Alternatively, solvents such as liquid water or other reaction pathways not investigated in this study might be responsible for a much higher activity of Ru(0001) sites at low temperature than observed in this study. In this context, GVL could be produced from LA via formation of angelica lactone (AGL), a pathway not investigated in this study. AGL has been reported to be a dominant reaction intermediate in acidic reaction media and at high temperatures.[22]

Finally we found that at higher temperatures (>423 K), Ru(0001) sites are relatively active with TOF values ranging from $\sim 10^{-3} - 10^{0}$ s^{-1}. In this high temperature range, we compute kinetic parameters such as the apparent activation barrier and LA and hydrogen reaction orders that are at least for our 2-site model fairly close to the experimentally observed values. Here, the dominant reaction pathway involves LA adsorption, hydrogenation of LA to an alkoxy intermediate, surface ring closure, and –OH group removal. LA hydrogenation to the alkoxy intermediate and LA adsorption (due to the low free site coverage) were identitifed to be rate controlling.

2.6 Acknowledgements

We greatfully acknowledge financial support from the National Science Foundation (CBET-1159863). M. F. acknowledges financial support from the U.S. Department of Energy, Office of Basic Energy Sciences under contract DE-SC0007167. Computational resources have been provided by the National Energy Research Scientific

Computing Center (NERSC) and Pacific Northwest National Laboratory (PNNL). We thank Dr. Guido Buzzi-Ferraris and Dr. Flavio Manenti for helpful discussions on solving systems of differential algebraic equations.

2.7 Tables and figures

Table 2.1: Species nomenclature, chemical formula, binding mode and number of adsorption sites of various surface species

Species	Chemical Formula	Binding mode	No. of Adsorption sites
LA	$CH_3 - CO - CH_2 - CH_2 - COOH$	$\eta_2\mu_3(O,O)$	2
Al	$CH_3 - CH(\dot{O}) - CH_2 - CH_2 - COOH$	$\eta_2\mu_4(O,O)$	2
Hy	$CH_3 - \dot{C}(OH) - CH_2 - CH_2 - COOH$	$\eta_2\mu_2(O,C)$	2
HPA	$CH_3 - CH(OH) - CH_2 - CH_2 - COOH$	$\eta_3\mu_3(O,C,O)$	3
I-01	$CH_3 - CH(OH) - CH_2 - CH_2 - \dot{C}O$	$\eta_3\mu_4(O,C,O)$	3
I-02	$CH_3 - CH(OH) - CH_2 - CH_2$	$\eta_2\mu_2(O,C)$	2
I-03	$CH_3 - \dot{C}H - CH_2 - CH_2 - COOH$	$\eta_2\mu_3(C,O)$	2
I-04	$CH_3 - CH(OH) - CH_2 - CH_2 - \dot{C}(OH)$	$\eta_1\mu_1(C)$	1
I-05	$CH_3 - CH(\dot{O}) - CH_2 - CH_2 - \dot{C}(OH)_2$	$\eta_2\mu_5(O,C)$	2
I-06	$CH_3 - CH(\dot{O}) - CH_2 - CH_2 - \dot{C}O$	$\eta_3\mu_5(O,C,O)$	3
I-07	$CH_3 - CH(\dot{O}) - CH_2 - CH_2 - \dot{C}(OH)$	$\eta_2\mu_3(O,C)$	2
I-08	$C_4OH_5(OH)(CH_3)$	$\eta_2\mu_2(C,O)$	2
I-09	$CH_3 - \dot{C}H - CH_2 - CH_2 - CO\dot{O}$	$\eta_3\mu_3(O,O,C)$	3
I-10	$CH_3 - CO - CH_2 - CH_2 - \dot{C}O$	$\eta_3\mu_3(O,C,O)$	3
I-11	$CH_3 - CO - CH_2 - CH_2 - CO\dot{O}$	$\eta_3\mu_3(O,O,O)$	3
I-12	$CH_3 - CH(\dot{O}) - CH_2 - CH_2 - CO\dot{O}$	$\eta_3\mu_3(O,O,O)$	3
I-13	$C_4OH_4(CH_3)(OH)(OH)$	$\eta_1\mu_1(C)$	1
I-14	$CH_3 - \ddot{C} - CH_2 - CH_2 - COOH$	$\eta_1\mu_2(C)$	1
I-15	$C_4OH_4(CH_3)(O)$	$\eta_1\mu_1(C)$	1
I-16	$C_4OH_4(CH_3)(OH)$	$\eta_2\mu_2(C,C)$	2
I-17	$C_4OH_5(CH_3)(\dot{O})(\dot{O})$	$\eta_2\mu_3(O,O)$	2
I-18	$C_4OH_5(CH_3)(\dot{O})(OH)$	$\eta_1\mu_1(O)$	1
GVL	$C_4OH_5(CH_3)(O)$	$\eta_2\mu_2(O,O)$	2
OH	OH	$\eta_1\mu_3(O)$	1

H	H	$\eta_1\mu_3(H)$	1
H_2O	H_2O	$\eta_1\mu_1(O)$	1
O	O	$\eta_1\mu_3(O)$	1

Table 2.2: Zero point corrected reaction energy (ΔE_0), zero point corrected activation barrier ($\Delta E_0^{\ddagger}$), imaginary frequency of TS (ν_i), TS bond length, and free energies of reaction and activation at 423 K for all the elementary reaction steps

Step	Reaction	ΔE_0 (eV)	$\Delta E_0^{\ddagger}$ (eV)	ν_i (cm^{-1})	TS $bond$ (Å)	$\Delta G(T, P^0)$ $P^0 = 1\ bar$ @423K	$\Delta G^{\ddagger}(T, P^0)$ $P^0 = 1\ bar$ @423K
r_1	$C_5H_8O_3(g) + 2* \rightarrow C_5H_8O_3{**}$	-1.33	N/A	N/A	N/A	-0.33	N/A
r_2	$H_2(g) + 2* \rightarrow 2H*$	-1.30	N/A	N/A	N/A	-0.82	N/A
r_3	$C_5H_8O_3{**} + H* \rightarrow C_5H_9O_3{**} + *$	0.06	0.67	818	1.57	0.09	0.70
r_4	$C_5H_8O_3{**} + H* \rightarrow C_5H_9O_3{**} + *$	0.88	1.36	1249	1.39	0.87	1.35
r_5	$C_5H_9O_3{**} + H* \rightarrow C_5H_{10}O_3{***}$	0.76	1.29	1194	1.40	0.78	1.22
r_6	$C_5H_9O_3{**} + H* \rightarrow C_5H_{10}O_3{***}$	-0.05	0.76	964	1.48	0.00	0.75
r_7	$C_5H_{10}O_3{***} + * \rightarrow C_5H_9O_2{***} + OH*$	-0.66	0.15	255	1.99	-0.67	0.14
r_8	$C_5H_{10}O_3{***} + H* \rightarrow C_5H_{11}O_3{**} + 2*$	0.55	1.02	1311	1.40	0.56	1.03
r_9	$C_5H_8O_3{**} + H* \rightarrow C_5H_9O_3* + 2*$	-0.04	0.32	1226	1.33	-0.05	0.30
r_{10}	$C_5H_{10}O_3{***} \rightarrow C_5H_9O_2{**} + OH*$	-0.34	0.99	241	2.34	-0.38	1.00
r_{11}	$C_5H_9O_2{***} + * \rightarrow C_5H_8O_2{**} + H*$	-0.88	0.36	1237	1.41	-0.83	0.37
r_{12}	$C_5H_9O_2{***} + H* \rightarrow C_5H_{10}O_2* + 3*$	0.83	1.54	847	1.49	0.82	1.49
r_{13}	$C_5H_{11}O_3{**} \rightarrow C_5H_{10}O_2* + OH*$	-0.37	0.29	223	1.97	-0.42	0.25
r_{14}	$C_5H_9O_3{**} + 2* \rightarrow C_5H_8O_2{***} + OH*$	-0.77	0.12	273	1.86	-0.73	0.18
r_{15}	$C_5H_{11}O_3{**} + * \rightarrow C_5H_{10}O_3{**} + H*$	-0.25	0.64	900	1.46	-0.27	0.65
r_{16}	$C_5H_9O_3{**} + H* \rightarrow C_5H_{10}O_3{**} + *$	1.06	1.41	1350	1.35	1.07	1.44
r_{17}	$C_5H_9O_3{**} \rightarrow C_5H_9O_3* + *$	0.22	0.33	138	1.94	0.25	0.37
r_{18}	$C_5H_9O_3{**} \rightarrow C_5H_8O_2* + OH*$	-0.61	0.84	392	1.95	-0.65	0.84
r_{19}	$C_5H_9O_3{**} \rightarrow C_5H_9O_3* + *$	0.04	0.60	N/A	N/A	0.13	0.61
r_{20}	$C_5H_9O_2{**} \rightarrow C_5H_9O_2{**}$	0.28	0.81	N/A	N/A	0.32	0.82
r_{21}	$C_5H_9O_2{**} + 2* \rightarrow C_5H_8O_2{***} + H*$	-0.98	0.34	1277	1.31	-0.93	0.33
r_{22}	$C_5H_{10}O_2* + 2* \rightarrow C_5H_9O_2{**} + H*$	-0.44	0.59	1280	1.38	-0.44	0.60
r_{23}	$C_5H_{10}O_3{**} + * \rightarrow C_5H_9O_2{**} + OH*$	-0.56	0.75	501	1.77	-0.59	0.78
r_{24}	$C_5H_9O_2{**} \rightarrow C_5H_9O_2{**}$	0.21	1.28	293	1.93	0.23	1.31
r_{25}	$C_5H_9O_3* + 2* \rightarrow C_5H_8O_2{**} + OH*$	-0.24	0.04	241	1.95	-0.24	0.04
r_{26}	$C_5H_8O_2* + * \rightarrow C_5H_8O_2{**}$	0.16	0.48	264	2.03	0.24	0.60
r_{27}	$C_5H_9O_3* + 2* \rightarrow C_5H_8O_2{**} + OH*$	-0.42	0.86	206	2.40	-0.45	0.83
r_{28}	$C_5H_8O_3{**} + H* \rightarrow C_5H_9O_3* + 2*$	-0.50	0.73	1216	1.30	-0.53	0.75
r_{29}	$C_5H_8O_2{**} \rightarrow C_5H_7O_2* + H*$	0.35	0.87	825	1.48	0.33	0.87
r_{30}	$C_5H_8O_2{***} \rightarrow C_5H_8O_2{**} + *$	0.76	1.24	282	1.79	0.73	1.22
r_{31}	$C_5H_9O_2{**} + * \rightarrow C_5H_8O_2{**} + H*$	-0.72	0.75	1365	1.28	-0.71	0.75
r_{32}	$C_5H_7O_2* + H* \rightarrow C_5H_8O_2{**}$	0.13	0.97	714	1.42	0.15	0.97
r_{33}	$C_5H_8O_2{***} \rightarrow C_5H_8O_2{**} + *$	0.54	1.04	N/A	N/A	0.54	1.06
r_{34}	$C_5H_8O_3{**} + 2* \rightarrow C_5H_7O_2{***} + OH*$	-0.61	0.71	264	1.70	-0.54	0.75
r_{35}	$C_5H_8O_3{**} + 2* \rightarrow C_5H_7O_3{***} + H*$	-1.13	0.06	1045	1.39	-1.11	0.04
r_{36}	$C_5H_7O_2{***} \rightarrow C_5H_7O_2* + 2*$	0.52	0.87	266	1.67	0.49	0.89
r_{37}	$C_5H_7O_2{***} + H* \rightarrow C_5H_8O_2{***} + *$	-0.10	0.70	736	1.46	-0.10	0.67
r_{38}	$C_5H_7O_3{**} + H* \rightarrow C_5H_8O_3{***}$	0.45	0.68	486	1.87	0.47	0.71
r_{39}	$C_5H_8O_3{***} \rightarrow C_5H_8O_3{**} + *$	1.01	1.49	N/A	N/A	1.03	1.59
r_{40}	$C_5H_8O_2{**} \rightarrow C_5H_8O_2(g) + 2*$	1.05	N/A	N/A	N/A	0.13	N/A
r_{41}	$OH* + H* \rightarrow H_2O* + *$	0.58	1.16	1105	1.48	0.51	1.13
r_{42}	$H_2O* \rightarrow H_2O(g) + *$	0.55	N/A	N/A	N/A	-0.03	N/A
r_{43}	$OH* + * \rightarrow H^* + O^*$	-0.84	0.65	1310	1.26	-0.81	0.66
r_{44}	$HPA* \rightarrow HPA(g) + *$	1.33	N/A	N/A	N/A	0.29	N/A

Table 2.3: Computed and experimental turnover frequency and hydrogen and free site coverage at various temperatures. For the computed data, we report predictions with 1 site model with PBE-D3 functional and in the square brackets with 2 site model with PBE-D3 functional. All surface coverages for both models can be found in the appendix A

Temp (K)	$\boldsymbol{\theta_H}$	$\boldsymbol{\theta_O}$	$\boldsymbol{\theta_*}$	**TOF (s^{-1})**	**Experimental TOF (s^{-1})[9]**
323	1.000 [1.000]	1.94×10^{-6} [2.12×10^{-4}]	1.47×10^{-6} [3.97×10^{-5}]	2.67×10^{-9} [1.94×10^{-6}]	2.00×10^{-3}
373	0.991 [1.000]	7.35×10^{-5} [3.82×10^{-4}]	2.05×10^{-5} [9.95×10^{-5}]	1.83×10^{-5} [4.33×10^{-4}]	N/A
423	0.923 [1.000]	4.69×10^{-4} [5.18×10^{-4}]	1.12×10^{-4} [2.43×10^{-4}]	4.09×10^{-3} [1.94×10^{-2}]	4.80×10^{-1}
473	0.846 [0.999]	1.15×10^{-3} [5.86×10^{-4}]	4.09×10^{-4} [6.48×10^{-4}]	1.05×10^{-1} [2.90×10^{-1}]	N/A
523	0.797 [0.997]	1.65×10^{-3} [5.93×10^{-4}]	1.30×10^{-3} [1.79×10^{-3}]	8.99×10^{-1} [2.08]	N/A

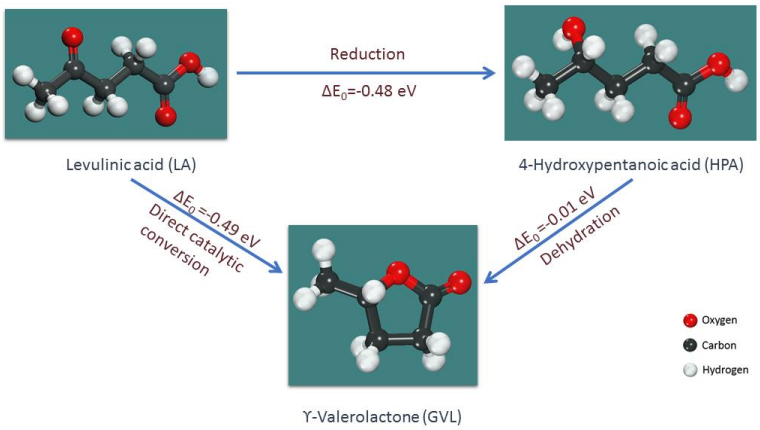

Figure 2.1: Reaction pathways investigated in this study. Also illustrated are the gas phase zero point corrected reaction energies of the reactants and products computed with PBE-D3

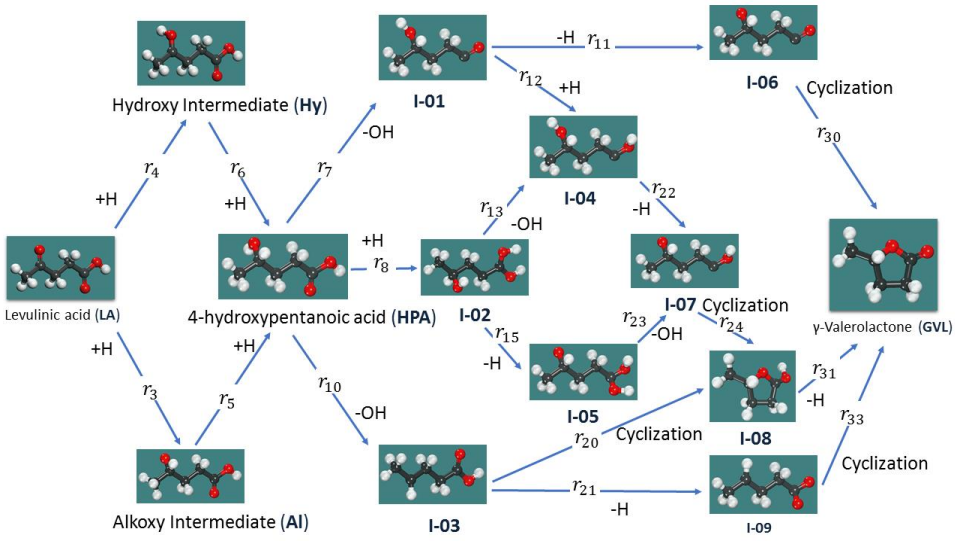

(A)

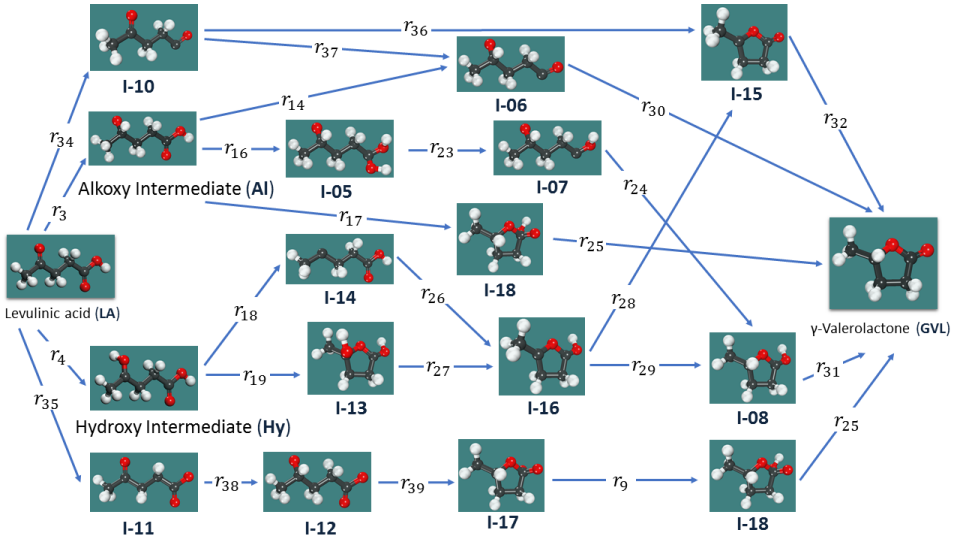

(B)

Figure 2.2: Various reaction pathways investigated for the hydrodeoxygenation of levulinic acid (LA) to γ-valerolactone (GVL). (A) Pathways involving 4-hydroxypentanoic acid (HPA) as reaction intermediate. Catalytic hydrogenation of LA at carbonyl functional group leads to HPA, which is then dehydrated and cyclized to form GVL. (B) Pathways avoiding the formation of HPA as reaction intermediate. One hydrogen is added to LA and one –OH is removed. The removed –OH then forms water with the hydrogen that is left

from the dissociative adsorption of hydrogen gas. Finally, the deoxygenated LA structure undergoes a cyclization process to form GVL

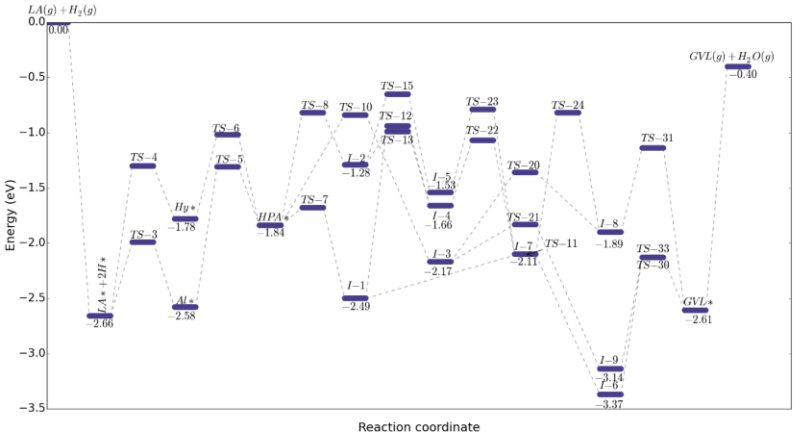

(A)

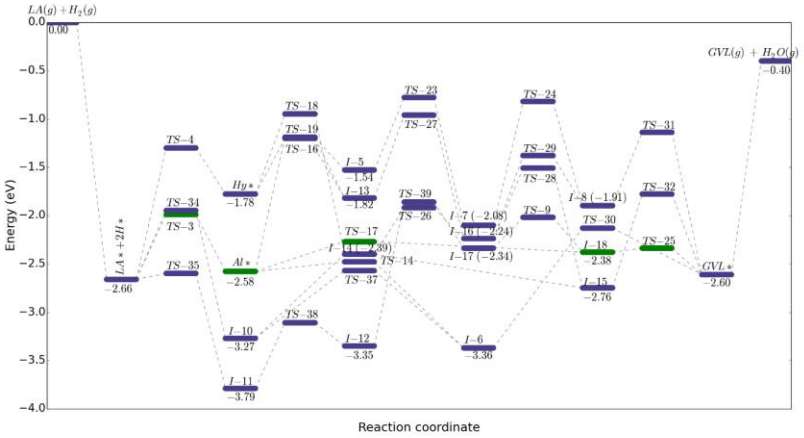

(B)

Figure 2.3: Zero point corrected energy diagram for the HDO of LA over Ru(0001). Stationary points in green are on dominant reaction pathway. (A) LA hydrogenation followed by dehydration pathways. (B) Direct catalytic conversion of LA to GVL

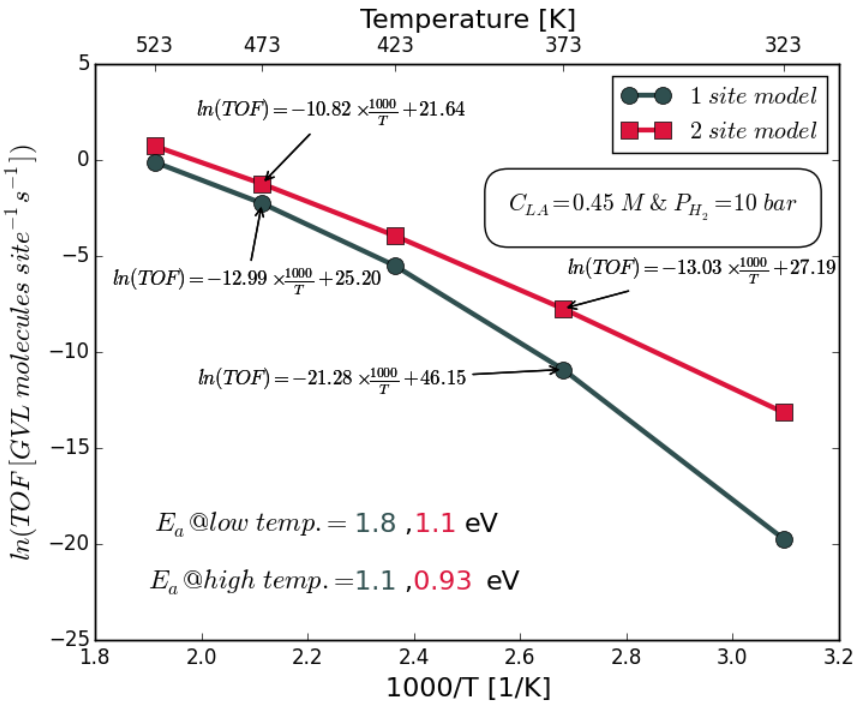
Temperature [K]
523
473
423
373
323
$ln(TOF) = -10.82 \times \frac{1000}{T} + 21.64$
1 site model
2 site model
$C_{LA} = 0.45\ M\ \&\ P_{H_2} = 10\ bar$
$ln(TOF) = -13.03 \times \frac{1000}{T} + 27.19$
$ln(TOF) = -12.99 \times \frac{1000}{T} + 25.20$
$ln(TOF) = -21.28 \times \frac{1000}{T} + 46.15$
E_a @low temp. = 1.8 ,1.1 eV
E_a @high temp. =1.1 ,0.93 eV
$ln(TOF\ [GVL\ molecules\ site^{-1}\ s^{-1}])$
1000/T [1/K]

(A)

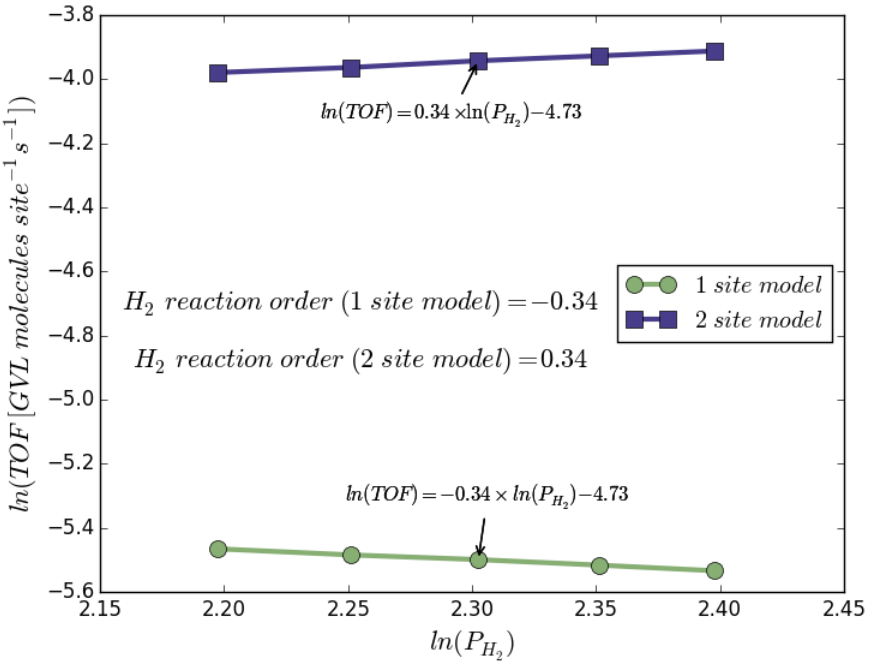
$ln(TOF) = 0.34 \times \ln(P_{H_2}) - 4.73$
H_2 reaction order (1 site model) = −0.34
H_2 reaction order (2 site model) = 0.34
1 site model
2 site model
$ln(TOF) = -0.34 \times ln(P_{H_2}) - 4.73$
$ln(TOF\ [GVL\ molecules\ site^{-1}\ s^{-1}])$
$ln(P_{H_2})$

(B)

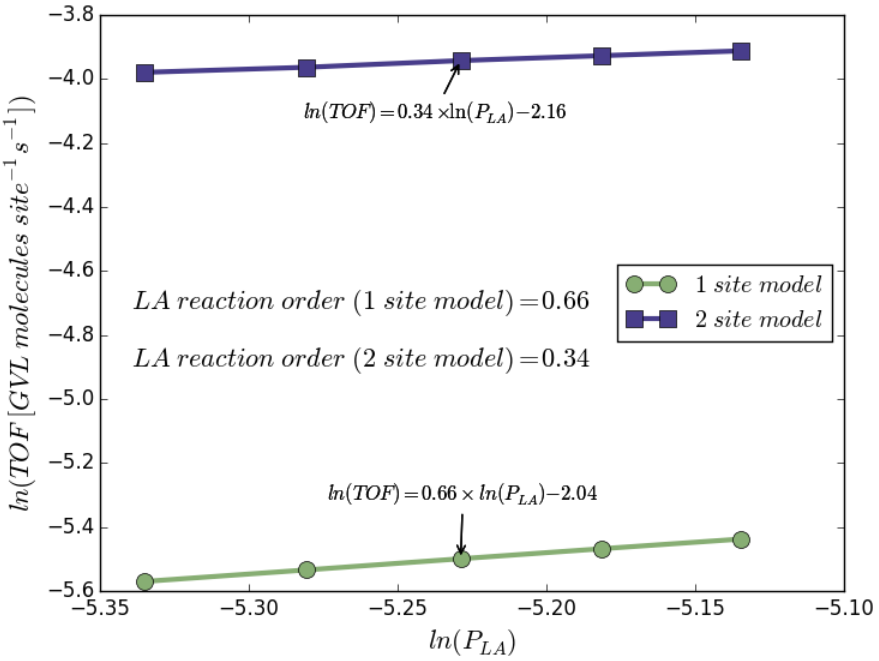

(C)

Figure 2.4: Kinetic parameters determined from one site and two site models. In the one site model adsorbed hydrogen competes with all other surface species, while in the two site model hydrogen adsorption is non-competitive with all other surface species. (A) Arrhenius plot for the conversion of LA to GVL over Ru(0001) in the temperature range 423-523 K. (B) Hydrogen reaction order at 423 K. (C) LA reaction order at 423 K

2.8 Bibliography

1. Serrano-Ruiz, J. C.; Luque, R.; Sepulveda-Escribano, A., *Chem. Soc. Rev.* **2011,** *40*, 5266-5281.
2. Dodds, D. R.; Gross, R. A., *Science* **2007,** *318*, 1250-1251.
3. Alonso, D. M.; Wettstein, S. G.; Dumesic, J. A., *Green Chem.* **2013,** *15*, 584-595.
4. Bozell, J. J.; Petersen, G. R., *Green Chem.* **2010,** *12*, 539-554.
5. Xiong, K.; Yu, W.; Vlachos, D. G.; Chen, J. G., *ChemCatChem* **2015,** *7*, 1402-1421.
6. Assary, R. S.; Redfern, P. C.; Hammond, J. R.; Greeley, J.; Curtiss, L. A., *J. Phys. Chem. B* **2010,** *114*, 9002-9009.
7. Nelson, R. C.; Baek, B.; Ruiz, P.; Goundie, B.; Brooks, A.; Wheeler, M. C.; Frederick, B. G.; Grabow, L. C.; Austin, R. N., *ACS Catal.* **2015,** *5*, 6509-6523.
8. Girisuta, B.; Janssen, L. P. B. M.; Heeres, H. J., *Chem. Eng. Res. Des.* **2006,** *84*, 339-349.
9. Braden, D. J.; Henao, C. A.; Heltzel, J.; Maravelias, C. C.; Dumesic, J. A., *Green Chem.* **2011,** *13*, 1755-1765.
10. Serrano-Ruiz, J. C.; Braden, D. J.; West, R. M.; Dumesic, J. A., *Appl. Catal., B* **2010,** *100*, 184-189.
11. Alonso, D. M.; Gallo, J. M. R.; Mellmer, M. A.; Wettstein, S. G.; Dumesic, J. A., *Catal. Sci. Technol.* **2013,** *3*, 927-931.
12. Qi, L.; Horváth, I. T., *ACS Catal.* **2012,** *2*, 2247-2249.
13. Vasiliu, M.; Guynn, K.; Dixon, D. A., *J. Phys. Chem. C* **2011,** *115*, 15686-15702.
14. Wettstein, S. G.; Alonso, D. M.; Chong, Y.; Dumesic, J. A., *Energy Environ. Sci.* **2012,** *5*, 8199-8203.
15. Balat, M.; Balat, H., *Energy Sources, Part A* **2009,** *31*, 1280-1293.
16. Bond, J. Q.; Alonso, D. M.; Wang, D.; West, R. M.; Dumesic, J. A., *Science* **2010,** *327*, 1110-1114.
17. Horvath, I. T.; Mehdi, H.; Fabos, V.; Boda, L.; Mika, L. T., *Green Chem.* **2008,** *10*, 238-242.
18. Serrano-Ruiz, J. C.; Wang, D.; Dumesic, J. A., *Green Chem.* **2010,** *12*, 574-577.
19. Manzer, L. E., *Appl. Catal., A* **2004,** *272*, 249-256.
20. Luo, W.; Sankar, M.; Beale, A. M.; He, Q.; Kiely, C. J.; Bruijnincx, P. C. A.; Weckhuysen, B. M., *Nat. Commun.* **2015,** *6*, 6540.
21. Cao, S.; Monnier, J. R.; Williams, C. T.; Diao, W.; Regalbuto, J. R., *J. Catal.* **2015,** *326*, 69-81.
22. Abdelrahman, O. A.; Heyden, A.; Bond, J. Q., *ACS Catal.* **2014,** *4*, 1171-1181.
23. Sinha, N. K.; Neurock, M., *J. Catal.* **2012,** *295*, 31-44.
24. Michel, C.; Zaffran, J.; Ruppert, A. M.; Matras-Michalska, J.; Jedrzejczyk, M.; Grams, J.; Sautet, P., *Chem. Commun.* **2014,** *50*, 12450-12453.
25. Kresse, G.; Hafner, J., *Phys. Rev. B* **1993,** *47*, 558-561.
26. Blöchl, P. E., *Phys. Rev. B* **1994,** *50*, 17953-17979.
27. Perdew, J. P.; Yue, W., *Phys. Rev. B* **1986,** *33*, 8800-8802.
28. Perdew, J. P.; Wang, Y., *Phys. Rev. B* **1992,** *45*, 13244-13249.
29. Karp, E. M.; Silbaugh, T. L.; Crowe, M. C.; Campbell, C. T., *J. Am. Chem. Soc.* **2012,** *134*, 20388-20395.

30. Grimme, S.; Antony, J.; Ehrlich, S.; Krieg, H., *J. Chem. Phys.* **2010,** *132*, 154104.
31. Finkel, V. A.; Kovtun, G. P.; Palatnik, M. I., *Phys. Met. Metallogr.* **1971,** *32*, 231.
32. Monkhorst, H. J.; Pack, J. D., *Phys. Rev. B* **1976,** *13*, 5188-5192.
33. Methfessel, M.; Paxton, A. T., *Phys. Rev. B* **1989,** *40*, 3616-3621.
34. Henkelman, G.; Uberuaga, B. P.; Jónsson, H., *J. Chem. Phys.* **2000,** *113*, 9901-9904.
35. Henkelman, G.; Jónsson, H., *J. Chem. Phys.* **1999,** *111*, 7010-7022.
36. Heyden, A.; Bell, A. T.; Keil, F. J., *J. Chem. Phys.* **2005,** *123*, 14.
37. Olsen, R. A.; Kroes, G. J.; Henkelman, G.; Arnaldsson, A.; Jónsson, H., *J. Chem. Phys.* **2004,** *121*, 9776-9792.
38. Sheppard, D.; Terrell, R.; Henkelman, G., *J. Chem. Phys.* **2008,** *128*, 134106.
39. Henkelman, G.; Arnaldsson, A.; Jónsson, H., *J. Chem. Phys.* **2006,** *124*, 044706.
40. Bronsted, J. N., *Chem. Rev.* **1928,** *5*, 231-338.
41. Evans, M. G.; Polanyi, M., *Trans. Faraday Soc.* **1938,** *34*, 11-24.
42. Buzzi-Ferraris, G.; Manenti, F., BzzMath: Library Overview and Recent Advances in Numerical Methods. In *Computer Aided Chemical Engineering*, Ian David Lockhart, B.; Michael, F., Eds. Elsevier: 2012; Vol. Volume 30, pp 1312-1316.
43. Grabow, L.; Hvolbæk, B.; Nørskov, J., *Top. Catal.* **2010,** *53*, 298-310.
44. Hammer, B.; Hansen, L. B.; Nørskov, J. K., *Phys. Rev. B* **1999,** *59*, 7413-7421.
45. Walker, E.; Ammal, S. C.; Terejanu, G. A.; Heyden, A., *J. Phys. Chem. C* **2016,** *120*, 10328-10339.
46. Stegelmann, C.; Andreasen, A.; Campbell, C. T., *J. Am. Chem. Soc.* **2009,** *131*, 8077-8082.
47. Hellman, A.; Baerends, E. J.; Biczysko, M.; Bligaard, T.; Christensen, C. H.; Clary, D. C.; Dahl, S.; van Harrevelt, R.; Honkala, K.; Jonsson, H.; Kroes, G. J.; Luppi, M.; Manthe, U.; Nørskov, J. K.; Olsen, R. A.; Rossmeisl, J.; Skúlason, E.; Tautermann, C. S.; Varandas, A. J. C.; Vincent, J. K., *J. Phys. Chem. B* **2006,** *110*, 17719-17735.
48. Hellman, A.; Honkala, K.; Remediakis, I. N.; Logadóttir, Á.; Carlsson, A.; Dahl, S.; Christensen, C. H.; Nørskov, J. K., *Surf. Sci.* **2009,** *603*, 1731-1739.

CHAPTER 3 : ON THE IMPORTANCE OF ANGELICA LACTONE FORMATION IN THE HYDRODEOXYGENATION OF LEVULINIC ACID TO γ-VALEROLACTONE OVER Ru (0001) MODEL SURFACE: A DENSITY FUNCTIONAL THEORY INVESTIGATION

Mamun, O.; Saleheen, M.; Bond, J.Q.; Heyden, A.

To be submitted

3.1 Abstract

Using mean-field microkinetic modeling with parameters derived from first-principles density functional theory (DFT) calculations, we modeled steady-state catalytic hydrodeoxygenation of levulinic acid (LA) to γ-valerolactone (GVL) on Ru(0001) model surface, an important catalytic system with applications in the treatment of biomass platform chemicals to produce second generation biofuels with less oxygen content and high energy density. Focusing on the intramolecular esterification of LA to its stable derivative α-angelica lactone (AGL), we studied the sensitivity of the reaction kinetics on both external (i.e. pressure, temperature etc.) and internal (i.e. thermodynamic and kinetic states of the system) parameters, and at various reactants composition (4-40 bar hydrogen partial pressure and 0.025-1.5 M LA solution). In this study, we particularly emphasize on the activity of the metallic phase (Ru0001 model surface) of the catalysts and identified two different active regimes characterized by very different activation barriers and reaction orders at high (>423K) and low (<373K) temperatures at typical reaction conditions (10 bar hydrogen partial pressure and 0.45 M LA solution). Our model, derived from competitive Langmuir-Hinshelwood interpretation of reaction mechanism, shows that with increasing temperature the metallic surface transitions from an H-poisoned surface (θ_H ~ 1.00 @323K) to a moderately H-covered surface (θ_H ~ 0.70 @523K). Our study also shows that the AGL formation pathway has a detrimental effect on the high temperature reaction kinetics as some of its derivatives adsorb strongly on the catalytic surface. As a result, a poor kinetic performance of the model surface is observed which confirms the experimental observation that AGL formation pathway is mainly responsible for the reversible catalyst deactivation.

key words: ruthenium; density functional theory (DFT); hydrodeoxygenation; biomass; microkinetic modeling; levulinic acid; α-angelica lactone; γ-valerolactone

3.2 Introduction

Efficient production of biomass derived second generation biofuels requires the development of active, selective, and stable catalytic materials for the reductive deoxygenation of platform chemicals, i.e. Levulinic acid (LA), Succinic acid (SA), etc. One such way to achieve catalytic deoxygenation of biomass platform chemical is hydrodeoxygenation process over supported/unsupported transition metal catalytic materials using external molecular hydrogen source where hydrogen donor helps to lower the oxygen content. Levulinic acid (LA) hydrodeoxygenation (HDO), a crucial biomass conversion process to produce γ-Valerolactone (GVL) that can be used as fuel additive, food ingredients, nylon intermediate, or renewable solvent, using hydrogen gas occurs in both gas and liquid phase (in both organic and aqueous solvent medium) environments in the presence of supported transition metal nanoparticles. Recent studies show[1] that LA hydrodeoxygenation, unlike petroleum industries where conventional hydrogenation catalysts such as palladium (Pd), rhodium (Rh), and nickel (Ni) are tailored to obtain high activities and selectivities, is best performed with oxophillic ruthenium based mono/bi metallic catalysts. Manzar et al. studied the hydrogenation of levulinic acid in dioxane with 800 psig (~55 bar) H_2 pressure at 150 ^{0}C with several different carbon supported metal catalysts such as Ir, Rh, Pd, Ru, Pt, Re, and Ni. Their study shows superior activity and selectivity of carbon supported Ru catalyst among all the catalysts screened for this conversion process[2]. Another study with different reaction conditions (Temperature 130 ^{0}C, hydrogen pressure 1.5 MPa (~15 bar), 5 wt% catalyst loading, and methanol solvent)

also found Ru/C catalyst performs better in terms of activity and selectivity than other catalysts, e.g. carbon supported palladium catalyst, Raney nickel, and Urushibara nickel etc.[3] A comprehensive mechanistic study by Dumesic and co-workers also reported Ru/C catalyst to be the most active and selective catalyst under aqueous phase environment[4], they also observed that carbon supported bimetallic RuRe catalyst performs better than supported monometallic Ru catalyst. In the presence of sulfuric acid, metal oxide supported Pt catalysts (Pt/TiO_2 or Pt/ZrO_2) are reported to be superior catalysts than metal oxide supported PtRu catalysts @ 200 ^{0}C temperature, 1 wt% metal on support, and 4MPa (~40 bar) hydrogen partial pressure[5]. Ftouni et al.[6] recently compared the catalytic activity and selectivity of various supported Ru catalysts (ZrO_2, TiO_2, and carbon) at 423 K temperature, 30 bar hydrogen pressure, and 1,4-dioxane solvent conditions. They found that all the supported Ru catalysts showed excellent yields; however, only ZrO_2 was able to maintain these high yields after multiple regeneration steps. Although the catalytic activity of ruthenium surface is greatly influenced by the choice of the support, but in general, catalytic performance of ruthenium nanoparticle was found to be better than any other transition metals' catalytic surfaces.

Polar solvents (i.e. water), having the capacity to donate H^+/H_3O^+, has a marked effect on the reaction kinetics of the hydrogenation of LA towards the formation of its subsequent alcohol product, 4-hydroxypentanoic acid (HPA). A high throughput screening of monometallic catalysts for the hydrogenation of biomass derived oxygenates by Huber et al. confirmed that in aqueous phase environment, Ru is the most active catalyst for the hydrogenation of carbonyl groups[7]. The rate of 2-butanone hydrogenation was found to be 7 to 75 times higher in water than that found in isopropyl alcohol (IPA) solvent using the

same reaction conditions (5 wt% Ru/SiO_2 at 303.15 K and 1 bar of hydrogen partial pressure)[8]. A combined experimental and computational study on the hydrogenation of LA to GVL by Michel et al.[9] also demonstrated a strong positive influence of polar solvents (i.e. water) on the hydrogenation kinetics.

In this chapter, we use mean-field microkinetic modeling based on the parameters obtained from atomistic DFT computations to describe catalytic behavior of Ru for the conversion of LA to GVL via intermediate production of both AGL and HPA under experimental reaction conditions. We use no experimental data/fitting parameters, and a clean Ru(0001) slab is used to mimic the catalytic behavior of carbon supported Ru catalysts in the vapor phase experimental conditions which also represents the non-polar aprotic solvent environment, e.g. 1,4-dioxane, DMSO etc. This chapter is organized as follows. In section 3.3, we briefly discuss the computational methodology and modeling strategy we adopted for the study of LA HDO over Ru(0001) surface. Then, in section 3.4, we present a detailed DFT analysis of the various pathways for LA conversion to GVL via intermediate formation of AGL. The results obtained from our microkinetic models and predictions regarding the dominant reaction mechanism, rate controlling steps, and reaction orders were analyzed in section 3.5. We conclude with a discussion about the detrimental effect of intramolecular esterification of LA to AGL on high temperature catalytic performance of Ru(0001) model surface.

3.3 Methods

In this computational study, Vienna Ab initio Simulation Package (VASP)[10-11] is used to perform periodic DFT calculations, and the projector augmented wave method (PAW) is used to describe the ionic core potentials[12-13]. The Kohn-Sham one electron

valance states are expanded in a basis of plane waves with kinetic energies below 400 eV. The self-consistent cycle (electronic degrees of freedom minimization) is converged up to 1×10^{-7} eV, which is a standard SCF energy convergence criteria used for computational analysis of biomass molecule on model transition metal catalytic surfaces. The ionic cycle is converged using a force based criteria of $0.01\, eV/\text{Å}$ on each relaxed atom. The Methfessel-Paxton smearing scheme is used[14], with a Fermi population of the Kohn-Sham excited states at $k_B T = 0.1\, eV$, and at the end of the optimization, total energy is extrapolated to 0K. To describe the exchange and correlation effects, we used PBE functional from Perdew, Burke, and Ernzerhof[15]. The rationale behind choosing GGA based PBE functional is 1) it is already proven to be very accurate (both qualitatively and quantitatively) for describing transition metal-adsorbate (containing carbon, oxygen, and hydrogen) interactions, and 2) our gas phase thermodynamics with PBE-D3 returns the lowest error with respect to CCSD(T) (which is often regarded as 'gold standard' for computational chemistry application) level of theory. We used Grimme's D3 method[16] to consider the long range dynamic correlation between fluctuating charge distributions. Though, at present, local environment dependent self-consistent dispersion inclusion method[17] is available, but we used non self-consistent D3 method as it is well parameterized for PBE functional and can be trusted to give better energetics with no extra computational cost.

A four layer, $p(4 \times 4)$ slab, which is sufficiently large to minimize the lateral interactions of adsorbates and their periodic images, is used as the surface model. The top two layers of the slab is allowed to relax, while the bottom two layers are kept fixed in their relaxed optimized position. A vacuum spacing of 15Å is used between two successive

metal slabs. For bulk Ru optimization, we used $20 \times 20 \times 20$ Monkhorst-Pack k-point mesh[18]. The surface Brillouin zone is sampled with a $4 \times 4 \times 1$ k-point mesh, and convergence with respect to k-point, cut-off energy, and slab depth is ensured by performing convergence test on model reactions involving C, O, and H atoms. For gas phase molecule optimization in vacuum, we used a box size of $20\ \text{Å} \times 20\ \text{Å} \times 20\ \text{Å}$ with $1 \times 1 \times 1$ Monkhorst-Pack k-point sampling technique. During gas phase molecule optimization, electronic SC-loop is optimized up to $1 \times 10^{-7}\ eV$ while ionic cycle is optimized up to 0.005 eV/Å within Conjugate-gradient algorithm scheme.

To locate the transition state of each elementary reaction, we used a two-step procedure. First, an NEB[19] calculation is carried out with the initial and final state conformations and 5-7 images have been generated along the reaction coordinate to scan the potential energy surface. Then the image that represents the TS better (both geometrically and energetically) has been chosen as the initial guess for dimer[20-21] calculations. All transition states are optimized using the same 0.01 eV/Å force based criteria. Then dynamical matrix calculation based on numerical second order derivative has been performed with a 0.001 Å displacement to ensure that the TS has an imaginary frequency along the reaction coordinate. Here, we also want to point out that we could not find desired convergence accuracy for 5 elementary reaction steps ($r_{13}, r_{28}, r_{53}, r_{66}$ & r_{74}) and for these transition states, we used BEP relation that we discuss in the microkinetic model section later. To confirm that the uncertainty in BEP relation does not affect our conclusions, we performed a kinetic rate control analysis of all the TSs. Our calculations indicate that our model results are robust with respect to the high uncertainty of these missing transition states. (See section B.7).

3.3.1 Microkinetic modeling

In the microkinetic model, we used 4-40 bar partial pressure for hydrogen, the pressure range at which Dumesic et al[4] and Bond et al[22] performed their experimental studies. As for LA partial pressure, we used LA chemical potential equivalent to 0.025M-1.5M liquid LA solution using modified Raoult's law,

$$f_{LA}^{v} = P_{LA} = x_{LA} \times \gamma_{LA} \times P_{LA}^{sat} \tag{3.1}$$

In eq. 3.1 activity coefficient and saturation vapor pressure were calculated using TURBOMOLE and COSMOTHERM[23-24] program packages.

All elementary reactions were assumed to be reversible, which means no equilibrium and/or irreversibility assumptions were made in the microkinetic model. The rate of reaction for all intermediate reactions were calculated as

$$r_i = k_i^{+} \prod_m \theta_m^{\vartheta_{m,i}} - k_i^{-} \prod_n \theta_n^{\vartheta_{n,i}} \tag{3.2}$$

Where k^+ and k^- are forward and reverse rate constants, and θ's are the normalized surface coverage of reactants, m, or products, n. Forward and backward rate constants were calculated using harmonic Transition State Theory (hTST)

$$k_{forward} = \frac{k_B T}{h} e^{-\frac{\Delta G^{\ddagger}}{k_B T}} \tag{3.3}$$

Here, $\Delta G^{\ddagger}$, k_B, and h refers to the free energy of activation, Boltzmann's constant, and Planck's constant, respectively. The free energy of activation is calculated using the following formula where the zero point correction and vibrational partition functions are calculated using eq. 3.5 and eq. 3.6, respectively.

$$\Delta G^{\ddagger} = \Delta E^{\ddagger}_{scf} + \Delta E^{\ddagger}_{ZPE} - k_B T ln \frac{q^{TS}_{vib}}{q^{reactant}_{vib}} \tag{3.4}$$

$$E_{zpe} = \frac{1}{2}\sum_i h\nu_i \tag{3.5}$$

$$q_{vib} = \frac{1}{1 - e^{-h\nu/k_B T}} \tag{3.6}$$

Here, ν_i's are the phonon vibrational frequencies, obtained by density functional perturbation theory (DFPT)[25]. The adsorption and desorption processes were treated within the collision theory approach,

$$k_{forward} = \frac{\sigma}{N_0\sqrt{2\pi m k_B T}} \tag{3.7}$$

Here, σ is sticking coefficient which is assumed to be 1 in all of our calculations, N_0 is the number of sites per area and m denotes the molecular weight of adsorbate. The reverse rate is calculated using,

$$k_{reverse} = \frac{k_{forward}}{K_{equilibrium}} \tag{3.8}$$

Where,

$$K_{equilibrium} = e^{-\frac{\Delta G}{k_B T}} \tag{3.9}$$

For the calculation of free energy of a surface reaction, we included vibrational degrees of freedom for both reactant and product states. For free energy of adsorption process, in addition to the vibrational partition function, we also included rotational and translational partition function of molecules. Here, we assumed that adsorbed species have no rotational or translational degrees of freedom as the diffusion barrier is very high in comparison to the thermal energy of the adsorbates. Next, we developed a transient mass balance equation system by writing a mass balance equation for each adsorbed species,

$$\frac{\partial \theta_i}{\partial t} = \sum_l \vartheta_{i,l} r_l \tag{3.10}$$

In eq. 3.10, θ_i, $\vartheta_{i,l}$, and r_l refers to the site coverage of adsorbed species i, stoichiometric coefficient of adsorbed species in the elementary reaction rate equation l, and elementary reaction rate, respectively. The overall site balance equation was used for empty sites coverage calculation,

$$\sum_i n_i \theta_i = 1 \tag{3.11}$$

Here, n_i is the number of sites occupied by each adsorbed species. A complete list of all the elementary reaction rate equations and site balance equations are provided in the supplementary information. We used SUNDIALS DAE solver package to solve the system of differential algebraic equations to calculate steady-state surface coverages and reaction rates[26].

3.4 Potential energy surface and adsorption energies

3.4.1 Thermodynamics and geometries of gas phase structures

Figure 3.1 illustrates the calculated optimized gas phase configurations along with the thermodynamics. For any adsorbed species, the most stable optimized structures are energetically favored by approximately 0.05-0.10 eV in comparison to the other different geometric configurations. In our calculation, the C=O bond distance of the ketone group in levulinic acid (LA) is found to be 1.23 Å, while for the hydrogenated 4-hydroxypentanoic acid (HPA) the corresponding C-O bond length is found to be 1.44 Å. Because of the C=O pi bond scission, the interaction is slightly weak and hence the C-O bond length is longer

than the C=O bond length. In contrast, C=O (1.22 Å) and C-OH (1.37 Å) bond length of the carboxylic group in both LA and HPA has the same bond length. In case of AGL, C=O bond length of associated ketone group is 1.20 Å, while C-O bond length with C_1 is 1.39 Å and with C_4 is 1.41 Å. This apparent dissimilarity between the bond lengths of similar C-O bond lies in the fact that electronic attraction from methyl group results in electron cloud depletion on C_4, as a result a slightly weaker bond is formed. In GVL, though the C-O bond length (1.38Å) with C_1 remains the same, but with C_4, the bond length is 1.46 Å (0.08 Å longer) due to the increased electron depletion effect from another attached hydrogen at C_4. Next, we compared our gas phase thermodynamics with available experimental data, and found reasonable agreement within widely accepted chemical accuracy of 2 kcal/mol. In this context, we also compared our gas phase PBE-D3 computed thermodynamics and found consistent results in comparison to CCSD(T) data (see section A.1). For LA to GVL conversion, experimentally observed heat of reaction is -10.3 kcal/mol[27] while we found it to be -11.7 kcal/mol in our calculation. Similarly, for HPA ring closure reaction, experimentally observed heat of reaction for HPA to GVL is slightly exothermic (-0.72 kcal/mol)[22] which is similar to our DFT computed data (-0.23 kcal/mol). In summary, both gas phase thermodynamics and geometric data prediction is very reliable in comparison to the experimentally reported data.

3.4.2 Adsorption of the levulinic acid and hydrogen

Reaction selectivity is sensitive to the adsorption geometry and site preference, which in turn is sensitive to the choice of functional. Fortunately, though different DFT functionals give different geometric parameters (such as bond lengths) but qualitatively they can predict the relative adsorption strength of different configurations very well. LA

adsorbs on the metal surface through two unsaturated terminal oxygen atoms (one from carbonyl group and another one from carboxyl group) with an adsorption strength of 1.33 eV (throughout this chapter, unless otherwise specified, zero point corrected energies are reported). Hydrogen adsorbs dissociatively on the neighboring FCC sites with an adsorption energy of 0.65 eV per hydrogen atom.

Our DFT analysis of reaction pathways for Levulinic acid (LA) hydrogenation to GVL via intermediate formation of 4-hydroxypentanoic acid (HPA), and LA direct catalytic conversion to γ-valerolactone (GVL) has been discussed in chapter 2, and will not be discussed here. In the next two subsections, we will briefly discuss the DFT computed thermodynamic and kinetic data of the LA conversion to GVL via intermediate AGL formation pathways with/without HPA formation and we will try to analyze different competitive reaction pathways.

3.4.3 4-Hydroxypentanoic acid (HPA) dehydration to γ-valero lactone (GVL) via intermediate α-angelica lactone (AGL) formation

HPA dehydration and ring closing reaction leads to the formation of cyclic ring structure AGL (similar to GVL), which is also a stable intermediate product. Dehydration mechanism requires both H and OH group elimination process. In our reaction network, HPA undergoes two different OH group removal from both alcohol and carboxyl functional group. Alternatively, it may go through H removal process from β-carbon. We also found that initial ring formation reaction is not favored as HPA is a highly-saturated molecule; thus ring formation leads to highly strained geometric structures which is not thermodynamically favored. Herein, we adopt the $\eta_i\mu_j$ nomenclature to describe

adsorption mode where η_i and μ_j indicates the number of adsorbate and metal atoms participating in the adsorption process, respectively. Initial OH group removal from carboxylic group of HPA yields I-26 via the elementary reaction process r_{57} (see figure 3.2(A)), this reaction is exothermic with 0.66 eV reaction energy, and the activation energy is relatively small (0.15 eV) which indicates this process is both thermodynamically and kinetically favorable. I-26 ($CH_3 - CH(OH) - CH_2 - CH_2 - \dot{C}O$) binds in $\eta_3\mu_3(O,C,O)$ mode, which means in the bond formation process of I-26 with the metal surface, three atoms from I-26 participate to make bonds with three metal atoms, also in the parentheses we write the adsorbate atoms that participate in the bond formation process. Alternatively, an OH group removal from alcohol group at γ-carbon leads to the formation of I-10 ($CH_3 - \dot{C}H - CH_2 - CH_2 - COOH$) which adsorbs on the surface in $\eta_2\mu_2(C,O)$ mode. This reaction process (r_{21}) is thermodynamically downhill by 0.34 eV and has a high activation barrier (0.99 eV). Furthermore, a hydrogen elimination process (r_{20}) from β-carbon of HPA can produce I-9 ($CH_3 - CH(OH) - \dot{C}H - CH_2 - COOH$) with a reaction and activation energy of -0.22 eV and 0.51 eV, respectively. Next, I-26, one of the aforementioned HPA derivative, is converted to I-27 ($CH_3 - \dot{C}(OH) - CH_2 - CH_2 - \dot{C}O$) by a C-H bond scission process (r_{58}) at γ-carbon (ΔE_0 = -0.33 eV, $E_{a,0}$ = 0.73 eV). I-26 can also be dehydrogenated to form I-28 ($CH_3 - CH(\dot{O}) - CH_2 - CH_2 - \dot{C}O$), this step ($r_{60}$) is exothermic by 0.88 eV with an activation energy of 0.36 eV. I-26 follows another alternative route that involves the formation of I-13 through a dehydrogenation step at β-carbon (ΔE_0 = -0.30 eV, $E_{a,0}$ = 0.42 eV). An O-H bond scission process (r_{62}) at the γ-carbon of intermediate I-27 leads to the formation of I-7 ($CH_3 - CO - CH_2 - CH_2 - \dot{C}O$) which binds to the surface in $\eta_3\mu_3(O,C,O)$ mode. This process is exothermic by 0.45 eV

with a moderate activation energy of 0.51 eV. Conversely, I-27 can be dehydrogenated at γ-carbon to form I-19 ($CH_3 - \dot{C}(OH) - \dot{C}H - CH_2 - \dot{C}O$) which binds to the surface in $\eta_4\mu_3(O,C,C,C)$ mode. This reaction, r_{61}, is exothermic by 0.52 eV with an activation energy of 0.30 eV. I-28, produced from I-26 via O-H bond scission as discussed above, is then dehydrogenated either at β-carbon or γ-carbon to form I-18 and I-7 with a heat of reaction of 0.26 eV and 0.10 eV and an activation energy of 0.96 eV and 0.80 eV, respectively. I-13, the other intermediate formed from dehydrogenation of I-26, also leads to the formation of I-18 and I-19 by undergoing an O-H bond (r_{33}) and a C-H bond scission (r_{34}) at γ-carbon, respectively. Both these steps are accompanied by a reaction energy of -0.32 and -0.55 eV, and activation energy of 0.19 and 0.40 eV, respectively. I-9, formed from HPA by dehydrogenation at β-carbon, can undergo three different elementary reactions, namely 1) C-H bond scission (r_{22}) of γ-carbon to form I-11 ($CH_3 - \dot{C}(OH) - \dot{C}H - CH_2 - COOH$) ($\Delta E_0$ = -0.56 eV, $E_{a,0}$ = 0.29), 2) C-OH bond scission (r_{23}) to strip off the alcohol group to produce I-12 ($CH_3 - \dot{C}H - \dot{C}H - CH_2 - COOH$) ($\Delta E_0$ = -0.82 eV, $E_{a,0}$ = 0.44 eV), and 3) C-OH group elimination from carboxyl group (r_{24}) to yield I-13 ($CH_3 - CH(OH) - \dot{C}H - CH_2 - \dot{C}O$) ($\Delta E_0$ = -0.73 eV, $E_{a,0}$ = 0.44 eV). The other surface intermediate formed from HPA, I-10, can undergo four different elementary reactions, namely 1) C-H bond scission (r_{25}) of β-carbon to form I-12 ($CH_3 - \dot{C}H - \dot{C}H - CH_2 - COOH$) ($\Delta E_0$ = -0.71 eV, $E_{a,0}$ = 0.30 eV), 2) O-H bond scission (r_{26}) from the terminal carboxyl group to produce I-14 ($CH_3 - \dot{C}H - CH_2 - CH_2 - CO\dot{O}$) ($\Delta E_0$ = -0.98 eV, $E_{a,0}$ = 0.34 eV) 3), C-H group elimination from γ-carbon (r_{27}) to yield I-15 ($CH_3 - \ddot{C} - CH_2 - CH_2 - COOH$) ($\Delta E_0$ = -0.23 eV, $E_{a,0}$ = 0.06 eV) , and 4) ring formation reaction (r_{28}) to yield I-16 ($CH_3 - C_4OH_5 - OH$) (ΔE_0 = 0.28 eV, $E_{a,0}$ = 0.81 eV). I-7, formed from I-27 in

reaction step r_{62}, is then dehydrogenated (ΔE_0 = -0.70 eV, $E_{a,0}$ = 0.54 eV) at γ-carbon to form I-6 ($CH_3 - CO - \dot{C}H - CH_2 - \dot{C}O$), a highly unsaturated molecule, which is then converted to AGL by a ring formation process (r_{16}). This ring formation step is highly endothermic process with a heat of reaction of 0.86 eV and a high activation energy (1.06 eV), which renders this process to be both thermodynamically and kinetically unfavorable. Alternatively, C-O ring closing reaction of I-7 can lead to the formation of I-8 (ΔE_0 = 0.52 eV, $E_{a,0}$ = 0.87 eV). On the other hand, I-18, a derivative of I-13, is converted to I-24 via a ring closing reaction (ΔE_0 = 0.50 eV, $E_{a,0}$ = 0.77 eV). I-18 can also be converted to I-6 via a dehydrogenation process at γ-carbon. I-19, another derivative of I-13, follows another exothermic dehydrogenation step at the alcohol group to produce I-6 ($CH_3 - CO - \dot{C}H - CH_2 - \dot{C}O$) ($\Delta E_0$ = -0.63 eV, $E_{a,0}$ = 0.31 eV). Next, I-6 is converted to AGL via r_{16} elementary reaction process which has been discussed before. In the next step, AGL is hydrogenated at β-carbon to form I-8 (ΔE_0 = 0.37 eV, $E_{a,0}$ = 0.70 eV) via reaction process r_{18}. I-8 is then converted to γ-valerolactone (GVL) by forming a C-H bond at γ-carbon. This process (r_{65}) is thermodynamically slightly uphill by 0.13 eV with a high activation energy (0.97 eV). In addition to process r_{18}, AGL can also follow process r_{54} which is an endothermic hydrogenation step with a reaction energy and activation energy of 0.50 eV and 0.56 eV, respectively, to form I-24. I-24 is then hydrogenated at β-carbon to produce GVL via a thermoneutral process, r_{56}, with ΔE_0 = 0.00 eV and $E_{a,0}$ = 0.84 eV. In figure 3.2B, the intermediate species produced from I-9 and I-10 (discussed above) follow different routes to produce final product GVL. Next, we will briefly discuss the energetics (both thermodynamic and kinetic) of each reaction steps. I-11, produced from I-9, is then either transformed to I-17 ($CH_3 - \ddot{C} - \dot{C}H - CH_2 - COOH$) or I-19 ($CH_3 - \dot{C}(OH) -$

$\dot{C}H - CH_2 - \dot{C}O$). Reaction pathways regarding I-19 leading to GVL formation ($r_{30} \rightarrow r_{45} \rightarrow r_{16}$) has already been discussed above, so we will not discuss it here again. I-17 is produced from I-11 by removal of OH (r_{29}) from the alcohol functional group, this step is accompanied by a -0.60 eV heat of reaction with a high activation energy of 1.03 eV. Then I-17 can either form ring structure I-23 by forming C-O ring closing reaction process (r_{41}) which has a reaction and activation energy of 0.57 eV and 1.29 eV, respectively, or it can form I-25 (this route is discussed below). I-23, produced from I-17 via ring closure process, undergoes an O-H bond scission process at the terminal alcohol group to form ketone group of the lactone (AGL), this step is exothermic by 0.47 eV with an activation energy of 0.72 eV. In the other route producing intermediate I-25, I-17 follows the opposite order of elementary reaction process to form AGL, I-17 is first dehydrogenated to form I-25 via r_{42} (ΔE_0 = -1.02 eV, $E_{a,0}$ = 0.31 eV) and then I-25 undergoes ring closing reaction to form AGL via r_{55} (ΔE_0 = 1.12 eV, $E_{a,0}$ = 1.16 eV). I-12, another I-9 derivative, can either be converted to I-17 by C-H bond scission (r_{31}) at γ-carbon (ΔE_0 = -0.33 eV, $E_{a,0}$ = 0.19 eV) which then follows the elementary reactions discussed above to form AGL, or I-20 by O-H bond scission (r_{32}) from terminal carboxyl group (ΔE_0 = -0.58 eV, $E_{a,0}$ = 0.40 eV). I-20 conversion to AGL requires the formation of ring structure and a C-H bond scission process. Ring formation (r_{46}) of I-20 leads to the formation of I-24 (ΔE_0 = 0.85 eV, $E_{a,0}$ = 2.25 eV), this step has a very high activation energy because of the steric strain associated with the formation of ring structure, from this simple kinetic data we can predict that this reaction step is highly unlikely to occur because the entropic penalty for ring closing process is higher than the electronic stabilization due to the bond formation between two adjacent atoms in I-24. Another possible route from I-20 involves C-H bond scission at the

γ-carbon of I-20 which yields I-25, this step has a reaction energy of -0.78 eV with an activation energy of 0.57 eV. Both, I-24 and I-25, produced from I-20, is then form AGL by following elementary reaction step r_{54} and r_{55}, respectively, which has already been discussed above. I-13, also produced from I-9, is then converted to I-18 (r_{33}) or I-19 (r_{34}) by a dehydrogenation step from alcohol group or γ-carbon, respectively. Subsequent elementary reactions discussed above leads to the formation GVL from these two intermediates. Next, we turn our discussion to reaction routes that produce AGL from I-10 derivatives. I-14, produced via reaction step r_{26}, undergoes a C-H bond scission at β-carbon to form I-20 via reaction step r_{35} which has a reaction energy and activation energy of -0.31 eV and 1.09 eV, respectively. Alternative to r_{35}, a C-H bond scission of γ-carbon leads to the formation of I-21 ($CH_3 - \ddot{C} - CH_2 - CH_2 - CO\dot{O}$) via reaction step r_{36} (ΔE_0 = -0.36 eV, $E_{a,0}$ = 0.20 eV). I-20, produced in r_{35}, is then converted to I-25 via reaction step r_{47} which is accompanied by a reaction energy and activation energy of -0.78 and 0.57 eV, respectively, then it follows r_{55} to form AGL via ring closing reaction. On the other hand, I-21, apart from being produced from I-14, can also be formed by O-H bond dissociation of carboxyl group of I-15, this reaction step (r_{38}) is exothermic by 1.11 eV with an activation energy 0.26 eV. I-21 then follows either r_{48} (C-H bond dissociation) to form I-25, or r_{49} (ring closing reaction to form I-8), first reaction is exothermic by 0.73 eV while the second reaction is endothermic by 0.76 eV. I-16, produced from ring formation reaction of I-10, undergoes a C-H bond scission reaction (r_{40}) at γ-carbon to yield I-22 ($CH_3 - C_4OH_4 - OH$) (ΔE_0 = -0.35 eV, $E_{a,0}$ = 0.52 eV). I-22 can also be produced from I-15 by ring closing reaction step r_{39} which has an endothermic heat of reaction (ΔE_0 = 0.16 eV). O-H bond dissociation of terminal OH group of I-22 leads to the formation of I-8

reaction intermediates via reaction step r_{50} (ΔE_0 = -0.50 eV, $E_{a,0}$ = 0.73 eV). Alternatively, C-H bond scission (r_{51}) of β-carbon yields I-23, this step is thermodynamically downhill by 0.40 eV with an activation energy of 0.29 eV. All the intermediates then follow the reaction routes (discussed above) depicted in fig. 3.2(B) to form our desired product GVL. It is worth noting that the oxygen of the ring structure of AGL/GVL comes from the alcohol group of HPA if it follows reaction routes that involves the formation of intermediates I-26 and I-9, but if it involves the formation of I-10 that oxygen comes from carboxylic acid group of HPA.

3.4.4 Levulinic acid direct conversion to γ-valero lactone (GVL) via intermediate α-angelica lactone (AGL) formation

LA can directly be converted to GVL via intermediate formation of AGL, without the formation of HPA. First we will discuss the reaction routes shown in Fig 3.3(A), and then we will analyze DFT energetics of the reaction network shown in Fig 3.3(B). LA dehydrogenation at β-carbon leads to the formation of intermediate I-1 ($CH_3 - CO - \dot{C}H - CH_2 - COOH$) which adsorbs on the surface in $\eta_3\mu_3(O,C,O)$ mode. This step, r_7, has a reaction energy and activation energy of -0.47 eV and 0.10 eV, respectively. I-1 then follows three alternative routes to form AGL. In the first route, I-1 undergoes a ring closing reaction (r_{13}) to produce 5 member ring structure I-5 (ΔE_0 = 0.40 eV, $E_{a,0}$ = 0.93 eV) which is then converted to AGL by subsequent hydrogen removal (r_{14}) from the carbon of the carbonyl functional group with a reaction energy and activation energy of -0.38 eV and 0.24 eV, respectively. In the second route, Hydrogen removal (r_9) from terminal carboxyl group of I-1 yields I-2 (ΔE_0 = -0.94 eV, $E_{a,0}$ = 0.32 eV) which is

then undergoes a ring closing reaction (r_{10}) to form I-3 with a reaction energy and activation energy of 0.85 and 2.07, respectively. To remove the oxygen from γ-carbon, I-3 is hydrogenated (r_{11}) to form I-4 (ΔE_0 = -0.62 eV, $E_{a,0}$ = 0.51 eV) which then undergoes a C-OH bond scission process (r_{19}) to form AGL (ΔE_0 = 0.40 eV, $E_{a,0}$ = 0.93 eV). The high activation energy of r_{10} renders this route to be kinetically improbable. In the third route, a C-OH bond scission from I-1 leads to the formation of I-6 via elementary process r_{12} which is a 0.83 eV exothermic process with a 0.81eV activation energy. I-6 then follows reaction step r_{16} to form AGL. Alternatively, LA, instead of converting to I-1, can be converted to I-7 by removing a OH group from the terminal carboxyl group (ΔE_0 = -0.61 eV, $E_{a,0}$ = 0.71 eV). Reaction routes producing AGL from I-7 is already discussed above. LA conversion to GVL via intermediate formation of hydroxy (Hy) in fig 3.3 (B), which is obtained by hydrogenation of oxygen of the associated ketone group of LA, is an important reaction mechanism and we also studied this reaction mechanism in detail. LA hydrogenation leads to the formation of hydroxy intermediate (ΔE_0 = 0.88 eV, $E_{a,0}$ = 1.36 eV) which then proceed via five different routes, 1) Ring closing reaction (r_{66}) of hydroxy yields I-30 which is a highly saturated molecule. This reaction is thermoneutral (ΔE_0 = 0.04 eV) with an activation energy 0.60 eV. 2) Instead, if hydroxy intermediate undergoes C-H bond scission (r_{67}) of γ-carbon it produces I-11 which is accompanied by an exothermic heat of reaction (ΔE_0 = -0.83 eV, $E_{a,0}$ = 0.09 eV). 3) Alternatively, a C-OH bond dissociation from the carboxyl group helps the formation of I-27. This step (r_{68}) is thermodynamically downhill by 1.04 eV with a 0.58 eV activation barrier. 4) Alcohol group removal (r_{69}) of hydroxy leads to the formation of I-15, and 5) finally, H removal from terminal carboxyl group yields I-31 which step is labelled as r_{70} in our reaction

network. Next, each of these Hy derivatives produced here undergo three more reaction steps to form AGL (see fig 3.3(B)). In the first steps, I-30, the first derivative of Hy, is converted to I-32 and I-22 via O-H bond scission, r_{72} (ΔE_0 = -0.57 eV, $E_{a,0}$ = 0.25 eV), and C-OH bond scission, r_{71} (ΔE_0 = -0.42 eV, $E_{a,0}$ = 0.86 eV), respectively. I-32 then undergoes a C-H bond cleavage process (r_{76}) at γ-carbon to produce I-4 which is then form AGL via reaction step r_{19} with a reaction energy and activation energy of -0.62 and 0.51 eV, respectively. On the other hand, I-22 can either be transformed into I-8 (ΔE_0 = -0.50 eV, $E_{a,0}$ = 0.73 eV) via O-H bond scission, or I-23 (ΔE_0 = -0.40 eV, $E_{a,0}$ = 0.29 eV) via C-H bond scission at γ-carbon. Both of the reaction intermediates (I-23 and I-8) formed here produced AGL via r_{52} and r_{18}, respectively. I-11, the second derivative of Hy, is converted to AGL via different competitive routes all of which has already been discussed previously. The third Hy derivative I-27 produces I-19 and I-7 via reaction step r_{61} and r_{62}, respectively. r_{61} is a C-H bond cleavage process at γ-carbon with a heat of reaction and activation energy of -0.52 and 0.30 eV, respectively. Conversely, r_{62}, an H elimination process from the alcohol group of Hy, is an exothermic reaction (0.45 eV) with a reaction barrier of 0.51 eV. Both I-19 and I-7 is converted to AGL via reaction steps described above. The fourth Hy derivative, I-15, conversion to AGL is already described in the previous section (see fig 3.2(B)). Finally, I-31, produced from Hy, forms I-21 by stripping off the alcohol group (r_{73}), or I-29 by C-H bond cleavage (r_{75}). Both of these reactions are exothermic (-1.00 and -1.01 eV) with an activation barrier of 0.53 and 0.09 eV, respectively. I-21 conversion to AGL is also described above. I-29, finally, produce AGL via intermediate formation of I-4 and I-25 via reaction process r_{53} (ring closure) ad r_{77} (C-OH bond scission), respectively. Considering the thermodynamic and kinetic data, it is

fairly obvious that r_{53} is neither thermodynamically (reaction energy=1.03 eV) nor kinetically (activation energy= 1.51 eV) favorable. The other reaction step r_{77} is accompanied by a heat of reaction of -0.72 eV with an activation energy of 0.50 eV. I-25, produced from I-29 is converted to AGL via r_{55}.

In these two subsections, we discussed the computed DFT energetics of the reaction network delineated in fig 3.2 (A & B) and 3.3 (A& B). In fig 3.4, we show the reaction network for direct catalytic conversion and intermediate HPA formation pathways that don't include intermediate AGL formation. Next, we turn our attention to the desorption of final products from the catalytic surface.

3.4.5 HPA, GVL, and water desorption from the surface

In our microkinetic model, we allowed desorption of stable reaction intermediate HPA, desired product GVL, and water. Desorption reactions are, as expected, endothermic processes with desorption energies of 1.32 eV, 1.05 eV, and 0.55 eV for HPA, GVL, and water, respectively.

3.4.6 Scaling relationships for activation energy prediction of ring forming reaction

DFT investigation of reaction mechanism concerning large biomass model molecules involves significant computational cost. As a result, computational investigation of molecules with more than 4 carbon is prohibitively expensive. To get a reliable estimation of electronic structure and physical properties, scaling relation based on d-band theory and/or bond order conservation theory based model has been developed. Brønsted-Evans-Polanyi (BEP) relationship is a reliable method to efficiently estimate reaction barriers without explicit TS search algorithms. In this study, a BEP relation, obtained from

electronic structure calculations of C-O ring formation steps, is used to find the activation energy of similar type of ring formation reaction,

$$E_A = 0.08 \times \Delta E + 0.56 \quad (3.11)$$

In this equation, E_A, activation energy, is expressed as a function of ΔE, reaction energy. For a detailed discussion about this BEP relation, we refer the reader to the appendix A.

3.5 Gas-phase microkinetic model

For a rational understanding of the reaction kinetics governing the hydrodeoxygenation of LA, we developed a Langmuir-Hinshelwood type mean-field microkinetic model. The underlying assumptions of the mean-field approximation are, the system is well mixed and no spatial correlation or adsorbate-adsorbate interaction exists among the adsorbates. These assumptions have been proven to be very effective and are very powerful to reduce the complexity of the model; however, it may break down if there is 1) significant attractive interaction among adsorbates, 2) local fluctuation of surface coverages, and 3) slow diffusion of adsorbed species, all of which can result in island formation. First, we used competitive adsorption model where all the adsorbates are competing for the same site. In this model, we are normalizing our surface coverages on a per site basis and coverage of any adsorbate indicates the fraction of a site occupied by that adsorbate. Next, a non-competitive two site model was also developed where all the adsorbates except hydrogen were competing for one type of site (denoted as *) while hydrogen adsorbed non-competitively on a distinct type of site denoted as triangle (Δ).

Although we developed our model within mean-field approach; however, it causes serious inconsistencies between experimental kinetics and computational results because

of the aforementioned limitations of mean-field modeling. One way to circumvent this problem is to include adsorbate-adsorbate interactions (or so called "lateral interaction") using an empirical model which is parameterized using DFT calculations. There are few methods available for considering lateral interactions and most of them are very complex and computationally expensive to implement. Among all those models, we choose the one proposed by Grabow et al.[28] because of its simplicity and availability of benchmark calculations. In the preliminary results of our microkinetic model, we found that the most abundant surface species in our system of interest are hydrogen and oxygen. From adsorption energy calculations of H and O on Ru (0001) at various coverages ($\theta_{H/O} = {}^{1}/_{16},\ {}^{2}/_{16},\ {}^{3}/_{16},\ {}^{4}/_{16},\ {}^{8}/_{16},\ {}^{12}/_{16},\ {}^{16}/_{16}$), we determined the differential adsorption energy of H and O as a function of $\theta_H \ and \ \theta_O$, respectively.

$$E_H{}^{differential}(\theta_H, \theta_O) = \begin{cases} -0.68 + 0.15(\theta_H - 0.12) + 0.31 \times \theta_O \ + \\ 3.99 \times \theta_O \ \sqrt{\theta_H \ \theta_O} \quad if\ (\theta_H - 0.12) > 0 \\ -0.68 + 0.31 \times \theta_O \ + \\ 3.99 \times \theta_O \ \sqrt{\theta_H \ \theta_O} \quad if\ (\theta_H - 0.12) \leq 0 \end{cases} \tag{3.12}$$

$$E_O{}^{differential}(\theta_O, \theta_H) = \begin{cases} -2.994 + 2.014(\theta_O - 0.07) + 0.31 \times \theta_H \ + \\ 3.99 \times \theta_H \ \sqrt{\theta_O \ \theta_H} \quad if\ (\theta_O - 0.07) > 0 \\ -2.994 + 0.31 \times \theta_H \ + \\ 3.99 \times \theta_H \ \sqrt{\theta_O \ \theta_H} \quad if\ (\theta_O - 0.07) \leq 0 \end{cases} \tag{3.13}$$

Then, with these lateral interaction parameters we ran our microkinetic model. Model results obtained from the simulation are described in the next section (3.5.1).

3.5.1 Reaction rates and dominant reaction mechanism

Our simulation results for the 1 site model at 323 K and typical reactants conc. (0.45 M LA and 10 bar hydrogen pressure) (see table 3.3) predicts an overall turn-over frequency (TOF) of $2.67 \times 10^{-9}\ s^{-1}$ with a hydrogen coverage of ~100%. In contrast, for the two site model our model predicted TOF and hydrogen coverage at the same temperature condition are $2.23 \times 10^{-6}\ s^{-1}$ and ~100%, respectively. Although the two site model predicts a TOF 3 order of magnitude higher than the one site model, but it is still 3 order of magnitude lower than the experimentally observed TOF ($2.00 \times 10^{-3}\ s^{-1}$) by Abdelrahman et al.[22]. Considering that the two site model is robust to the overestimation of the hydrogen binding energy, which is why we found a high hydrogen surface coverage, we can conclude that the model Ru(0001) surface is not the experimentally observed active site for the HDO of LA for the production of GVL at low temperature region. Interestingly, at moderate temperature (such as 423 K), our one site and two site model predicted TOFs are $3.44 \times 10^{-3}\ s^{-1}$ and $1.30 \times 10^{-2}\ s^{-1}$, respectively, which is comparable to the experimentally observed TOF of $4.80 \times 10^{-1}\ s^{-1}$. This indicates that at moderate temperature (i.e. 423 K), Ru(0001) constitutes the majority of the experimentally observed active sites. Note that in experimental catalysis, Ru nanoparticles (NP) have different exposed surface facets, for example Ru(0001), Ru(100), Ru(101), and interface sites. Our hypothesis is that at moderate temperature Ru(0001) mainly contributes to the experimentally observed reaction kinetics, while at low temperature some other surface facets may become more active, thus a higher experimental TOF has been realized that we couldn't mimic in our simulation which explores only a part of the potential energy surface.

Currently, we are in the process of exploring a much broader potential energy surface that includes different Ru facets, interaction with the solvent molecules etc.

Our microkinetic model also suggests that HDO pathways involving the formation of AGL intermediates are unfavorable. Pathways involving the formation of AGL and its derivatives are order of magnitudes slower in comparison to the overall turn-over frequency. In the interest of brevity, for the later analysis, unless otherwise stated, we limit our discussion to the simulation results obtained from 1 site model as the qualitative trend for both models are same. For example, at 10 bar hydrogen partial pressure and 0.45 M LA, our model predicted AGL formation rate is $6.49 \times 10^{-18}\ s^{-1}$ while the model predicts an overall TOF of $3.44 \times 10^{-3}\ s^{-1}$ for the production of GVL at 423 K temperature. Similarly, at high temperature (523K), AGL and GVL production rates are $6.40 \times 10^{-10}\ s^{-1}$ and $3.37 \times 10^{-1}\ s^{-1}$, respectively. Experimental observation by Abdelrahman et al. also reported a similar order of magnitude difference in AGL and GVL site time yield (STY). In their scientific study[22], they report at 423K a STY (site time yield is a comparable measurement of TOF) of $5 \times 10^{-7}\ s^{-1}$ for AGL formation pathway while the reported STY of LA is $5 \times 10^{-3}\ s^{-1}$. In summary, for 1 site model we found that AGL formation pathways do not contribute to the overall product yield, furthermore, some of the AGL derivatives bind strongly on the metallic surface thus resulting in mild surface poisoning which has a detrimental effect on the high temperature (>423K) reaction kinetics. The simulation results for 2 site model also suggests that AGL formation pathways have negligible turn-over as compared to direct catalytic conversion pathway and AGL derivatives contribute to the surface poisoning at high temperatures.

Our analysis of the dominant reaction mechanism (see figure 3.4) suggests that the dominant reaction occurs via direct catalytic conversion pathway, not via intermediate HPA and/or AGL formation pathway. The dominant reaction mechanism includes the following elementary reaction steps:

1. LA hydrogenation towards surface alkoxy formation via C-H bond formation step (r_3) which is a thermoneutral process (0.06 eV) with an activation barrier of 0.67 eV.
2. C-O bond formation step to yield I-80 from alkoxy via ring closing reaction (r_{86}). This step is accompanied by a reaction energy and activation barrier of 0.22 eV and 0.33 eV, respectively.
3. Finally, a C-OH bond scission leads to the formation of final product, GVL via reaction step r_{90}.

From the energetics of the dominant reaction pathway, we see that the potential energy surface followed by the dominant mechanism is mostly flat except for a 0.67 eV barrier for the first hydrogenation process. From this analysis, we can expect that the first LA hydrogenation to be the rate controlling reaction for the HDO of LA process.

3.5.2 Reaction order and apparent activation barrier

We calculated apparent activation barrier (see figure 3.5 and 3.6) and reaction order (see figure 3.7 and 3.8) with respect to gas phase partial pressures for they give us valuable information about the sensitivity of TOF on extensive parameters such as temperature and reactants partial pressures.

$$E_a = -R\frac{\partial ln(TOF)}{\partial(^1/_T)} \tag{3.14}$$

$$n_i = \frac{\partial ln(TOF)}{\partial ln(P_i)} \tag{3.15}$$

From figure 3.5 and 3.6, we see that temperature effect is more prominent at low temperature region as empty sites coverage increases owing to the increased desorption of hydrogen from the surface. . In contrast, at high temperature region (>423K) that effect is subsiding due to the increasing hydrocarbon coverage, which inhibits rate of empty site formation. Further investigation reveals that some AGL derivatives, specifically I-20, I-25 and I-46, bind strongly and contribute to the surface poisoning. Experimental work by Lange et al. reported carbon poisoning effect at high temperatures[5], our computational analysis at high temperatures confirms this experimental observations. From the simulation of 1 site model for a 0.025 M LA solution, our model predicted activation barrier is very high, for example, our predicted E_a at 323K-423K is 1.7-1.8 eV for varying hydrogen partial pressures of 4-40 bar. In contrast, in the high temperature region, apparent activation energy varies from 0.92-1.2 eV for the same hydrogen partial pressure range. From these analyses, we observe an increase in apparent activation energy with increasing hydrogen partial pressure. Next, we predict the apparent activation energy for 0.45 M LA solution for the same hydrogen partial pressure range which is calculated to be in the range of 1.6-1.8 eV in the low temperature region while the high temperature range is 0.83-1.00 eV. To confirm the positive effect of LA concentration on the reaction kinetics, our model also predicts the apparent activation energy at 1.5 M LA solution, our model predicted E_a is 1.5-1.7 eV and 0.80-0.95 eV, respectively, at low and high temperature region at this condition for the same hydrogen partial pressure range previously noted.

Figure 3.7 (B) and 3.8 (B) reveal that hydrogen partial pressure has a negligible effect on the activity of the Ru(0001) surface for both 1 site and 2 site model. At high temperatures, catalytic activity is the same for a wide range of hydrogen partial pressures (4-40 bar), though at low temperatures, catalytic activity decreases with increasing hydrogen partial pressures. For instance, at 523 K and 0.45 M LA solution, TOF changes from 0.30 to 0.35 for a hydrogen partial pressure change from 4 bar to 40 bar, but at 323 K, TOF decreases roughly by 1 order of magnitude. In contrast, LA concentration (Fig 3.7(A) and 3.8(A)) has a marked positive effect on the reaction activity at both high and low temperatures. At typical reaction conditions of 0.45 M LA concentration and 10 bar hydrogen partial pressure at 423 K temperature, our model predicts an LA reaction order of 0.64 for a ±10% concentration change, and hydrogen reaction order of -0.26 in the 9-11 bar hydrogen partial pressure range. At low temperature (323 K) and the same operating conditions, our model predicted LA and hydrogen reaction orders are 0.99 and -0.99, respectively, since surface is fully hydrogen covered at that temperature. At elevated temperature (523 K), our model predicts LA reaction order to be 0.48 and hydrogen reaction order to be 0.09. From the order analysis, we see that at low temperature our model predicts a higher sensitivity towards partial pressures, e.g. high absolute reaction order of reactants, which indicates that at low temperature, surface adsorption is limiting the reaction kinetics.

Similarly, the 2 site model predicts high activation barrier at low temperature regions (323-423 K) and low activation barrier at high temperature regions (423-523 K). Interestingly, 2 site model suggested hydrogen orders agree quite well with the

experimentally predicted hydrogen order (0.5)[22], which confirms that hydrogen adsorption is indeed a non-competitive adsorption process.

3.5.3 Rate control analysis

To identify rate controlling parameters and to find the sensitivity of intensive parameters such as free energy of adsorbed species and TSs, we used Campbell's degree of rate control analysis[29]. Kinetic rate control is defined as,

$$KRC_i = \frac{\partial ln(TOF)}{\partial(-\frac{G^0_{TS,i}}{k_B T})} = \frac{\partial ln(TOF)}{\partial ln(k_i^+)} \tag{3.16}$$

In this equation, $G^0_{TS,i}$ and k_i^+ are the free energy of activation and forward rate constant of elementary reaction i, respectively. The sensitivity of adsorbed species energy on the TOF is termed as thermodynamic rate control and is defined as

$$TRC_i = \frac{\partial ln(TOF)}{\partial(-\frac{G^0_{n,i}}{k_B T})} \tag{3.17}$$

Here, $G^0_{n,i}$ is the free energy of adsorbed species which is computed from our DFT calculations. Our microkinetic model suggests LA adsorption ($KRC = 0.52$) and LA hydrogenation to alkoxy intermediate ($KRC = 0.48$) are the rate controlling elementary reaction steps for 1 site model. For the 2 site model, our calculations predict the same elementary steps to be rate controlling with different weights, 0.26 and 0.74 for LA adsorption and LA hydrogenation to alkoxy, respectively. Our TRC analysis for both models suggests that hydrogen adsorption energy is the rate controlling thermodynamic state.

3.6 Conclusions

Hydrodeoxygenation of levulinic acid to produce γ-valerolactone including the endothermic formation of angelica lactone (AGL) has been studied on terrace type Ru (0001) model catalytic surface using plane wave density functional theory and mean field microkinetic modeling. We studied the temperature and pressure dependence of the turnover frequency (TOF) at typical reaction conditions where the catalyst is modeled as pure metallic slab. Comparing our simulation results with experimental data, we qualitatively mimicked the catalytic behavior of the Ru(0001) facet. In particular, we identified that AGL pathways are not the dominant reaction pathways and they contribute to the surface poisoning at high temperatures. We also identified two different active regimes based on the operating temperatures that are described by very different activation energies. This suggests that the metallic surface is not active at low temperatures; however, it is moderately active at high temperatures and we precisely reproduced the experimental activation energy. Further analysis of our microkinetic model shows that the low temperature inactivity of the metallic phase of the catalysts can be explained as the result of hydrogen poisoning effect. In this regime, the low activation barrier stems from the inaccurate consideration of lateral interactions. We used explicit Grabow's lateral interaction model, which is a good model in itself; however, it is unable to capture the local chemical environment dependence of the lateral interaction energies. In conclusion, though our model incorporates an approximate explicit lateral interaction model; however, the insights afforded by this mean-field microkinetic model simulations will enable us to design better catalysts for the hydrodeoxygenation of model biomass molecules.

3.7 Acknowledgements

We gratefully acknowledge financial support from the National Science Foundation (CBET-1159863) and in part from the U.S. Department of Energy, Office of Basic Energy Sciences (SC0007167). Computational resources have been provided by the National Energy Research Scientific Computing Center (NERSC) and Pacific Northwest National Laboratory (PNNL).

3.8 Tables and figures

Table 3.1: Species nomenclature, chemical formula, binding mode and number of adsorption sites of various surface species.

Species	Chemical Formula	Binding mode	No. of Adsorption site
LA	$CH_3 - CO - CH_2 - CH_2 - COOH$	$\eta_2\mu_3(O,O)$	2
Al	$CH_3 - CH(\dot{O}) - CH_2 - CH_2$	$\eta_2\mu_4(O,O)$	2
Hy	$CH_3 - \dot{C}(OH) - CH_2 - CH_2$	$\eta_2\mu_2(O,C)$	2
HPA	$CH_3 - CH(OH) - CH_2 - CH_2$	$\eta_3\mu_3(O,C,O)$	3
I-01	$CH_3 - CO - \dot{C}H - CH_2 - COOH$	$\eta_3\mu_3(O,C,O)$	3
I-02	$CH_3 - CO - \dot{C}H - CH_2 - CO\dot{O}$	$\eta_4\mu_4(O,O,O,C)$	4
I-03	$C_4OH_3(CH_3)(O)(O)$	$\eta_2\mu_3(C,O)$	2
I-04	$C_4OH_3(CH_3)(OH)(O)$	$\eta_2\mu_2(C,O)$	2
I-05	$CH_3 - C_4OH_3(OH) = O$	$\eta_2\mu_2(O,O)$	2
I-06	$CH_3 - CO - \dot{C}H - CH_2 - \dot{C}O$	$\eta_3\mu_3(O,C,O)$	3
I-07	$CH_3 - CO - CH_2 - CH_2 - \dot{C}O$	$\eta_3\mu_3(O,C,O)$	3
I-08	$CH_3 - C_4OH_4 = O$	$\eta_2\mu_2(C,O)$	2
I-09	$CH_3 - CH(OH) - \dot{C}H - CH_2$	$\eta_3\mu_3(O,C,C)$	3
I-10	$CH_3 - \dot{C}H - CH_2 - CH_2 - COOH$	$\eta_2\mu_2(C,O)$	2
I-11	$CH_3 - \dot{C}(OH) - \dot{C}H - CH_2$	$\eta_3\mu_3(C,C,O)$	3
I-12	$CH_3 - \dot{C}H - \dot{C}H - CH_2 - COOH$	$\eta_3\mu_3(C,C,O)$	3
I-13	$CH_3 - CH(OH) - \dot{C}H - CH_2$	$\eta_3\mu_4(C,C,O)$	3
I-14	$CH_3 - \dot{C}H - CH_2 - CH_2 - CO\dot{O}$	$\eta_3\mu_3(O,O,C)$	3
I-15	$CH_3 - \ddot{C} - CH_2 - CH_2 - COOH$	$\eta_1\mu_1(C)$	2
I-16	$CH_3 - C_4OH_5 - OH$	$\eta_2\mu_2(C,O)$	2
I-17	$CH_3 - \ddot{C} - \dot{C}H - CH_2 - COOH$	$\eta_3\mu_3(O,C,C)$	3
I-18	$CH_3 - CH(\dot{O}) - \dot{C}H - CH_2 - \dot{C}O$	$\eta_3\mu_3(O,C,C)$	3

I-19	$CH_3 - \dot{C}(OH) - \dot{C}H - CH_2 - \dot{C}O$	$\eta_4\mu_3(O,C,C,C)$	3
I-20	$CH_3 - \dot{C}H - \dot{C}H - CH_2 - CO\dot{O}$	$\eta_2\mu_2(O,O)$	2
I-21	$CH_3 - \ddot{C} - CH_2 - CH_2 - CO\dot{O}$	$\eta_3\mu_3(O,O,C)$	3
I-22	$CH_3 - C_4OH_4 - OH$	$\eta_2\mu_2(C,C)$	2
I-23	$CH_3 - C_4OH_3 - OH$	$\eta_2\mu_2(C,C)$	2
I-24	$CH_3 - C_4OH_4 = O$	$\eta_2\mu_2(C,O)$	2
I-25	$CH_3 - \ddot{C} - \dot{C}H - CH_2 - CO\dot{O}$	$\eta_3\mu_3(O,O,C)$	3
I-26	$CH_3 - CH(OH) - CH_2 - CH_2$	$\eta_3\mu_3(O,C,O)$	3
I-27	$CH_3 - \dot{C}(OH) - CH_2 - CH_2 - \dot{C}O$	$\eta_2\mu_2(C,C)$	2
I-28	$CH_3 - CH(\dot{O}) - CH_2 - CH_2 - \dot{C}O$	$\eta_3\mu_3(O,O,C)$	3
I-29	$CH_3 - \dot{C}(OH) - \dot{C}H - CH_2$	$\eta_4\mu_4(O,O,C,C)$	4
I-30	$CH_3(OH) - C_4OH_4 - OH$	$\eta_2\mu_2(C,O)$	2
I-31	$CH_3 - \dot{C}(OH) - CH_2 - CH_2$	$\eta_3\mu_3(O,O,C)$	3
I-32	$CH_3(OH) - C_4OH_4 = O$	$\eta_2\mu_2(O,O)$	2
I-33	$CH_3 - CH(OH) - CH_2 - CH_2$	$\eta_2\mu_2(O,C)$	2
I-34	$CH_3 - CH(OH) - CH_2 - CH_2$	$\eta_1\mu_1(C)$	1
I-35	$CH_3 - CH(\dot{O}) - CH_2 - CH_2$	$\eta_2\mu_5(O,C)$	2
I-36	$CH_3 - CH(\dot{O}) - CH_2 - CH_2$	$\eta_2\mu_3(O,C)$	2
I-37	$CH_3 - CO - CH_2 - CH_2 - CO\dot{O}$	$\eta_3\mu_3(O,O,O)$	3
I-38	$CH_3 - CH(\dot{O}) - CH_2 - CH_2$	$\eta_3\mu_3(O,O,O)$	3
I-39	$C_4OH_5(CH_3)(\dot{O})(\dot{O})$	$\eta_2\mu_3(O,O)$	2
I-40	$C_4OH_5(CH_3)(\dot{O})(OH)$	$\eta_1\mu_1(O)$	1
AGL	$CH_3 - C_4OH_3 = O$	$\eta_2\mu_2(C,C)$	2
GVL	$CH_3 - C_4OH_5 = O$	$\eta_2\mu_2(O,O)$	2
OH	OH	$\eta_1\mu_3(O)$	1
H	H	$\eta_1\mu_3(H)$	1
H_2O	H_2O	$\eta_1\mu_1(O)$	1
O	O	$\eta_1\mu_3(O)$	1

Table 3.2: Zero-point corrected reaction and activation energies, imaginary frequencies of the transition state structures, and free energies of reaction and activation for all elementary reactions at 423K.

Step	**Reaction**	ΔE_0 **(eV)**	$\Delta E_0^{\ddagger}$ **(eV)**	ν_i (cm^{-1})	$\Delta G(T, P^0)$	$\Delta G^{\ddagger}(T, P^0)$
r_1	$LA(g) + 2* \rightarrow LA*$	-1.36	N/A	N/A	-0.42	N/A
r_2	$H_2(g) + 2* \rightarrow 2H*$	-1.30	N/A	N/A	-0.82	N/A
r_3	$LA* + H* \rightarrow Al* + *$	0.06	0.67	818	0.09	0.70
r_4	$LA* + H* \rightarrow Hy* + *$	0.88	1.36	1249	0.87	1.35
r_5	$Al* + H* \rightarrow HPA*$	0.76	1.29	1194	0.78	1.23
r_6	$Hy* + H* \rightarrow HPA*$	-0.05	0.76	964	0.00	0.76
r_7	$LA* + 2* \rightarrow I - 1* + H*$	-0.47	0.21	780	-0.42	0.29
r_8	$LA* + 2* \rightarrow I - 7* + OH*$	-0.61	0.71	264	-0.54	0.75

r_9	$I-1*+2*\rightarrow I-2*+H*$	-0.94	0.32	1090	-0.94	0.29
r_{10}	$I-2*\rightarrow I-3*+2*$	0.85	2.07	375	0.87	2.07
r_{11}	$I-3*+H*\rightarrow I-4*+*$	0.74	0.90	1287	0.72	0.92
r_{12}	$I-1*+*\rightarrow I-6*+OH*$	-0.83	0.81	332	-0.87	0.80
r_{13}	$I-1*\rightarrow I-5*+*$	0.40	0.93	N/A	0.39	0.89
r_{14}	$I-5*+*\rightarrow AGL*+OH*$	-0.38	0.24	173	-0.35	0.25
r_{15}	$I-7*+*\rightarrow I-6*+H*$	-0.70	0.54	794	-0.75	0.48
r_{16}	$I-6*\rightarrow AGL*+*$	0.86	1.08	291	0.90	1.14
r_{17}	$I-7*\rightarrow I-8*+*$	0.52	0.87	266	0.49	0.89
r_{18}	$AGL*+H*\rightarrow I-8*+*$	0.37	0.70	919	0.33	0.68
r_{19}	$I-4*+*\rightarrow AGL*+OH*$	-0.62	0.51	223	-0.61	0.55
r_{20}	$HPA*+*\rightarrow I-9*+H*$	-0.22	0.51	814	-0.23	0.49
r_{21}	$HPA***\rightarrow I-10**+OH*$	-0.34	0.99	241	-0.38	1.01
r_{22}	$I-9*+*\rightarrow I-11*+H*$	-0.56	0.29	899	-0.57	0.28
r_{23}	$I-9*+*\rightarrow I-12*+OH*$	-0.82	0.44	326	-0.84	0.39
r_{24}	$I-9*+*\rightarrow I-13*+OH*$	-0.73	0.44	331	-0.71	0.45
r_{25}	$I-10*+2*\rightarrow I-12*+H*$	-0.71	0.30	936	-0.69	0.30
r_{26}	$I-10*+2*\rightarrow I-14*+H*$	-0.98	0.34	1277	-0.93	0.34
r_{27}	$I-10*+*\rightarrow I-15*+H*$	-0.23	0.06	796	-0.25	0.09
r_{28}	$I-10*\rightarrow I-16*$	0.28	0.81	N/A	0.32	0.82
r_{29}	$I-11*+*\rightarrow I-17*+OH*$	-0.60	1.03	413	-0.65	1.04
r_{30}	$I-11*+*\rightarrow I-19*+OH*$	-0.73	0.37	319	-0.70	0.43
r_{31}	$I-12*+*\rightarrow I-17*+H*$	-0.33	0.19	814	-0.37	0.18
r_{32}	$I-12*\rightarrow I-20*+H*$	-0.58	0.40	1330	-0.61	0.36
r_{33}	$I-13*+*\rightarrow I-18*+H*$	-0.32	0.42	1121	-0.33	0.41
r_{34}	$I-13*+*\rightarrow I-19*+H*$	-0.55	0.74	879	-0.56	0.71
r_{35}	$I-14*\rightarrow I-20*+H*$	-0.31	1.09	880	-0.37	1.06
r_{36}	$I-14*+*\rightarrow I-21*+H*$	-0.36	0.20	804	-0.35	0.21
r_{37}	$I-15*+2*\rightarrow I-17*+H*$	-0.81	0.22	938	-0.82	0.26
r_{38}	$I-15*+2*\rightarrow I-21***+H*$	-1.11	0.26	1028	-1.03	0.30
r_{39}	$I-15**\rightarrow I-22**$	0.16	0.48	263	0.24	0.60
r_{40}	$I-16**+*\rightarrow I-22*+H*$	-0.35	0.52	825	-0.33	0.54
r_{41}	$I-17*\rightarrow I-23*+*$	0.57	1.29	410	0.66	1.41
r_{42}	$I-17*+*\rightarrow I-25*+H*$	-1.02	0.31	1137	-0.93	0.36
r_{43}	$I-18*+*\rightarrow I-6*+H*$	-0.86	0.50	560	-0.89	0.48
r_{44}	$I-18*\rightarrow I-24*+*$	0.50	0.77	265	0.52	0.80
r_{45}	$I-19*+*\rightarrow I-6*+H*$	-0.63	0.31	1286	-0.66	0.30
r_{46}	$I-20*\rightarrow I-24*$	0.85	2.25	463	0.95	2.27
r_{47}	$I-20*+2*\rightarrow I-25*+H*$	-0.78	0.57	785	-0.69	0.64
r_{48}	$I-21*+*\rightarrow I-25*+H*$	-0.73	0.28	966	-0.71	0.28
r_{49}	$I-21*\rightarrow I-8*+*$	0.76	0.80	282	0.74	0.82
r_{50}	$I-22*+*\rightarrow I-8*+H*$	-0.50	0.73	1216	-0.53	0.75
r_{51}	$I-22*+*\rightarrow I-23*+H*$	-0.40	0.29	721	-0.40	0.30
r_{52}	$I-23*+*\rightarrow AGL*+H*$	-0.47	0.72	1208	-0.46	0.69
r_{53}	$I-29*\rightarrow I-4*+2*$	1.03	1.51	N/A	1.03	1.59
r_{54}	$AGL*+H*\rightarrow I-24*+*$	0.50	0.56	698	0.51	0.56
r_{55}	$I-25*\rightarrow AGL*+*$	1.12	1.16	321	1.13	1.17
r_{56}	$I-24*+H*\rightarrow GVL*+*$	0.00	0.84	923	-0.03	0.85
r_{57}	$HPA*+*\rightarrow I-26*+OH*$	-0.66	0.15	254	-0.67	0.14
r_{58}	$I-26*\rightarrow I-27*+H*$	-0.33	0.73	962	-0.32	0.72
r_{59}	$I-26*+*\rightarrow I-13*+H*$	-0.30	0.42	853	-0.26	0.42
r_{60}	$I-26*+*\rightarrow I-28*+H*$	-0.88	0.36	1237	-0.83	0.37

r_{61}	$I-27*+2* \rightarrow I-19*+H*$	-0.52	0.30	435	-0.51	0.33
r_{62}	$I-27*+2* \rightarrow I-7*+H*$	-0.45	0.51	1269	-0.42	0.52
r_{63}	$I-28*+* \rightarrow I-7*+H*$	0.10	0.80	736	0.10	0.76
r_{64}	$I-28*+* \rightarrow I-18*+H*$	0.26	0.96	856	0.24	0.95
r_{65}	$I-8*+H* \rightarrow GVL*+*$	0.13	0.97	714	0.15	0.97
r_{66}	$Hy* \rightarrow I-30*$	0.04	0.60	N/A	0.13	0.61
r_{67}	$Hy*+2* \rightarrow I-11*+H*$	-0.83	0.09	934	-0.81	0.12
r_{68}	$Hy*+* \rightarrow I-27*+OH*$	-1.04	0.58	309	-1.01	0.60
r_{69}	$Hy*+* \rightarrow I-15*+OH*$	-0.62	0.84	392	-0.65	0.84
r_{70}	$Hy*+2* \rightarrow I-31*+H*$	-0.73	0.44	951	-0.67	0.42
r_{71}	$I-30*+* \rightarrow I-22*+OH*$	-0.42	0.86	206	-0.45	0.83
r_{72}	$I-30*+* \rightarrow I-32*+H*$	-0.57	0.25	1297	-0.63	0.26
r_{73}	$I-31*+* \rightarrow I-21*+OH*$	-1.00	0.53	405	-1.01	0.52
r_{74}	$I-31* \rightarrow I-32*+*$	0.12	0.67	N/A	0.08	0.56
r_{75}	$I-31*+2* \rightarrow I-29*+H*$	-1.01	0.09	949	-1.01	0.10
r_{76}	$I-32*+* \rightarrow I-4*+H*$	-0.10	0.81	876	-0.06	0.84
r_{77}	$I-29* \rightarrow I-25*+OH*$	-0.72	0.50	281	-0.71	0.52
r_{78}	$GVL* \rightarrow GVL(g)+2*$	1.01	N/A	N/A	0.07	N/A
r_{79}	$OH*+H* \rightarrow H_2O*+*$	0.58	1.16	1105	0.52	1.13
r_{80}	$HPA*+H* \rightarrow I-33*+2*$	0.55	1.02	1311	0.56	1.03
r_{81}	$I-39*+H* \rightarrow I-40*+2*$	-0.04	0.32	1226	-0.05	0.32
r_{82}	$I-26*+H* \rightarrow I-34*+3*$	0.83	1.54	847	0.82	1.49
r_{83}	$I-33* \rightarrow I-34*+OH*$	-0.37	0.29	223	-0.41	0.25
r_{84}	$I-33*+* \rightarrow I-35*+H*$	-0.25	0.64	900	-0.26	0.65
r_{85}	$Al*+H* \rightarrow I-35*+*$	1.06	1.41	1350	1.07	1.44
r_{86}	$Al* \rightarrow I-40*+*$	0.22	0.33	138	0.24	0.37
r_{87}	$I-34*+2* \rightarrow I-36*+H*$	-0.44	0.59	1280	-0.44	0.60
r_{88}	$I-35*+* \rightarrow I-36*+OH*$	-0.56	0.75	501	-0.58	0.78
r_{89}	$I-36* \rightarrow I-16*$	0.21	1.28	293	0.23	1.31
r_{90}	$I-40*+2* \rightarrow GVL*+OH*$	-0.24	0.04	241	-0.24	0.05
r_{91}	$LA*+2* \rightarrow I-37*+H*$	-1.13	0.06	1045	-1.11	0.04
r_{92}	$I-37*+H* \rightarrow I-38*$	0.45	0.68	486	0.46	0.71
r_{93}	$I-38* \rightarrow I-39*+*$	1.01	1.49	N/A	1.03	1.59
r_{94}	$H_2O* \rightarrow H_2O(g)+*$	0.55	N/A	N/A	0.04	N/A
r_{95}	$OH*+* \rightarrow H*$+O*	-0.84	0.65	1310	-0.82	0.66
r_{96}	$HPA* \rightarrow HPA(g)+*$	1.33	N/A	N/A	0.41	N/A

Table 3.3: Computed turnover frequencies at various reaction temperatures, hydrogen partial pressures, and 0.45 M LA solution.

a) 1 site model

TOF (s^{-1})		**Hydrogen partial pressure (bar)**			
		4	**10**	**20**	**40**
Temperature (K)	**323**	6.66×10^{-9}	2.67×10^{-9}	1.34×10^{-9}	6.68×10^{-10}
	373	2.53×10^{-5}	1.62×10^{-5}	9.43×10^{-6}	4.97×10^{-6}
	423	4.10×10^{-3}	3.44×10^{-3}	2.71×10^{-3}	1.85×10^{-3}
	473	1.07×10^{-1}	9.97×10^{-2}	8.78×10^{-2}	7.02×10^{-2}
	523	3.00×10^{-1}	3.37×10^{-1}	3.52×10^{-1}	3.52×10^{-1}

b) 2 site model

TOF (s^{-1})		Hydrogen partial pressure (bar)			
		4	**10**	**20**	**40**
Temperature (K)	**323**	1.64×10^{-6}	2.23×10^{-6}	2.81×10^{-6}	3.53×10^{-6}
	373	3.23×10^{-4}	4.38×10^{-4}	5.52×10^{-4}	6.95×10^{-4}
	423	9.52×10^{-3}	1.30×10^{-2}	1.64×10^{-2}	2.08×10^{-2}
	473	1.09×10^{-2}	1.64×10^{-2}	2.24×10^{-2}	3.03×10^{-2}
	523	2.09×10^{-2}	3.23×10^{-2}	4.47×10^{-2}	6.14×10^{-2}

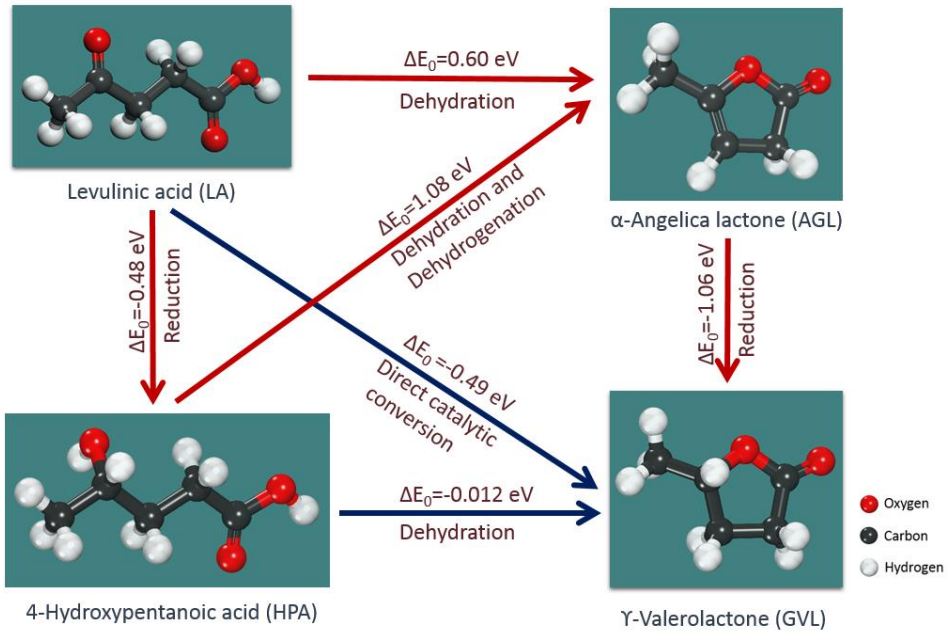

Figure 3.1: Possible reaction pathways for the hydrodeoxygenation (HDO) of levulinic acid (LA) to γ-valerolactone (GVL). Pathways involving the formation of angelica lactone (AGL) are displayed with red arrows. Zero-point corrected reaction energies for various gas phase reactions have been computed at the PBE-D3 level of theory.

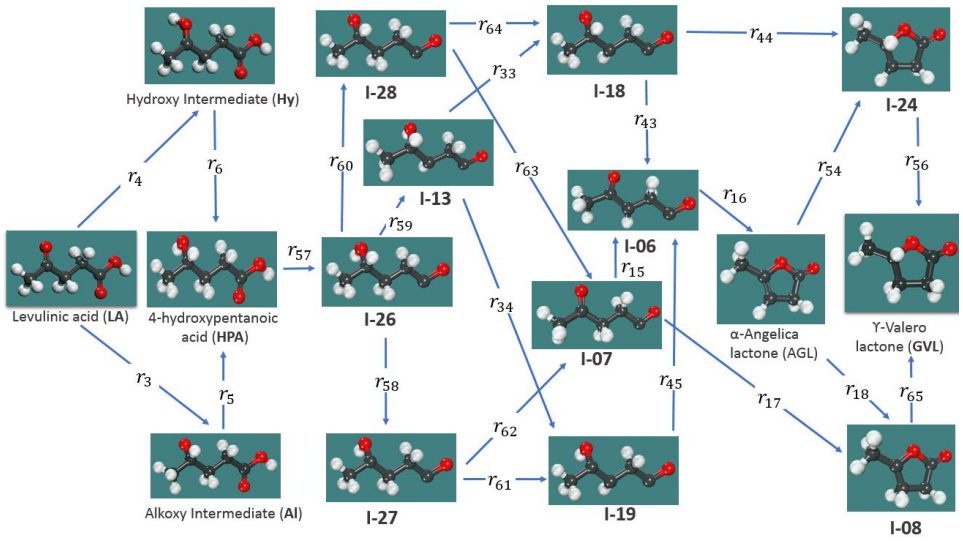

(A)

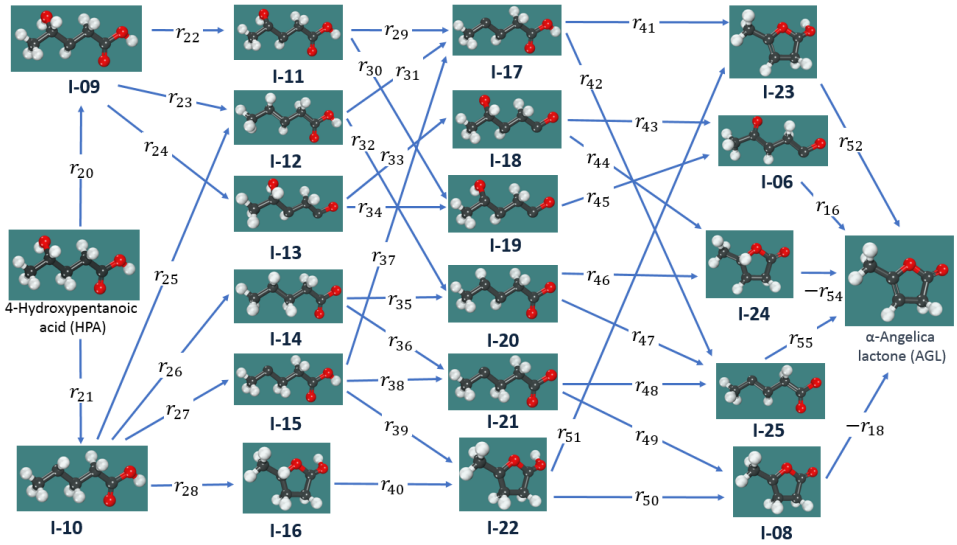

(B)

Figure 3.2: Different pathways for LA hydrodeoxygenation to form GVL via LA hydrogenation to HPA, subsequent dehydration and dehydrogenation to form AGL which is followed by hydrogenation of AGL to form GVL. A) Pathways leading to GVL formation via –OH group removal of HPA is shown B) pathways for HPA to AGL formation via intermediate I-9 and I-10 is shown.

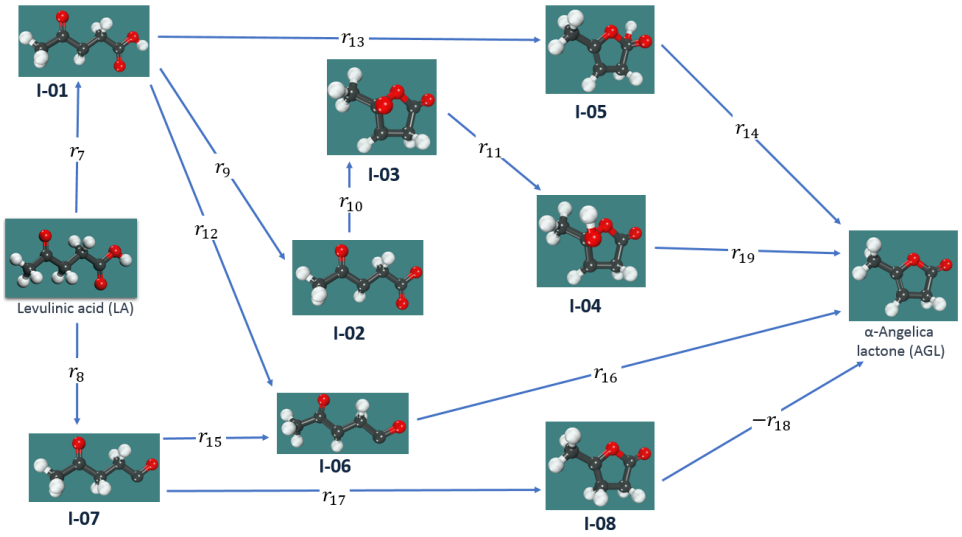

(A)

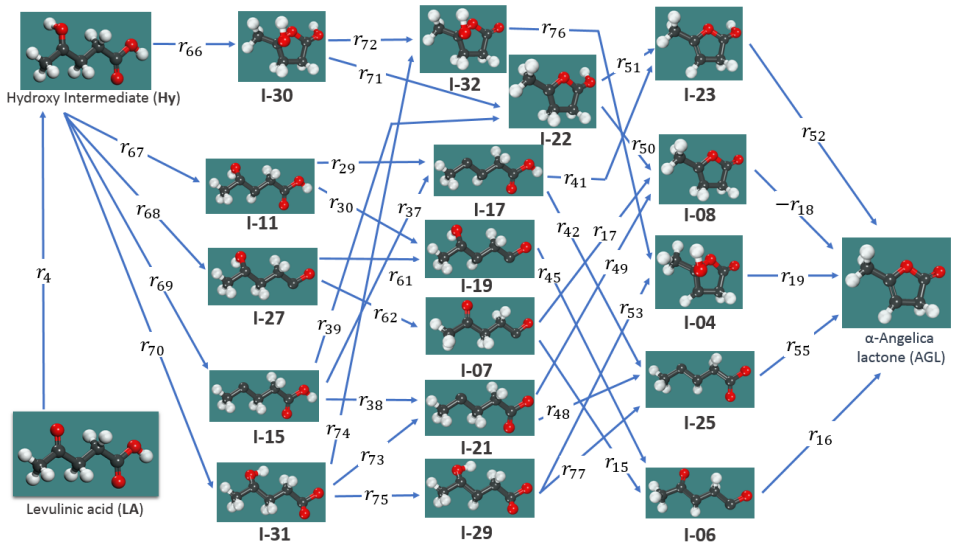

(B)

Figure 3.3: Different pathways for LA hydrodeoxygenation to form GVL via direct catalytic conversion of LA to AGL through dehydration A) LA conversion to AGL via intermediate I-1 and I-7 is shown B) pathways for LA to AGL formation via intermediate Hy is shown.

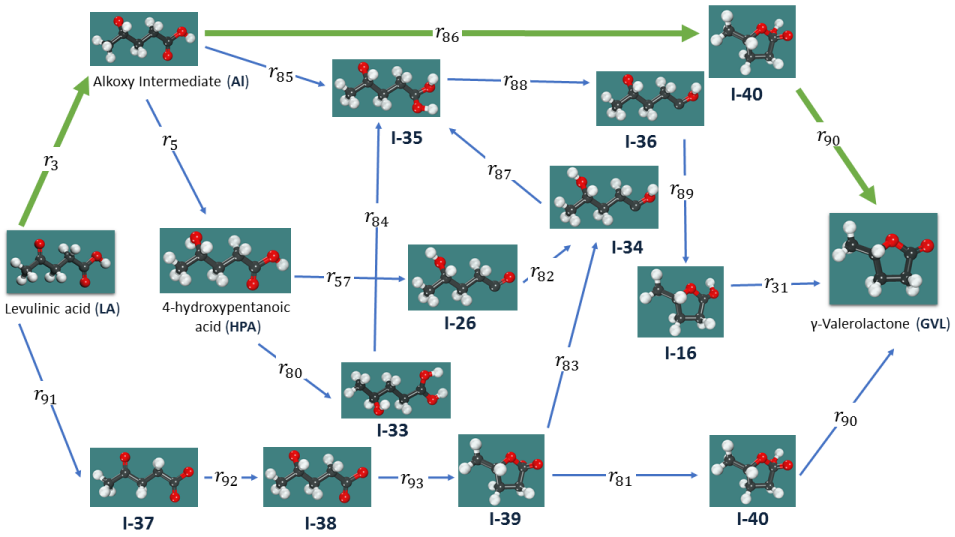

Figure 3.4: Pathways for LA hydrodeoxygenation to form GVL via direct catalytic conversion and hydrogenation. Pathway marked in green shows the dominant reaction mechanism.

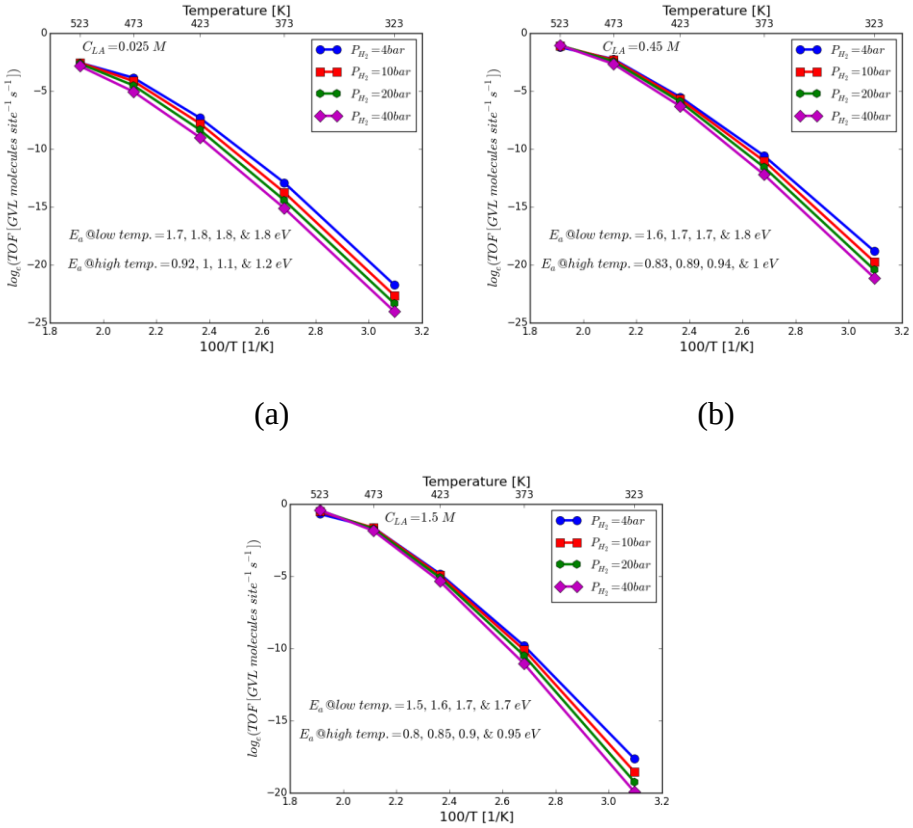

Figure 3.5: Turn over frequencies for the HDO of LA predicted by the mean-field microkinetic model on Ru(0001) surface for 1 site competitive Langmuir-Hinshelwood type reaction mechanism at a) 0.025 M LA solution, b) 0.45 M LA solution, and c) 1.5 M LA solution. Apparent activation energies at both low temperature (323K-423K) and high temperature (423K-523K) regions are also reported here for varying hydrogen partial pressures.

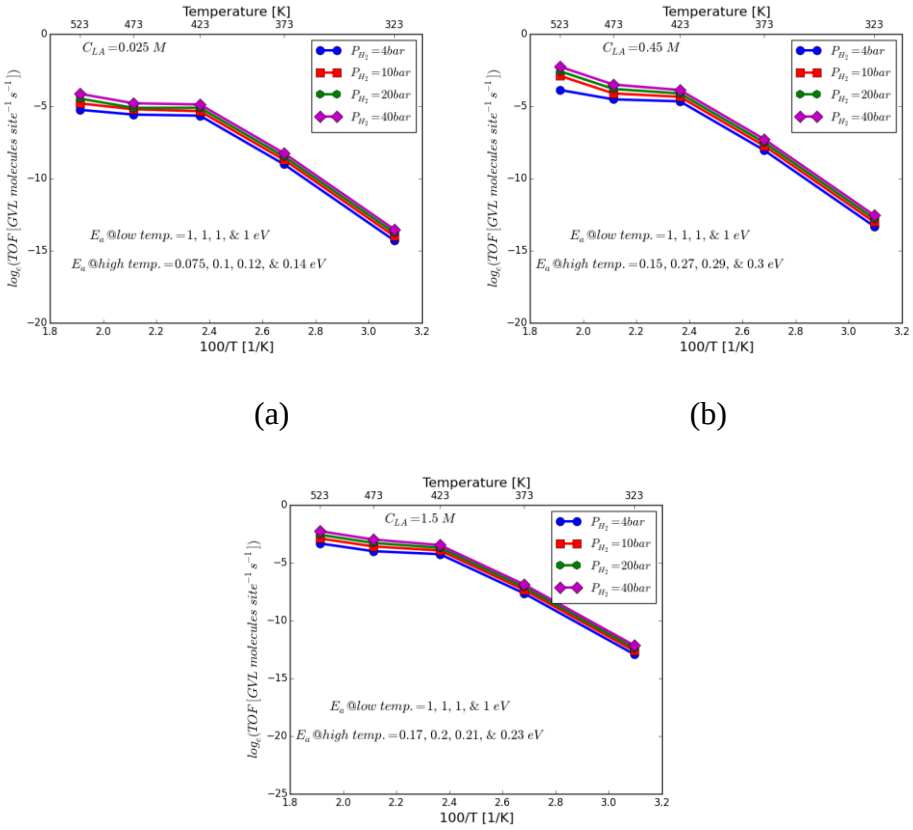

Figure 3.6: Turn over frequencies for the HDO of LA predicted by the mean-field microkinetic model on Ru(0001) surface for the 2 site model at a) 0.025 M LA solution, b) 0.45 M LA solution, and c) 1.5 M LA solution. Apparent activation energies at both low temperature (323K-423K) and high temperature (423K-523K) regions are also reported here for varying hydrogen partial pressures.

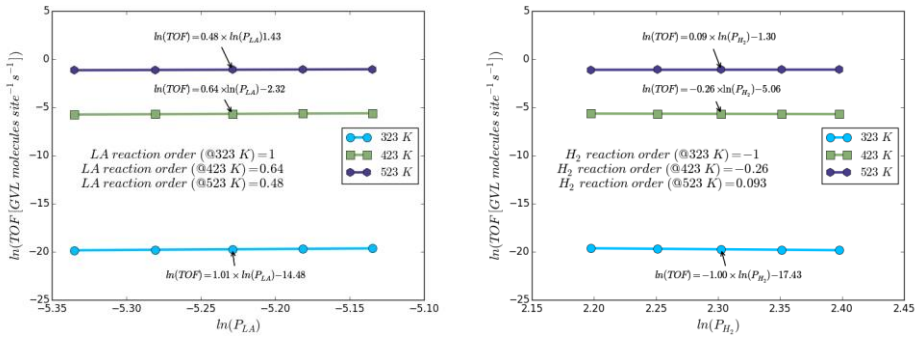

(a) (b)

Figure 3.7: Reaction orders calculated for the HDO of LA on Ru(0001) surface for 1 site competitive Langmuir-Hinshelwood type reaction mechanism, a) order of LA at various reaction temperatures (323 K, 423 K and 523 K) at 10 bar hydrogen partial pressure and b) order of hydrogen at various reaction temperatures (323 K, 423 K and 523 K) at 0.45 M LA concentration.

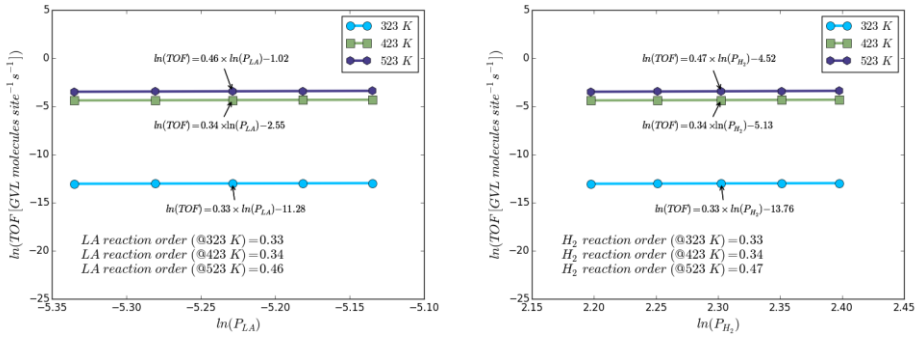

(a) (b)

Figure 3.8: Reaction orders calculated for the HDO of LA on Ru(0001) for 2 site model, a) order of LA at various reaction temperatures (323 K, 423 K and 523 K) at 10 bar hydrogen partial pressure and b) order of hydrogen at various reaction temperatures (323 K, 423 K and 523 K) at 0.45 M LA concentration.

3.9 Bibliography

1. Luo, W.; Sankar, M.; Beale, A. M.; He, Q.; Kiely, C. J.; Bruijnincx, P. C. A.; Weckhuysen, B. M., *Nat. Commun.* **2015,** *6*, 6540.
2. Manzer, L. E., *Appl. Catal., A* **2004,** *272*, 249-256.
3. Yan, Z.-p.; Lin, L.; Liu, S., *Energy Fuels* **2009,** *23*, 3853-3858.
4. Braden, D. J.; Henao, C. A.; Heltzel, J.; Maravelias, C. C.; Dumesic, J. A., *Green Chem.* **2011,** *13*, 1755-1765.
5. Lange, J.-P.; Price, R.; Ayoub, P. M.; Louis, J.; Petrus, L.; Clarke, L.; Gosselink, H., *Angew. Chem. Int. Ed.* **2010,** *49*, 4479-4483.
6. Ftouni, J.; Muñoz-Murillo, A.; Goryachev, A.; Hofmann, J. P.; Hensen, E. J. M.; Lu, L.; Kiely, C. J.; Bruijnincx, P. C. A.; Weckhuysen, B. M., *ACS Catal.* **2016,** *6*, 5462-5472.
7. Lee, J.; Xu, Y.; Huber, G. W., *Appl. Catal., B* **2013,** *140–141*, 98-107.
8. Akpa, B. S.; D'Agostino, C.; Gladden, L. F.; Hindle, K.; Manyar, H.; McGregor, J.; Li, R.; Neurock, M.; Sinha, N.; Stitt, E. H.; Weber, D.; Zeitler, J. A.; Rooney, D. W., *J. Catal.* **2012,** *289*, 30-41.
9. Michel, C.; Zaffran, J.; Ruppert, A. M.; Matras-Michalska, J.; Jedrzejczyk, M.; Grams, J.; Sautet, P., *Chem. Commun.* **2014,** *50*, 12450-12453.
10. Kresse, G.; Furthmüller, J., Efficiency of ab-initio total energy calculations for metals and semiconductors using a plane-wave basis set. In *Computational Materials Science*, 1996; Vol. 6, pp 15-50.
11. Kresse, G.; Hafner, J., *Phys. Rev. B* **1993,** *47*, 558-561.
12. Kresse, G.; Joubert, D., *Phys. Rev. B* **1999,** *59*, 1758-1775.
13. Blöchl, P. E., *Phys. Rev. B* **1994,** *50*, 17953-17979.
14. Methfessel, M.; Paxton, A. T., *Phys. Rev. B* **1989,** *40*, 3616-3621.
15. Perdew, J. P.; Burke, K.; Ernzerhof, M., *Phys. Rev. Lett.* **1996,** *77*, 3865-3868.
16. Grimme, S.; Antony, J.; Ehrlich, S.; Krieg, H., *J. Chem. Phys.* **2010,** *132*, 154104.
17. Tkatchenko, A.; Scheffler, M., *Phys. Rev. Lett.* **2009,** *102*, 073005.
18. Monkhorst, H. J.; Pack, J. D., *Phys. Rev. B* **1976,** *13*, 5188-5192.
19. Henkelman, G.; Uberuaga, B. P.; Jónsson, H., *J. Chem. Phys.* **2000,** *113*, 9901-9904.
20. Henkelman, G.; Jónsson, H., *J. Chem. Phys.* **1999,** *111*, 7010-7022.
21. Heyden, A.; Bell, A. T.; Keil, F. J., *J. Chem. Phys.* **2005,** *123*, 14.
22. Abdelrahman, O. A.; Heyden, A.; Bond, J. Q., *ACS Catal.* **2014,** *4*, 1171-1181.
23. Ahlrichs, R.; Bär, M.; Häser, M.; Horn, H.; Kölmel, C., *Chem. Phys. Lett.* **1989,** *162*, 165-169.
24. Schafer, A.; Klamt, A.; Sattel, D.; Lohrenz, J. C. W.; Eckert, F., *Phys. Chem. Chem. Phys.* **2000,** *2*, 2187-2193.
25. Baroni, S.; de Gironcoli, S.; Dal Corso, A.; Giannozzi, P., *Reviews of Modern Physics* **2001,** *73*, 515-562.
26. Hindmarsh, A. C.; Brown, P. N.; Grant, K. E.; Lee, S. L.; Serban, R.; Shumaker, D. E.; Woodward, C. S., *ACM Trans. Math. Softw.* **2005,** *31*, 363-396.
27. Serrano-Ruiz, J. C.; West, R. M.; Dumesic, J. A., *Annu. Rev. Chem. Biomol. Eng.* **2010,** *1*, 79-100.
28. Grabow, L.; Hvolbæk, B.; Nørskov, J., *Top. Catal.* **2010,** *53*, 298-310.

29. Stegelmann, C.; Andreasen, A.; Campbell, C. T., *J. Am. Chem. Soc.* **2009,** *131*, 8077-8082.

CHAPTER 4 : INVESTIGATION OF THE SOLVENT EFFECTS ON THE HYDRODEOXYGENATION OF LEVULINIC ACID OVER Ru(0001)

Mamun, O.; Saleheen, M.; Bond, J.Q.; Heyden, A.

To be submitted

4.1 Abstract

Reductive deoxygenation (RD) of biomass derived platform chemicals over heterogeneous transition metal catalytic surface in a solvent medium provides an efficient scheme to produce fuel-range hydrocarbons from lignocellulosic biomass. In this chapter, the solvation effects on the reaction kinetics of the hydrodeoxygenation (HDO), a RD process where hydrogen is used as the reducing agent, of Levulinic acid (LA) toward the formation of γ-Valerolactone (GVL) over Ru(0001) has been studied in three different condensed phase medium, e.g., water, methanol, and 1,4-dioxane. A detail microkinetic model has been developed incorporating different catalytic pathways, i.e., with or without the formation of intermediate 4-Hydroxypentanoic acid (HPA) and/or α-Angelicalactone (AGL), to simulate the catalytic activity of Ru(0001) in different reaction conditions, e.g., pressure, temperature etc. Our microkinetic model suggests that direct catalytic conversion pathway with intermediate alkoxy formation is the preferred reaction mechanism in all reaction environments. Furthermore, our study also finds that water facilitates the reaction kinetics by de/stabilizing key thermodynamic and kinetic state which explains why in our previous gas phase study we obtained a very low turn-over frequency in the low temperature region (T<373 K). Overall, the activity of Ru(0001) model surface in the low temperature region is 2-4 order of magnitude higher in liquid water in comparison to the activity in gas phase. Additionally, our model also predicts that activity of Ru(0001) in 1,4-dioxane and methanol are, as expected, similar to that of activity computed in the gas phase simulation. Though, both 1,4-dioxane and methanol facilitate the LA hydrogenation to alkoxy formation step; however, the overall increase of activity in 1,4-dioxane and methanol with respect to gas phase activity is negligible, mainly due to the competitive

adsorption of solvent molecules on the catalytic surface which reduces the number of empty sites available for efficient catalysis.

key words: solvent effects; ruthenium; density functional theory (DFT); hydrodeoxygenation; biomass; microkinetic modeling; levulinic acid; water; 1,4-dioxane; γ-valerolactone

4.2 Introduction

At the onset of global climate change and declining fossil fuel reserves, the search for alternative energy sources poses a major challenge to policy makers, the scientific community and society as a whole. Biofuels, mainly obtained from the hydrolysis of the cellulose and hemi-cellulose fragments of the (ligno-) cellulosic biomass in the presence of acidic medium, have been identified as an attractive alternative with an abundant supply of raw materials. In order to replace fossil fuels, biofuels must be economically competitive, and at the same time, the process must be environmentally benign in accordance to "the Twelve Principles of Green Chemistry"[1-3]; which makes it an arduous undertaking. In particular, during the biomass upgrading process, the main objective is to reduce the functionality of oxygenated feedstocks to resemble the petroleum refinery products to make biomass a suitable candidate for producing petroleum-derived chemicals[3]. In this respect, platform chemicals, characterized by their multi-functionality suited for the conversion to various commercially viable products, provide an excellent starting point for the biomass conversion process[4]. Dehydration is usually carried out to lower the oxygen content of biomass derived platform chemicals[5]; however, hydrogenation followed by subsequent dehydration or vice versa can also be used to lower the oxygen

content without reducing hydrogen content. In catalysis literature, this combinatorial approach to reductive deoxygenation of biomass chemicals is commonly referred to as hydrodeoxygenation (HDO)[6-7].

Levulinic acid, a versatile platform chemical, can be transformed into another platform chemical, γ-Valerolactone (GVL); this transformation facilitates the separation of the desired chemical from the solution it is produced in[8]. GVL, being a non-toxic chemical, have been identified as a very promising green platform chemical with sufficient functionality for upgrading to a variety of end products, i.e., fine chemicals, fuel additives, solvents etc.[9-10]. LA hydrodeoxygenation towards GVL can be obtained by using molecular hydrogen source[11] or by using an external hydrogen source. The later, known as catalytic transfer hydrogen (CTH)[12], with equimolar mixture of LA and formic acid (FA) can be used to produce GVL in high yield by in-situ generation of hydrogen via the decomposition of formic acid[13]. The advantage of such a transfer hydrogenation process is, unlike direct molecular hydrogenation process where noble heterogeneous or homogeneous catalytic materials are used which are neither durable nor economically efficient, it can utilize both the products (e.g., LA and FA) formed during the hydrolysis process of carbohydrates and can be accomplished in an acid catalyzed environment with rare earth materials such as Ru/C catalysts. However, one particular caveat of transfer catalytic hydrogenation of LA with FA is that it does not achieve effective conversion, and furthermore, Ru/C catalyst leads to the undesirable side reaction, such as dehydration of FA, which reduces the hydrogen production rate and consequently, affects the catalytic activity and selectivity[14]. Remarkably, though ruthenium is considered to be a poor hydrogenation catalyst, but for LA hydrogenation to GVL with molecular hydrogen source it is found to have the best

performance in comparison to other monometallic transition metal catalysts, e.g., Pt, Pd, Ir, Ni etc., by several different independent experimental studies[15-16]. In these studies, oxides supports such as zirconia, and titania were also reported to play an important role[17]; however, no study on the support effect of carbon has been published yet, and moreover, carbon is a neutral material that is primarily being used for mechanical support rather than for altering chemical properties of the catalytic materials. Recently, Reports from Dumesic and co-workers indicated that the presence of Re has a beneficial role[16] in the activity of Ru-based catalysts for the HDO of LA. Although only a few experimental studies, over the years, have been published to understand the role of Re on the synergistic catalytic effect on the Ru catalysts, mainly due to the catalytic activity of bi-metallic catalysts being strongly dependent on the preparation method, structural characteristics, and composition.

Solvent is capable of making drastic change in the intrinsic kinetic activity of the heterogeneously catalyzed reaction, 1) by blocking active site[18], i.e., competitive adsorption process, 2) by changing the phase stability of the metal nanoparticle[19], i.e., due to high oxygen chemical potential, metal surface is more likely to form oxide, 3) by perturbing the stability of relevant thermodynamic and kinetic state[20], i.e., it is well known that polar solvent reinforces the adsorption strength of non-polar adsorbates, and 4) by actively participating in the reaction mechanism[21], i.e., water mediated/assisted reaction mechanism. Investigation of the catalytic phenomena at the solid-liquid interfaces are at the heart of modern-day heterogeneous catalysis technology, and it provides a challenge to the various different computational catalysis methods, such as microkinetic modeling, proton shuttling mechanism etc. It is the objective of this study to investigate the HDO mechanism of LA over Ru(0001) model surface in liquid phase environments from the first

principles calculations and mean-field microkinetic modeling that will allow rational correlation of computational predictions with the experimental observations. Specifically, In this investigation, we focused on two different types of solvent depending on their polarity and proton donating ability, i.e., polar/protic solvent (water) and non-polar/aprotic solvent (1, 4-dioxane). For polar adsorbate in contact with polar solvent, the electrostatic interaction is the dominating factor among different interactions contributing to the solvation effect, i.e. cavitation, dispersion, polarization etc. On the other hand, for non-polar adsorbate-solvent system, dispersion (i.e. Van-der Waals force) is likely to be the major contributing factor[22]. Solvent effects in the heterogeneous catalysis study has long been rationalized by correlating product distributions and selectivity in terms of polarity or di-electric constants[20, 23-24]. Our computational strategy for a theoretical study of the solvent effect on the HDO of LA comes with several different challenging task including, 1) identification of an accurate and computationally tractable catalyst model, 2) precise description of free energy of reaction and free energy of activation at solid-liquid interface, 3) managing a comprehensive reaction network that incorporates all the relevant reaction pathways, and 4) determination of activity and selectivity descriptors for the rational design of new catalysts. Incorporating the free-energy of solvation, we compute kinetic parameters for all the elementary reaction processes from first principles quantum chemical calculations. Next, we develop a mean-field microkinetic reactor model to investigate the solvent effect on the reaction kinetics. Furthermore, we identified rate determining step, reaction orders, and activation energy. Finally, we compare our computed data with experimental observations by several different experimental research groups for a rational theoretical understanding of the effect of different solvent medium. We organize this

chapter as follows. In section 4.3, we begin with a brief discussion of the theoretical method we employ in this investigation. Next, in section 4.4, we present a discussion of the effects of solvation on various competitive pathways for LA conversion to GVL. In section 4.5, we will discuss our simulation results obtained from microkinetic modeling. Finally, we conclude with a discussion of different hypotheses to explain our results and future research direction.

4.3 Computational strategy

4.3.1 Solvation model

In this scientific study, we use iSMS method (Implicit Solvation Scheme for Metal Surface), developed and validated by Faheem et al.[25], to compute the free energy of reaction and free energy of activation for various elementary reactions in the condense phase. iSMS method is already proven to be very powerful for studying solvation phenomena for the conversion of ligno-cellulosic biomass derived chemicals on heterogeneous metal catalytic surface, for example our group successfully applied iSMS to study the effect of solvation on the reaction kinetics of the HDO of methyl propionate over Pd(111) surface and the HDO of propanoic acid over both Pd(111) and Pd(211) metal surfaces.[26-28] In the implicit solvation scheme, we include long-range metallic interactions by periodic slab calculations using projector augmented wave (PAW) method[29-30] while the short-range interactions between solute-solvent and metal-solvent are included via cluster model embedded in polarizable continuum solvent. Similar to the widely celebrated ONIOM[31] model by Morokuma and co-workers, we can write a subtraction scheme to compute the free energy of adsorbed complex (surface + adsorbate) in a liquid environment

$$G^{liquid}_{surface+intermediate} = G^{vacuum}_{surface+intermediate} + (G^{liquid}_{cluster+intermediate} - E^{vacuum}_{cluster+intermediate}) \quad (4.1)$$

Here, $G^{vacuum}_{surface+intermediate}$ is the free energy of adsorbed species in the absence of fluid phase environment which is calculated using plane-wave DFT calculations on the periodic slab model. In addition to the gas phase SCF contribution, we also included vibrational contribution to the free energy of gas phase adsorbed species using dynamical matrix calculation[32]. $G^{liquid}_{cluster+intermediate}$ is the free energy of adsorbed moiety on a non-periodic cluster model surrounded in a continuum solvent environment and $E^{vacuum}_{cluster+intermediate}$ is the energy of the cluster-adsorbed species complex in the absence of solvent medium.

4.3.2 Computational methods

For periodic slab calculations, we use Vienna ab initio simulation package (VASP). In the interest of brevity, we refer interested readers to the method section of our gas phase manuscript[33] for a detail description of the computational methods employed to perform plane-wave calculations. Cluster model DFT calculations are performed using electronic structure program TURBOMOLE version 7.1.[34] First, we build a hexagonal cluster model with 2 layer Ru(0001) which is expanded and extracted from the optimized periodic slab, comprising of a total of 46 metal atoms. To ensure the convergence of iSMS results with respect to the system size, i.e., cluster depth, lateral size, we performed convergence test on a model reaction. All adsorbates are then described by all-electron basis sets of triple-ζ quality (TZVP)[35-37]. Ru atoms, being a transition metal with electron configuration

[Kr]$4d^7 5s^1$, are represented by a relativistic small core effective potential (ECPs) together with basis sets of the same triple-ζ quality. Specifically, we treat 28 electrons, out of total 44 electrons, of Ru atoms within effective core potential, and the rest are treated with full TZVP basis sets. To make calculation faster and more efficient, the coulomb potential is approximated with the RI-J approximation using auxiliary basis sets[38-39]. Then, we run single point energy calculation with different spin configurations to identify the lowest energy spin state where the electron-ion interactions are described using BP-86[40] functional as required by the COSMO-RS parameterization[41-42], the convergence criterion used for self-consistent cycle is 1.00×10^{-7} Ha with a spherical grid m4, which is the recommended grid settings for numerical optimization for clusters with more than 50 atoms[39]. Next, we perform a COSMO calculation on the lowest energy spin state with an infinite di-electric constant, as a result, it will provide a flexible input for COSMO-RS calculations. For cavity construction, we use optimized radii for carbon, oxygen, and hydrogen, and default cavity radii (2.223 Å) for Ru atoms. For COSMO-RS calculations, we use the BP_TZVP_C30_1701.ctd parameterization which is the latest parameterization available to date. In this regard, we also note that this new parameterization gives better solvation energies than the previous parameterizations, i.e., BP_TZVP_C21_0110.ctd, because of having better and improved parameterization with extensive experimental data.

4.3.3 Choice of solvents

Aside from the motivation that water and 1,4-dioxane are the most commonly used solvent for HDO of LA[11, 43-44], we choose three different solvent medium, methanol and the two aforementioned solvents (water & 1,4-dioxane), based on their polarity and ability to donate or accept proton to see the relative reaction kinetic behavior in different solvents

having well-defined different physical properties. To quantify the extent of polarity of a fluid phase, we use Taft and Kamlet parameters, i.e., π^*, α, and β for polarizability, acidity, and basicity, respectively[45-46]. In table 4.1, we report the dipolarity/polarizability (π^*), hydrogen bond donor parameter (α), hydrogen bond acceptor parameter (β), normalized empirical solvent polarity parameter E_T^N , and di-electric constant (ε_r) for all the three solvent medium we use in our study. From the table, we can see that water is the most protic solvent with exceptional ability to donate proton. In contrast, 1,4-dioxane is the least protic solvent, more commonly referred to as aprotic solvent, with no hydrogen donation ability. To make a correlation between normalized polarity parameter and reaction activity, we choose to use methanol which has intermediate properties thus allowing us to see the effect of solvation on the reaction kinetics as a function of physical property of the solvent medium.

4.3.4 Mean-field microkinetic modeling

For calculation of rate constant of any surface reaction process, we use Eyring equation[47] within harmonic transition state theory approximation.

$$k_{forward} = \kappa \frac{k_B T}{h} e^{-\frac{\Delta G^{\ddagger}}{k_B T}} \tag{4.2}$$

Here, k_B is the Boltzmann constant, T denotes the reaction temperature, h is the Planck constant, $\Delta G^{\ddagger}$ is the free energy of activation, and κ is the Eckart tunneling correction factor which is defined as the ratio of the quantum mechanical to the classical barrier crossing rate (for a detail description of the method employed to compute tunneling correction factor, we refer the reader to the scientific article by Harold et al.[48] and section C.1). In the supporting information section, we tabulate all the computed Eckart tunneling

correction factor for all the reaction processes at various different temperatures. Free energy of activation and free energy of reaction are calculated as,

$$\Delta G^{\ddagger}_{solvent} = \Delta G^{\ddagger}_{gas} + G_{TS}(solv) - G_{IS}(solv) \tag{4.3}$$

$$\Delta G_{solvent} = \Delta G_{gas} + G_{FS}(solv) - G_{IS}(solv) \tag{4.4}$$

Where $G_{IS}(solv)$,$G_{TS}(solv)$, and $G_{FS}(solv)$ are the free energy of solvation of the initial, transition, and final states, respectively.

Adsorption is assumed to be a non-activated process, which is to say there is no discernible transition state in the adsorption process of the gas phase molecules; collision theory is used to calculate the rate constant of the adsorption process. Next, we use the equilibrium constant, in addition to forward rate constant, to compute the backward rate constant of an adsorption process.

$$k_{forward} = \frac{\sigma}{N_0\sqrt{2\pi m k_B T}} \tag{4.5}$$

$$K_{equilibrium} = e^{-\frac{\Delta G}{k_B T}};\ \ k_{reverse} = \frac{k_{forward}}{K_{equilibrium}} \tag{4.6}$$

Here, in eq. 4.5, σ is sticking coefficient, assumed to be 1, N_0 is the number of sites per area, and m denotes the molecular weight of adsorbate. With all the calculated parameters, a mean-field microkinetic reactor model is developed as a system of differential algebraic equations (DAE) where the total number of sites are conserved and normalized to 1.

$$\frac{\partial \theta_i}{\partial t} = \sum_l \vartheta_{i,l} r_l \tag{4.7}$$

In eq. 4.7, θ_i, $\vartheta_{i,l}$, and r_l refers to the site coverage of adsorbed species i, stoichiometric coefficient of adsorbed species in the elementary reaction rate equation l,

and elementary reaction rate, respectively. The overall site balance equation was used for empty sites coverage calculation,

$$\sum_i n_i \theta_i = 1 \tag{4.8}$$

Here, n_i is the number of sites occupied by each adsorbed species. Finally, the system of DAE is solved until the steady-state is reached to compute fractional coverage of different surface intermediates and reaction rates of all the elementary reactions at different reaction conditions, i.e. temperatures, and pressures etc.

4.3.5 Adsorbate-adsorbate interactions

Though mean-field microkinetic model is derived based on the assumption of the absence of local chemical environment dependence of the adsorption energy; however, it is well known that without inclusion of lateral interaction, the results obtained from mean-field microkinetic analysis is questionable[49]. Specifically, in our microkinetic model, we included hydrogen and oxygen lateral interaction to rationalize our simulation results to that of experimental results. We use Grabow's[50] two parameter lateral interaction model to find the coverage dependent adsorption energy of hydrogen and oxygen with the following functional form,

$$\mathrm{E_H}^{differential}(\theta_\mathrm{H}, \theta_\mathrm{O}) = \begin{cases} -0.68 + 0.15(\theta_\mathrm{H} - 0.12) + 0.31 \times \theta_\mathrm{O} \; + \\ 3.99 \times \theta_\mathrm{O} \sqrt{\theta_\mathrm{H} \; \theta_\mathrm{O}} \quad if\ (\theta_\mathrm{H} - 0.12) > 0 \\ -0.68 + 0.31 \times \theta_\mathrm{O} \; + \\ 3.99 \times \theta_\mathrm{O} \sqrt{\theta_\mathrm{H} \; \theta_\mathrm{O}} \quad if\ (\theta_\mathrm{H} - 0.12) \leq 0 \end{cases} \tag{4.9}$$

$$E_O{}^{differential}(\theta_O, \theta_H) = \begin{cases} -2.994 + 2.014(\theta_O - 0.07) + 0.31 \times \theta_H \quad + \\ 3.99 \times \ \theta_H \ \sqrt{\theta_O \ \ \theta_H} \quad if\ (\theta_O - 0.07) > 0 \\ \qquad -2.994 + 0.31 \times \theta_H \quad + \\ 3.99 \times \ \theta_H \ \sqrt{\theta_O \ \ \theta_H} \quad if\ (\theta_O - 0.07) \leq 0 \end{cases} \tag{4.10}$$

Where, θ_H and θ_O are the hydrogen and oxygen coverage, respectively.

4.3.6 BEP relation for predicting activation energy of c-o ring opening reaction

One frequently encountered bottleneck of computational investigation of heterogeneously catalyzed chemical reaction over a transition metal catalyst is the identification of transition state geometries. Success of a mean-field modeling depends largely on the accurate prediction of the transition state energies. A typical computational search of transition state geometries takes 48 hours to as long as 168 hours on a 48 cores computer. Furthermore, without good initial guess, it is almost impossible to identify a transition state geometry if it involves slightly complicated reaction coordinate, such as C-O ring opening reaction. In our reaction network, we could not identify 6 transition state geometries with convincing numerical accuracy. To identify these missing TSs, we develop a BEP like relation for C-O ring opening reaction with the available computational data for other C-O ring opening reaction (total 12 data points are used to fit the BEP relation). Though, there is some scatter in the data, our rate control analysis suggests that our model results are not sensitive to the uncertainty in these missing transition states energies.

$$E_A = 0.08 \times \Delta E + 0.56 \tag{4.11}$$

In this equation, E_A, activation energy, is expressed as a function of ΔE, reaction energy.

4.4 Results and discussions

4.4.1 Solvent effects on the adsorption strength of reaction intermediates

In figure 4.1, different overall reaction pathways, with or without intermediate HPA and AGL formation, are shown. In total, we investigated 50 surface intermediates in our reaction network that includes LA, HPA, AGL, GVL, and their derivatives. In figure 4.2 and 4.3, we show various pathways for the production of GVL via intermediate formation of HPA and AGL from the HDO of LA and the molecular structure of various intermediates. Also in table 4.2, we list all the reaction intermediates with their chemical formula and relative adsorption strength at 323 K and 423 K in different reaction medium. In the presence of solvents, the adsorption strength of different intermediates change due to solvent-solute interactions and solvent-metal interactions. Solvent-intermediate interactions can directly alter the adsorption strength by forming chemical bonds between solvent molecule and adsorbed species. On the other hand, solvent-metal interactions indirectly modify the adsorption strength by changing the electronic structure of the metal atoms. To investigate the change in the adsorption strength ($\Delta(G_{ads,A})$) of adsorbed species in the presence of solvent medium, we compute the difference in adsorption free energy in the absence and presence of the solvent

$$A(g) + *(g) \leftrightarrow A*(g) \tag{4.12}$$

$$A(g) + *(l) \leftrightarrow A*(l) \tag{4.13}$$

$$\Delta(G_{ads,A}) = G_{ads,A}(l) - G_{ads,A}(g) \tag{4.14}$$

$$= [G^{A*}(l) - G^{A*}(g)] - [G^{*}(l) - G^{*}(g)] = \Delta(\Delta G)$$

Where, $G_{ads,A}(l)$ and $G_{ads,A}(g)$ are the free energy of adsorption of a gas molecule of intermediate A in the presence and absence of the solvent medium. This method allows us to compare the relative adsorption strength in the solvent environment with respect to the gas phase adsorption strength. Below, we discuss the effect of solvation on the adsorption strength on key surface intermediates.

For reaction intermediates, such as LA, alkoxy (Al), hydroxy (Hy), 4-hydroxypentanoic acid (HPA), we observe that their adsorption strength is weaker in the presence of solvent medium by 0.05-0.17 eV. Specifically, the solvent effect is, as expected, more prominent in water than in the other two solvents, for example $\Delta(\Delta G)$ of LA, Al, Hy, and HPA in water are 0.12, 0.11, 0.06, and 0.16 eV, respectively. This large solvation effect can be attributed to the fact that all of these species have an acid group as well as an alcohol group/ketone group, all of which make the solvent-solute interactions more favorable in polar solvent thus reduce the adsorption strength. Dehydrogenated derivatives of LA ($CH_3 - CO - CH_x - CH_y - COOH_z, x = [1,2], y = [1,2], z = [0,1]$) and HPA ($CH_3 - CH_w(OH) - CH_x - CH_y - COOH_z, w = [0,1], x = [1,2],\ y = [1,2], z = [0,1]$), obtained by a primary C-H bond scission, are also destabilized in the presence of solvent medium, except I-31 which is slightly stabilized in the solvent. Similarly, most of the LA and GVL derivatives, obtained via (de/) hydroxylation and/or dehydration are also destabilized in solvent medium for the same aforementioned reason. Water also weakens the adsorption strength of small molecules, such as H, OH, O, and H_2O, mainly due to the formation of hydrogen bonding. In our calculations with previous COSMO-RS parameterization, we saw a very small solvation effects on the small atoms. One of the limitation of our implicit solvation scheme was that the hydrogen bonding

description was inexact because of the absence of tangible water degrees of freedom during our electronic minimization process. To capture the approximate effect of hydrogen bonding, a parameterized hydrogen bonding term is used in our solvation scheme; however, due to not having enough experimental data, COSMO-RS previous parameterization was not fully successful in capturing the hydrogen bonding effect. Fortunately, in the new parameterization, due to the inclusion of the hydrogen-bonding corrected misfit term, we find very good agreement between our computed microkinetic model results and experimental observations. One approximate way to quantify the contribution of hydrogen bonding toward the overall solvation energy is the difference in solvation energy in water and 1,4-dioxane, with the assumption that 1,4-dioxane is unable to form any hydrogen bond. Based on this approximation, we can see that hydrogen bonding is relatively more significant in small molecules than in large hydrocarbons.

In section C.2, we also report the enthalpic and the entropic contribution to the $\Delta\Delta G$ of the adsorbed species; we use the Van't Hoff equation to separate the temperature dependent term from the temperature independent term using linear regression formula. It gives us valuable insight into the sensitivity of the adsorption strength on the temperature of the reaction system. As we can see in the table C.2, we found that adsorption strength of some adsorbed species are more sensitive to the temperature than that of some other species, i.e., for some species the entropic term dominates over the enthalpic term.

4.4.2 Solvent effects on the free energy of reaction and free energy of activation

Herein, we explain the effects of solvents on the free energy of reaction and the free energy of activation of various elementary processes. Due to having unbalanced solvation effects on the reactants, transition states, and products, free energy of reaction and free

energy of activation are affected both positively and negatively, depending on the reaction states involved. Since reaction rates and coverages largely depend on the free energy of reaction and free energy of activation, solvent has the capacity to facilitate/inhibit various competitive reaction routes. In table 4.3, we summarize the free energy of reaction and free energy of activation for all the elementary reaction processes at 423 K in different condensed phase medium.

We start our discussion to solvent effect on the free energy of, reaction and activation by investigating the adsorption of levulinic acid and hydrogen on Ru(0001) in fluid phase medium. In our gas phase calculation, we predicted a free energy of adsorption -0.42 eV/molecule and -0.41 eV/molecule at 423 K for LA and hydrogen, respectively. Our liquid phase calculations suggest that both the adsorption process is destabilized in the presence of solvent due to the solute-solvent interaction which weakens the solute-metal interaction. Specifically, we find for LA a $\Delta G_{liq} - \Delta G_{gas}$ of 0.12 eV, 0.06 eV, and 0.05 eV in water, 1,4-dioxane, and methanol, respectively. Water, being highly polar, influences the adsorption energy the most because of the high degree of interaction between solute and solvent in comparison to the other two solvents. Similarly, we see that hydrogen adsorption energy is also weakened in the presence of the solvent in a same manner as LA. Next, LA is hydrogenated at the ketone group to form alkoxy intermediate, via C-H bond formation process, or hydroxy intermediate, via O-H bond formation process. In our previous study, we found that alkoxy formation is both thermodynamically and kinetically favored over hydroxy formation. In our liquid phase study, alkoxy formation step remains the facile reaction step in comparison to the hydroxy formation step in all the three solvent medium. Interestingly, activation barrier for alkoxy formation step, which was found to be

the rate limiting step according to our kinetic control analysis in gas phase simulation, is reduced significantly in water ($\Delta G^{\ddagger}_{liq} - \Delta G^{\ddagger}_{gas} = 0.17\ eV$) than in 1,4-dioxane (0.04 eV) and methanol (0.07 eV). From this analysis, we can already see that water has a significant beneficial effect on this reaction step which could possibly lead us to reconcile the dispute between low temperature kinetic performance observed in simulation and in experiment. Dehydrogenation of LA at β-carbon produces I-1 ($CH_3 - CO - \dot{C}H - CH_2 - COOH$) intermediate which is accompanied by a free energy of reaction and free energy of activation -0.23 eV and 0.26 eV, respectively, in water. Dehydroxylation of the –COOH group of LA, on the other hand, leads to the formation of I-7 with a $\Delta G_{liq} - \Delta G_{gas} = 0.33, 0.26, and\ 0.26\ eV$ in liquid water, 1,4-dioxane, and methanol, respectively, while $\Delta G^{\ddagger}_{liq} - \Delta G^{\ddagger}_{gas} = 0.09, 0.05, and\ 0.06\ eV$, respectively. Finally, LA forms levulinate, I-37, ($CH_3 - CO - CH_2 - CH_2 - CO\dot{O}$) via reaction step r_{91} which is highly exergonic with practically no reaction barrier. Among the five possible LA intermediates, the most plausible steps are, on the basis of thermodynamic and kinetic data, alkoxy and I-1 formation process.

There are three possible I-1 derivatives which occur via 1) dehydrogenation (r_9) of the –COOH group to form I-2 ($CH_3 - CO - \dot{C}H - CH_2 - CO\dot{O}$), 2) dehydroxylation ($r_{12}$) of the carboxylic group to form I-6 ($CH_3 - CO - \dot{C}H - CH_2 - \dot{C}O$), and 3) ring closing reaction (r_{13}) to produce close ring intermediate I-5 ($CH_3 - C_4OH_3(OH) = O$). After initial C-H bond scission, the free energy barrier for

another hydrogen abstraction from COOH group (r_9) is 0.30-0.31 eV in different solvent. In contrast, other two reaction pathways are kinetically improbable with a free energy barrier of 0.80-0.81 eV and 0.90 eV for r_{12} and r_{13}, respectively, which indicates that I-1 would follow the reaction pathway that leads to the formation of levulinate derivative I-2 rather than producing ring structure I-5 or dehydroxylated product I-6. Then, I-2 undergoes a C-O bond formation process to form I-3 ($C_4OH_3(CH_3)(O)(O)$) via reaction process r_{10} which is neither thermodynamically nor kinetically facile. This step is accompanied by a free energy of reaction 0.79 eV, 0.77 eV, and 0.77 eV in liquid water, 1,4-dioxane, ands methanol, respectively, while the free energy of activation for this step is 2.03 eV, 1.98 eV, and 1.99 eV, respectively. From our analysis of the potential free energy description of the whole network (table 4.3), we see that for some otherwise facile reaction route ring closing reaction is the fundamental obstruction for the production of GVL.

On the other hand, further hydrogenation of ketone group of alkoxy leads to the formation of HPA via reaction step $r_5$which has a high free energy barrier 1.24 eV, 1.27 eV, and 1.28 eV in liquid water, 1,4-dioxane, and methanol, respectively. Because of the high energy barrier for the production of HPA from alkoxy in the gas phase, we could not see appreciable production of HPA in our gas phase simulation as observed experimentally by Abdelrahman et al.[11] Now with similar high free energy of activation in liquid phase medium, it is our hypothesis that direct proton donation from the aqueous solution is necessary to produce HPA from the alkoxy intermediate. In future, we plan to publish an independent scientific study to elucidate the role of acid medium on the reaction kinetics for the production of HPA. Similarly, the other reaction intermediate I-35, produced from

hydrogenation of alkoxy, is also associated with a high energy cost with a free energy of activation of 1.45 eV, 1.50 eV, and 1.50 eV in liquid water, 1,4-dioxane, and methanol, respectively, which also makes this process to be kinetically unfavorable. However, ring closing reaction r_{86} to produce I-40 from alkoxy is both thermodynamically and kinetically very facile with a free energy of activation of 0.51 eV, 0.46 eV, and 0.48 eV in water, 1,4-dioxane, and methanol, respectively. Finally, a C-OH bond scission from the α-carbon leads to the formation of the final desired product GVL which is also not an energy intensive process. The free energy barrier associated with this step is calculated to be 0.18 eV, 0.11 eV, and 0.15 eV in water, 1,4-dioxane, and methanol, respectively. Lastly, GVL desorbs from the surface which is an exergonic process in all the reaction solvent medium. On the other hand, H and OH combine together to form water with a free energy of activation of 0.83 eV, 0.93 eV, and 0.92 eV, respectively, in the three aforementioned solvent medium.

Our purely computational analysis thus identifies the key reaction steps for the HDO of LA. However, this analysis, so far, couldn't predict the relative reaction flux of individual route in real heterogeneous catalytic environments. To estimate the reaction flux of each reaction step, we carry out a mean-field microkinetic simulation of the whole reaction mechanism including all the elementary reactions.

4.4.3 Results from microkinetic modeling

In the previous chapters (chapter 2 & 3), we investigated the gas phase kinetics of the HDO of LA over Ru(0001)[33], where we found that, 1) in a vapor phase condition or in a non-polar solvent, Ru(0001) is the experimentally measured active site in the high temperature (T>373K) reaction condition, 2) The dominant reaction path constitutes of

three different reactions; i.e. LA hydrogenation to alkoxy, alkoxy ring closing reaction, and finally, a C-OH bond scission reaction to produce GVL, 3) At low temperature (T<373 K), Ru(0001) is not the experimentally observed active sites in vapor phase condition or a non-polar solvent medium, and 4) AGL derivatives are likely to be responsible for the reversible catalyst deactivation at high temperature region (T > 473 K). In this study, we carefully develop a microkinetic model to account for the effect of solvation, including the change in free energy of reaction and free energy of activation in solvent, with forward and reverse kinetic rate parameters shown in the appendix (section A.3). In table 4.4, we tabulate the vapor pressures, calculated using COSMOTHERM program package, of different solvents at different temperatures which we use as the chemical potential/partial pressure of the corresponding solvent. As for the reactants, e.g. LA and hydrogen, we use concentration typically used in the experimental studies[11, 15-17, 43-44, 51-52]. For LA, we use a partial pressure corresponding to a 0.45 M LA solution, and for hydrogen, we use a 10 bar partial pressure at all reaction temperatures. For products partial pressures, other than the solvent itself, we assume a 0.11% conversion of LA to compute the partial pressure of the products in the effluent stream which is also typical of different experimental studies.

Similar to our previous study, we use two different physical model based on different interpretation for hydrogen adsorption process, i.e., 1-site and 2-site model. In a 1-site model, we describe the adsorption and surface reaction process using competitive Langmuir-Hinshelwood mechanism, which is to say, all adsorbed intermediate species are competing each other to occupy surface sites. However, in a 2-site model, hydrogen adsorbs on a completely different lattice sites and does not compete with other adsorbed species for a free sites. A summary of our microkinetic simulation results for both 1-site

and 2-site model at different reaction environments are presented in table 5. In the next three subsections, we will discuss, in detail, microkinetic model results for three different solvents, i.e., water, 1,4-dioxane, and methanol in lieu with the available experimental results. Later, based on the comparison of simulation results with experimentally found effects in different solvent medium from different experimental group, we will attempt to rationalize our findings to help guide synthesis of catalysts with higher activity and selectivity. For simplicity, all simulation results obtained from 1-site model (competitive adsorption kinetics model) are reported in the next three subsections with 2-site model (non-competitive hydrogen adsorption kinetics) results reported within square ([]) brackets. Note that, for all simulations, we employ same coverage dependent adsorption energies for hydrogen and oxygen.

4.4.3.1 Liquid water effects

In the presence of liquid water as solvent, at 323 K and 0.124 bar water partial pressure, we find that the most abundant surface species is hydrogen with a coverage of 99.2 % [~100%]. Other than hydrogen, we have trace amount of I-46, 0.8%, which grows to 99.9 % in 2-site model simulation owing to the fact that it is not competing with hydrogen for a free site. In both 1-site and 2-site model, empty sites coverage is on the order of -2, which is around 2 [1] order of magnitude higher than the gas phase simulation results. The overall TOF measured in this condition is $1.00 \times 10^{-5}\ s^{-1}$ [$2.43 \times 10^{-4}\ s^{-1}$] which is about four [two] order of magnitude higher than the TOF predicted in our gas phase simulation at the same reaction condition. In our previous gas phase study[33], we concluded that at low reaction temperature Ru(0001) is not the experimentally observed active site in a non-polar aprotic environments. In that study, despite the development of a

detail comprehensive reaction model from first principles calculations with reasonable assumptions, we were unable to explain the origin of the exceptionally high activity of Ru nanoparticles (NP) at low reaction temperature found in experimental investigations, mainly due to our inability to include solvation effects in the description of the free energy profile of different reaction pathways. Now, with the inclusion of solvent effects, we see a much higher turnover frequency at low temperature (T=323 K) which perfectly reconciles our simulation results with the experimental observations. For instance, Abdelrahman et al.[11] reported a TOF of $2.00 \times 10^{-3}\ s^{-1}$at 323 K temperature in an aqueous medium over a monometallic Ru/C catalysts with a single metal loading (5wt%) using a 35 bar hydrogen partial pressure and 0.5 M liquid LA conc. Upon comparison of our results at 323 K with experimental observation, we are underestimating TOF by two [one] order of magnitude in our computational simulation. The reason for this apparent dissimilarity between theoretical and experimental predictions lies in the fact that, 1) uncertainty in DFT prediction, which is often assumed to be 0.1-0.2 eV[53], can alter the reaction kinetics by 1-2 order of magnitude that might be the source of principal error in our microkinetic analysis, and 2) experimentally, TOF is calculated by normalizing the reaction rate with the number of sites computed by chemisorption method which is not free of measurement uncertainty/error. Considering all the relevant source of uncertainty, we can conclude that in the presence of aqueous medium, Ru(0001) is the active site for the HDO of LA at a low temperature condition. In a slightly elevated temperature (373 K), our model predicts a turnover frequency $6.43 \times 10^{-3}\ s^{-1}$ $[1.43 \times 10^{-2}\ s^{-1}]$ with a hydrogen coverage 83.2 % [99.9%] while the $TOF_{gas} = 1.62 \times 10^{-5}\ s^{-1}$ $[4.38 \times 10^{-4}\ s^{-1}]$ with $\theta_{H,gas} =$ 99.10% [~100%].

At 423 K and 4.76 bar water partial pressure, the overall TOF increased by a factor 2 [1] from $TOF_{gas} = 3.44 \times 10^{-3}\ s^{-1}$ [$1.30 \times 10^{-2}\ s^{-1}$] to $TOF_{water} = 2.39 \times 10^{-1}\ s^{-1}$ [$3.09 \times 10^{-1}\ s^{-1}$]. Interestingly, computed TOF in aqueous phase at moderate temperature ranges within a factor of 1-2 with respect to the experimentally observed TOF. At 423 K, Abdelrahman et al. found a TOF $4.80 \times 10^{-1}\ s^{-1}$ in the same aforementioned reaction condition[11]. In a different study, a TOF $2.42 \times 10^{-1}\ s^{-1}$ is measured over a 3 wt% Ru/C catalyst at the same reaction temperature (423 K) with a hydrogen partial pressure 4.5 MPa (~45 bar)[54]. Due to slightly different reaction condition, TOF measured in different experimental study differs by a factor of 1-2. At 423 K, we found that our model can reliably predict TOF which is within numerical accuracy of DFT simulation, considering the uncertainties involved in various stages of our computation. Hydrogen coverage predicted in our simulation is 62.3% [99.4%] which is likely to be the origin of the dramatic increase in the activity of Ru(0001) phase with increasing temperature. Thanks to the higher entropic contribution at higher temperature, which makes hydrogen adsorption a less favorable process thus creates free sites for more facile catalysis.

4.4.3.2 Liquid 1,4-dioxane effects

Simulation in liquid 1,4-dioxane is performed under reaction conditions similar to the gas-phase simulations, i.e., without high water partial pressure. Additionally, to investigate the effect of site blocking by the solvent species, we allowed the adsorption/desorption of 1,4-dioxane, which is present in the simulation as an inert moiety and does not take part in any of the reaction processes. As expected, our simulation results show a slight quantitative improvement in the reaction activity in liquid 1,4-dioxane

solvent with reference to the gas phase simulations. In our previous analysis, we have shown that 1,4-dioxnae facilitates the key reaction steps, such as levulinic acid hydrogenation to alkoxy formation; however, this improvement is masked by the solvent coverage on the catalyst surface. Our simulation results are in good agreement, similar to simulation results in liquid water solution, with experimentally observed kinetics in liquid dioxane solution. At 473 K, we register a TOF of $3.23 \times 10^{-1}\ s^{-1}$ [$5.01 \times 10^{-1}\ s^{-1}$] while Luo et al. observed a TOF $5.36 \times 10^{-1}\ s^{-1}$ in their experimental study over a 1% Ru/TiO_2 catalyst at the same reaction temperature and 40 bar hydrogen partial pressure. At a slightly elevated temperature (493 K/220 ℃) and 1,4-dioxane medium, Shuo et al. measured a TOF $4.72 \times 10^{-1}\ s^{-1}$ over a catalysts prepared with a 4.4 wt% metal (Ru) loading on carbon support[43] which confirms the same temperature trend that we observe in our simulation.

4.4.3.2 Liquid methanol effects

Simulation in liquid methanol is also carried out in four different temperatures in the presence of methanol in the microkinetic model as an inert substance that can only adsorb and desorb from the surface. Reaction activity at low temperature is very low while at high temperature, we see an appreciable reaction activity. In our simulation, we compute a TOF $2.03 \times 10^{-2}\ s^{-1}$ [$9.14 \times 10^{-2}\ s^{-1}$] @ a reaction temperature 423 K. Palkovits and co-workers found in their experimental study a TOF $3.30 \times 10^{-2}\ s^{-1}$ and $2.70 \times 10^{-2}\ s^{-1}$ over 5 wt% Ru/C and 5 wt% Ru/TiO_2 catalysts, respectively, in alcohol solvent with a hydrogen supply at 12 bar and 403 K temperature[55].

As we already predicted from the solvation free energies, in the aprotic solvent, i.e., 1,4-dioxane, the TOFs are significantly sluggish than the TOFs in protic solvent, i.e., water, specifically at low temperature region (T<423 K). We observe that the activity of the metallic Ru(0001) phase follows a positive trend with the increasing polarity of the condense phase. For example, at 373 K, the overall TOF @ 1,4-dioxane is almost same as that in the gas phase, increases in methanol by a factor 1.5 [1.82] with respect to gas phase TOF, and finally, reaches a maximum in water, which is 13.83 [5.93] times higher than the gas phase TOF.

4.4.4 Apparent activation barrier, reaction orders, and sensitivity analysis

The apparent activation barrier (E_a), reaction orders (n_{LA} & n_{H_2}), and sensitivity analysis of the vapor phase kinetics of the HDO of LA on Ru(0001) have been discussed in our previous work[33]. In the gas phase simulation, we predicted an apparent activation barrier 1.5 eV [1 eV] in the temperature range of 323 K – 473 K. Experimentally estimated apparent activation barrier is reported to be in the range of 0.7-0.9 eV. In nonpolar, aprotic solvent, i.e., 1,4-dioxane, we predict an $E_a = 1.2\ eV$ [$0.84\ eV$], which indicates that the reaction activity in 1,4-dioxane is, at least, marginally more facile at high temperature than its gas phase counterpart. For methanol, we also predict an apparent activation barrier that is similar to that of 1,4-dioxane. However, in polar, protic solvent, i.e., water, we predict a lower apparent activation barrier (1 eV [0.82 eV]) in the same aforementioned temperature range (see fig. 4.4) which perfectly reconciles with the experimentally observed apparent activation energy of 0.7-0.9 eV. Next, we compare computed reaction order at liquid phase simulation to that of gas phase calculated orders. The reaction order, in gas phase, is calculated to be -0.34 [0.34] and 0.66 [0.34] with respect to hydrogen and LA, respectively,

for a partial pressure/concentration perturbation of ±5%. In 1,4-dioxane, we calculate LA and hydrogen order to be 0.64 [0.33] and 0.00 [0.33], respectively. In methanol, computed reaction order follow the same trend as 1,4-dioxane, 0.54 [0.33] and 0.00 [0.33] for LA and hydrogen, respectively. In water, LA and hydrogen orders are 0.48 [0.33] and 0.02 [0.33], respectively. Though our model is highly successful for the prediction of reaction activity and apparent activation barrier, however, due to the weak description of the lateral interactions, unfortunately, simulation predicted orders are far off in comparison to the experimentally found orders which are computed to be -0.04±0.04 and 0.6±0.2 for LA and hydrogen, respectively, in liquid water[11]. However, 2-site model predicted orders are in better agreement with the experimentally observed orders which also confirms the newly found observation that ketone hydrogenation on Ru(0001) can be better explained with a 2-site model description[56]. Finally, we perform a sensitivity analysis of the key transition states on the reaction activity. As predicted in our gas phase simulation, in all our liquid phase calculations in different solvent mediums, we predicted the LA hydrogenation to alkoxy step to be the rate controlling step. Degree of rate control (DRC) of C-H bond formation process of LA, to produce alkoxy, is found to be 0.55 [0.68], 0.53 [0.71], and 0.61 [0.75] in water, methanol, and 1,4-dioxane, respectively. Due to the very few empty sites available for efficient catalysis, our model predicts a significant DRC for the LA adsorption process. As expected, we found hydrogen adsorption energy to be the thermodynamic bottleneck in our simulation for all conditions.

4.5 Conclusions

Using rationally integrated plane-wave periodic DFT calculations, COSMO-RS implicit solvation calculations, and mean-field microkinetic modeling, we investigate the

solvation effects on the hydrodeoxygenation of levulinic acid over Ru(0001) surface. To account the specific role of each solvent, i.e., site blocking, chemical potential of solvent, we develop specifically tailored microkinetic model for each solvent at four different temperatures, e.g. 323 K, 373 K, 423 K, and 473 K, with a LA concentration of 0.45 M and a hydrogen partial pressure of 10 bar. Under all conditions, the direct catalytic conversion pathway is the dominant reaction mechanism with the most favored pathway following C-H bond formation prior to a ring closing, i.e., C-O bond formation, and C-OH bond scission reaction. The dominant reaction path can be described as,

1. LA hydrogenation at γ-carbon to form alkoxy intermediate via C-H bond formation process which is accompanied by a free energy of activation of 0.53, 0.66, and 0.63 eV in water, 1,4-dioxane, and methanol solvent, respectively.
2. Formation of I-40, a cyclic structure, from alkoxy intermediate via a C-O bond formation reaction. This step possesses a moderate activation barrier, ranging from 0.46-0.51 eV, in the three aforementioned solvent medium.
3. Finally, a C-OH bond scission at α-carbon leads to the final product GVL. This step is very facile in all reaction conditions with a very small free energy of activation that ranges from 0.11-0.15 eV in different solvent medium at a temperature of 423 K.

In nonpolar solvents such as 1,4-dioxane, we observe no significant solvent effects on the free energy profile and overall turnover frequency. In a slightly polar solvent, i.e., methanol, we observe a slight improvement in the free energy description of all the elementary reaction, but due to site blocking effect, we see no appreciable improvement in

the activity or turnover frequency in the methanol. However, in the presence of highly polar solvent, water, we see a dramatic improvement in the reaction activity, specifically at low temperature, which rectifies our previous work that suggested a low activity at low temperature. In water, catalytic activity of Ru(0001) is 4 and 2 order of magnitude higher at 323 K and 473 K, respectively, with respect to the gas phase activity. We compare our computed activity with that of the experimentally observed activity, and found reasonable agreement in all conditions. Interestingly, as suggested by Abdelrahman et al., our 2 site model can better explain the experimentally observed reaction orders and apparent activation barrier that is to say a non-competitive hydrogen adsorption mechanism is likely to be a more plausible adsorption mechanism than the competitive hydrogen adsorption process. Why hydrogen adsorption process is a non-competitive process on a Ru(0001) surface in the presence of large hydrocarbon molecules is a question we suggest to be ripe for the insight of surface scientists. Finally, a sensitivity analysis suggest that LA hydrogenation to the alkoxy is the rate controlling step in all reaction conditions. As a result, we conclude that C-H bond formation is likely to be an important activity descriptor for the future computational catalyst discovery and design study.

4.6 Acknowledgements

We gratefully acknowledge financial support from the National Science Foundation (CBET-1159863) and in part from the U.S. Department of Energy, Office of Basic Energy Sciences (SC0007167). Computational resources have been provided by the National Energy Research Scientific Computing Center (NERSC) and Pacific Northwest National Laboratory (PNNL).

4.7 Tables and figures

Table 4.1: Taft and Kamlet dipolarity/polarizability (π^*), hydrogen bond donor parameter (α), hydrogen bond acceptor parameter (β), normalized empirical solvent polarity parameter E_T^N, and di-electric constant (ε_r) at room temperature for all three solvent medium used in this study.

Solvent	$\boldsymbol{\pi^*}$	α	β	$\boldsymbol{E_T^N}$	$\boldsymbol{\varepsilon_r}$
Water	1.09	1.17	0.47	1	80.1
Methanol	0.60	0.98	0.66	0.762	30
1,4-dioxane	0.49	0	0.37	0.164	2.25

Table 4.2: Effects of solvents on adsorption strengths of intermediates in the HDO of LA on Ru(0001) model surface at 323 K and 423 K. Δ(ΔG) (eV) is a measure for the effect of solvent on adsorption energetics which is calculated by taking the difference of adsorption energy of adsorbate in the presence ($A(g) + * (l) \rightarrow A * (l)$) and absence ($A(g) + * (g) \rightarrow A * (g)$) of solvent environment.

Species	Chemical formula	Water		1,4-dioxane		Methanol	
		323 K	**423 K**	**323 K**	**423 K**	**323 K**	**423 K**
LA	$CH_3 - CO - CH_2 - CH_2$	0.137	0.122	0.072	0.057	0.071	0.054
Al	$CH_3 - CH(\dot{O}) - CH_2 - CH_2$	0.081	0.111	0.011	0.053	-0.005	0.039
Hy	$CH_3 - \dot{C}(OH) - CH_2 - CH_2$	0.017	0.066	0.023	0.066	-0.018	0.032
HPA	$CH_3 - CH(OH) - CH_2 - CH_2$	0.133	0.160	0.107	0.120	0.081	0.103
AGL	$CH_3 - C_4OH_3 = O$	0.172	0.168	0.160	0.132	0.138	0.120
GVL	$CH_3 - C_4OH_5 = O$	0.233	0.234	0.171	0.147	0.162	0.148
H	H	0.116	0.129	0.067	0.061	0.065	0.068
OH	OH	0.179	0.222	0.123	0.165	0.111	0.161
O	O	0.035	0.048	0.022	0.012	0.014	0.012
H_2O	H_2O	0.119	0.150	0.069	0.094	0.055	0.091
I-01	$CH_3 - CO - \dot{C}H - CH_2$	0.163	0.183	0.081	0.105	0.062	0.094
I-02	$CH_3 - CO - \dot{C}H - CH_2$	0.129	0.129	0.153	0.127	0.132	0.111
I-03	$C_4OH_3(CH_3)(O)(O)$	0.050	0.045	0.040	0.022	0.026	0.008
I-04	$C_4OH_3(CH_3)(OH)(O)$	0.008	0.022	0.009	0.031	-0.012	0.006
I-05	$CH_3 - C_4OH_3(OH) = O$	0.075	0.089	0.009	0.017	-0.002	0.011
I-06	$CH_3 - CO - \dot{C}H - CH_2 - \dot{C}O$	0.199	0.189	0.188	0.164	0.174	0.154
I-07	$CH_3 - CO - CH_2 - CH_2$	0.233	0.231	0.175	0.155	0.172	0.158
I-08	$CH_3 - C_4OH_4 = O$	0.187	0.174	0.137	0.112	0.131	0.111

I-09	$CH_3 - CH(OH) - \dot{C}H - CH_2$	-0.009	0.009	-0.003	0.005	-0.030	-0.018
I-10	$CH_3 - \dot{C}H - CH_2 - CH_2$	-0.051	-0.027	-0.112	-0.069	-0.126	-0.085
I-11	$CH_3 - \dot{C}(OH) - \dot{C}H - CH_2$	0.123	0.125	0.054	0.069	0.042	0.058
I-12	$CH_3 - \dot{C}H - \dot{C}H - CH_2$	-0.017	0.014	-0.067	-0.022	-0.089	-0.041
I-13	$CH_3 - CH(OH) - \dot{C}H - CH_2$	0.209	0.219	0.173	0.173	0.154	0.161
I-14	$CH_3 - \dot{C}H - CH_2 - CH_2$	0.137	0.135	0.097	0.073	0.086	0.069
I-15	$CH_3 - \ddot{C} - CH_2 - CH_2$	0.056	0.084	0.009	0.043	-0.015	0.024
I-16	$CH_3 - C_4OH_5 - OH$	0.227	0.227	0.146	0.131	0.137	0.132
I-17	$CH_3 - \ddot{C} - \dot{C}H - CH_2$	0.162	0.161	0.084	0.091	0.074	0.085
I-18	$CH_3 - CH(\dot{O}) - \dot{C}H - CH_2$	0.260	0.275	0.221	0.194	0.199	0.191
I-19	$CH_3 - \dot{C}(OH) - \dot{C}H - CH_2$	0.052	0.065	0.032	0.042	0.012	0.026
I-20	$CH_3 - \dot{C}H - \dot{C}H - CH_2$	0.152	0.147	0.077	0.061	0.072	0.059
I-21	$CH_3 - \ddot{C} - CH_2 - CH_2 - CO\dot{O}$	0.261	0.260	0.218	0.190	0.205	0.188
I-22	$CH_3 - C_4OH_4 - OH$	0.185	0.185	0.126	0.119	0.115	0.115
I-23	$CH_3 - C_4OH_3 - OH$	0.121	0.129	0.052	0.066	0.037	0.056
I-24	$CH_3 - C_4OH_4 = O$	0.075	0.062	0.066	0.047	0.056	0.037
I-25	$CH_3 - \ddot{C} - \dot{C}H - CH_2 - CO\dot{O}$	0.193	0.188	0.180	0.153	0.166	0.146
I-26	$CH_3 - CH(OH) - CH_2 - CH_2$	-0.007	-0.001	-0.040	-0.034	-0.049	-0.043
I-27	$CH_3 - \dot{C}(OH) - CH_2 - CH_2$	0.219	0.230	0.178	0.175	0.159	0.166
I-28	$CH_3 - CH(\dot{O}) - CH_2 - CH_2$	0.269	0.264	0.208	0.183	0.200	0.184
I-29	$CH_3 - \dot{C}(OH) - \dot{C}H - CH_2$	0.236	0.244	0.193	0.182	0.174	0.173
I-30	$CH_3(OH) - C_4OH_4 - OH$	0.140	0.142	0.093	0.087	0.081	0.080
I-31	$CH_3 - \dot{C}(OH) - CH_2 - CH_2$	-0.062	-0.055	-0.071	-0.065	-0.086	-0.082
I-32	$CH_3(OH) - C_4OH_4 = O$	0.023	0.033	0.032	0.016	0.005	-0.004
I-33	$CH_3 - CH(OH) - CH_2 - CH_2$	0.134	0.149	0.085	0.094	0.067	0.081
I-34	$CH_3 - CH(OH) - CH_2 - CH_2$	0.216	0.213	0.154	0.139	0.143	0.134
I-35	$CH_3 - CH(\dot{O}) - CH_2 - CH_2$	0.096	0.118	0.042	0.068	0.022	0.054
I-36	$CH_3 - CH(\dot{O}) - CH_2 - CH_2$	0.360	0.354	0.248	0.220	0.242	0.228
I-37	$CH_3 - CO - CH_2 - CH_2$	0.095	0.090	0.081	0.063	0.071	0.053
I-38	$CH_3 - CH(\dot{O}) - CH_2 - CH_2$	0.172	0.187	0.195	0.168	0.162	0.150
I-39	$C_4OH_5(CH_3)(\dot{O})(\dot{O})$	0.003	0.038	0.012	0.001	-0.039	-0.024
I-40	$C_4OH_5(CH_3)(\dot{O})(OH)$	0.016	0.033	-0.003	0.001	-0.022	-0.013

Table 4.3: Free energy of reaction ($\Delta \boldsymbol{G}$) and free energy of activation ($\Delta \boldsymbol{G}^{\ddagger}$), in eV, of each elementary reaction at 423 K. Both Gibbs free energy, free energy of reaction and free energy of activation, reported here is calculated using change in gas phase free energy and change in solvation energy for each elementary reaction.

Step	Reaction	Gas		Water		1,4-dioxane		Methanol	
		ΔG	$\Delta G^{\ddagger}$	ΔG	$\Delta G^{\ddagger}$	ΔG	$\Delta G^{\ddagger}$	ΔG	$\Delta G^{\ddagger}$
r_1	$LA(g) + 2* \rightarrow LA*$	-0.42	N/A	-0.30	N/A	-0.36	N/A	-0.37	N/A
r_2	$H_2(g) + 2* \rightarrow 2H*$	-0.82	N/A	-0.56	N/A	-0.70	N/A	-0.68	N/A
r_3	$LA* + H* \rightarrow Al* + *$	0.09	0.70	-0.05	0.53	0.02	0.66	0.01	0.63
r_4	$LA* + H* \rightarrow Hy* + *$	0.87	1.35	0.68	1.29	0.82	1.36	0.78	1.34
r_5	$Al* + H* \rightarrow HPA*$	0.78	1.23	0.70	1.24	0.79	1.27	0.78	1.28
r_6	$Hy* + H* \rightarrow HPA*$	0.00	0.76	-0.03	0.65	-0.01	0.68	0.00	0.68
r_7	$LA* + 2* \rightarrow I-1* + H*$	-0.42	0.29	-0.23	0.26	-0.31	0.30	-0.31	0.29
r_8	$LA* + 2* \rightarrow I-7* + OH*$	-0.54	0.75	-0.21	0.66	-0.28	0.70	-0.28	0.69
r_9	$I-1* + 2* \rightarrow I-2* + H*$	-0.94	0.29	-0.87	0.30	-0.86	0.30	-0.86	0.31
r_{10}	$I-2* \rightarrow I-3* + 2*$	0.87	2.07	0.79	2.03	0.77	1.98	0.77	1.99
r_{11}	$I-3* + H* \rightarrow I-4* + *$	0.72	0.92	0.57	0.86	0.67	0.92	0.65	0.92
r_{12}	$I-1* + * \rightarrow I-6* + OH*$	-0.87	0.80	-0.64	0.81	-0.64	0.80	-0.65	0.81
r_{13}	$I-1* \rightarrow I-5* + *$	0.39	0.89	0.30	0.90	0.30	0.90	0.31	0.90
r_{14}	$I-5* + * \rightarrow AGL* + OH*$	-0.35	0.25	-0.05	0.16	-0.07	0.18	-0.08	0.18
r_{15}	$I-7* + * \rightarrow I-6* + H*$	-0.75	0.48	-0.66	0.46	-0.68	0.48	-0.69	0.47
r_{16}	$I-6* \rightarrow AGL* + *$	0.90	1.14	0.88	1.15	0.87	1.12	0.87	1.13
r_{17}	$I-7* \rightarrow I-8* + *$	0.49	0.89	0.43	0.85	0.45	0.89	0.44	0.88
r_{18}	$AGL* + H* \rightarrow I-8* + *$	0.33	0.68	0.21	0.55	0.25	0.62	0.25	0.62
r_{19}	$I-4* + * \rightarrow AGL* + OH*$	-0.61	0.55	-0.24	0.64	-0.34	0.59	-0.34	0.60
r_{20}	$HPA* + * \rightarrow I-9* + H*$	-0.23	0.49	-0.25	0.48	-0.28	0.48	-0.28	0.48
r_{21}	$HPA** \rightarrow I-10** + OH*$	-0.38	1.01	-0.34	0.99	-0.40	1.01	-0.41	1.01
r_{22}	$I-9* + * \rightarrow I-11* + H*$	-0.57	0.28	-0.33	0.46	-0.44	0.40	-0.42	0.41
r_{23}	$I-9* + * \rightarrow I-12* + OH*$	-0.84	0.39	-0.61	0.31	-0.70	0.26	-0.70	0.26
r_{24}	$I-9* + * \rightarrow I-13* + OH*$	-0.71	0.45	-0.28	0.50	-0.38	0.48	-0.37	0.49
r_{25}	$I-10* + 2* \rightarrow I-12* + H*$	-0.69	0.30	-0.52	0.61	-0.58	0.57	-0.58	0.58
r_{26}	$I-10* + 2* \rightarrow I-14* + H*$	-0.93	0.34	-0.64	0.63	-0.73	0.58	-0.71	0.59
r_{27}	$I-10* + * \rightarrow I-15* + H*$	-0.25	0.09	-0.01	0.33	-0.08	0.30	-0.07	0.31
r_{28}	$I-10* \rightarrow I-16*$	0.32	0.82	0.57	0.79	0.52	0.80	0.54	0.80
r_{29}	$I-11* + * \rightarrow I-17* + OH*$	-0.65	1.04	-0.39	0.94	-0.46	0.97	-0.46	0.96
r_{30}	$I-11* + * \rightarrow I-19* + OH*$	-0.70	0.43	-0.54	0.32	-0.56	0.36	-0.57	0.35
r_{31}	$I-12* + * \rightarrow I-17* + H*$	-0.37	0.18	-0.09	0.28	-0.20	0.27	-0.18	0.28
r_{32}	$I-12* \rightarrow I-20* + H*$	-0.61	0.36	-0.35	0.60	-0.47	0.57	-0.44	0.58
r_{33}	$I-13* + * \rightarrow I-18* + H*$	-0.33	0.41	-0.15	0.41	-0.25	0.39	-0.23	0.40
r_{34}	$I-13* + * \rightarrow I-19* + H*$	-0.56	0.71	-0.59	0.50	-0.63	0.55	-0.63	0.54
r_{35}	$I-14* \rightarrow I-20* + H*$	-0.37	1.06	-0.23	1.17	-0.32	1.20	-0.31	1.18
r_{36}	$I-14* + * \rightarrow I-21* + H*$	-0.35	0.21	-0.10	0.30	-0.17	0.30	-0.16	0.30
r_{37}	$I-15* + 2* \rightarrow I-17* + H*$	-0.82	0.26	-0.61	0.28	-0.71	0.25	-0.69	0.27
r_{38}	$I-15* + 2* \rightarrow I-21*** + H*$	-1.03	0.30	-0.73	0.48	-0.82	0.45	-0.80	0.47
r_{39}	$I-15** \rightarrow I-22**$	0.24	0.60	0.34	0.77	0.32	0.75	0.33	0.77
r_{40}	$I-16** + * \rightarrow I-22* + H*$	-0.33	0.54	-0.24	0.51	-0.28	0.53	-0.28	0.52
r_{41}	$I-17* \rightarrow I-23* + *$	0.66	1.41	0.63	1.43	0.64	1.46	0.63	1.46
r_{42}	$I-17* + * \rightarrow I-25* + H*$	-0.93	0.36	-0.77	0.38	-0.81	0.40	-0.80	0.41
r_{43}	$I-18* + * \rightarrow I-6* + H*$	-0.89	0.48	-0.85	0.39	-0.86	0.43	-0.86	0.42
r_{44}	$I-18* \rightarrow I-24* + *$	0.52	0.80	0.31	0.71	0.37	0.76	0.37	0.75
r_{45}	$I-19* + * \rightarrow I-6* + H*$	-0.66	0.30	-0.41	0.50	-0.48	0.45	-0.46	0.47
r_{46}	$I-20* \rightarrow I-24*$	0.95	2.27	0.86	2.23	0.94	2.24	0.93	2.24
r_{47}	$I-20* + 2* \rightarrow I-25* + H*$	-0.69	0.64	-0.52	0.73	-0.54	0.72	-0.53	0.73
r_{48}	$I-21* + * \rightarrow I-25* + H*$	-0.71	0.28	-0.65	0.26	-0.69	0.27	-0.68	0.27
r_{49}	$I-21* \rightarrow I-8* + *$	0.74	0.82	0.65	0.67	0.66	0.72	0.66	0.71
r_{50}	$I-22* + * \rightarrow I-8* + H*$	-0.53	0.75	-0.41	0.73	-0.48	0.72	-0.47	0.72
r_{51}	$I-22* + * \rightarrow I-23* + H*$	-0.40	0.30	-0.33	0.18	-0.39	0.21	-0.39	0.20
r_{52}	$I-23* + * \rightarrow AGL* + H*$	-0.46	0.69	-0.29	0.73	-0.33	0.73	-0.33	0.74
r_{53}	$I-29* \rightarrow I-4* + 2*$	1.03	1.59	0.81	1.61	0.88	1.61	0.86	1.61
r_{54}	$AGL* + H* \rightarrow I-24* + *$	0.51	0.56	0.27	0.28	0.36	0.37	0.36	0.36
r_{55}	$I-25* \rightarrow AGL* + *$	1.13	1.17	1.11	1.22	1.11	1.20	1.10	1.20

r_{56}	$I-24*+H*\rightarrow GVL*+*$	-0.03	0.85	0.01	0.76	0.01	0.85	0.01	0.84
r_{57}	$HPA*+*\rightarrow I-26*+OH*$	-0.67	0.14	-0.61	0.11	-0.66	0.13	-0.65	0.13
r_{58}	$I-26*\rightarrow I-27*+H*$	-0.32	0.72	0.04	0.85	-0.05	0.86	-0.04	0.85
r_{59}	$I-26*+*\rightarrow I-13*+H*$	-0.26	0.42	0.09	0.56	0.01	0.54	0.01	0.54
r_{60}	$I-26*+*\rightarrow I-28*+H*$	-0.83	0.37	-0.44	0.64	-0.55	0.60	-0.54	0.61
r_{61}	$I-27*+2*\rightarrow I-19*+H*$	-0.51	0.33	-0.55	0.28	-0.58	0.29	-0.58	0.30
r_{62}	$I-27*+2*\rightarrow I-7*+H*$	-0.42	0.52	-0.29	0.54	-0.38	0.54	-0.36	0.54
r_{63}	$I-28*+*\rightarrow I-7*+H*$	0.10	0.76	0.20	0.69	0.13	0.73	0.14	0.72
r_{64}	$I-28*+*\rightarrow I-18*+H*$	0.24	0.95	0.38	0.85	0.31	0.88	0.32	0.87
r_{65}	$I-8*+H*\rightarrow GVL*+*$	0.15	0.97	0.08	0.83	0.12	0.91	0.12	0.90
r_{66}	$Hy*\rightarrow I-30*$	0.13	0.61	0.21	0.60	0.15	0.61	0.18	0.61
r_{67}	$Hy*+2*\rightarrow I-11*+H*$	-0.81	0.12	-0.62	0.24	-0.75	0.16	-0.72	0.19
r_{68}	$Hy*+*\rightarrow I-27*+OH*$	-1.01	0.60	-0.62	0.73	-0.73	0.68	-0.72	0.71
r_{69}	$Hy*+*\rightarrow I-15*+OH*$	-0.65	0.84	-0.41	0.88	-0.51	0.85	-0.50	0.87
r_{70}	$Hy*+2*\rightarrow I-31*+H*$	-0.67	0.42	-0.66	0.50	-0.74	0.46	-0.72	0.48
r_{71}	$I-30*+*\rightarrow I-22*+OH*$	-0.45	0.83	-0.19	0.74	-0.25	0.75	-0.25	0.75
r_{72}	$I-30*+*\rightarrow I-32*+H*$	-0.63	0.26	-0.61	0.28	-0.64	0.29	-0.64	0.29
r_{73}	$I-31*+*\rightarrow I-21*+OH*$	-1.01	0.52	-0.47	0.66	-0.59	0.65	-0.58	0.65
r_{74}	$I-31*\rightarrow I-32*+*$	0.08	0.56	0.17	0.55	0.16	0.55	0.16	0.55
r_{75}	$I-31*+2*\rightarrow I-29*+H*$	-1.01	0.10	-0.58	0.34	-0.70	0.31	-0.69	0.32
r_{76}	$I-32*+*\rightarrow I-4*+H*$	-0.06	0.84	0.06	0.82	0.02	0.84	0.02	0.84
r_{77}	$I-29*\rightarrow I-25*+OH*$	-0.71	0.52	-0.54	0.42	-0.57	0.45	-0.58	0.45
r_{78}	$GVL*\rightarrow GVL(g)+2*$	0.07	N/A	-0.16	N/A	-0.08	N/A	-0.08	N/A
r_{79}	$OH*+H*\rightarrow H_2O*+*$	0.52	1.13	0.32	0.83	0.39	0.93	0.38	0.92
r_{80}	$HPA*+H*\rightarrow I-33*+2*$	0.56	1.03	0.42	0.92	0.47	0.97	0.47	0.97
r_{81}	$I-39*+H*\rightarrow I-40*+2*$	-0.05	0.32	-0.18	0.27	-0.11	0.34	-0.11	0.35
r_{82}	$I-26*+H*\rightarrow I-34*+3*$	0.82	1.49	0.90	1.56	0.93	1.60	0.93	1.59
r_{83}	$I-33*\rightarrow I-34*+OH*$	-0.41	0.25	-0.12	0.14	-0.20	0.19	-0.20	0.17
r_{84}	$I-33*+*\rightarrow I-35*+H*$	-0.26	0.65	-0.16	0.66	-0.22	0.69	-0.22	0.68
r_{85}	$Al*+H*\rightarrow I-35*+*$	1.07	1.44	0.95	1.45	1.02	1.50	1.02	1.50
r_{86}	$Al*\rightarrow I-40*+*$	0.24	0.37	0.16	0.51	0.19	0.46	0.19	0.48
r_{87}	$I-34*+2*\rightarrow I-36*+H*$	-0.44	0.60	-0.17	0.69	-0.30	0.66	-0.28	0.67
r_{88}	$I-35*+*\rightarrow I-36*+OH*$	-0.58	0.78	-0.12	0.73	-0.26	0.73	-0.24	0.73
r_{89}	$I-36*\rightarrow I-16*$	0.23	1.31	0.10	0.98	0.14	1.05	0.13	1.03
r_{90}	$I-40*+2*\rightarrow GVL*+OH*$	-0.24	0.05	0.18	0.18	0.07	0.11	0.08	0.12
r_{91}	$LA*+2*\rightarrow I-37*+H*$	-1.11	0.04	-1.01	0.00	-1.04	0.02	-1.04	0.02
r_{92}	$I-37*+H*\rightarrow I-38*$	0.46	0.71	0.43	0.61	0.50	0.65	0.49	0.65
r_{93}	$I-38*\rightarrow I-39*+*$	1.03	1.59	0.88	1.60	0.86	1.61	0.86	1.61
r_{94}	$H_2O*\rightarrow H_2O(g)+*$	0.04	N/A	-0.11	N/A	-0.05	N/A	-0.05	N/A
r_{95}	$OH*+*\rightarrow H*$+O*	-0.82	0.66	-0.87	0.26	-0.91	0.40	-0.90	0.35
r_{96}	$HPA*\rightarrow HPA(g)+*$	0.41	N/A	0.25	N/A	0.29	N/A	0.31	N/A

Table 4.4: Computed vapor pressure, in bar, of different solvents at different reaction temperatures. Vapor pressures are calculated using thermodynamic property estimation software COSMOtherm[42].

Solvent	Temperature (K)			
	323	**373**	**423**	**473**
Water	0.124	1.014	4.76	15.35
1,4-dioxane	0.16	0.97	3.74	10.63
Methanol	0.53	3.60	13.92	40.25

Table 4.5: Computed turnover frequencies at various reaction temperatures, 10 bar hydrogen partial pressures, and 0.45 M LA solution in different solvent medium with two different physical adsorption model. For water, we report the experimentally observed TOF by Abdelrahman et al.[11]

TOF (s^{-1})		**Temperature (K)**			
		323	**373**	**423**	**473**
Gas	**1-site**	2.67×10^{-9}	1.62×10^{-5}	3.44×10^{-3}	1.05×10^{-1}
	2-site	2.23×10^{-6}	4.38×10^{-4}	1.30×10^{-2}	2.90×10^{-1}
Water	**1-site**	1.00×10^{-5}	6.43×10^{-3}	2.39×10^{-1}	2.51
	2-site	2.43×10^{-4}	1.43×10^{-2}	3.09×10^{-1}	2.76
	Exp.	2.00×10^{-3}	N/A	4.80×10^{-1}	N/A
1,4-dioxane	**1-site**	2.83×10^{-7}	4.65×10^{-4}	1.03×10^{-2}	3.23×10^{-1}
	2-site	3.73×10^{-5}	2.41×10^{-3}	5.35×10^{-2}	5.01×10^{-1}
Methanol	**1-site**	2.86×10^{-7}	6.97×10^{-4}	2.03×10^{-2}	6.46×10^{-1}
	2-site	7.43×10^{-5}	4.38×10^{-3}	9.14×10^{-2}	8.77×10^{-1}

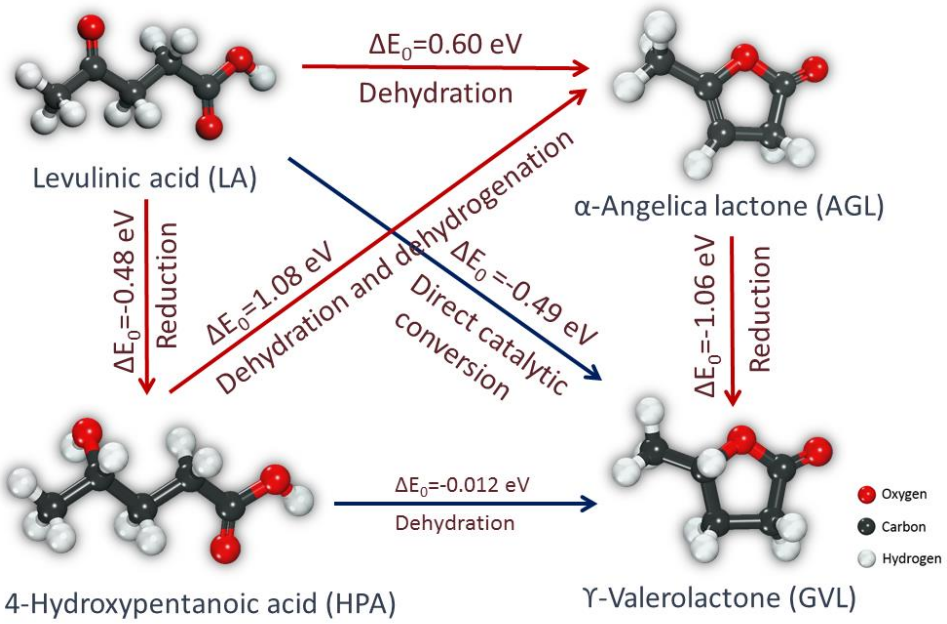

Figure 4.1: Different reaction pathways for the levulinic acid (LA) hydrodeoxygenation (HDO) to γ-valerolactone (GVL). Pathways leading to intramolecular esterification of angelica lactone (AGL) are displayed with red arrows. Zero-point corrected reaction energies for various gas phase reactions have been computed at the PBE-D3 level of theory.

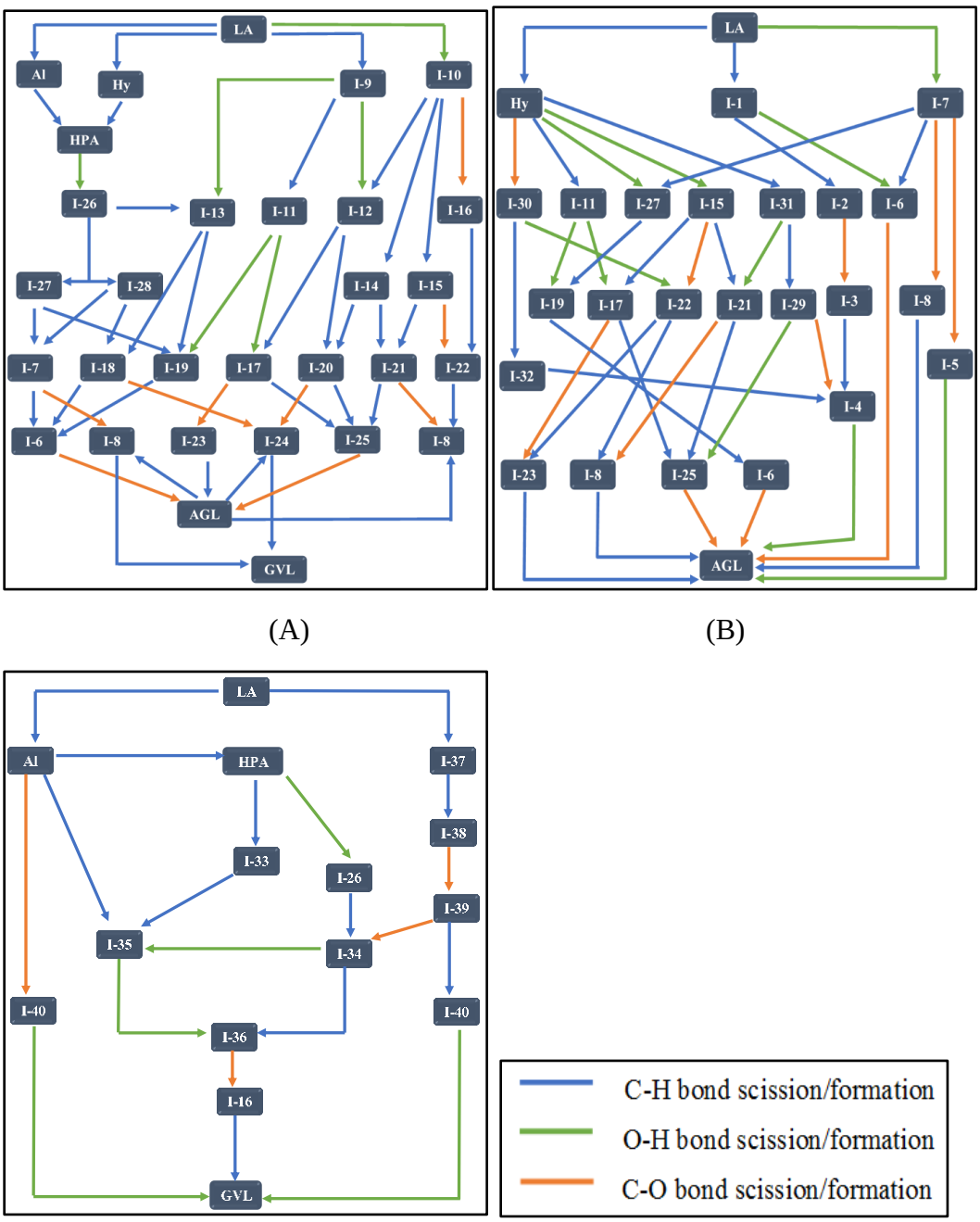

Figure 4.2: Different pathways for LA hydrodeoxygenation to form GVL, A) LA hydrogenation to HPA, subsequent dehydration and dehydrogenation to form AGL which is followed by hydrogenation of AGL to form GVL, B) direct catalytic conversion of LA to AGL, and C) Pathways for LA hydrodeoxygenation to form GVL via direct catalytic conversion and hydrogenation. Molecular structure of various intermediates are shown in figure 4.3.

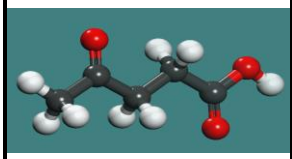	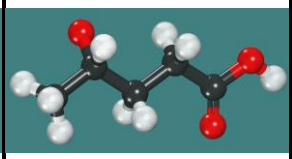	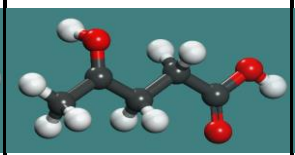	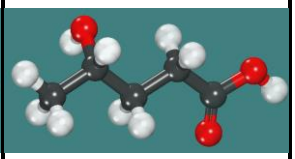
LA	Al	Hy	HPA
	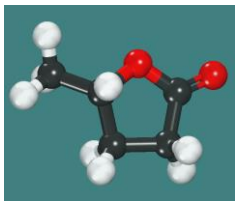	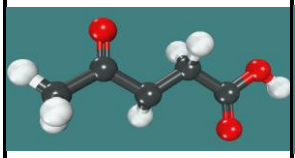	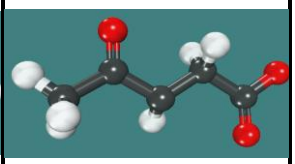
AGL	GVL	I-1	I-2
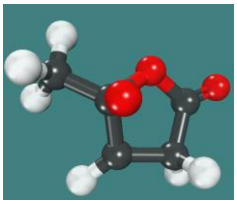	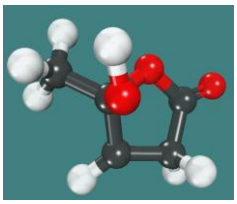	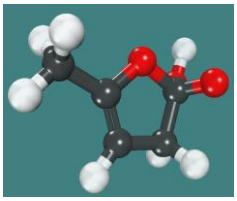	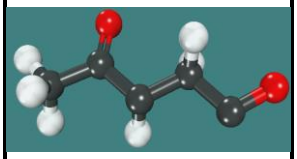
I-3	I-4	I-5	I-6
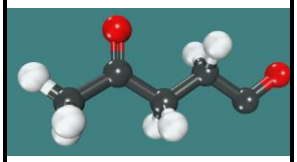	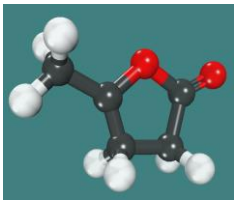	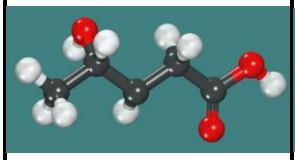	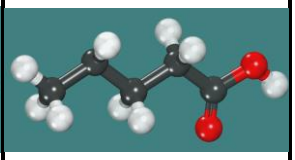
I-7	I-8	I-9	I-10
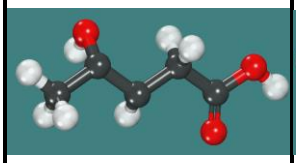	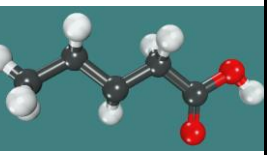	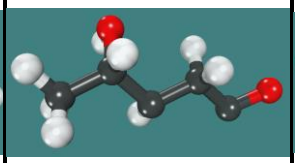	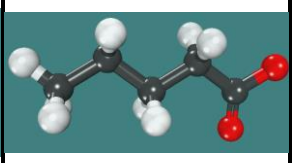
I-11	I-12	I-13	I-14
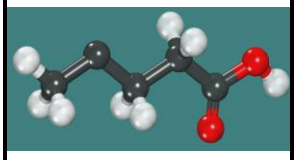	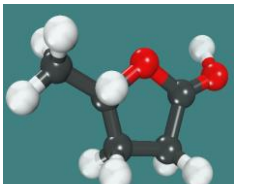	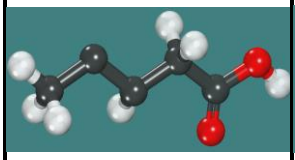	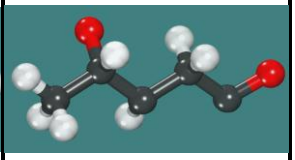
I-15	I-16	I-17	I-18

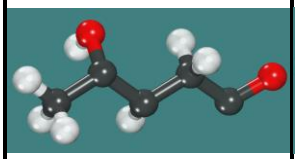	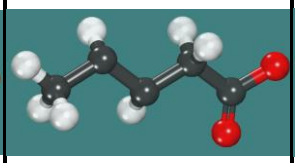	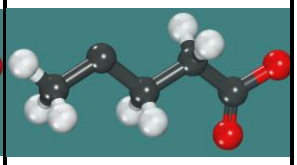	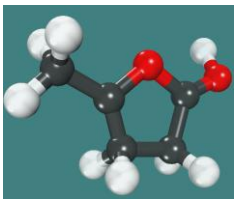
I-19	I-20	I-21	I-22
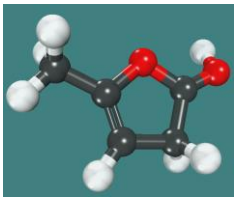	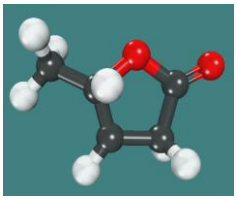	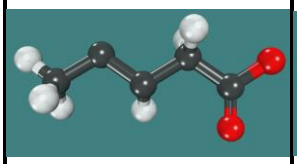	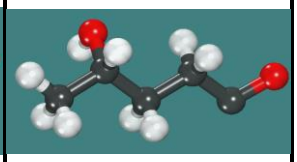
I-23	I-24	I-25	I-26
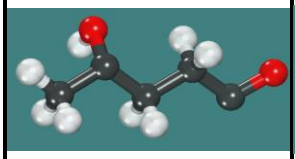	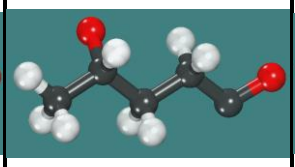	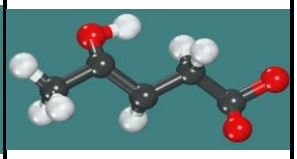	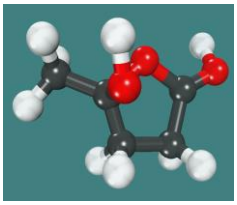
I-27	I-28	I-29	I-30
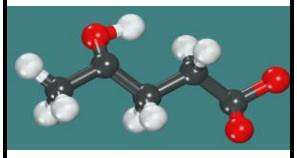	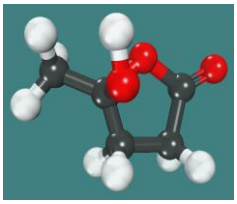	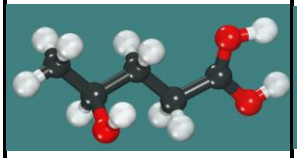	
I-31	I-32	I-33	I-34
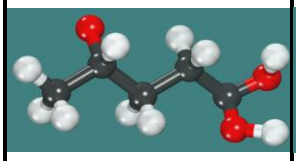	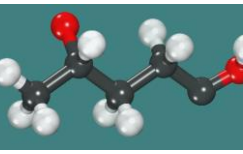	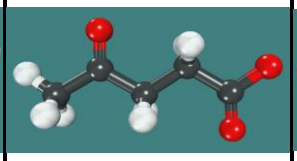	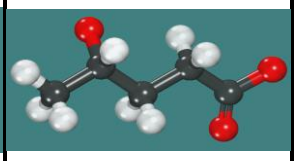
I-35	I-36	I-37	I-38
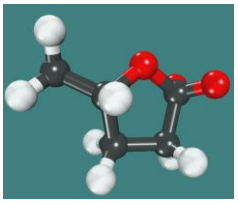	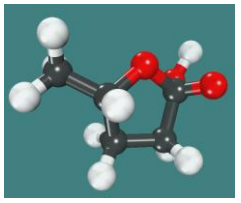		
I-39	I-40		

Figure 4.3: Molecular structure of various surface intermediates considered in the microkinetic modeling.

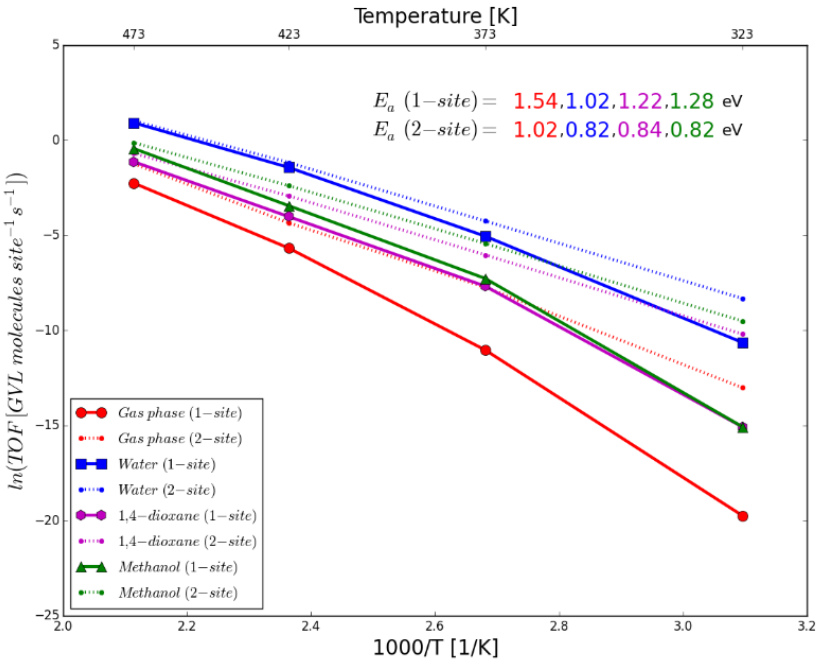

Figure 4.4: Arrhenius plot for the HDO of LA predicted by the mean-field microkinetic model on Ru(0001) surface for both 1 site and 2 site model in different solvent medium.

4.8 Bibliography

1. Anastas, P. T.; Warner, J. C., *Green Chemistry: Theory and Practice*. Oxford University Press: 2000.
2. Sheldon, R. A., *Chem. Soc. Rev.* **2012,** *41*, 1437-1451.
3. Bozell, J. J.; Petersen, G. R., *Green Chem.* **2010,** *12*, 539-554.
4. Serrano-Ruiz, J. C.; Luque, R.; Sepulveda-Escribano, A., *Chem. Soc. Rev.* **2011,** *40*, 5266-5281.
5. Huber, G. W.; Chheda, J. N.; Barrett, C. J.; Dumesic, J. A., *Science* **2005,** *308*, 1446-1450.
6. Bu, Q.; Lei, H.; Zacher, A. H.; Wang, L.; Ren, S.; Liang, J.; Wei, Y.; Liu, Y.; Tang, J.; Zhang, Q.; Ruan, R., *Bioresour. Technol.* **2012,** *124*, 470-477.
7. Elliott, D. C.; Baker, E. G., *Upgrading biomass liquefaction products through hydrodeoxygenation*. ; Pacific Northwest Lab., Richland, WA (USA): 1984; p Medium: X; Size: Pages: 29.
8. Wettstein, S. G.; Alonso, D. M.; Chong, Y.; Dumesic, J. A., *Energy Environ. Sci.* **2012,** *5*, 8199-8203.
9. Alonso, D. M.; Wettstein, S. G.; Dumesic, J. A., *Green Chem.* **2013,** *15*, 584-595.
10. Horvath, I. T.; Mehdi, H.; Fabos, V.; Boda, L.; Mika, L. T., *Green Chem.* **2008,** *10*, 238-242.
11. Abdelrahman, O. A.; Heyden, A.; Bond, J. Q., *ACS Catal.* **2014,** *4*, 1171-1181.
12. Boddien, A.; Loges, B.; Junge, H.; Beller, M., *ChemSusChem* **2008,** *1*, 751-758.
13. Kopetzki, D.; Antonietti, M., *Green Chem.* **2010,** *12*, 656-660.
14. Gürbüz, E. I.; Alonso, D. M.; Bond, J. Q.; Dumesic, J. A., *ChemSusChem* **2011,** *4*, 357-361.
15. Manzer, L. E., *Appl. Catal., A* **2004,** *272*, 249-256.
16. Braden, D. J.; Henao, C. A.; Heltzel, J.; Maravelias, C. C.; Dumesic, J. A., *Green Chem.* **2011,** *13*, 1755-1765.
17. Ftouni, J.; Muñoz-Murillo, A.; Goryachev, A.; Hofmann, J. P.; Hensen, E. J. M.; Lu, L.; Kiely, C. J.; Bruijnincx, P. C. A.; Weckhuysen, B. M., *ACS Catal.* **2016,** *6*, 5462-5472.
18. Rajadhyaksha, R. A.; Karwa, S. L., *Chem. Eng. Sci.* **1986,** *41*, 1765-1770.
19. Sievers, C.; Noda, Y.; Qi, L.; Albuquerque, E. M.; Rioux, R. M.; Scott, S. L., *ACS Catal.* **2016,** *6*, 8286-8307.
20. Singh, U. K.; Vannice, M. A., *Appl. Catal., A* **2001,** *213*, 1-24.
21. Zope, B. N.; Hibbitts, D. D.; Neurock, M.; Davis, R. J., *Science* **2010,** *330*, 74-78.
22. Mathew, K.; Sundararaman, R.; Letchworth-Weaver, K.; Arias, T. A.; Hennig, R. G., *The Journal of Chemical Physics* **2014,** *140*, 084106.
23. Gilbert, L.; Mercier, C., Solvent effects in heterogeneous catalysis : Application to the synthesis of fine chemicals. In *Studies in Surface Science and Catalysis*, M. Guisnet, J. B. J. B. C. B. D. D. G. P.; Montassier, C., Eds. Elsevier: 1993; Vol. Volume 78, pp 51-66.
24. Wehrli, J. T.; Baiker, A.; Monti, D. M.; Blaser, H. U.; Jalett, H. P., *J. Mol. Catal.* **1989,** *57*, 245-257.
25. Faheem, M.; Suthirakun, S.; Heyden, A., *The Journal of Physical Chemistry C* **2012,** *116*, 22458-22462.
26. Behtash, S.; Lu, J.; Faheem, M.; Heyden, A., *Green Chem.* **2014,** *16*, 605-616.

27. Behtash, S.; Lu, J.; Mamun, O.; Williams, C. T.; Monnier, J. R.; Heyden, A., *The Journal of Physical Chemistry C* **2016,** *120*, 2724-2736.
28. Behtash, S.; Lu, J.; Walker, E.; Mamun, O.; Heyden, A., *J. Catal.* **2016,** *333*, 171-183.
29. Blöchl, P. E., *Phys. Rev. B* **1994,** *50*, 17953-17979.
30. Kresse, G.; Joubert, D., *Phys. Rev. B* **1999,** *59*, 1758-1775.
31. Chung, L. W.; Sameera, W. M. C.; Ramozzi, R.; Page, A. J.; Hatanaka, M.; Petrova, G. P.; Harris, T. V.; Li, X.; Ke, Z.; Liu, F.; Li, H.-B.; Ding, L.; Morokuma, K., *Chem. Rev.* **2015,** *115*, 5678-5796.
32. Baroni, S.; de Gironcoli, S.; Dal Corso, A.; Giannozzi, P., *Reviews of Modern Physics* **2001,** *73*, 515-562.
33. Mamun, O.; Walker, E.; Faheem, M.; Bond, J. Q.; Heyden, A., *ACS Catal.* **2016**, 215-228.
34. Ahlrichs, R.; Bär, M.; Häser, M.; Horn, H.; Kölmel, C., *Chem. Phys. Lett.* **1989,** *162*, 165-169.
35. Weigend, F., *Phys. Chem. Chem. Phys.* **2006,** *8*, 1057-1065.
36. Weigend, F.; Ahlrichs, R., *Phys. Chem. Chem. Phys.* **2005,** *7*, 3297-3305.
37. Weigend, F.; Häser, M.; Patzelt, H.; Ahlrichs, R., *Chem. Phys. Lett.* **1998,** *294*, 143-152.
38. Eichkorn, K.; Treutler, O.; Öhm, H.; Häser, M.; Ahlrichs, R., *Chem. Phys. Lett.* **1995,** *242*, 652-660.
39. Eichkorn, K.; Weigend, F.; Treutler, O.; Ahlrichs, R., *Theor. Chem. Acc.* **1997,** *97*, 119-124.
40. Becke, A. D., *Physical Review A* **1988,** *38*, 3098-3100.
41. Klamt, A.; Jonas, V.; Bürger, T.; Lohrenz, J. C. W., *The Journal of Physical Chemistry A* **1998,** *102*, 5074-5085.
42. Schafer, A.; Klamt, A.; Sattel, D.; Lohrenz, J. C. W.; Eckert, F., *Phys. Chem. Chem. Phys.* **2000,** *2*, 2187-2193.
43. Cao, S.; Monnier, J. R.; Williams, C. T.; Diao, W.; Regalbuto, J. R., *J. Catal.* **2015,** *326*, 69-81.
44. Luo, W.; Sankar, M.; Beale, A. M.; He, Q.; Kiely, C. J.; Bruijnincx, P. C. A.; Weckhuysen, B. M., *Nat. Commun.* **2015,** *6*, 6540.
45. Reichardt, C.; Welton, T., Empirical Parameters of Solvent Polarity. In *Solvents and Solvent Effects in Organic Chemistry*, Wiley-VCH Verlag GmbH & Co. KGaA: 2010; pp 425-508.
46. Olmstead, W. N.; Margolin, Z.; Bordwell, F. G., *The Journal of Organic Chemistry* **1980,** *45*, 3295-3299.
47. Eyring, H., *The Journal of Chemical Physics* **1935,** *3*, 107-115.
48. Johnston, H. S.; Heicklen, J., *The Journal of Physical Chemistry* **1962,** *66*, 532-533.
49. Lu, J.; Behtash, S.; Mamun, O.; Heyden, A., *ACS Catal.* **2015**, 2423-2435.
50. Grabow, L.; Hvolbæk, B.; Nørskov, J., *Top. Catal.* **2010,** *53*, 298-310.
51. Serrano-Ruiz, J. C.; West, R. M.; Dumesic, J. A., *Annu. Rev. Chem. Biomol. Eng.* **2010,** *1*, 79-100.
52. Yan, Z.-p.; Lin, L.; Liu, S., *Energy Fuels* **2009,** *23*, 3853-3858.
53. Walker, E.; Ammal, S. C.; Terejanu, G. A.; Heyden, A., *J. Phys. Chem. C* **2016,**

120, 10328-10339.
54. Yang, Y.; Gao, G.; Zhang, X.; Li, F., *ACS Catal.* **2014,** *4*, 1419-1425.
55. Al-Shaal, M. G.; Wright, W. R. H.; Palkovits, R., *Green Chem.* **2012,** *14*, 1260-1263.
56. Abdelrahman, O. A.; Heyden, A.; Bond, J. Q., *J. Catal.* **2017,** *348*, 59-74.

APPENDIX A: SUPPORTING INFORMATION FOR THEORETICAL INVESTIGATION OF THE HYDRODEOXYGENATION OF LEVULINIC ACID TO γ-VALEROLACTONE OVER Ru (0001)

Mamun, O.; Walker, E.; Faheem, M.; Bond, J.Q..; Heyden, A. *ACS Catalysis*, **2016**, 7(1), 215-228.

A.1 DFT functional validation

To confirm the accuracy of the PBE-D3 functional, we compare PBE-D3 gas phase reaction energies against CCSD(T) data. In particular, for the coupled cluster calculations, all geometries were first optimized using the MP2/def2-TZVPP level of theory. Then, a coupled cluster (CCSD(T)) single point calculation was performed on the optimized geometry using the same basis set. The zero point energy is computed at the MP2 level of theory. Overall, the deviations of PBE-D3 relative to the coupled cluster calculations are less then 2 kcal/mole.

	Zero-point corrected reaction energy [kcal/mol]	
	CCSD(T) corrected MP2/def2-TZVPP	PBE-D3 deviation
LA -> GVL	-9.4*	0.6
LA -> HPA	-11.6	0.6
HPA -> GVL	2.2	0.0
LA -> AGL	16.1	-1.4
AGL -> GVL	-25.4	2.0

*experimental value: -10.3 kcal/mol.[1]

A.2 Brønsted-Evans-Polanyi (BEP) and transition state scaling relations for C-O ring opening reactions relevant for the HDO of levulinic acid over Ru(0001)

BEP relations[2-3] have previously been used to predict catalytic phenomena of a similar set of reactions over various catalytic surfaces [4]. The Newns-Anderson[5-6] model demonstrated that catalytic action of a transition metal is strongly dependent on the d-band center of that metal. This model explains the fundamental idea of the formulation of BEP relations, i.e., the activation energy, E_A, of a reaction can be expressed as a linear function of the reaction energy, ΔE. Similarly, Liu and Hu [7] formulated a relation known as

'Transition state scaling' (TSS) which states that the transition state energy, E_{TS}, can be expressed as a linear function of final state energy, E_{FS}.

$$E_A = \alpha \cdot \Delta E + \beta \quad \text{(A1)}$$

$$E_{TS} = \alpha \cdot E_{FS} + \beta \quad \text{(A2)}$$

Considering the difficulty in reliably identifying a transition state for C-O ring opening reactions, we used BEP and TSS relations to predict the activation barriers for these processes from the C-O ring opening reactions for which we could identify transition states with our required accuracy. In particular, we used 12 converged ring opening transition states in our BEP and TSS relations (7 of which are not part of our reaction network). All transition state structures used in the BEP correlations that are not part of our reaction network are shown in Figure S3. C-O ring opening reactions are found to have a BEP slope of 0.08 and an intercept of 0.56 eV with a mean absolute error (MAE) of 0.37 eV. Such a relatively large MAE has also been reported by Wang et al. (0.45 eV) for C-O ring opening reactions.[8] We believe the origin for the relatively large MAE can be found in the large difference in steric orientation of reactants, products and transition state structures. For predicting kinetic parameters in our microkinetic model, we used a BEP relation in free energy, which can be represented as

$$G_A = \alpha \cdot \Delta G + \beta \quad \text{(A3)}$$

and shown in Figure A2.

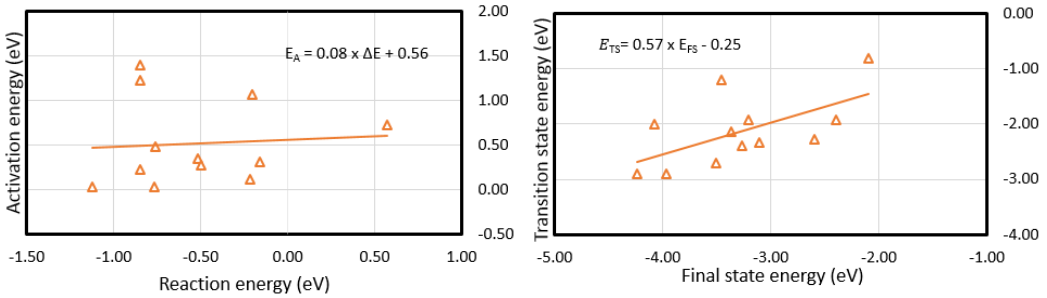

Figure A.1: BEP (Left) and TSS (right) relations for C-O bond scission reaction (ring opening) of various levulinic acid derivatives over Ru (0001) surface.

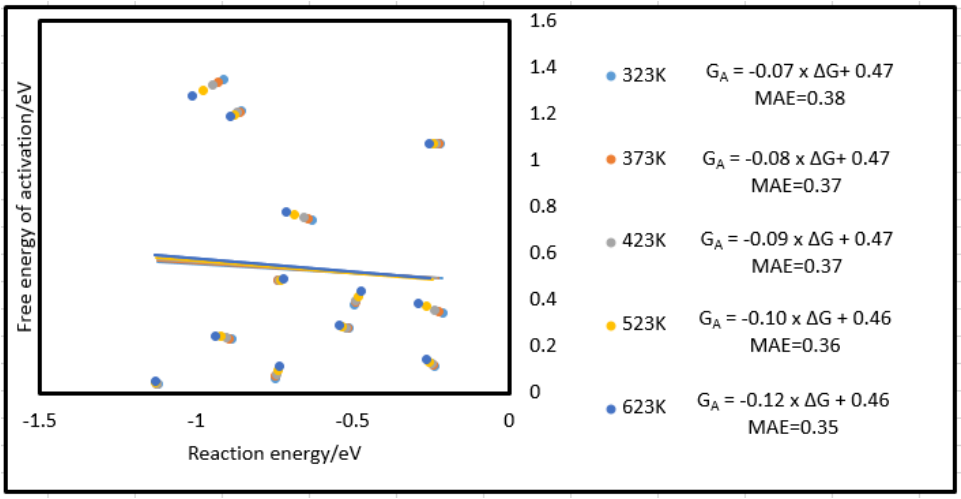

Figure A.2**:** BEP relation (free energy of activation as a function of standard free energy of reaction) for C-O ring opening reactions at various temperatures.

Table A.1**:** BEP estimated free energy of activation at different temperatures for reactions for which no reliable transition state could be identified.

Step	$BEP\ estimated\ \Delta G^{\ddagger}\ (eV)$				
	323 K	373 K	423 K	523 K	623 K
R-19	0.57	0.59	0.61	0.63	0.67
R-20	0.80	0.81	0.82	0.77	0.78
R-33	1.05	1.05	1.06	1.06	1.08
R-39	1.57	1.58	1.59	1.60	1.62

A.3 PBE-D3 optimized structures

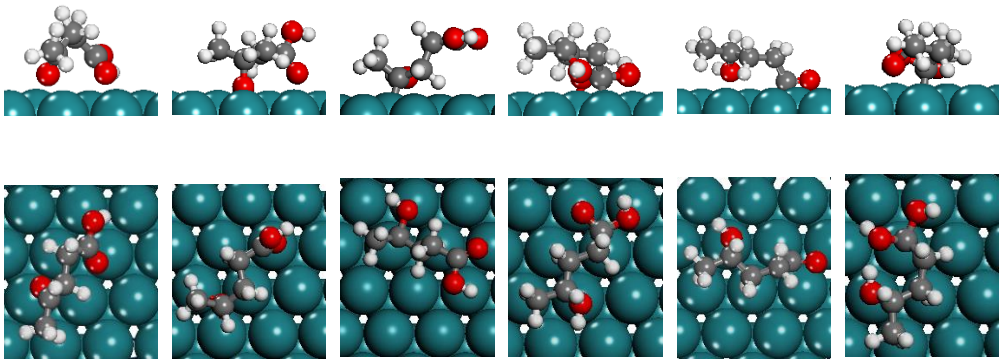

LA Al Hy HPA I-01 I-02

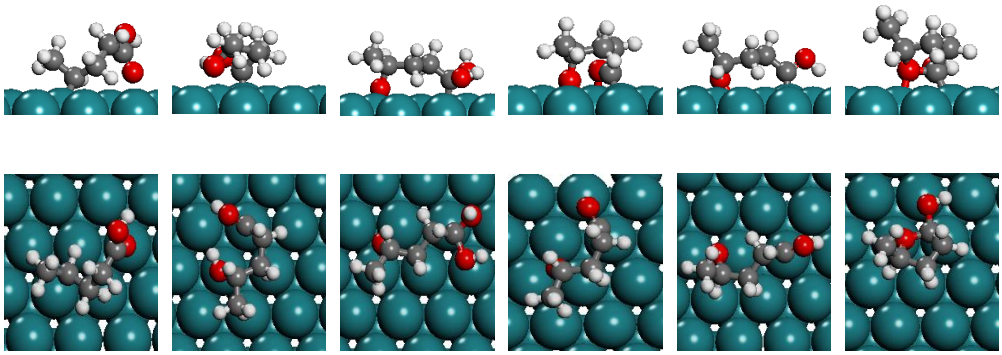

I-03 I-04 I-05 I-06 I-07 I-08

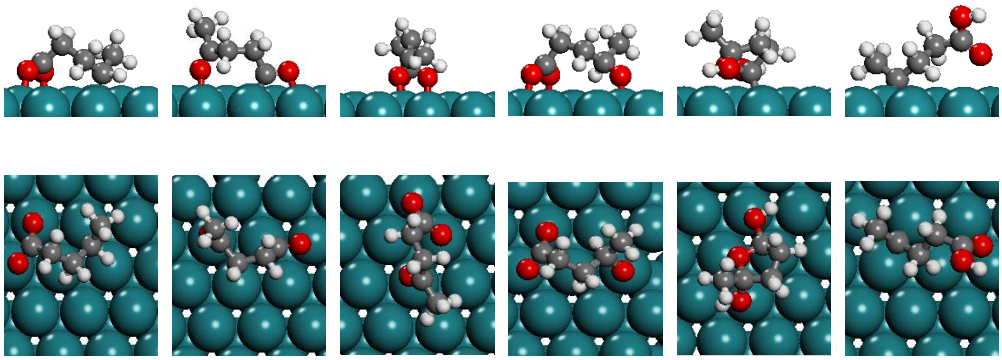

I-09 I-10 I-11 I-12 I-13 I-14

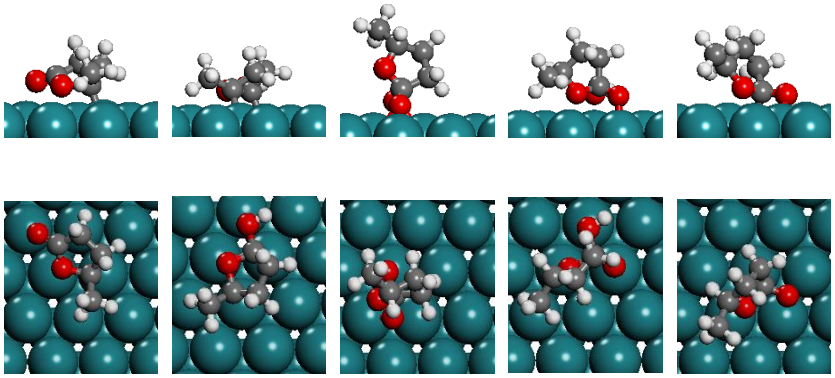

Figure A.3: PBE-D3 optimized geometries of various surface intermediates, reactants, and products.

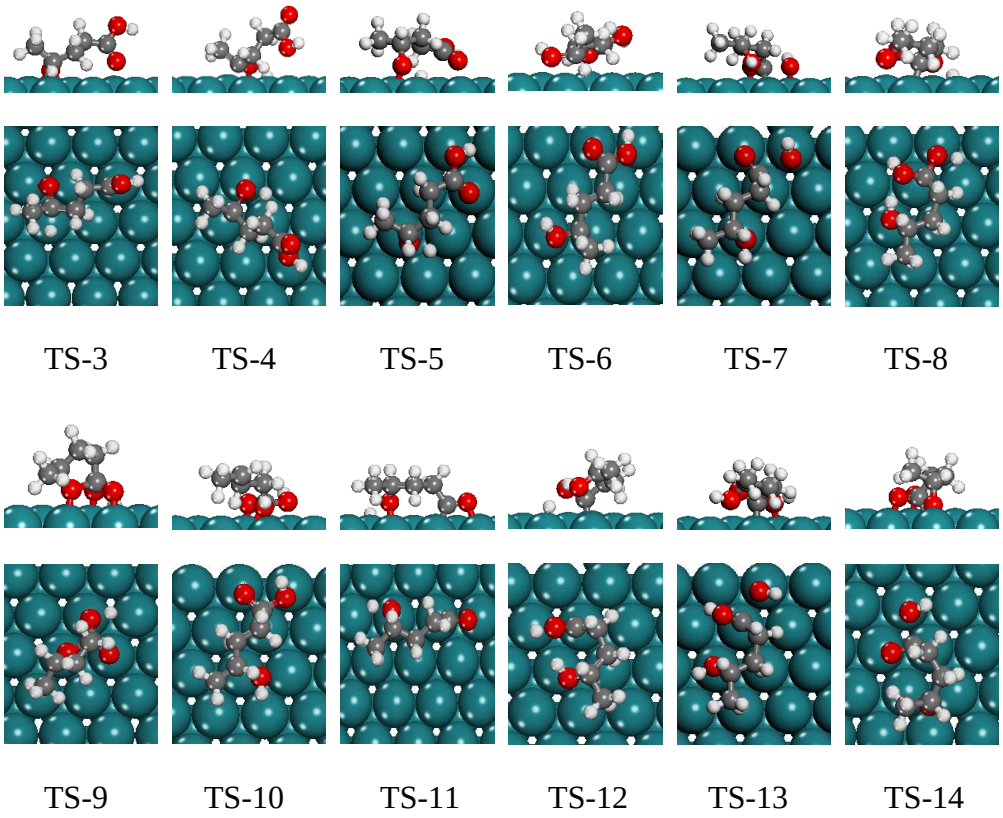

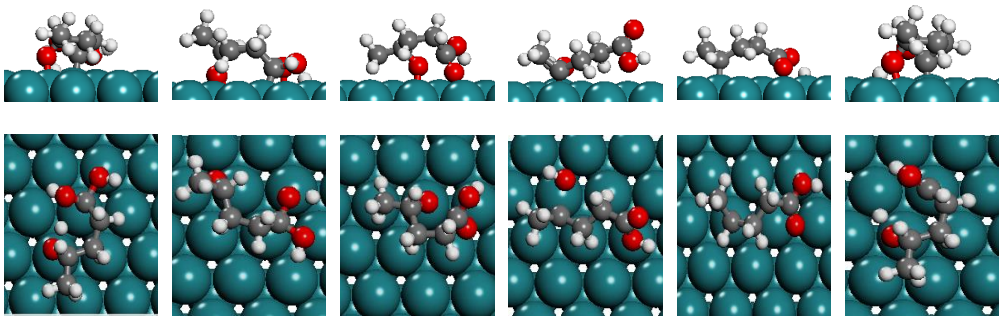

TS-15 TS-16 TS-17 TS-18 TS-21 TS-22

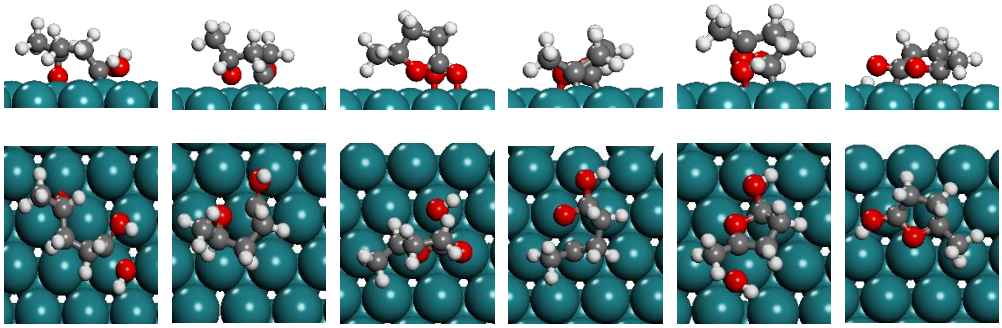

TS-23 TS-24 TS-25 TS-26 TS-27 TS-28

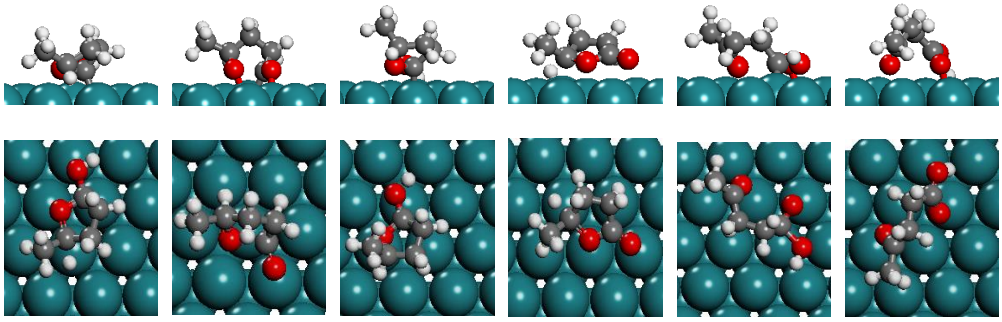

TS-29 TS-30 TS-31 TS-32 TS-34 TS-35

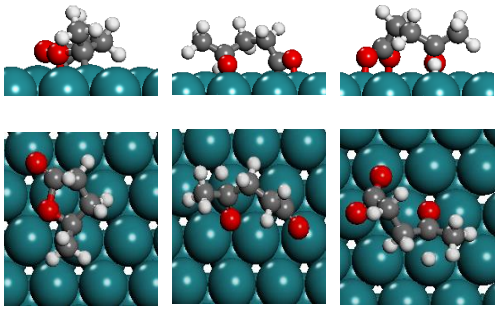

TS-36 TS-37 TS-38

Figure A4: PBE-D3 optimized transition state structures. The transition state number corresponds to the elementary reaction number in Table 2.2.

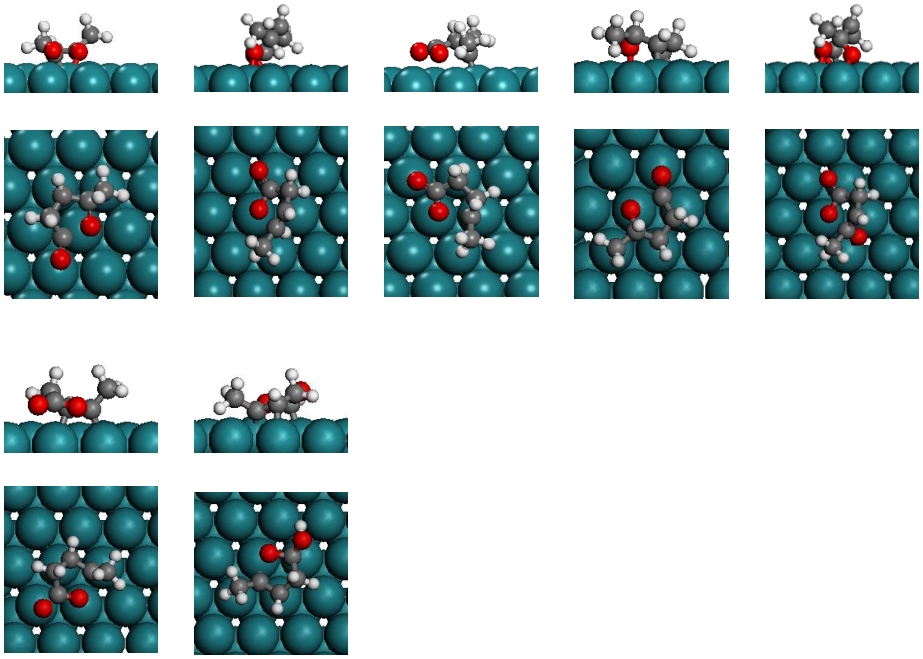

Figure A.5: To increase the number of data points in our BEP relations for C-O ring opening reactions, we added 7 transition state structures (shown above) that are not part of the reaction network to the BEP relation calculation.

A.4 Reactant and product partial pressure estimation

To compare our modeling results with experimental observations, we used typical reaction conditions in our models. Specifically, experiments are often performed under liquid phase conditions with a concentration of LA (0.15-0.45 M), GVL ($5 \times 10^{-4}\ to\ 1.5 \times 10^{-3}\ M$) and hydrogen (10 bar)[9]. As a result, we used for our microkinetic model a partial pressure of 10 bar for hydrogen. To find the corresponding partial pressure/fugacity of LA for a 0.45 M solution, we used the modified Raoult's law,

$$f_{LA}^{v} = P_{LA} = x_{LA} \times \gamma_{LA} \times P_{LA}^{sat} \tag{A4}$$

Here, thermodynamic data such as the activity coefficient and saturation pressure of LA were calculated using the COSMOtherm program package [10-12]. To compute the mole fraction of LA in solution for a 0.45 M solution, we used

$$x_{LA} = 0.45\ M \times v\ \frac{m^3}{kg} \times 18 \frac{kg}{kmol} \tag{A5}$$

(i.e., we assumed a dilute solution). Here, v is the specific volume of saturated, liquid water, for which we used standard thermodynamic property data [13]. Table 2 summarizes all data used to calculate the fugacity/partial pressure of LA at various temperatures. Since the LA to GVL ratio is about 900 under experimental reaction conditions, we assumed a conversion of 0.1% to estimate the fugacity of GVL.

Table A.2: LA partial pressure estimation using modified Raoult's law.

Temperature (K)	Mole fraction of LA	Activity coefficient of LA	Volume of saturated water (m^3/Kg)	Saturation pressure of LA (bar)	Partial pressure of LA (bar)
323	8.19×10^{-3}	7.21	1.01×10^{-3}	3.06×10^{-4}	1.80×10^{-5}
373	8.44×10^{-3}	6.51	1.04×10^{-3}	1.01×10^{-2}	5.57×10^{-4}
423	8.83×10^{-3}	5.57	1.09×10^{-3}	1.09×10^{-1}	5.36×10^{-3}
473	9.37×10^{-3}	4.31	1.25×10^{-3}	5.75×10^{-1}	2.32×10^{-2}
523	1.01×10^{-2}	3.32	1.25×10^{-3}	1.93	6.51×10^{-2}

A.5 Development of microkinetic model

In the following, we define the number of intermediate species *i* on the surface over the total number of surface sites (Ru(0001) surface atoms), θ_i as,

$$\theta_i = \frac{Number\ of\ \ intermediate\ i\ species\ adsorbed\ on\ the\ surface}{Total\ number\ of\ active\ surface\ sites}$$

We distinguish θ_i from the surface coverage, $\tilde{\theta}_i$, which is the product of θ_i and the number of sites occupied by intermediate *i* (please see the main article for a description of each surface intermediate I-i and r_i) . We note that θ_i is the activity of a lattice gas that occupies multiple sites.[14] As a result, we define the following set of elementary reactions:

$$r_1 = k_{1f} P_{LA} \theta_*^2 - k_{1b} \theta_{LA}$$

$$r_2 = k_{2f} P_{H_2} \theta_*^2 - k_{2b} {\theta_H}^2$$

$$r_3 = k_{3f} \theta_{LA} \theta_H - k_{3b} \theta_{Al} \theta_*$$

$$r_4 = k_{4f} \theta_{LA} \theta_H - k_{4b} \theta_{Hy} \theta_*$$

$$r_5 = k_{5f} \theta_{Al} \theta_H - k_{5b} \theta_{HPA}$$

$$r_6 = k_{6f}\theta_{Hy}\theta_H - k_{6b}\theta_{HPA}$$

$$r_7 = k_{7f}\theta_{HPA}\theta_* - k_{7b}\theta_{01}\theta_{OH}$$

$$r_8 = k_{8f}\theta_{HPA}\theta_H - k_{8b}\theta_{02}{\theta_*}^2$$

$$r_9 = k_{9f}\theta_{17}\theta_H - k_{9b}\theta_{18}{\theta_*}^2$$

$$r_{10} = k_{10f}\theta_{HPA} - k_{10b}\theta_{03}\theta_{OH}$$

$$r_{11} = k_{11f}\theta_{01}\theta_* - k_{11b}\theta_{06}\theta_H$$

$$r_{12} = k_{12f}\theta_{01}\theta_H - k_{12b}\theta_{04}{\theta_*}^3$$

$$r_{13} = k_{13f}\theta_{02} - k_{13b}\theta_{04}\theta_{OH}$$

$$r_{14} = k_{14f}\theta_{Al}{\theta_*}^2 - k_{14b}\theta_{06}\theta_{OH}$$

$$r_{15} = k_{15f}\theta_{02}\theta_* - k_{15b}\theta_{05}\theta_H$$

$$r_{16} = k_{16f}\theta_{Al}\theta_H - k_{16b}\theta_{05}\theta_*$$

$$r_{17} = k_{17f}\theta_{Al} - k_{17b}\theta_{18}\theta_*$$

$$r_{18} = k_{18f}\theta_{Hy} - k_{18b}\theta_{14}\theta_{OH}$$

$$r_{19} = k_{19f}\theta_{Hy} - k_{19b}\theta_{13}\theta_*$$

$$r_{20} = k_{20f}\theta_{03} - k_{20b}\theta_{08}$$

$$r_{21} = k_{21f}\theta_{03}{\theta_*}^2 - k_{21b}\theta_{09}\theta_H$$

$$r_{22} = k_{22f}\theta_{04}{\theta_*}^2 - k_{22b}\theta_{07}\theta_H$$

$$r_{23} = k_{23f}\theta_{05}\theta_* - k_{23b}\theta_{07}\theta_{OH}$$

$$r_{24} = k_{24f}\theta_{07} - k_{24b}\theta_{08}$$

$$r_{25} = k_{25f}\theta_{18}{\theta_*}^2 - k_{25b}\theta_{GVL}\theta_{OH}$$

$$r_{26} = k_{26f}\theta_{14}\theta_* - k_{26b}\theta_{16}$$

$$r_{27} = k_{27f}\theta_{13}{\theta_*}^2 - k_{27b}\theta_{16}\theta_{OH}$$

$$r_{28} = k_{28f}\theta_{16} - k_{28b}\theta_{15}\theta_H$$

$$r_{29} = k_{29f}\theta_{16}\theta_H - k_{29b}\theta_{08}\theta_*$$

$$r_{30} = k_{30f}\theta_{06} - k_{30b}\theta_{GVL}\theta_*$$

$$r_{31} = k_{31f}\theta_{08}\theta_* - k_{31b}\theta_{GVL}\theta_H$$

$$r_{32} = k_{32f}\theta_{15}\theta_H - k_{32b}\theta_{GVL}$$

$$r_{33} = k_{33f}\theta_{09} - k_{33b}\theta_{GVL}\theta_*$$

$$r_{34} = k_{34f}\theta_{LA}{\theta_*}^2 - k_{34b}\theta_{10}\theta_{OH}$$

$$r_{35} = k_{35f}\theta_{LA}{\theta_*}^2 - k_{35b}\theta_{11}\theta_H$$

$$r_{36} = k_{36f}\theta_{10} - k_{36b}\theta_{15}{\theta_*}^2$$

$$r_{37} = k_{37f}\theta_{10}\theta_H - k_{37b}\theta_{06}\theta_*$$

$$r_{38} = k_{38f}\theta_{11}\theta_H - k_{38b}\theta_{12}\theta_*$$

$$r_{39} = k_{39f}\theta_{12} - k_{39b}\theta_{17}\theta_*$$

$$r_{40} = k_{40f}\theta_{GVL} - k_{40b}P_{GVL}{\theta_*}^2$$

$$r_{41} = k_{41f}\theta_H\theta_{OH} - k_{41b}\theta_{H_2O}\theta_\Delta$$

$$r_{42} = k_{42f}\theta_{H_2O} - k_{42b}\theta_* P_{H_2O}$$

$$r_{43} = k_{43f}\theta_{OH}\theta_* - k_{43b}\theta_H\theta_O$$

$$r_{44} = k_{44f}\theta_{HPA} - k_{44b}P_{HPA}{\theta_*}^3$$

Species balance equations for all surface species and the overall mass balance lead to:

$$\frac{d\theta_{LA}}{dt} = r_1 - r_3 - r_4 - r_{34} - r_{35}$$

$$\frac{d\theta_{Al}}{dt} = r_3 - r_5 - r_{14} - r_{16} - r_{17}$$

$$\frac{d\theta_{Hy}}{dt} = r_4 - r_6 - r_{18} - r_{19}$$

$$\frac{d\theta_{HPA}}{dt} = r_5 + r_6 - r_7 - r_8 - r_{10} - r_{44}$$

$$\frac{d\theta_{01}}{dt} = r_7 - r_{11} - r_{12}$$

$$\frac{d\theta_{02}}{dt} = r_8 - r_{13} - r_{15}$$

$$\frac{d\theta_{03}}{dt} = r_{10} - r_{20} - r_{21}$$

$$\frac{d\theta_{04}}{dt} = r_{12} + r_{13} - r_{22}$$

$$\frac{d\theta_{05}}{dt} = r_{15} + r_{16} - r_{23}$$

$$\frac{d\theta_{06}}{dt} = r_{11} + r_{14} - r_{30} + r_{37}$$

$$\frac{d\theta_{07}}{dt} = r_{22} + r_{23} - r_{24}$$

$$\frac{d\theta_{08}}{dt} = r_{20} + r_{24} - r_{31} + r_{29}$$

$$\frac{d\theta_{09}}{dt} = r_{21} - r_{33}$$

$$\frac{d\theta_{10}}{dt} = r_{34} - r_{36} - r_{37}$$

$$\frac{d\theta_{11}}{dt} = r_{35} - r_{38}$$

$$\frac{d\theta_{12}}{dt} = r_{38} - r_{39}$$

$$\frac{d\theta_{13}}{dt} = r_{19} - r_{27}$$

$$\frac{d\theta_{14}}{dt} = r_{18} - r_{26}$$

$$\frac{d\theta_{15}}{dt} = r_{28} - r_{32} + r_{36}$$

$$\frac{d\theta_{16}}{dt} = r_{26} + r_{27} - r_{28} - r_{29}$$

$$\frac{d\theta_{17}}{dt} = r_{39} - r_{9}$$

$$\frac{d\theta_{18}}{dt} = r_{9} + r_{17} - r_{25}$$

$$\frac{d\theta_{GVL}}{dt} = r_{25} + r_{30} + r_{31} + r_{32} + r_{33} - r_{40}$$

$$\frac{d\theta_{H}}{dt} = 2r_{2} - r_{3} - r_{4} - r_{5} - r_{6} - r_{8} - r_{9} + r_{11} - r_{12} + r_{15} - r_{16} + r_{21} + r_{22} + r_{28} - r_{29} + r_{31} - r_{32} + r_{35} - r_{37} - r_{38} - r_{41} + r_{43}$$

$$\frac{d\theta_{OH}}{dt} = r_{7} + r_{10} + r_{13} + r_{14} + r_{18} + r_{23} + r_{25} + r_{27} + r_{34} - r_{41} - r_{43}$$

$$\frac{d\theta_{H_2O}}{dt} = r_{41} - r_{42}$$

$$\frac{d\theta_{O}}{dt} = r_{43}$$

And $2\theta_{LA} + 3\theta_{HPA} + 2\theta_{Al} + 2\theta_{Hy} + 3\theta_{01} + 2\theta_{02} + 2\theta_{03} + \theta_{04} + 2\theta_{05}$

$$+ 3\theta_{06} + 2\theta_{07} + 2\theta_{08} + 3\theta_{09} + 3\theta_{10} + 3\theta_{11}$$

$$+ 3\theta_{12} + \theta_{13} + \theta_{14} + \theta_{15} + 2\theta_{16} + 2\theta_{17} + \theta_{18}$$

$$+ 2\theta_{GVL} + \theta_H + \theta_{OH} + \theta_O + \theta_{H_2O} + \theta_* = 1.00$$

For the 2-*site model*, we used the following set of elementary reactions and differential surface species balances.

$$r_1 = k_{1f} P_{LA} \theta_*^2 - k_{1b} \theta_{LA}$$

$$r_2 = k_{2f} P_{H_2} \theta_\Delta^2 - k_{2b} {\theta_H}^2$$

$$r_3 = k_{3f} \theta_{LA} \theta_H - k_{3b} \theta_{Al} \theta_\Delta$$

$$r_4 = k_{4f} \theta_{LA} \theta_H - k_{4b} \theta_{Hy} \theta_\Delta$$

$$r_5 = k_{5f} \theta_{Al} \theta_H \theta_* - k_{5b} \theta_{HPA} \theta_\Delta$$

$$r_6 = k_{6f} \theta_{Hy} \theta_H \theta_* - k_{6b} \theta_{HPA} \theta_\Delta$$

$$r_7 = k_{7f} \theta_{HPA} \theta_* - k_{7b} \theta_{01} \theta_{OH}$$

$$r_8 = k_{8f} \theta_{HPA} \theta_H - k_{8b} \theta_{02} \theta_* \theta_\Delta$$

$$r_9 = k_{9f} \theta_{17} \theta_H - k_{9b} \theta_{18} \theta_* \theta_\Delta$$

$$r_{10} = k_{10f} \theta_{HPA} - k_{10b} \theta_{03} \theta_{OH}$$

$$r_{11} = k_{11f} \theta_{01} \theta_\Delta - k_{11b} \theta_{06} \theta_H$$

$$r_{12} = k_{12f} \theta_{01} \theta_H - k_{12b} \theta_{04} {\theta_*}^2 \theta_\Delta$$

$$r_{13} = k_{13f} \theta_{02} - k_{13b} \theta_{04} \theta_{OH}$$

$$r_{14} = k_{14f} \theta_{Al} {\theta_*}^2 - k_{14b} \theta_{06} \theta_{OH}$$

$$r_{15} = k_{15f} \theta_{02} \theta_\Delta - k_{15b} \theta_{05} \theta_H$$

$$r_{16} = k_{16f} \theta_{Al} \theta_H - k_{16b} \theta_{05} \theta_\Delta$$

$$r_{17} = k_{17f}\theta_{Al} - k_{17b}\theta_{18}\theta_{*}$$

$$r_{18} = k_{18f}\theta_{Hy} - k_{18b}\theta_{14}\theta_{OH}$$

$$r_{19} = k_{19f}\theta_{Hy} - k_{19b}\theta_{13}\theta_{*}$$

$$r_{20} = k_{20f}\theta_{03} - k_{20b}\theta_{08}$$

$$r_{21} = k_{21f}\theta_{03}\theta_{*}\theta_{\Delta} - k_{21b}\theta_{09}\theta_{H}$$

$$r_{22} = k_{22f}\theta_{04}\theta_{*}\theta_{\Delta} - k_{22b}\theta_{07}\theta_{H}$$

$$r_{23} = k_{23f}\theta_{05}\theta_{*} - k_{23b}\theta_{07}\theta_{OH}$$

$$r_{24} = k_{24f}\theta_{07} - k_{24b}\theta_{08}$$

$$r_{25} = k_{25f}\theta_{18}{\theta_{*}}^{2} - k_{25b}\theta_{GVL}\theta_{OH}$$

$$r_{26} = k_{26f}\theta_{14}\theta_{*} - k_{26b}\theta_{16}$$

$$r_{27} = k_{27f}\theta_{13}{\theta_{*}}^{2} - k_{27b}\theta_{16}\theta_{OH}$$

$$r_{28} = k_{28f}\theta_{16}\theta_{\Delta} - k_{28b}\theta_{15}\theta_{H}\theta_{*}$$

$$r_{29} = k_{29f}\theta_{16}\theta_{H} - k_{29b}\theta_{08}\theta_{\Delta}$$

$$r_{30} = k_{30f}\theta_{06} - k_{30b}\theta_{GVL}\theta_{*}$$

$$r_{31} = k_{31f}\theta_{08}\theta_{\Delta} - k_{31b}\theta_{GVL}\theta_{H}$$

$$r_{32} = k_{32f}\theta_{15}\theta_{H}\theta_{*} - k_{32b}\theta_{GVL}\theta_{\Delta}$$

$$r_{33} = k_{33f}\theta_{09} - k_{33b}\theta_{GVL}\theta_{*}$$

$$r_{34} = k_{34f}\theta_{LA}{\theta_{*}}^{2} - k_{34b}\theta_{10}\theta_{OH}$$

$$r_{35} = k_{35f}\theta_{LA}\theta_{*}\theta_{\Delta} - k_{35b}\theta_{11}\theta_{H}$$

$$r_{36} = k_{36f}\theta_{10} - k_{36b}\theta_{15}{\theta_{*}}^{2}$$

$$r_{37} = k_{37f}\theta_{10}\theta_{H} - k_{37b}\theta_{06}\theta_{\Delta}$$

$$r_{38} = k_{38f}\theta_{11}\theta_H - k_{38b}\theta_{12}\theta_\Delta$$

$$r_{39} = k_{39f}\theta_{12} - k_{39b}\theta_{17}\theta_*$$

$$r_{40} = k_{40f}\theta_{GVL} - k_{40b}P_{GVL}{\theta_*}^2$$

$$r_{41} = k_{41f}\theta_H\theta_{OH} - k_{41b}\theta_{H_2O}\theta_\Delta$$

$$r_{42} = k_{42f}\theta_{H_2O} - k_{42b}\theta_* P_{H_2O}$$

$$r_{43} = k_{43f}\theta_{OH}\theta_\Delta - k_{43b}\theta_H\theta_O$$

$$r_{44} = k_{44f}\theta_{HPA} - k_{44b}P_{HPA}{\theta_*}^3$$

Species balance equations for all surface species and the overall mass balance lead to:

$$\frac{d\theta_{LA}}{dt} = r_1 - r_3 - r_4 - r_{34} - r_{35}$$

$$\frac{d\theta_{Al}}{dt} = r_3 - r_5 - r_{14} - r_{16} - r_{17}$$

$$\frac{d\theta_{Hy}}{dt} = r_4 - r_6 - r_{18} - r_{19}$$

$$\frac{d\theta_{HPA}}{dt} = r_5 + r_6 - r_7 - r_8 - r_{10} - r_{44}$$

$$\frac{d\theta_{01}}{dt} = r_7 - r_{11} - r_{12}$$

$$\frac{d\theta_{02}}{dt} = r_8 - r_{13} - r_{15}$$

$$\frac{d\theta_{03}}{dt} = r_{10} - r_{20} - r_{21}$$

$$\frac{d\theta_{04}}{dt} = r_{12} + r_{13} - r_{22}$$

$$\frac{d\theta_{05}}{dt} = r_{15} + r_{16} - r_{23}$$

$$\frac{d\theta_{06}}{dt} = r_{11} + r_{14} - r_{30} + r_{37}$$

$$\frac{d\theta_{07}}{dt} = r_{22} + r_{23} - r_{24}$$

$$\frac{d\theta_{08}}{dt} = r_{20} + r_{24} - r_{31} + r_{29}$$

$$\frac{d\theta_{09}}{dt} = r_{21} - r_{33}$$

$$\frac{d\theta_{10}}{dt} = r_{34} - r_{36} - r_{37}$$

$$\frac{d\theta_{11}}{dt} = r_{35} - r_{38}$$

$$\frac{d\theta_{12}}{dt} = r_{38} - r_{39}$$

$$\frac{d\theta_{13}}{dt} = r_{19} - r_{27}$$

$$\frac{d\theta_{14}}{dt} = r_{18} - r_{26}$$

$$\frac{d\theta_{15}}{dt} = r_{28} - r_{32} + r_{36}$$

$$\frac{d\theta_{16}}{dt} = r_{26} + r_{27} - r_{28} - r_{29}$$

$$\frac{d\theta_{17}}{dt} = r_{39} - r_{9}$$

$$\frac{d\theta_{18}}{dt} = r_{9} + r_{17} - r_{25}$$

$$\frac{d\theta_{GVL}}{dt} = r_{25} + r_{30} + r_{31} + r_{32} + r_{33} - r_{40}$$

$$\frac{d\theta_{H}}{dt} = 2r_{2} - r_{3} - r_{4} - r_{5} - r_{6} - r_{8} - r_{9} + r_{11} - r_{12} + r_{15} - r_{16} + r_{21} + r_{22} + r_{28} - r_{29} + r_{31} - r_{32} + r_{35} - r_{37} - r_{38} - r_{41} + r_{43}$$

$$\frac{d\theta_{OH}}{dt} = r_{7} + r_{10} + r_{13} + r_{14} + r_{18} + r_{23} + r_{25} + r_{27} + r_{34} - r_{41} - r_{43}$$

$$\frac{d\theta_{H_2O}}{dt} = r_{41} - r_{42}$$

$$\frac{d\theta_O}{dt} = r_{43}$$

$$2\theta_{LA} + 3\theta_{HPA} + 2\theta_{Al} + 2\theta_{Hy} + 3\theta_{01} + 2\theta_{02} + 2\theta_{03} + \theta_{04} + 2\theta_{05} + 3\theta_{06} + 2\theta_{07} + 2\theta_{08} + 3\theta_{09} + 3\theta_{10} + 3\theta_{11} + 3\theta_{12} + \theta_{13} + \theta_{14} + \theta_{15} + 2\theta_{16} + 2\theta_{17} + \theta_{18} + 2\theta_{GVL} + \theta_{OH} + \theta_O + \theta_{H_2O} + \theta_* = 1.00$$

and $$\theta_H + \theta_\Delta = 1.00$$

A.6 Lateral interaction parameter estimation for hydrogen and oxygen on Ru (0001)

(A) Hydrogen lateral interaction estimation data

Coverage	Average energy (eV)	Integral energy (DFT)	Fitted integral energy
0.065	-0.67944	-0.04246	-0.04218
0.125	-0.67348	-0.08419	-0.08493
0.187	-0.67458	-0.12648	-0.12707
0.250	-0.67928	-0.16982	-0.16861
0.500	-0.65578	-0.32789	-0.32874
0.750	-0.63972	-0.47979	-0.4792
1.00	-0.61982	-0.61982	-0.61999

(B) Oxygen lateral interaction estimation data

Coverage	Average energy (eV)	Integral energy (DFT)	Fitted integral energy
0.065	-2.99468	-0.18717	-0.18693
0.125	-2.97661	-0.37208	-0.37188
0.187	-2.95635	-0.55432	-0.54897
0.250	-2.9289	-0.73223	-0.71818
0.500	-2.61431	-1.30715	-1.31628
0.750	-2.3815	-1.78613	-1.7884
1.00	-2.13709	-2.13709	-2.13454

$$E_{avg} = \frac{(E_{metal+adsorbate} - E_{slab} - \frac{n}{2}E_{H_2})}{n}$$

where n is the number of adsorbed hydrogen atoms. The integral energy (DFT) is calculated as

$$E_{DFT}^{integral} = E_{avg} \times \theta_H$$

and the fitted integral energy is calculated as (where E_0 is the low coverage adsorption energy and ε and $\theta_{H,0}$ are fitting parameters)[15]

$$E_{DFT}^{fitted} = E_0 \times \theta_H + \varepsilon(\theta_H - \theta_{H,0})^2$$

$$Error = E_{DFT}^{integral} - E_{DFT}^{fitted}$$

The sum of the square of the error was minimized to find the parameters of this two parameter model (E_0 is taken to be equal to the adsorption energy at 1/16 ML).

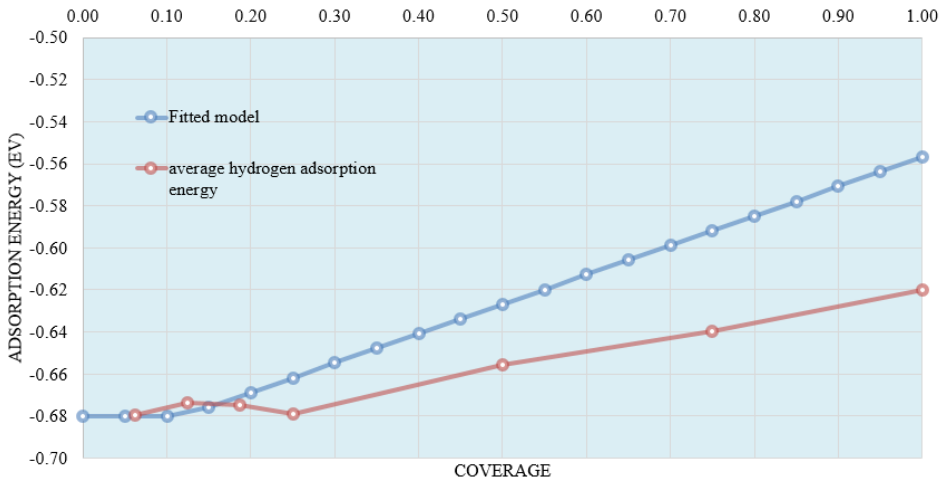

(A)

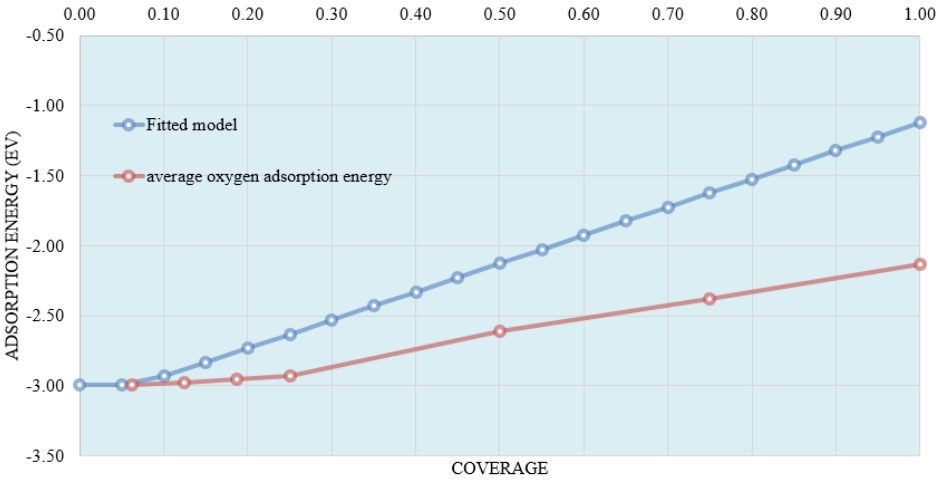

(B)

Figure A.6: Coverage dependent adsorption energy calculated using a two parameter lateral interaction model for (A) hydrogen and (B) oxygen.

A.7 Rates of all elementary reaction (s^{-1}) at various reaction temperatures

Table A.3: rates of all elementary reaction (s^{-1}) at various reaction temperatures

(A) 1 site microkinetic model

Reaction step	Temperature (K)				
	323	373	423	473	523
r_1	2.67E-09	1.83E-05	4.09E-03	1.05E-01	8.99E-01
r_2	2.67E-09	1.83E-05	4.09E-03	1.05E-01	8.99E-01
r_3	2.67E-09	1.83E-05	4.09E-03	1.05E-01	8.99E-01
r_4	1.04E-19	2.03E-14	5.66E-11	1.03E-08	3.99E-07
r_5	1.02E-19	5.27E-16	-7.67E-12	9.76E-10	2.03E-07
r_6	9.82E-20	1.89E-14	5.11E-11	8.98E-09	3.38E-07
r_7	2.00E-19	1.94E-14	4.32E-11	9.75E-09	5.14E-07
r_8	7.48E-27	6.88E-21	4.28E-17	1.41E-14	9.87E-13
r_9	-2.55E-23	-2.48E-17	-8.71E-14	-1.32E-11	4.39E-10
r_{10}	1.95E-26	1.60E-20	1.01E-16	3.47E-14	2.50E-12
r_{11}	2.00E-19	1.94E-14	4.32E-11	9.75E-09	5.14E-07
r_{12}	2.77E-24	6.53E-19	2.46E-15	1.08E-12	1.31E-10
r_{13}	9.65E-24	1.40E-18	2.94E-15	4.65E-13	1.88E-11
r_{14}	2.07E-13	4.95E-09	2.82E-06	2.73E-04	8.69E-03
r_{15}	-9.65E-24	-1.40E-18	-2.89E-15	-4.51E-13	-1.78E-11
r_{16}	9.65E-24	1.40E-18	2.91E-15	4.57E-13	1.83E-11
r_{17}	2.67E-09	1.83E-05	4.08E-03	1.05E-01	8.91E-01
r_{18}	5.38E-21	1.45E-15	5.45E-12	1.28E-09	6.09E-08
r_{19}	2.63E-28	1.16E-21	2.74E-17	2.65E-14	4.36E-12
r_{20}	1.45E-16	5.38E-12	3.10E-09	1.52E-07	2.20E-06
r_{21}	-1.45E-16	-5.38E-12	-3.10E-09	-1.52E-07	-2.20E-06
r_{22}	2.77E-24	3.94E-19	4.95E-15	1.55E-12	1.50E-10
r_{23}	1.90E-27	1.96E-21	1.42E-17	5.80E-15	5.46E-13
r_{24}	2.77E-24	3.95E-19	4.96E-15	1.55E-12	1.50E-10
r_{25}	2.67E-09	1.83E-05	4.08E-03	1.05E-01	8.91E-01
r_{26}	5.37E-21	1.45E-15	5.45E-12	1.28E-09	6.09E-08
r_{27}	2.63E-28	1.16E-21	2.74E-17	2.65E-14	4.36E-12
r_{28}	1.45E-16	5.38E-12	3.10E-09	1.53E-07	2.26E-06
r_{29}	-1.45E-16	-5.38E-12	-3.10E-09	-1.52E-07	-2.20E-06
r_{30}	2.05E-13	4.79E-09	2.64E-06	2.45E-04	7.45E-03
r_{31}	-5.99E-22	-3.96E-17	-4.79E-14	-4.50E-12	-9.62E-11
r_{32}	2.11E-15	1.69E-10	1.85E-07	2.79E-05	1.24E-03
r_{33}	-1.45E-16	-5.38E-12	-3.10E-09	-1.52E-07	-2.20E-06
r_{34}	1.11E-21	1.87E-15	1.61E-11	6.93E-09	7.18E-07
r_{35}	-2.55E-23	-2.49E-17	-8.71E-14	-1.32E-11	4.39E-10

r_{36}	1.97E-15	1.63E-10	1.82E-07	2.78E-05	1.24E-03
r_{37}	-1.97E-15	-1.63E-10	-1.82E-07	-2.78E-05	-1.24E-03
r_{38}	-2.17E-19	-8.88E-16	-1.14E-13	-1.27E-11	4.29E-10
r_{39}	-2.55E-23	-2.48E-17	-8.71E-14	-1.32E-11	4.39E-10
r_{40}	2.67E-09	1.83E-05	4.09E-03	1.05E-01	8.99E-01
r_{41}	2.67E-09	1.83E-05	4.09E-03	1.05E-01	8.99E-01
r_{42}	2.67E-09	1.83E-05	4.09E-03	1.05E-01	8.99E-01
r_{43}	-3.52E-24	3.05E-20	-2.08E-17	-4.44E-16	-4.44E-15
r_{44}	4.30E-24	1.51E-17	2.76E-13	2.05E-10	2.65E-08

(B) 2 site microkinetic model

Reaction step	Temperature (K)				
	323	373	423	473	523
r_1	1.94E-06	4.33E-04	1.94E-02	2.90E-01	2.08E+00
r_2	1.94E-06	4.33E-04	1.94E-02	2.90E-01	2.08E+00
r_3	1.94E-06	4.33E-04	1.94E-02	2.90E-01	2.08E+00
r_4	4.90E-17	2.06E-13	7.45E-11	5.42E-09	1.36E-07
r_5	9.40E-24	1.66E-18	1.60E-14	1.77E-11	3.10E-09
r_6	3.55E-20	2.69E-16	1.83E-13	2.89E-11	1.67E-09
r_7	-1.43E-18	-4.84E-15	-1.52E-12	-1.90E-10	-6.67E-09
r_8	2.41E-23	5.93E-20	7.60E-17	1.39E-14	4.20E-13
r_9	-8.11E-18	-8.28E-15	-6.61E-13	-3.81E-11	-3.62E-09
r_{10}	6.41E-23	1.45E-19	1.75E-16	3.14E-14	1.02E-12
r_{11}	-1.43E-18	-4.84E-15	-1.53E-12	-1.92E-10	-6.93E-09
r_{12}	4.62E-22	1.41E-18	3.72E-15	2.17E-12	2.64E-10
r_{13}	1.14E-21	2.59E-18	2.84E-15	4.67E-13	1.87E-11
r_{14}	3.02E-11	3.94E-08	1.09E-05	9.54E-04	2.69E-02
r_{15}	-1.12E-21	-2.53E-18	-2.77E-15	-4.53E-13	-1.83E-11
r_{16}	1.13E-21	2.55E-18	2.79E-15	4.61E-13	1.89E-11
r_{17}	1.94E-06	4.33E-04	1.93E-02	2.90E-01	2.05E+00
r_{18}	4.90E-17	2.06E-13	7.43E-11	5.40E-09	1.34E-07
r_{19}	6.48E-23	8.28E-19	8.36E-16	1.79E-13	1.33E-11
r_{20}	2.71E-14	3.27E-12	1.15E-10	2.00E-09	2.07E-08
r_{21}	-2.71E-14	-3.27E-12	-1.15E-10	-2.00E-09	-2.07E-08
r_{22}	1.61E-21	4.01E-18	6.57E-15	2.64E-12	2.83E-10
r_{23}	5.96E-24	1.72E-20	2.71E-17	7.81E-15	6.20E-13
r_{24}	1.61E-21	4.03E-18	6.59E-15	2.64E-12	2.84E-10
r_{25}	1.94E-06	4.33E-04	1.93E-02	2.90E-01	2.05E+00
r_{26}	4.90E-17	2.06E-13	7.43E-11	5.40E-09	1.34E-07
r_{27}	6.48E-23	8.28E-19	8.36E-16	1.79E-13	1.33E-11
r_{28}	2.72E-14	3.48E-12	1.90E-10	7.40E-09	1.55E-07
r_{29}	-2.71E-14	-3.27E-12	-1.15E-10	-2.00E-09	-2.10E-08

r_{30}	3.02E-11	3.94E-08	1.09E-05	9.54E-04	2.69E-02
r_{31}	-4.03E-21	-4.72E-18	-7.82E-16	-3.88E-14	-6.23E-13
r_{32}	5.21E-18	2.13E-13	7.34E-10	3.60E-07	3.30E-05
r_{33}	-2.71E-14	-3.27E-12	-1.15E-10	-2.00E-09	-2.07E-08
r_{34}	5.86E-16	1.03E-12	3.29E-10	4.08E-08	2.52E-06
r_{35}	-8.11E-18	-8.28E-15	-6.61E-13	-3.81E-11	-3.62E-09
r_{36}	-2.71E-14	-3.26E-12	5.44E-10	3.53E-07	3.29E-05
r_{37}	2.77E-14	4.29E-12	-2.15E-10	-3.12E-07	-3.04E-05
r_{38}	-8.24E-18	-8.29E-15	-6.61E-13	-3.81E-11	-3.62E-09
r_{39}	-8.11E-18	-8.28E-15	-6.61E-13	-3.81E-11	-3.62E-09
r_{40}	1.94E-06	4.33E-04	1.94E-02	2.90E-01	2.08E+00
r_{41}	1.94E-06	4.33E-04	1.94E-02	2.90E-01	2.08E+00
r_{42}	1.94E-06	4.33E-04	1.94E-02	2.90E-01	2.08E+00
r_{43}	-1.59E-21	-1.08E-19	2.08E-17	4.44E-16	-1.78E-15
r_{44}	1.47E-18	5.11E-15	1.72E-12	2.36E-10	1.14E-08

A.8 Surface coverage of all adsorbed surface species at various reaction temperatures

Table A.4: surface coverage of all adsorbed surface species at various reaction temperatures

(A) 1 site microkinetic model

Adsorbed species	Temperature (K)				
	323	373	423	473	523
I-1	1.40E-13	1.59E-11	1.94E-10	9.54E-10	3.11E-09
I-2	7.03E-24	2.75E-20	7.16E-18	5.23E-17	1.02E-16
I-3	3.53E-16	2.99E-13	1.00E-11	5.24E-11	1.01E-10
I-4	5.62E-12	1.00E-10	1.21E-09	2.12E-09	2.34E-09
I-5	2.03E-22	3.68E-19	2.95E-17	3.53E-16	1.68E-15
I-6	3.74E-06	7.76E-05	2.02E-04	2.87E-04	3.78E-04
I-7	8.34E-17	3.41E-14	2.63E-12	1.84E-11	7.68E-11
I-8	4.70E-21	1.29E-17	1.06E-15	1.16E-14	4.89E-14
I-9	2.47E-09	1.33E-07	5.61E-07	6.27E-07	4.94E-07
I-10	1.46E-13	7.20E-11	1.68E-09	1.33E-08	7.85E-08
I-11	1.36E-05	2.74E-03	2.52E-02	5.02E-02	6.62E-02
I-12	9.30E-13	1.49E-09	6.23E-08	3.91E-07	1.31E-06
I-13	2.28E-16	6.72E-14	1.83E-12	9.11E-12	1.69E-11
I-14	1.39E-08	5.15E-07	2.16E-06	2.36E-06	1.41E-06
I-15	1.07E-09	2.91E-08	1.12E-07	1.84E-07	3.96E-07
I-16	9.39E-18	9.03E-15	3.35E-13	1.94E-12	4.95E-12
I-17	7.95E-22	5.45E-18	7.37E-16	1.27E-14	9.84E-14
I-18	2.22E-09	6.27E-08	2.21E-07	2.30E-07	1.50E-07
LA	2.25E-11	5.75E-09	1.10E-07	4.15E-07	7.47E-07

Al	1.25E-23	7.51E-20	1.10E-17	1.92E-16	1.21E-15
Hy	1.68E-11	2.43E-09	2.20E-08	4.58E-08	5.81E-08
HPA	1.08E-20	4.44E-17	6.72E-15	1.24E-13	7.41E-13
H	1.00E+00	9.91E-01	9.23E-01	8.46E-01	7.97E-01
OH	2.17E-06	8.94E-05	5.42E-04	8.48E-04	6.80E-04
GVL	6.56E-12	3.20E-10	1.69E-09	2.37E-09	2.02E-09
Free sites	1.47E-06	2.05E-05	1.12E-04	4.09E-04	1.30E-03
H_2O	1.45E-12	4.92E-11	3.25E-10	1.01E-09	2.46E-09
O	1.94E-06	7.35E-05	4.69E-04	1.15E-03	1.65E-03

Note: All reported numbers are the surface coverage over the number of adsorption sites.

(B) 2 site microkinetic model

Adsorbed species	Temperature (K)				
	323	373	423	473	523
I-1	2.47E-09	1.36E-09	1.02E-09	2.14E-09	5.67E-09
I-2	1.46E-16	3.18E-16	2.51E-16	1.19E-16	7.67E-17
I-3	1.36E-09	1.40E-09	1.06E-09	6.63E-10	3.77E-10
I-4	1.61E-07	5.17E-08	1.35E-08	3.63E-09	1.87E-09
I-5	2.51E-18	2.57E-17	8.97E-17	3.62E-16	1.43E-15
I-6	6.62E-02	6.91E-03	1.47E-03	1.14E-03	1.35E-03
I-7	6.44E-11	8.97E-11	8.77E-11	8.86E-11	1.67E-10
I-8	2.19E-14	7.62E-14	1.45E-13	1.88E-13	1.92E-13
I-9	4.84E-05	1.53E-05	5.76E-06	2.76E-06	1.58E-06
I-10	2.60E-09	6.71E-09	1.70E-08	9.44E-08	5.54E-07
I-11	2.66E-01	3.26E-01	3.31E-01	3.31E-01	3.31E-01
I-12	4.91E-07	8.25E-07	1.27E-06	2.30E-06	4.60E-06
I-13	7.69E-14	1.96E-12	1.15E-11	2.41E-11	2.71E-11
I-14	9.71E-08	6.78E-08	5.65E-08	6.10E-08	5.60E-08
I-15	2.90E-08	1.50E-07	4.37E-07	1.55E-06	4.04E-06
I-16	1.76E-15	5.78E-15	1.89E-14	7.92E-14	2.71E-13
I-17	9.85E-18	4.16E-16	4.32E-15	4.10E-14	3.22E-13
I-18	1.01E-06	9.42E-07	4.32E-07	2.64E-07	1.81E-07
LA	1.64E-08	1.35E-07	4.80E-07	9.74E-07	1.38E-06
Al	4.25E-18	2.55E-17	6.88E-17	2.21E-16	5.20E-16
Hy	2.07E-07	1.77E-07	9.27E-08	8.34E-08	9.71E-08
HPA	9.88E-17	6.30E-15	9.13E-14	5.19E-13	1.63E-12
H	1.00E+00	1.00E+00	1.00E+00	9.99E-01	9.97E-01
OH	1.57E-03	2.00E-03	1.71E-03	1.12E-03	6.38E-04
GVL	4.77E-09	7.55E-09	8.00E-09	6.56E-09	4.65E-09
Free sites (*)	3.97E-05	9.95E-05	2.43E-04	6.48E-04	1.79E-03
H_2O	3.96E-11	2.46E-10	7.27E-10	1.66E-09	3.51E-09
O	2.12E-04	3.82E-04	5.18E-04	5.86E-04	5.93E-04

Free sites (Δ)	1.48E-06	2.16E-05	1.69E-04	8.58E-04	3.18E-03

A.9 Kinetic degree of rate control of key transition states at 423 k

Table A.5: kinetic degree of rate control of key transition states at 423 k

Step	**KRC** (1 site microkinetic model)	**KRC** (2 site microkinetic model)
r_1	5.30E-01	2.61E-01
r_3	4.66E-01	7.32E-01
r_{25}	1.42E-03	1.18E-03
r_{40}	1.52E-03	3.14E-03
r_{41}	8.60E-04	3.07E-03

A.10 Bibliography

1. Serrano-Ruiz, J. C.; West, R. M.; Dumesic, J. A., *Annu. Rev. Chem. Biomol. Eng.* **2010,** *1*, 79-100.
2. Bronsted, J. N., *Chem. Rev.* **1928,** *5*, 231-338.
3. Evans, M. G.; Polanyi, M., *Trans. Faraday Soc.* **1938,** *34*, 11-24.
4. Stamatakis, M.; Vlachos, D. G., *ACS Catal.* **2012,** *2*, 2648-2663.
5. Newns, D. M., *Phys. Rev.* **1969,** *178*, 1123-1135.
6. Anderson, P. W., *Phys. Rev.* **1961,** *124*, 41-53.
7. Liu, Z. H.; Hu, P.; Liu, Z. H.; Hu, P., *J. Chem. Phys.* **2001,** *115*, 4977-4980.
8. Wang, S.; Vorotnikov, V.; Sutton, J. E.; Vlachos, D. G., *ACS Catal.* **2014,** *4*, 604-612.
9. Abdelrahman, O. A.; Heyden, A.; Bond, J. Q., *ACS Catal.* **2014,** *4*, 1171-1181.
10. Schafer, A.; Klamt, A.; Sattel, D.; Lohrenz, J. C. W.; Eckert, F., *Phys. Chem. Chem. Phys.* **2000,** *2*, 2187-2193.
11. Ahlrichs, R.; Bär, M.; Häser, M.; Horn, H.; Kölmel, C., *Chem. Phys. Lett.* **1989,** *162*, 165-169.
12. Treutler, O.; Ahlrichs, R., *J. Chem. Phys.* **1995,** *102*, 346-354.
13. Elliott, J. R.; Lira, C. T., *Introductory Chemical Engineering Thermodynamics*. Prentice Hall PTR: 1999.
14. Nitta, T.; Shigetomi, T.; Kuro-Oka, M.; Katayama, T., *J. Chem. Eng. Jpn.* **1984,** *17*, 39-45.
15. Grabow, L.; Hvolbæk, B.; Nørskov, J., *Top. Catal.* **2010,** *53*, 298-310.

APPENDIX B : SUPPORTING INFORMATION FOR ON THE IMPORTANCE OF ANGELICAL LACTONE FORMATION IN THE HYDRODEOXYGENATION OF LEVULINIC ACID TO γ-VALEROLACTONE OVER Ru (0001) MODEL SURFACE: A DENSITY FUNCTIONAL THEORY INVESTIGATION

Mamun, O.; Saleheen, M.; Bond, J.Q.; Heyden, A.

To be submitted

B.1 PBE-D3 optimized structures

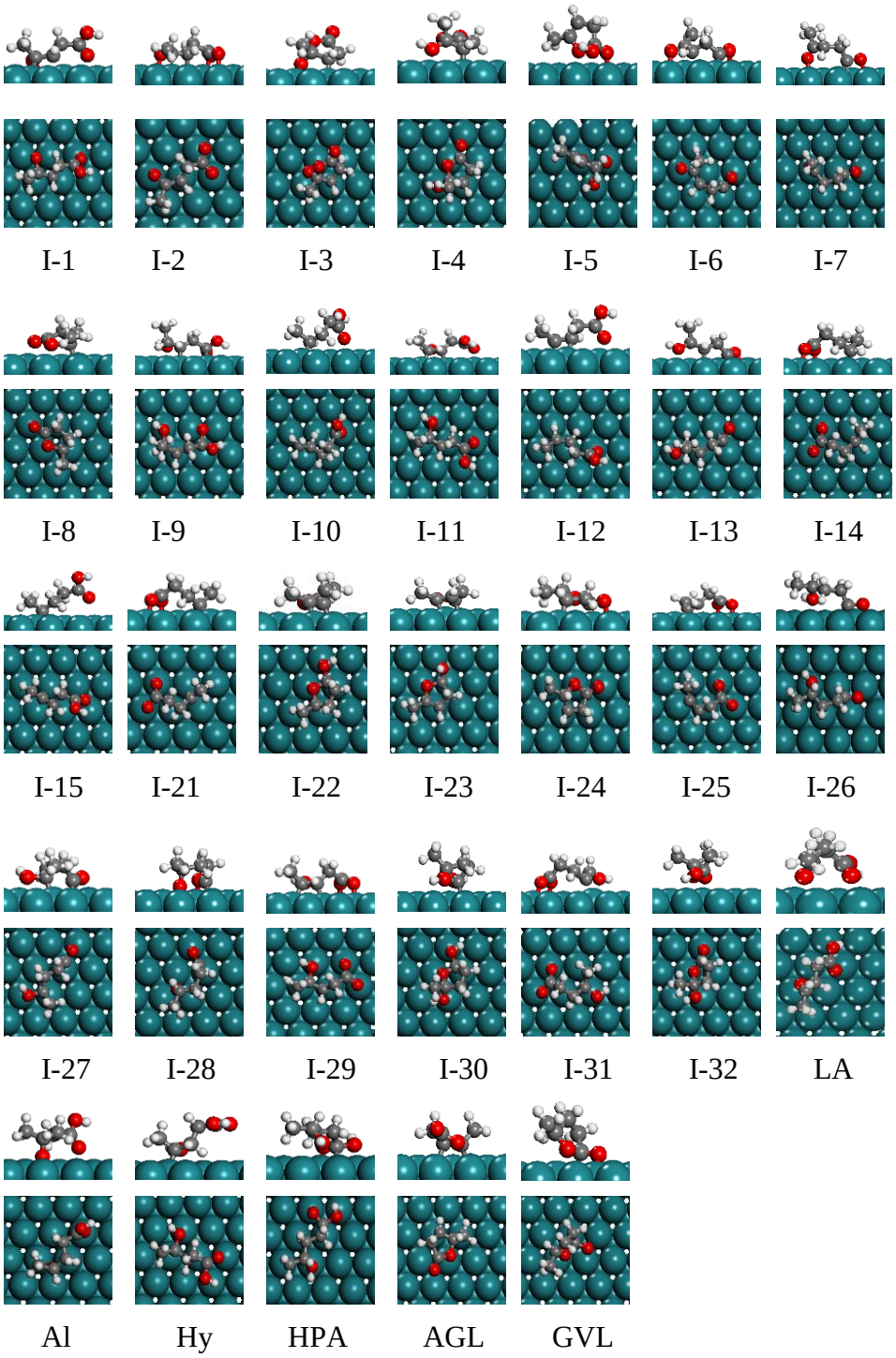

Figure B.1: PBE-D3 optimized structures of surface intermediates, reactants and products.

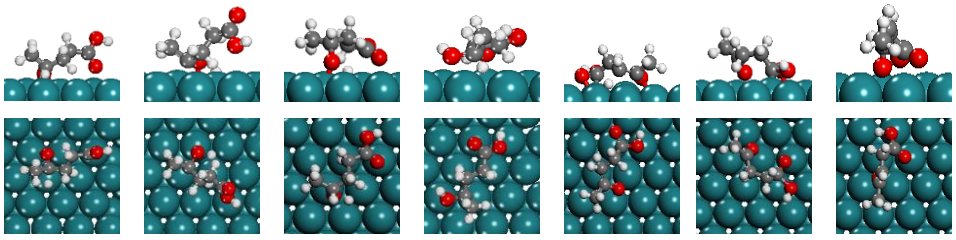

TS-3 TS-4 TS-5 TS-6 TS-7 TS-8 TS-9

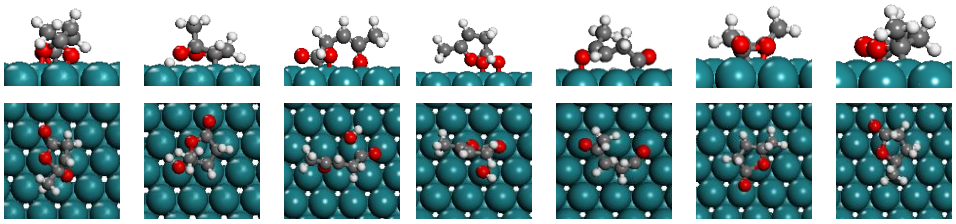

TS-10 TS-11 TS-12 TS-14 TS-15 TS-16 TS-17

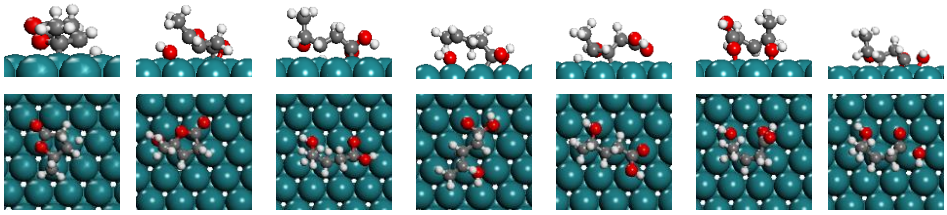

TS-18 TS-19 TS-20 TS-21 TS-22 TS-23 TS-24

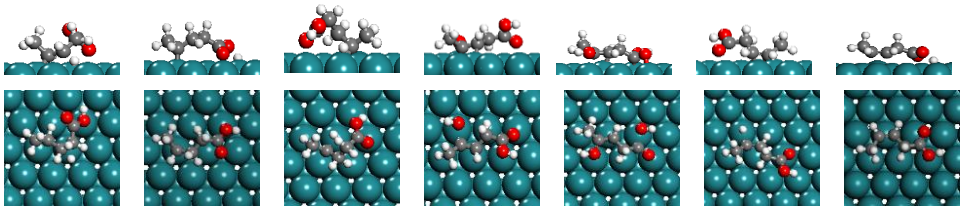

TS-25 TS-26 TS-27 TS-29 TS-30 TS-31 TS-32

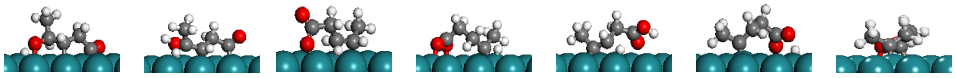

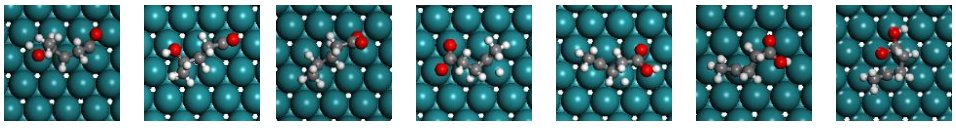

TS-33 TS-34 TS-35 TS-36 TS-37 TS-38 TS-39

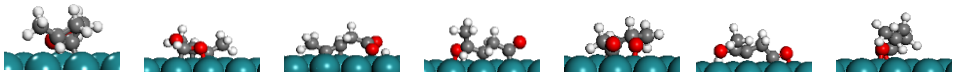

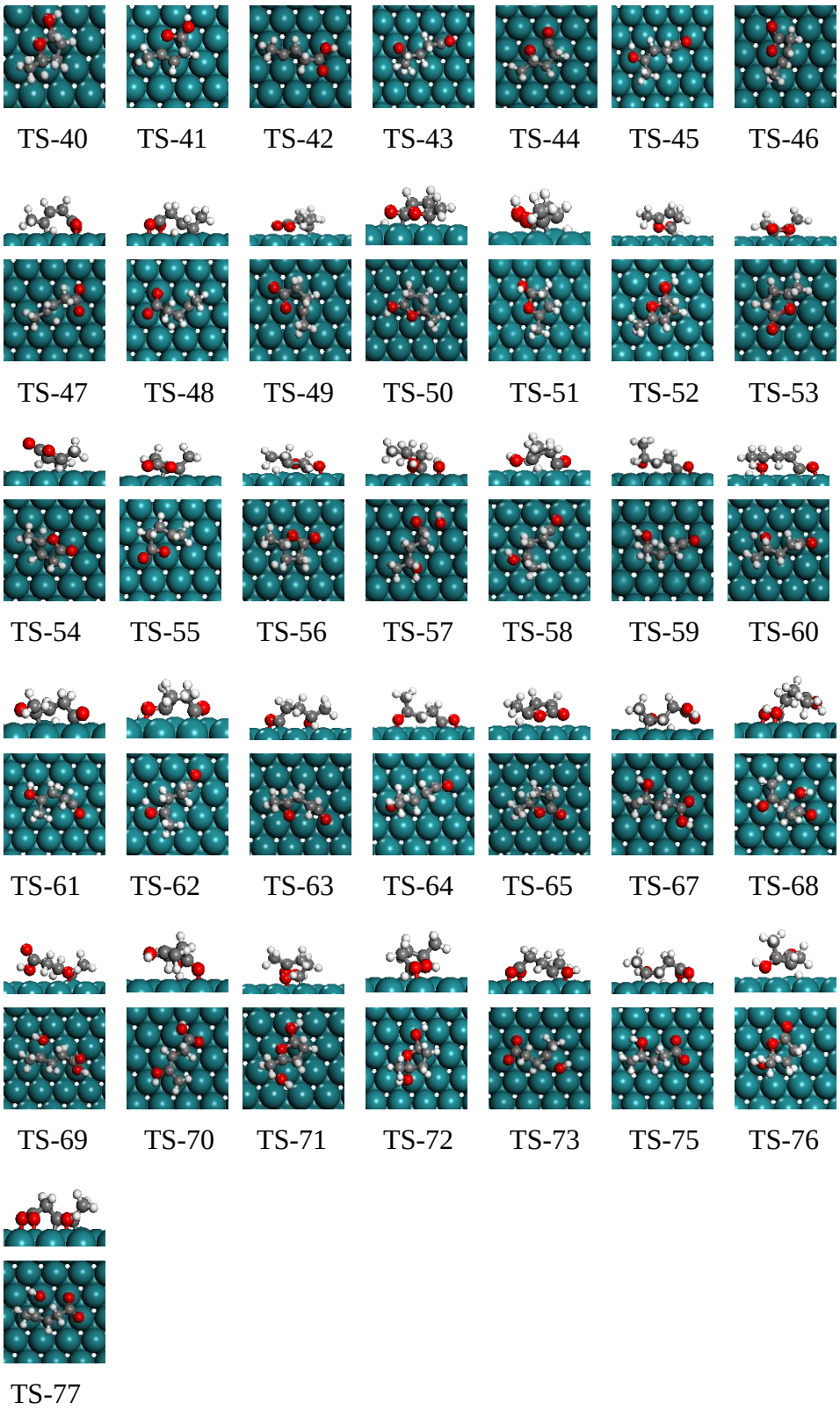

Figure B.2: PBE-D3 optimized transition state structures for various elementary reactions. The transition state number corresponds to the reaction number in Table 3.2

B.2 Development of microkinetic model

Set of elementary reactions for one site model

$$r_1 = k_{1f} P_{LA} \theta_*^2 - k_{1b} \theta_{LA}$$

$$r_2 = k_{2f} P_{H_2} \theta_*^2 - k_{2b} {\theta_H}^2$$

$$r_3 = k_{3f} \theta_{LA} \theta_H - k_{3b} \theta_{Al} \theta_*$$

$$r_4 = k_{4f} \theta_{LA} \theta_H - k_{4b} \theta_{Hy} \theta_*$$

$$r_5 = k_{5f} \theta_{Al} \theta_H - k_{5b} \theta_{HPA}$$

$$r_6 = k_{6f} \theta_{Hy} \theta_H - k_{6b} \theta_{HPA}$$

$$r_7 = k_{7f} \theta_{LA} \theta_*^2 - k_{7b} \theta_{01} \theta_H$$

$$r_8 = k_{8f} \theta_{LA} \theta_*^2 - k_{8b} \theta_{07} \theta_{OH}$$

$$r_9 = k_{9f} \theta_{01} {\theta_*}^2 - k_{9b} \theta_{02} \theta_H$$

$$r_{10} = k_{10f} \theta_{02} - k_{10b} \theta_{03} {\theta_*}^2$$

$$r_{11} = k_{11f} \theta_{03} \theta_H - k_{11b} \theta_{04} \theta_*$$

$$r_{12} = k_{12f} \theta_{01} \theta_* - k_{12b} \theta_{06} \theta_{OH}$$

$$r_{13} = k_{13f} \theta_{01} - k_{13b} \theta_{05} \theta_*$$

$$r_{14} = k_{14f} \theta_{05} \theta_* - k_{14b} \theta_{AGL} \theta_{OH}$$

$$r_{15} = k_{15f} \theta_{07} \theta_* - k_{15b} \theta_{06} \theta_H$$

$$r_{16} = k_{16f} \theta_{06} - k_{16b} \theta_{AGL} \theta_*$$

$$r_{17} = k_{17f} \theta_{07} - k_{17b} \theta_{08} \theta_*$$

$$r_{18} = k_{18f} \theta_{AGL} \theta_H - k_{18b} \theta_{08} \theta_*$$

$$r_{19} = k_{19f} \theta_{04} \theta_* - k_{19b} \theta_{AGL} \theta_{OH}$$

$$r_{20} = k_{20f}\theta_{HPA}\theta_{*} - k_{20b}\theta_{09}\theta_{H}$$

$$r_{21} = k_{21f}\theta_{HPA} - k_{21b}\theta_{10}\theta_{OH}$$

$$r_{22} = k_{22f}\theta_{09}\theta_{*} - k_{22b}\theta_{11}\theta_{H}$$

$$r_{23} = k_{23f}\theta_{09}\theta_{*} - k_{23b}\theta_{12}\theta_{OH}$$

$$r_{24} = k_{24f}\theta_{09}\theta_{*} - k_{24b}\theta_{13}\theta_{OH}$$

$$r_{25} = k_{25f}\theta_{10}\theta_{*}^{2} - k_{25b}\theta_{12}\theta_{H}$$

$$r_{26} = k_{26f}\theta_{10}\theta_{*}^{2} - k_{26b}\theta_{14}\theta_{H}$$

$$r_{27} = k_{27f}\theta_{10}\theta_{*} - k_{27b}\theta_{15}\theta_{H}$$

$$r_{28} = k_{28f}\theta_{10} - k_{28b}\theta_{16}$$

$$r_{29} = k_{29f}\theta_{11}\theta_{*} - k_{29b}\theta_{17}\theta_{OH}$$

$$r_{30} = k_{30f}\theta_{11}\theta_{*} - k_{30b}\theta_{19}\theta_{OH}$$

$$r_{31} = k_{31f}\theta_{12}\theta_{*} - k_{31b}\theta_{17}\theta_{H}$$

$$r_{32} = k_{32f}\theta_{12} - k_{32b}\theta_{20}\theta_{H}$$

$$r_{33} = k_{33f}\theta_{13}\theta_{*} - k_{33b}\theta_{18}\theta_{H}$$

$$r_{34} = k_{34f}\theta_{13}\theta_{*} - k_{34b}\theta_{19}\theta_{H}$$

$$r_{35} = k_{35f}\theta_{14} - k_{35b}\theta_{20}\theta_{H}$$

$$r_{36} = k_{36f}\theta_{14}\theta_{*} - k_{36b}\theta_{21}\theta_{H}$$

$$r_{37} = k_{37f}\theta_{15}\theta_{*}^{2} - k_{37b}\theta_{17}\theta_{H}$$

$$r_{38} = k_{38f}\theta_{15}\theta_{*}^{2} - k_{38b}\theta_{21}\theta_{H}$$

$$r_{39} = k_{39f}\theta_{15} - k_{39b}\theta_{22}$$

$$r_{40} = k_{40f}\theta_{16}\theta_{*} - k_{40b}\theta_{22}\theta_{H}$$

$$r_{41} = k_{41f}\theta_{17} - k_{41b}\theta_{23}\theta_*$$

$$r_{42} = k_{42f}\theta_{17}\theta_* - k_{42b}\theta_{25}\theta_H$$

$$r_{43} = k_{43f}\theta_{18}\theta_* - k_{43b}\theta_{06}\theta_H$$

$$r_{44} = k_{44f}\theta_{18} - k_{44b}\theta_{24}\theta_*$$

$$r_{45} = k_{45f}\theta_{19}\theta_* - k_{45b}\theta_{06}\theta_H$$

$$r_{46} = k_{46f}\theta_{20} - k_{46b}\theta_{24}$$

$$r_{47} = k_{47f}\theta_{20}{\theta_*}^2 - k_{47b}\theta_{25}\theta_H$$

$$r_{48} = k_{48f}\theta_{21}\theta_* - k_{48b}\theta_{25}\theta_H$$

$$r_{49} = k_{49f}\theta_{21} - k_{49b}\theta_{08}\theta_*$$

$$r_{50} = k_{50f}\theta_{22}\theta_* - k_{50b}\theta_{08}\theta_H$$

$$r_{51} = k_{51f}\theta_{22}\theta_* - k_{51b}\theta_{23}\theta_H$$

$$r_{52} = k_{52f}\theta_{23}\theta_* - k_{52b}\theta_{AGL}\theta_H$$

$$r_{53} = k_{53f}\theta_{29} - k_{53b}\theta_{04}{\theta_*}^2$$

$$r_{54} = k_{54f}\theta_{AGL}\theta_H - k_{54b}\theta_{24}\theta_*$$

$$r_{55} = k_{55f}\theta_{25} - k_{55b}\theta_{AGL}\theta_H$$

$$r_{56} = k_{56f}\theta_{24}\theta_H - k_{56b}\theta_{GVL}\theta_*$$

$$r_{57} = k_{57f}\theta_{HPA}\theta_* - k_{57b}\theta_{26}\theta_{OH}$$

$$r_{58} = k_{58f}\theta_{26} - k_{58b}\theta_{27}\theta_H$$

$$r_{59} = k_{59f}\theta_{26}\theta_* - k_{59b}\theta_{13}\theta_H$$

$$r_{60} = k_{60f}\theta_{26}\theta_* - k_{60b}\theta_{28}\theta_H$$

$$r_{61} = k_{61f}\theta_{27}{\theta_*}^2 - k_{61b}\theta_{19}\theta_H$$

$$r_{62} = k_{62f}\theta_{27}{\theta_*}^2 - k_{62b}\theta_{07}\theta_H$$

$$r_{63} = k_{63f}\theta_{28}\theta_* - k_{63b}\theta_{07}\theta_H$$

$$r_{64} = k_{64f}\theta_{28}\theta_* - k_{64b}\theta_{18}\theta_H$$

$$r_{65} = k_{65f}\theta_{08}\theta_H - k_{65b}\theta_{GVL}\theta_*$$

$$r_{66} = k_{66f}\theta_{Hy} - k_{66b}\theta_{30}$$

$$r_{67} = k_{67f}\theta_{Hy}{\theta_*}^2 - k_{67b}\theta_{11}\theta_H$$

$$r_{68} = k_{68f}\theta_{Hy}\theta_* - k_{68b}\theta_{27}\theta_{OH}$$

$$r_{69} = k_{69f}\theta_{Hy}\theta_* - k_{69b}\theta_{15}\theta_{OH}$$

$$r_{70} = k_{70f}\theta_{Hy}{\theta_*}^2 - k_{70b}\theta_{31}\theta_H$$

$$r_{71} = k_{71f}\theta_{30}\theta_* - k_{71b}\theta_{22}\theta_{OH}$$

$$r_{72} = k_{72f}\theta_{30}\theta_* - k_{72b}\theta_{32}\theta_H$$

$$r_{73} = k_{73f}\theta_{31}\theta_* - k_{73b}\theta_{21}\theta_{OH}$$

$$r_{74} = k_{74f}\theta_{31} - k_{74b}\theta_{32}\theta_*$$

$$r_{75} = k_{75f}\theta_{31}{\theta_*}^2 - k_{75b}\theta_{29}\theta_H$$

$$r_{76} = k_{76f}\theta_{32}\theta_* - k_{76b}\theta_{04}\theta_H$$

$$r_{77} = k_{77f}\theta_{29} - k_{77b}\theta_{25}\theta_{OH}$$

$$r_{78} = k_{78f}\theta_{GVL} - k_{78b}P_{GVL}{\theta_*}^2$$

$$r_{79} = k_{79f}\theta_H\theta_{OH} - k_{79b}\theta_{H_2O}\theta_*$$

$$r_{80} = k_{80f}\theta_{HPA}\theta_H - k_{80b}\theta_{33}{\theta_*}^2$$

$$r_{81} = k_{81f}\theta_{39}\theta_H - k_{81b}\theta_{40}{\theta_*}^2$$

$$r_{82} = k_{82f}\theta_{26}\theta_H - k_{82b}\theta_{34}{\theta_*}^2$$

$$r_{83} = k_{83f}\theta_{33} - k_{83b}\theta_{34}\theta_{OH}$$

$$r_{84} = k_{84f}\theta_{33}\theta_{*} - k_{84b}\theta_{35}\theta_{H}$$

$$r_{85} = k_{85f}\theta_{Al}\theta_{H} - k_{85b}\theta_{35}\theta_{*}$$

$$r_{86} = k_{86f}\theta_{Al} - k_{86b}\theta_{40}\theta_{*}$$

$$r_{87} = k_{87f}\theta_{34}\theta_{*}^{2} - k_{87b}\theta_{36}\theta_{H}$$

$$r_{88} = k_{88f}\theta_{35}\theta_{*} - k_{88b}\theta_{36}\theta_{OH}$$

$$r_{89} = k_{89f}\theta_{36} - k_{89b}\theta_{16}$$

$$r_{90} = k_{90f}\theta_{40}\theta_{*}^{2} - k_{90b}\theta_{GVL}\theta_{OH}$$

$$r_{91} = k_{91f}\theta_{LA}\theta_{*}^{2} - k_{91b}\theta_{37}\theta_{H}$$

$$r_{92} = k_{92f}\theta_{37}\theta_{H} - k_{92b}\theta_{38}$$

$$r_{93} = k_{93f}\theta_{38} - k_{93b}\theta_{39}\theta_{*}$$

$$r_{94} = k_{94f}\theta_{H_2O} - k_{94b}P_{H_2O}\theta_{*}$$

$$r_{95} = k_{95f}\theta_{OH}\theta_{*} - k_{95b}\theta_{O}\theta_{H}$$

$$r_{96} = k_{96f}\theta_{HPA} - k_{96b}P_{HPA}\theta_{*}^{3}$$

Steady state species balance and the overall site balance for 1 site model:

$$\frac{d\theta_{LA}}{dt} = r_1 - r_3 - r_4 - r_7 - r_8 - r_{91}$$

$$\frac{d\theta_{Al}}{dt} = r_3 - r_5 - r_{85} - r_{86}$$

$$\frac{d\theta_{Hy}}{dt} = r_4 - r_6 - r_{66} - r_{67} - r_{68} - r_{69} - r_{70}$$

$$\frac{d\theta_{HPA}}{dt} = r_5 + r_6 - r_{20} - r_{21} - r_{57} - r_{80} - r_{96}$$

$$\frac{d\theta_{01}}{dt} = r_7 - r_9 - r_{12} - r_{13}$$

$$\frac{d\theta_{02}}{dt} = r_9 - r_{10}$$

$$\frac{d\theta_{03}}{dt} = r_{10} - r_{11}$$

$$\frac{d\theta_{04}}{dt} = r_{11} - r_{19} + r_{76} + r_{53}$$

$$\frac{d\theta_{05}}{dt} = r_{13} - r_{14}$$

$$\frac{d\theta_{06}}{dt} = r_{12} + r_{15} - r_{16} + r_{43} + r_{45}$$

$$\frac{d\theta_{07}}{dt} = r_8 - r_{15} - r_{17} + r_{62} + r_{63}$$

$$\frac{d\theta_{08}}{dt} = r_{17} + r_{18} + r_{49} + r_{50} - r_{65}$$

$$\frac{d\theta_{09}}{dt} = r_{20} - r_{22} - r_{23} - r_{24}$$

$$\frac{d\theta_{10}}{dt} = r_{21} - r_{25} - r_{26} - r_{27} - r_{28}$$

$$\frac{d\theta_{11}}{dt} = r_{22} - r_{29} - r_{30} + r_{67}$$

$$\frac{d\theta_{12}}{dt} = r_{23} + r_{25} - r_{31} - r_{32}$$

$$\frac{d\theta_{13}}{dt} = r_{24} - r_{33} - r_{34} + r_{59}$$

$$\frac{d\theta_{14}}{dt} = r_{26} - r_{35} - r_{36}$$

$$\frac{d\theta_{15}}{dt} = r_{27} - r_{37} - r_{38} - r_{39} + r_{69}$$

$$\frac{d\theta_{16}}{dt} = r_{28} - r_{40} + r_{89}$$

$$\frac{d\theta_{17}}{dt} = r_{29} + r_{31} + r_{37} - r_{41} - r_{42}$$

$$\frac{d\theta_{18}}{dt} = r_{33} - r_{43} - r_{44} + r_{64}$$

$$\frac{d\theta_{19}}{dt} = r_{30} + r_{34} - r_{45} + r_{61}$$

$$\frac{d\theta_{20}}{dt} = r_{32} + r_{35} - r_{46} - r_{47}$$

$$\frac{d\theta_{21}}{dt} = r_{36} + r_{38} - r_{48} - r_{49} + r_{73}$$

$$\frac{d\theta_{22}}{dt} = r_{39} + r_{40} - r_{50} - r_{51} + r_{71}$$

$$\frac{d\theta_{23}}{dt} = r_{41} + r_{51} - r_{52}$$

$$\frac{d\theta_{24}}{dt} = r_{44} + r_{46} + r_{54} - r_{56}$$

$$\frac{d\theta_{25}}{dt} = r_{42} + r_{47} + r_{48} - r_{55} + r_{77}$$

$$\frac{d\theta_{26}}{dt} = r_{57} - r_{58} - r_{59} - r_{60} - r_{82}$$

$$\frac{d\theta_{27}}{dt} = r_{58} - r_{61} - r_{62} + r_{68}$$

$$\frac{d\theta_{28}}{dt} = r_{60} - r_{63} - r_{64}$$

$$\frac{d\theta_{29}}{dt} = r_{75} - r_{77} - r_{53}$$

$$\frac{d\theta_{30}}{dt} = r_{66} - r_{71} - r_{72}$$

$$\frac{d\theta_{31}}{dt} = r_{70} - r_{73} - r_{74} - r_{75}$$

$$\frac{d\theta_{32}}{dt} = r_{72} - r_{76} + r_{74}$$

$$\frac{d\theta_{33}}{dt} = r_{80} - r_{83} - r_{84}$$

$$\frac{d\theta_{34}}{dt} = r_{82} + r_{43} - r_{87}$$

$$\frac{d\theta_{35}}{dt} = r_{84} + r_{85} - r_{88}$$

$$\frac{d\theta_{36}}{dt} = r_{87} + r_{88} - r_{89}$$

$$\frac{d\theta_{37}}{dt} = r_{91} - r_{92}$$

$$\frac{d\theta_{38}}{dt} = r_{92} - r_{93}$$

$$\frac{d\theta_{39}}{dt} = r_{93} - r_{81}$$

$$\frac{d\theta_{40}}{dt} = r_{81} + r_{86} - r_{90}$$

$$\frac{d\theta_{AGL}}{dt} = r_{14} + r_{16} - r_{18} + r_{19} + r_{52} - r_{54} + r_{55}$$

$$\frac{d\theta_{GVL}}{dt} = r_{56} + r_{65} - r_{78} + r_{90}$$

$$\frac{d\theta_H}{dt} = 2r_2 - r_3 - r_4 - r_5 - r_6 + r_7 + r_9 - r_{11} + r_{15} - r_{18} + r_{20}$$
$$+ r_{22} + r_{25} + r_{26} + r_{27} + r_{31} + r_{32} + r_{33} + r_{34} + r_{35}$$
$$+ r_{36} + r_{37} + r_{38} + r_{40} + r_{42} + r_{43} + r_{45} + r_{47} + r_{48}$$
$$+ r_{50} + r_{51} + r_{52} - r_{54} - r_{56} + r_{58} + r_{59} + r_{60} + r_{61}$$
$$+ r_{62} + r_{63} + r_{64} - r_{65} + r_{67} + r_{70} + r_{72} + r_{75} + r_{76}$$
$$- r_{79} - r_{80} - r_{81} - r_{82} + r_{84} - r_{85} + r_{87} + r_{91} - r_{92}$$
$$+ r_{95}$$

$$\frac{d\theta_{OH}}{dt} = r_8 + r_{12} + r_{14} + r_{19} + r_{21} + r_{23} + r_{24} + r_{29} + r_{30} + r_{57}$$
$$+ r_{68} + r_{69} + r_{71} + r_{73} + r_{77} - r_{79} + r_{83} + r_{88} + r_{90}$$
$$- r_{95}$$

$$\frac{d\theta_{H_2O}}{dt} = r_{79} - r_{94}$$

$$\frac{d\theta_O}{dt} = r_{95}$$

and $$2\theta_{LA} + 3\theta_{HPA} + 2\theta_{Al} + 2\theta_{Hy} + 3\theta_{01} + 4\theta_{02} + 2\theta_{03} +$$
$$2\theta_{04} + 2\theta_{05} + 3\theta_{06} + 3\theta_{07} + 2\theta_{08} + 3\theta_{09} + 2\theta_{10} + 3\theta_{11} +$$
$$3\theta_{12} + 3\theta_{13} + 3\theta_{14} + 2\theta_{15} + 2\theta_{16} + 3\theta_{17} + 3\theta_{18} + 3\theta_{19} + 2\theta_{20} +$$
$$3\theta_{21} + 2\theta_{22} + 2\theta_{23} + 2\theta_{24} + 3\theta_{25} + 3\theta_{26} + 2\theta_{27} + 3\theta_{28} +$$
$$4\theta_{29} + 2\theta_{30} + 3\theta_{31} + 3\theta_{32} + 2\theta_{33} + \theta_{34} + 2\theta_{35} + 2\theta_{36} + 3\theta_{37} +$$
$$3\theta_{38} + 2\theta_{39} + \theta_{40} + 2\theta_{AGL} + 2\theta_{GVL} + \theta_H + \theta_{OH} + \theta_* = 1.00$$

Set of elementary reactions for two site model

$$r_1 = k_{1f} P_{LA} \theta_*^2 - k_{1b} \theta_{LA}$$

$$r_2 = k_{2f} P_{H_2} \theta_{\Delta}^2 - k_{2b} {\theta_H}^2$$

$$r_3 = k_{3f} \theta_{LA} \theta_H - k_{3b} \theta_{Al} \theta_{\Delta}$$

$$r_4 = k_{4f} \theta_{LA} \theta_H - k_{4b} \theta_{Hy} \theta_{\Delta}$$

$$r_5 = k_{5f} \theta_{Al} \theta_H \theta_* - k_{5b} \theta_{HPA} \theta_{\Delta}$$

$$r_6 = k_{6f} \theta_{Hy} \theta_H \theta_* - k_{6b} \theta_{HPA} \theta_{\Delta}$$

$$r_7 = k_{7f} \theta_{LA} \theta_* \theta_{\Delta} - k_{7b} \theta_{01} \theta_H$$

$$r_8 = k_{8f} \theta_{LA} \theta_*^2 - k_{8b} \theta_{07} \theta_{OH}$$

$$r_9 = k_{9f} \theta_{01} \theta_* \theta_{\Delta} - k_{9b} \theta_{02} \theta_H$$

$$r_{10} = k_{10f} \theta_{02} - k_{10b} \theta_{03} {\theta_*}^2$$

$$r_{11} = k_{11f} \theta_{03} \theta_H - k_{11b} \theta_{04} \theta_{\Delta}$$

$$r_{12} = k_{12f} \theta_{01} \theta_* - k_{12b} \theta_{06} \theta_{OH}$$

$$r_{13} = k_{13f} \theta_{01} - k_{13b} \theta_{05} \theta_*$$

$$r_{14} = k_{14f} \theta_{05} \theta_* - k_{14b} \theta_{AGL} \theta_{OH}$$

$$r_{15} = k_{15f} \theta_{07} \theta_{\Delta} - k_{15b} \theta_{06} \theta_H$$

$$r_{16} = k_{16f} \theta_{06} - k_{16b} \theta_{AGL} \theta_*$$

$$r_{17} = k_{17f} \theta_{07} - k_{17b} \theta_{08} \theta_*$$

$$r_{18} = k_{18f} \theta_{AGL} \theta_H - k_{18b} \theta_{08} \theta_{\Delta}$$

$$r_{19} = k_{19f} \theta_{04} \theta_* - k_{19b} \theta_{AGL} \theta_{OH}$$

$$r_{20} = k_{20f} \theta_{HPA} \theta_{\Delta} - k_{20b} \theta_{09} \theta_H$$

$$r_{21} = k_{21f} \theta_{HPA} - k_{21b} \theta_{10} \theta_{OH}$$

$$r_{22} = k_{22f} \theta_{09} \theta_{\Delta} - k_{22b} \theta_{11} \theta_H$$

$$r_{23} = k_{23f}\theta_{09}\theta_* - k_{23b}\theta_{12}\theta_{OH}$$

$$r_{24} = k_{24f}\theta_{09}\theta_* - k_{24b}\theta_{13}\theta_{OH}$$

$$r_{25} = k_{25f}\theta_{10}\theta_*\theta_\Delta - k_{25b}\theta_{12}\theta_H$$

$$r_{26} = k_{26f}\theta_{10}\theta_*\theta_\Delta - k_{26b}\theta_{14}\theta_H$$

$$r_{27} = k_{27f}\theta_{10}\theta_\Delta - k_{27b}\theta_{15}\theta_H$$

$$r_{28} = k_{28f}\theta_{10} - k_{28b}\theta_{16}$$

$$r_{29} = k_{29f}\theta_{11}\theta_* - k_{29b}\theta_{17}\theta_{OH}$$

$$r_{30} = k_{30f}\theta_{11}\theta_* - k_{30b}\theta_{19}\theta_{OH}$$

$$r_{31} = k_{31f}\theta_{12}\theta_\Delta - k_{31b}\theta_{17}\theta_H$$

$$r_{32} = k_{32f}\theta_{12}\theta_\Delta - k_{32b}\theta_{20}\theta_H\theta_*$$

$$r_{33} = k_{33f}\theta_{13}\theta_\Delta - k_{33b}\theta_{18}\theta_H$$

$$r_{34} = k_{34f}\theta_{13}\theta_\Delta - k_{34b}\theta_{19}\theta_H$$

$$r_{35} = k_{35f}\theta_{14}\theta_\Delta - k_{35b}\theta_{20}\theta_H\theta_*$$

$$r_{36} = k_{36f}\theta_{14}\theta_\Delta - k_{36b}\theta_{21}\theta_H$$

$$r_{37} = k_{37f}\theta_{15}\theta_*\theta_\Delta - k_{37b}\theta_{17}\theta_H$$

$$r_{38} = k_{38f}\theta_{15}\theta_*\theta_\Delta - k_{38b}\theta_{21}\theta_H$$

$$r_{39} = k_{39f}\theta_{15} - k_{39b}\theta_{22}$$

$$r_{40} = k_{40f}\theta_{16}\theta_\Delta - k_{40b}\theta_{22}\theta_H$$

$$r_{41} = k_{41f}\theta_{17} - k_{41b}\theta_{23}\theta_*$$

$$r_{42} = k_{42f}\theta_{17}\theta_\Delta - k_{42b}\theta_{25}\theta_H$$

$$r_{43} = k_{43f}\theta_{18}\theta_\Delta - k_{43b}\theta_{06}\theta_H$$

$$r_{44} = k_{44f}\theta_{18} - k_{44b}\theta_{24}\theta_{*}$$

$$r_{45} = k_{45f}\theta_{19}\theta_{\Delta} - k_{45b}\theta_{06}\theta_{H}$$

$$r_{46} = k_{46f}\theta_{20} - k_{46b}\theta_{24}$$

$$r_{47} = k_{47f}\theta_{20}\theta_{*}\theta_{\Delta} - k_{47b}\theta_{25}\theta_{H}$$

$$r_{48} = k_{48f}\theta_{21}\theta_{\Delta} - k_{48b}\theta_{25}\theta_{H}$$

$$r_{49} = k_{49f}\theta_{21} - k_{49b}\theta_{08}\theta_{*}$$

$$r_{50} = k_{50f}\theta_{22}\theta_{\Delta} - k_{50b}\theta_{08}\theta_{H}$$

$$r_{51} = k_{51f}\theta_{22}\theta_{\Delta} - k_{51b}\theta_{23}\theta_{H}$$

$$r_{52} = k_{52f}\theta_{23}\theta_{\Delta} - k_{52b}\theta_{AGL}\theta_{H}$$

$$r_{53} = k_{53f}\theta_{29} - k_{53b}\theta_{04}\theta_{*}^{\ 2}$$

$$r_{54} = k_{54f}\theta_{AGL}\theta_{H} - k_{54b}\theta_{24}\theta_{\Delta}$$

$$r_{55} = k_{55f}\theta_{25}\theta_{\Delta} - k_{55b}\theta_{AGL}\theta_{H}\theta_{*}$$

$$r_{56} = k_{56f}\theta_{24}\theta_{H} - k_{56b}\theta_{GVL}\theta_{\Delta}$$

$$r_{57} = k_{57f}\theta_{HPA}\theta_{*} - k_{57b}\theta_{26}\theta_{OH}$$

$$r_{58} = k_{58f}\theta_{26}\theta_{\Delta} - k_{58b}\theta_{27}\theta_{H}\theta_{*}$$

$$r_{59} = k_{59f}\theta_{26}\theta_{\Delta} - k_{59b}\theta_{13}\theta_{H}$$

$$r_{60} = k_{60f}\theta_{26}\theta_{\Delta} - k_{60b}\theta_{28}\theta_{H}$$

$$r_{61} = k_{61f}\theta_{27}\theta_{*}\theta_{\Delta} - k_{61b}\theta_{19}\theta_{H}$$

$$r_{62} = k_{62f}\theta_{27}\theta_{*}\theta_{\Delta} - k_{62b}\theta_{07}\theta_{H}$$

$$r_{63} = k_{63f}\theta_{28}\theta_{\Delta} - k_{63b}\theta_{07}\theta_{H}$$

$$r_{64} = k_{64f}\theta_{28}\theta_{\Delta} - k_{64b}\theta_{18}\theta_{H}$$

$$r_{65} = k_{65f}\theta_{08}\theta_H - k_{65b}\theta_{GVL}\theta_\Delta$$

$$r_{66} = k_{66f}\theta_{Hy} - k_{66b}\theta_{30}$$

$$r_{67} = k_{67f}\theta_{Hy}\theta_*\theta_\Delta - k_{67b}\theta_{11}\theta_H$$

$$r_{68} = k_{68f}\theta_{Hy}\theta_* - k_{68b}\theta_{27}\theta_{OH}$$

$$r_{69} = k_{69f}\theta_{Hy}\theta_* - k_{69b}\theta_{15}\theta_{OH}$$

$$r_{70} = k_{70f}\theta_{Hy}\theta_*\theta_\Delta - k_{70b}\theta_{31}\theta_H$$

$$r_{71} = k_{71f}\theta_{30}\theta_* - k_{71b}\theta_{22}\theta_{OH}$$

$$r_{72} = k_{72f}\theta_{30}\theta_\Delta - k_{72b}\theta_{32}\theta_H$$

$$r_{73} = k_{73f}\theta_{31}\theta_* - k_{73b}\theta_{21}\theta_{OH}$$

$$r_{74} = k_{74f}\theta_{31} - k_{74b}\theta_{32}\theta_*$$

$$r_{75} = k_{75f}\theta_{31}\theta_*\theta_\Delta - k_{75b}\theta_{29}\theta_H$$

$$r_{76} = k_{76f}\theta_{32}\theta_\Delta - k_{76b}\theta_{04}\theta_H$$

$$r_{77} = k_{77f}\theta_{29} - k_{77b}\theta_{25}\theta_{OH}$$

$$r_{78} = k_{78f}\theta_{GVL} - k_{78b}P_{GVL}{\theta_*}^2$$

$$r_{79} = k_{79f}\theta_H\theta_{OH} - k_{79b}\theta_{H_2O}\theta_\Delta$$

$$r_{80} = k_{80f}\theta_{HPA}\theta_H - k_{80b}\theta_{33}\theta_*\theta_\Delta$$

$$r_{81} = k_{81f}\theta_{39}\theta_H - k_{81b}\theta_{40}\theta_*\theta_\Delta$$

$$r_{82} = k_{82f}\theta_{26}\theta_H - k_{82b}\theta_{34}\theta_*\theta_\Delta$$

$$r_{83} = k_{83f}\theta_{33} - k_{83b}\theta_{34}\theta_{OH}$$

$$r_{84} = k_{84f}\theta_{33}\theta_\Delta - k_{84b}\theta_{35}\theta_H$$

$$r_{85} = k_{85f}\theta_{Al}\theta_H - k_{85b}\theta_{35}\theta_\Delta$$

$$r_{86} = k_{86f}\theta_{Al} - k_{86b}\theta_{40}\theta_{*}$$

$$r_{87} = k_{87f}\theta_{34}\theta_{*}\theta_{\Delta} - k_{87b}\theta_{36}\theta_{H}$$

$$r_{88} = k_{88f}\theta_{35}\theta_{*} - k_{88b}\theta_{36}\theta_{OH}$$

$$r_{89} = k_{89f}\theta_{36} - k_{89b}\theta_{16}$$

$$r_{90} = k_{90f}\theta_{40}\theta_{*}^{2} - k_{90b}\theta_{GVL}\theta_{OH}$$

$$r_{91} = k_{91f}\theta_{LA}\theta_{*}\theta_{\Delta} - k_{91b}\theta_{37}\theta_{H}$$

$$r_{92} = k_{92f}\theta_{37}\theta_{H}\theta_{*} - k_{92b}\theta_{38}\theta_{\Delta}$$

$$r_{93} = k_{93f}\theta_{38} - k_{93b}\theta_{39}\theta_{*}$$

$$r_{94} = k_{94f}\theta_{H_2O} - k_{94b}P_{H_2O}\theta_{*}$$

$$r_{95} = k_{95f}\theta_{OH}\theta_{\Delta} - k_{95b}\theta_{O}\theta_{H}$$

$$r_{96} = k_{96f}\theta_{HPA} - k_{96b}P_{HPA}\theta_{*}^{3}$$

Steady state species balance and the overall site balance for 2 site model:

$$\frac{d\theta_{LA}}{dt} = r_1 - r_3 - r_4 - r_7 - r_8 - r_{91}$$

$$\frac{d\theta_{Al}}{dt} = r_3 - r_5 - r_{85} - r_{86}$$

$$\frac{d\theta_{Hy}}{dt} = r_4 - r_6 - r_{66} - r_{67} - r_{68} - r_{69} - r_{70}$$

$$\frac{d\theta_{HPA}}{dt} = r_5 + r_6 - r_{20} - r_{21} - r_{57} - r_{80} - r_{96}$$

$$\frac{d\theta_{01}}{dt} = r_7 - r_9 - r_{12} - r_{13}$$

$$\frac{d\theta_{02}}{dt} = r_9 - r_{10}$$

$$\frac{d\theta_{03}}{dt} = r_{10} - r_{11}$$

$$\frac{d\theta_{04}}{dt} = r_{11} - r_{19} + r_{76} + r_{53}$$

$$\frac{d\theta_{05}}{dt} = r_{13} - r_{14}$$

$$\frac{d\theta_{06}}{dt} = r_{12} + r_{15} - r_{16} + r_{43} + r_{45}$$

$$\frac{d\theta_{07}}{dt} = r_{8} - r_{15} - r_{17} + r_{62} + r_{63}$$

$$\frac{d\theta_{08}}{dt} = r_{17} + r_{18} + r_{49} + r_{50} - r_{65}$$

$$\frac{d\theta_{09}}{dt} = r_{20} - r_{22} - r_{23} - r_{24}$$

$$\frac{d\theta_{10}}{dt} = r_{21} - r_{25} - r_{26} - r_{27} - r_{28}$$

$$\frac{d\theta_{11}}{dt} = r_{22} - r_{29} - r_{30} + r_{67}$$

$$\frac{d\theta_{12}}{dt} = r_{23} + r_{25} - r_{31} - r_{32}$$

$$\frac{d\theta_{13}}{dt} = r_{24} - r_{33} - r_{34} + r_{59}$$

$$\frac{d\theta_{14}}{dt} = r_{26} - r_{35} - r_{36}$$

$$\frac{d\theta_{15}}{dt} = r_{27} - r_{37} - r_{38} - r_{39} + r_{69}$$

$$\frac{d\theta_{16}}{dt} = r_{28} - r_{40} + r_{89}$$

$$\frac{d\theta_{17}}{dt} = r_{29} + r_{31} + r_{37} - r_{41} - r_{42}$$

$$\frac{d\theta_{18}}{dt} = r_{33} - r_{43} - r_{44} + r_{64}$$

$$\frac{d\theta_{19}}{dt} = r_{30} + r_{34} - r_{45} + r_{61}$$

$$\frac{d\theta_{20}}{dt} = r_{32} + r_{35} - r_{46} - r_{47}$$

$$\frac{d\theta_{21}}{dt} = r_{36} + r_{38} - r_{48} - r_{49} + r_{73}$$

$$\frac{d\theta_{22}}{dt} = r_{39} + r_{40} - r_{50} - r_{51} + r_{71}$$

$$\frac{d\theta_{23}}{dt} = r_{41} + r_{51} - r_{52}$$

$$\frac{d\theta_{24}}{dt} = r_{44} + r_{46} + r_{54} - r_{56}$$

$$\frac{d\theta_{25}}{dt} = r_{42} + r_{47} + r_{48} - r_{55} + r_{77}$$

$$\frac{d\theta_{26}}{dt} = r_{57} - r_{58} - r_{59} - r_{60} - r_{82}$$

$$\frac{d\theta_{27}}{dt} = r_{58} - r_{61} - r_{62} + r_{68}$$

$$\frac{d\theta_{28}}{dt} = r_{60} - r_{63} - r_{64}$$

$$\frac{d\theta_{29}}{dt} = r_{75} - r_{77} - r_{53}$$

$$\frac{d\theta_{30}}{dt} = r_{66} - r_{71} - r_{72}$$

$$\frac{d\theta_{31}}{dt} = r_{70} - r_{73} - r_{74} - r_{75}$$

$$\frac{d\theta_{32}}{dt} = r_{72} - r_{76} + r_{74}$$

$$\frac{d\theta_{33}}{dt} = r_{80} - r_{83} - r_{84}$$

$$\frac{d\theta_{34}}{dt} = r_{82} + r_{43} - r_{87}$$

$$\frac{d\theta_{35}}{dt} = r_{84} + r_{85} - r_{88}$$

$$\frac{d\theta_{36}}{dt} = r_{87} + r_{88} - r_{89}$$

$$\frac{d\theta_{37}}{dt} = r_{91} - r_{92}$$

$$\frac{d\theta_{38}}{dt} = r_{92} - r_{93}$$

$$\frac{d\theta_{39}}{dt} = r_{93} - r_{81}$$

$$\frac{d\theta_{40}}{dt} = r_{81} + r_{86} - r_{90}$$

$$\frac{d\theta_{AGL}}{dt} = r_{14} + r_{16} - r_{18} + r_{19} + r_{52} - r_{54} + r_{55}$$

$$\frac{d\theta_{GVL}}{dt} = r_{56} + r_{65} - r_{78} + r_{90}$$

$$\begin{aligned}\frac{d\theta_H}{dt} = {} & 2r_2 - r_3 - r_4 - r_5 - r_6 + r_7 + r_9 - r_{11} + r_{15} - r_{18} + r_{20} \\ & + r_{22} + r_{25} + r_{26} + r_{27} + r_{31} + r_{32} + r_{33} + r_{34} + r_{35} \\ & + r_{36} + r_{37} + r_{38} + r_{40} + r_{42} + r_{43} + r_{45} + r_{47} + r_{48} \\ & + r_{50} + r_{51} + r_{52} - r_{54} - r_{56} + r_{58} + r_{59} + r_{60} + r_{61} \\ & + r_{62} + r_{63} + r_{64} - r_{65} + r_{67} + r_{70} + r_{72} + r_{75} + r_{76} \\ & - r_{79} - r_{80} - r_{81} - r_{82} + r_{84} - r_{85} + r_{87} + r_{91} - r_{92} \\ & + r_{95}\end{aligned}$$

$$\frac{d\theta_{OH}}{dt} = r_8 + r_{12} + r_{14} + r_{19} + r_{21} + r_{23} + r_{24} + r_{29} + r_{30} + r_{57}$$

$$+ r_{68} + r_{69} + r_{71} + r_{73} + r_{77} - r_{79} + r_{83} + r_{88} + r_{90}$$

$$- r_{95}$$

$$\frac{d\theta_{H_2O}}{dt} = r_{79} - r_{94}$$

$$\frac{d\theta_O}{dt} = r_{95}$$

$$2\theta_{LA} + 3\theta_{HPA} + 2\theta_{Al} + 2\theta_{Hy} + 3\theta_{01} + 4\theta_{02} + 2\theta_{03} +$$

$$2\theta_{04} + 2\theta_{05} + 3\theta_{06} + 3\theta_{07} + 2\theta_{08} + 3\theta_{09} + 2\theta_{10} + 3\theta_{11} +$$

$$3\theta_{12} + 3\theta_{13} + 3\theta_{14} + 2\theta_{15} + 2\theta_{16} + 3\theta_{17} + 3\theta_{18} + 3\theta_{19} + 2\theta_{20} +$$

$$3\theta_{21} + 2\theta_{22} + 2\theta_{23} + 2\theta_{24} + 3\theta_{25} + 3\theta_{26} + 2\theta_{27} + 3\theta_{28} +$$

$$4\theta_{29} + 2\theta_{30} + 3\theta_{31} + 3\theta_{32} + 2\theta_{33} + \theta_{34} + 2\theta_{35} + 2\theta_{36} + 3\theta_{37} +$$

$$3\theta_{38} + 2\theta_{39} + \theta_{40} + 2\theta_{AGL} + 2\theta_{GVL} + \theta_{OH} + \theta_* = 1.00$$

and

$$\theta_H + \theta_\Delta = 1.00$$

B.3 Equilibrium and reaction rate constants at various temperatures for all reaction steps considered in the reaction mechanism for the HDO of LA

Table B.1: Equilibrium and reaction rate constants for all the elementary reaction steps considered in the development of the microkinetic model

*All rate constants are in units of inverse seconds and bar.

Step	**Constant**	**Temperature (K)**		
		423	473	523
r_1	K_1	1.09×10^{5}	2.38×10^{3}	1.09×10^{2}
	k_1^+	7.53×10^{7}	7.13×10^{7}	6.78×10^{7}
r_2	K_2	5.14×10^{9}	9.30×10^{7}	3.56×10^{6}
	k_2^+	5.74×10^{8}	5.43×10^{8}	5.16×10^{8}
r_3	K_3	8.60×10^{-2}	9.67×10^{-2}	1.05×10^{-1}
	k_3^+	4.04×10^{4}	2.99×10^{5}	1.51×10^{6}
r_4	K_4	4.17×10^{-11}	5.32×10^{-10}	4.16×10^{-9}
	k_4^+	6.81×10^{-4}	4.01×10^{-2}	1.09
r_5	K_5	5.35×10^{-10}	5.07×10^{-9}	3.14×10^{-8}
	k_5^+	2.09×10^{-2}	1.06	2.58×10^{1}
r_6	K_6	1.10	9.21×10^{-1}	7.93×10^{-1}
	k_6^+	8.26×10^{3}	8.59×10^{4}	5.73×10^{5}
r_7	K_7	1.03×10^{5}	2.52×10^{4}	8.19×10^{3}
	k_7^+	3.40×10^{9}	6.79×10^{9}	1.21×10^{10}
r_8	K_8	2.78×10^{6}	4.89×10^{5}	1.22×10^{5}
	k_8^+	1.16×10^{4}	9.98×10^{4}	5.74×10^{5}
r_9	K_9	1.50×10^{11}	9.71×10^{9}	1.07×10^{9}
	k_9^+	2.88×10^{9}	8.33×10^{9}	1.98×10^{10}
r_{10}	K_{10}	4.64×10^{-11}	5.06×10^{-10}	3.48×10^{-9}
	k_{10}^+	1.69×10^{-12}	7.60×10^{-10}	1.07×10^{-7}
r_{11}	K_{11}	2.45×10^{-9}	2.17×10^{-8}	1.26×10^{-7}
	k_{11}^+	8.50×10^{1}	1.28×10^{3}	1.15×10^{4}
r_{12}	K_{12}	2.10×10^{10}	2.09×10^{9}	3.27×10^{8}
	k_{12}^+	2.76×10^{3}	3.28×10^{4}	2.45×10^{5}
r_{13}	K_{13}	2.43×10^{-5}	7.89×10^{-5}	2.05×10^{-4}
	k_{13}^+	2.07×10^{2}	3.26×10^{3}	1.93×10^{5}
r_{14}	K_{14}	1.49×10^{4}	5.02×10^{3}	2.10×10^{3}
	k_{14}^+	9.45×10^{9}	2.03×10^{10}	3.77×10^{10}
r_{15}	K_{15}	7.76×10^{8}	1.08×10^{8}	2.20×10^{7}
	k_{15}^+	1.79×10^{7}	9.95×10^{7}	4.02×10^{8}
r_{16}	K_{16}	1.72×10^{-11}	1.89×10^{-10}	1.32×10^{-9}
	k_{16}^+	2.27×10^{-1}	5.27	6.72×10^{1}
	K_{17}	1.52×10^{-6}	6.89×10^{-6}	2.33×10^{-5}

r_{17}	k_{17}^{+}	2.46×10^{2}	3.15×10^{3}	2.48×10^{4}
r_{18}	K_{18}	1.14×10^{-4}	3.37×10^{-4}	8.05×10^{-4}
	k_{18}^{+}	7.25×10^{4}	6.23×10^{5}	3.55×10^{6}
r_{19}	K_{19}	2.12×10^{7}	3.72×10^{6}	9.19×10^{5}
	k_{19}^{+}	2.29×10^{6}	1.06×10^{7}	3.67×10^{7}
r_{20}	K_{20}	5.59×10^{2}	3.00×10^{2}	1.82×10^{2}
	k_{20}^{+}	1.12×10^{7}	5.48×10^{7}	2.00×10^{8}
r_{21}	K_{21}	3.61×10^{4}	1.48×10^{4}	7.21×10^{3}
	k_{21}^{+}	9.27	1.84×10^{2}	2.09×10^{3}
r_{22}	K_{22}	5.94×10^{6}	1.19×10^{6}	3.25×10^{5}
	k_{22}^{+}	4.32×10^{9}	1.13×10^{10}	2.50×10^{10}
r_{23}	K_{23}	1.09×10^{10}	1.05×10^{9}	1.60×10^{8}
	k_{23}^{+}	2.07×10^{8}	8.56×10^{8}	2.71×10^{9}
r_{24}	K_{24}	2.55×10^{8}	3.17×10^{7}	5.92×10^{6}
	k_{24}^{+}	3.87×10^{7}	1.48×10^{8}	4.39×10^{8}
r_{25}	K_{25}	1.68×10^{8}	2.13×10^{7}	4.05×10^{6}
	k_{25}^{+}	2.22×10^{9}	6.04×10^{9}	1.37×10^{10}
r_{26}	K_{26}	1.32×10^{11}	7.47×10^{9}	7.35×10^{8}
	k_{26}^{+}	8.16×10^{8}	2.44×10^{9}	6.01×10^{9}
r_{27}	K_{27}	9.09×10^{2}	4.82×10^{2}	2.91×10^{2}
	k_{27}^{+}	8.16×10^{11}	1.05×10^{12}	1.30×10^{12}
r_{28}	K_{1}	1.37×10^{-4}	2.84×10^{-4}	5.09×10^{-4}
	k_{28}^{+}	1.37×10^{3}	1.32×10^{4}	4.37×10^{5}
r_{29}	K_{29}	5.15×10^{7}	1.02×10^{7}	2.76×10^{6}
	k_{29}^{+}	4.03	8.72×10^{1}	1.06×10^{3}
r_{30}	K_{30}	2.13×10^{8}	2.81×10^{7}	5.53×10^{6}
	k_{30}^{+}	6.61×10^{7}	2.11×10^{8}	5.44×10^{8}
r_{31}	K_{31}	2.82×10^{4}	1.15×10^{4}	5.60×10^{3}
	k_{31}^{+}	6.26×10^{10}	1.24×10^{11}	2.19×10^{11}
r_{32}	K_{32}	2.07×10^{7}	4.03×10^{6}	1.08×10^{6}
	k_{32}^{+}	4.45×10^{8}	1.64×10^{9}	4.80×10^{9}
r_{33}	K_{33}	7.82×10^{3}	3.08×10^{3}	1.46×10^{3}
	k_{33}^{+}	1.15×10^{8}	4.45×10^{8}	1.35×10^{9}
r_{34}	K_{34}	4.96×10^{6}	1.05×10^{6}	3.04×10^{5}
	k_{34}^{+}	3.12×10^{4}	3.18×10^{5}	2.11×10^{6}
r_{35}	K_{35}	2.63×10^{4}	1.15×10^{4}	5.94×10^{3}
	k_{35}^{+}	2.09	5.74×10^{1}	8.48×10^{2}
r_{36}	K_{36}	1.42×10^{4}	5.01×10^{3}	2.18×10^{3}
	k_{36}^{+}	2.45×10^{10}	4.87×10^{10}	8.59×10^{10}
r_{37}	K_{37}	5.21×10^{9}	5.08×10^{8}	7.79×10^{7}
	k_{37}^{+}	7.59×10^{9}	1.55×10^{10}	2.79×10^{10}
r_{38}	K_{38}	2.06×10^{12}	7.76×10^{10}	5.50×10^{9}
	k_{38}^{+}	2.64×10^{9}	6.05×10^{9}	1.20×10^{10}
	K_{39}	1.38×10^{-3}	2.00×10^{-3}	2.71×10^{-3}

r_{39}	k_{39}^{+}	6.69×10^{5}	2.56×10^{6}	7.64×10^{6}
r_{40}	K_{40}	9.12×10^{3}	3.40×10^{3}	1.55×10^{3}
	k_{40}^{+}	3.28×10^{6}	1.65×10^{7}	6.16×10^{7}
r_{41}	K_{41}	1.47×10^{-8}	7.05×10^{-8}	2.51×10^{-7}
	k_{41}^{+}	1.37×10^{-4}	5.68×10^{-3}	1.16×10^{-1}
r_{42}	K_{42}	1.21×10^{11}	5.73×10^{9}	4.88×10^{8}
	k_{42}^{+}	4.98×10^{8}	1.30×10^{9}	2.86×10^{9}
r_{43}	K_{43}	4.21×10^{10}	3.68×10^{9}	5.17×10^{8}
	k_{43}^{+}	1.86×10^{7}	9.24×10^{7}	3.41×10^{8}
r_{44}	K_{44}	5.87×10^{-7}	2.35×10^{-6}	7.22×10^{-6}
	k_{44}^{+}	2.37×10^{3}	2.29×10^{4}	1.44×10^{5}
r_{45}	K_{45}	6.63×10^{7}	1.08×10^{7}	2.47×10^{6}
	k_{45}^{+}	2.37×10^{9}	6.53×10^{9}	1.49×10^{10}
r_{46}	K_{46}	5.20×10^{-12}	5.41×10^{-11}	3.60×10^{-10}
	k_{46}^{+}	7.55×10^{-15}	5.51×10^{-12}	1.15×10^{-9}
r_{47}	K_{47}	1.65×10^{8}	1.63×10^{7}	2.54×10^{6}
	k_{47}^{+}	1.91×10^{5}	1.03×10^{6}	4.05×10^{6}
r_{48}	K_{48}	3.07×10^{8}	3.75×10^{7}	6.91×10^{6}
	k_{48}^{+}	4.33×10^{9}	1.10×10^{10}	2.37×10^{10}
r_{49}	K_{49}	1.36×10^{-9}	1.24×10^{-8}	7.44×10^{-8}
	k_{49}^{+}	1.37×10^{3}	1.45×10^{4}	9.76×10^{4}
r_{50}	K_{50}	2.03×10^{6}	4.82×10^{5}	1.51×10^{5}
	k_{50}^{+}	1.00×10^{4}	9.36×10^{4}	5.75×10^{5}
r_{51}	K_{51}	5.56×10^{4}	1.79×10^{4}	7.21×10^{3}
	k_{51}^{+}	2.44×10^{9}	6.29×10^{9}	1.37×10^{10}
r_{52}	K_{52}	3.20×10^{5}	7.99×10^{4}	2.60×10^{4}
	k_{52}^{+}	4.65×10^{4}	4.22×10^{5}	2.53×10^{6}
r_{53}	K_{53}	5.86×10^{-13}	1.13×10^{-11}	1.23×10^{-10}
	k_{53}^{+}	1.03×10^{-6}	1.13×10^{-4}	4.85×10^{-1}
r_{54}	K_{54}	8.12×10^{-7}	3.37×10^{-6}	1.06×10^{-5}
	k_{54}^{+}	1.92×10^{6}	1.07×10^{7}	4.31×10^{7}
r_{55}	K_{55}	3.89×10^{-14}	9.84×10^{-13}	1.34×10^{-11}
	k_{55}^{+}	1.12×10^{-1}	3.39	5.35×10^{1}
r_{56}	K_{56}	2.46	2.47	2.45
	k_{56}^{+}	7.42×10^{2}	9.23×10^{3}	7.10×10^{4}
r_{57}	K_{57}	1.04×10^{8}	1.67×10^{7}	3.84×10^{6}
	k_{57}^{+}	1.87×10^{11}	3.25×10^{11}	5.08×10^{11}
r_{58}	K_{58}	6.08×10^{3}	2.38×10^{3}	1.12×10^{3}
	k_{58}^{+}	2.15×10^{4}	2.05×10^{5}	1.28×10^{6}
r_{59}	K_{59}	1.37×10^{3}	5.68×10^{2}	2.81×10^{2}
	k_{59}^{+}	7.99×10^{7}	2.96×10^{8}	8.62×10^{8}
r_{60}	K_{60}	8.53×10^{9}	6.21×10^{8}	7.47×10^{7}
	k_{60}^{+}	3.80×10^{8}	1.20×10^{9}	3.08×10^{9}
	K_{61}	1.12×10^{6}	2.52×10^{5}	7.60×10^{4}

r_{61}	k_{61}^{+}	9.85×10^{8}	2.50×10^{9}	5.36×10^{9}
r_{62}	K_{62}	9.56×10^{4}	2.51×10^{4}	8.54×10^{3}
	k_{62}^{+}	6.23×10^{6}	2.96×10^{7}	1.05×10^{8}
r_{63}	K_{63}	6.82×10^{-2}	9.61×10^{-2}	1.28×10^{-1}
	k_{63}^{+}	7.11×10^{3}	8.47×10^{4}	6.36×10^{5}
r_{64}	K_{64}	1.26×10^{-3}	2.82×10^{-3}	5.47×10^{-3}
	k_{64}^{+}	4.50×10^{1}	8.24×10^{2}	8.77×10^{3}
r_{65}	K_{65}	1.75×10^{-2}	2.47×10^{-2}	3.24×10^{-2}
	k_{65}^{+}	2.54×10^{1}	4.65×10^{2}	4.90×10^{3}
r_{66}	K_{66}	3.07×10^{-2}	3.01×10^{-2}	2.96×10^{-2}
	k_{66}^{+}	4.96×10^{5}	2.13×10^{6}	8.36×10^{6}
r_{67}	K_{67}	4.97×10^{9}	4.47×10^{8}	6.42×10^{7}
	k_{67}^{+}	3.62×10^{11}	5.03×10^{11}	6.62×10^{11}
r_{68}	K_{68}	9.47×10^{11}	4.99×10^{10}	4.67×10^{9}
	k_{68}^{+}	6.11×10^{5}	3.65×10^{6}	1.57×10^{7}
r_{69}	K_{69}	4.91×10^{7}	8.94×10^{6}	2.27×10^{6}
	k_{69}^{+}	8.14×10^{2}	1.04×10^{4}	8.22×10^{4}
r_{70}	K_{70}	1.02×10^{8}	1.18×10^{7}	2.08×10^{6}
	k_{70}^{+}	8.50×10^{7}	3.52×10^{8}	1.12×10^{9}
r_{71}	K_{71}	2.03×10^{5}	6.61×10^{4}	2.70×10^{4}
	k_{71}^{+}	1.23×10^{3}	1.77×10^{4}	1.54×10^{5}
r_{72}	K_{72}	3.57×10^{7}	7.29×10^{6}	2.02×10^{6}
	k_{72}^{+}	7.63×10^{9}	1.75×10^{10}	3.46×10^{10}
r_{73}	K_{73}	9.92×10^{11}	5.87×10^{10}	6.02×10^{9}
	k_{73}^{+}	5.68×10^{6}	3.02×10^{7}	1.18×10^{8}
r_{74}	K_{74}	1.17×10^{-1}	1.67×10^{-1}	2.22×10^{-1}
	k_{74}^{+}	2.13×10^{6}	1.38×10^{7}	1.04×10^{8}
r_{75}	K_{75}	9.51×10^{11}	5.15×10^{10}	4.91×10^{9}
	k_{75}^{+}	5.10×10^{11}	7.20×10^{11}	9.62×10^{11}
r_{76}	K_{76}	4.77	3.49	2.73
	k_{76}^{+}	9.89×10^{2}	1.15×10^{4}	8.52×10^{4}
r_{77}	K_{77}	3.20×10^{8}	4.28×10^{7}	8.47×10^{6}
	k_{77}^{+}	5.44×10^{6}	2.59×10^{7}	9.21×10^{7}
r_{78}	K_{78}	1.61×10^{-1}	2.81	2.78×10^{1}
	k_{78}^{+}	1.30×10^{7}	2.16×10^{8}	2.03×10^{9}
r_{79}	K_{79}	9.61×10^{-7}	5.67×10^{-6}	2.37×10^{-5}
	k_{79}^{+}	0.27	9.18	160.24
$\boldsymbol{r_{80}}$	K_{80}	2.00×10^{-7}	9.49×10^{-7}	3.32×10^{-6}
	k_{80}^{+}	4.39	9.22×10^{1}	1.09×10^{3}
$\boldsymbol{r_{81}}$	K_{81}	4.11	3.59	3.20
	k_{81}^{+}	1.35×10^{9}	3.74×10^{9}	8.57×10^{9}
$\boldsymbol{r_{82}}$	K_{82}	1.77×10^{-10}	1.95×10^{-9}	1.35×10^{-8}
	k_{82}^{+}	1.45×10^{-5}	1.48×10^{-3}	6.24×10^{-2}
	K_{83}	9.18×10^{4}	3.43×10^{4}	1.56×10^{4}

$\boldsymbol{r_{83}}$	k_{83}^{+}	8.75×10^{9}	2.38×10^{10}	5.41×10^{10}
$\boldsymbol{r_{84}}$	K_{84}	1.53×10^{3}	7.77×10^{2}	4.54×10^{2}
	k_{84}^{+}	1.70×10^{5}	1.24×10^{6}	6.31×10^{6}
$\boldsymbol{r_{85}}$	K_{85}	1.64×10^{-13}	3.74×10^{-12}	4.72×10^{-11}
	k_{85}^{+}	6.33×10^{-5}	4.14×10^{-3}	1.23×10^{-1}
$\boldsymbol{r_{86}}$	K_{86}	1.13×10^{-3}	2.06×10^{-3}	3.36×10^{-3}
	k_{86}^{+}	3.30×10^{8}	8.72×10^{8}	1.92×10^{9}
$\boldsymbol{r_{87}}$	K_{87}	1.58×10^{5}	4.39×10^{4}	1.56×10^{4}
	k_{87}^{+}	5.73×10^{5}	3.48×10^{6}	1.51×10^{7}
$\boldsymbol{r_{88}}$	K_{88}	9.50×10^{6}	1.94×10^{6}	5.37×10^{5}
	k_{88}^{+}	4.50×10^{3}	4.25×10^{4}	2.63×10^{5}
$\boldsymbol{r_{89}}$	K_{89}	1.71×10^{-3}	2.94×10^{-3}	4.54×10^{-3}
	k_{89}^{+}	2.48×10^{-3}	1.08×10^{-1}	2.28
$\boldsymbol{r_{90}}$	K_{90}	7.62×10^{2}	4.18×10^{2}	2.59×10^{2}
	k_{90}^{+}	2.56×10^{12}	3.10×10^{12}	3.62×10^{12}
$\boldsymbol{r_{91}}$	K_{91}	1.68×10^{13}	6.11×10^{11}	4.21×10^{10}
	k_{91}^{+}	2.59×10^{12}	3.45×10^{12}	4.39×10^{12}
$\boldsymbol{r_{92}}$	K_{92}	2.67×10^{-6}	9.21×10^{-6}	2.49×10^{-5}
	k_{92}^{+}	2.81×10^{4}	2.15×10^{5}	1.12×10^{6}
$\boldsymbol{r_{93}}$	K_{93}	5.28×10^{-13}	9.87×10^{-12}	1.06×10^{-10}
	k_{93}^{+}	9.16×10^{-7}	9.77×10^{-5}	4.27×10^{-3}
$\boldsymbol{r_{94}}$	K_{94}	2.12	10.92	40.15
	k_{94}^{+}	4.07×10^{8}	1.98×10^{9}	6.91×10^{9}
$\boldsymbol{r_{95}}$	K_{95}	4.48×10^{9}	3.65×10^{8}	4.81×10^{7}
	k_{95}^{+}	1.09×10^{5}	8.08×10^{5}	4.09×10^{6}
$\boldsymbol{r_{96}}$	K_{96}	3.34×10^{-4}	1.51×10^{-2}	3.27×10^{-1}
	k_{96}^{+}	2.50×10^{4}	1.07×10^{6}	2.19×10^{7}

B.4 Rates of all elementary reaction (s^{-1}) at various reaction temperatures (reported values are from simulation results obtained using 0.45 m LA and 10 bar hydrogen pressure)

Table B.2: Rates of all the elementary reaction rates at various temperatures for one site model

Reaction step	Temperature (K)				
	323	373	423	473	523
r_1	2.67E-09	1.81E-05	3.44E-03	9.97E-02	3.37E-01
r_2	2.67E-09	1.81E-05	3.44E-03	9.97E-02	3.36E-01
r_3	2.67E-09	1.81E-05	3.44E-03	9.97E-02	3.37E-01
r_4	1.03E-19	2.03E-14	5.08E-11	1.15E-08	2.01E-07
r_5	5.27E-19	8.69E-14	8.25E-11	1.21E-08	1.00E-07

r_6	9.96E-20	1.62E-14	3.16E-11	4.59E-09	7.81E-08
r_7	2.85E-17	1.04E-11	2.33E-08	6.13E-06	4.10E-04
r_8	1.10E-21	1.81E-15	1.17E-11	6.33E-09	1.27E-07
r_9	-2.65E-28	-2.25E-18	-1.71E-13	-4.49E-10	-3.60E-08
r_{10}	9.72E-33	2.19E-24	3.34E-19	2.61E-15	2.45E-13
r_{11}	-4.14E-32	3.10E-23	2.97E-18	6.78E-15	9.72E-13
r_{12}	9.67E-22	3.59E-15	3.21E-11	2.46E-08	4.47E-07
r_{13}	2.85E-17	1.04E-11	2.33E-08	6.10E-06	4.09E-04
r_{14}	2.85E-17	1.04E-11	2.33E-08	6.10E-06	4.09E-04
r_{15}	8.00E-21	1.34E-14	3.81E-11	-3.96E-10	5.05E-07
r_{16}	4.68E-19	9.08E-14	1.21E-10	9.46E-09	-8.60E-07
r_{17}	1.33E-20	-9.26E-15	-2.35E-11	8.30E-09	-1.51E-06
r_{18}	1.16E-21	-5.11E-14	-1.18E-10	3.32E-08	-6.37E-06
r_{19}	8.46E-25	3.08E-18	2.91E-14	1.58E-11	4.26E-10
r_{20}	-2.68E-23	-1.26E-17	-5.07E-14	-1.17E-11	-2.67E-10
r_{21}	1.73E-26	1.15E-20	5.47E-17	2.35E-14	8.10E-13
r_{22}	-3.25E-23	-2.26E-17	-1.31E-13	-4.95E-11	-1.40E-09
r_{23}	4.57E-24	8.34E-18	6.80E-14	3.23E-11	9.74E-10
r_{24}	1.08E-24	1.73E-18	1.27E-14	5.57E-12	1.57E-10
r_{25}	2.86E-22	-2.08E-17	3.36E-13	-7.76E-11	-1.24E-08
r_{26}	-2.88E-22	-6.33E-17	-5.90E-14	-2.73E-11	-3.08E-08
r_{27}	1.93E-24	8.65E-17	-2.91E-13	1.05E-10	4.26E-08
r_{28}	2.16E-26	-2.53E-18	1.38E-14	2.86E-13	5.94E-10
r_{29}	7.60E-31	2.02E-23	9.80E-19	2.07E-15	1.69E-13
r_{30}	3.42E-21	3.77E-15	1.61E-11	5.01E-09	8.72E-08
r_{31}	-2.16E-17	-5.10E-12	-6.71E-09	-1.58E-06	-9.70E-05
r_{32}	2.16E-17	5.10E-12	6.71E-09	1.58E-06	9.70E-05
r_{33}	6.67E-22	6.07E-16	-1.05E-12	7.24E-10	4.67E-09
r_{34}	7.04E-26	1.28E-18	2.09E-15	6.11E-13	6.05E-11
r_{35}	8.63E-19	-9.53E-14	2.19E-10	-8.29E-10	3.73E-06
r_{36}	-8.64E-19	9.51E-14	-2.19E-10	6.89E-10	-3.78E-06
r_{37}	1.99E-23	6.97E-17	-1.72E-13	9.72E-11	3.26E-08
r_{38}	-1.79E-23	1.58E-17	-1.20E-13	7.47E-12	9.58E-09
r_{39}	-1.81E-26	1.02E-18	2.74E-16	2.07E-13	4.20E-10
r_{40}	1.36E-26	-9.75E-19	-6.50E-17	-2.41E-13	-3.11E-10
r_{41}	-2.49E-28	-9.92E-21	1.75E-17	-2.15E-14	-1.50E-11
r_{42}	-2.16E-17	-5.10E-12	-6.71E-09	-1.58E-06	-9.70E-05
r_{43}	5.14E-23	1.16E-15	1.26E-12	3.98E-11	1.49E-08
r_{44}	7.57E-22	-3.84E-16	-1.13E-11	3.61E-10	-1.25E-08
r_{45}	4.61E-19	7.76E-14	8.26E-11	9.08E-09	1.88E-07
r_{46}	-7.20E-32	1.50E-24	-4.21E-20	2.46E-18	2.86E-16
r_{47}	-6.12E-18	2.32E-13	-1.94E-09	3.25E-08	-1.05E-04
r_{48}	7.30E-18	3.90E-13	-2.27E-10	5.57E-08	-1.41E-05
r_{49}	-8.17E-18	-2.95E-13	7.63E-12	-5.51E-08	1.03E-05
r_{50}	-3.49E-28	3.56E-22	2.23E-19	6.06E-15	-2.08E-12
r_{51}	-3.91E-27	4.73E-20	2.25E-16	-2.68E-14	1.11E-10
r_{52}	-4.16E-27	3.74E-20	2.42E-16	-4.86E-14	9.60E-11
r_{53}	-1.08E-30	-5.08E-23	-2.31E-18	-6.01E-15	-3.82E-11
r_{54}	-1.96E-18	-7.83E-14	-1.66E-11	-3.07E-09	4.65E-07

r_{55}	-3.09E-17	-1.06E-11	-2.35E-08	-6.08E-06	-4.15E-04
r_{56}	-1.96E-18	-7.87E-14	-2.79E-11	-2.71E-09	4.53E-07
r_{57}	6.27E-19	1.03E-13	1.14E-10	1.66E-08	1.65E-07
r_{58}	4.58E-19	7.36E-14	6.59E-11	4.15E-09	1.18E-07
r_{59}	6.66E-22	6.06E-16	-1.06E-12	7.19E-10	4.58E-09
r_{60}	1.68E-19	3.01E-14	5.05E-11	1.18E-08	5.74E-08
r_{61}	4.58E-19	7.38E-14	6.65E-11	4.08E-09	1.02E-07
r_{62}	-1.43E-22	-3.10E-16	-7.94E-13	5.84E-11	-1.10E-08
r_{63}	2.03E-20	2.61E-15	3.74E-12	1.51E-09	-1.12E-06
r_{64}	1.42E-22	1.67E-16	-8.95E-12	-3.23E-10	-2.28E-09
r_{65}	-8.15E-18	-3.55E-13	-1.34E-10	-1.36E-08	2.37E-06
r_{66}	3.46E-23	2.73E-16	2.74E-12	1.73E-09	3.15E-08
r_{67}	3.46E-21	3.79E-15	1.62E-11	5.06E-09	8.86E-08
r_{68}	5.55E-23	4.98E-17	2.67E-13	9.30E-11	2.55E-09
r_{69}	8.03E-27	2.54E-20	3.56E-16	2.64E-13	1.34E-11
r_{70}	3.21E-26	2.10E-19	3.50E-15	3.24E-12	1.37E-10
r_{71}	2.68E-28	1.02E-21	1.64E-17	1.34E-14	7.18E-13
r_{72}	3.46E-23	2.73E-16	2.74E-12	1.73E-09	3.15E-08
r_{73}	4.54E-24	2.50E-17	2.64E-13	1.64E-10	3.98E-09
r_{74}	-3.38E-23	-2.70E-16	-2.71E-12	-1.72E-09	-3.10E-08
r_{75}	2.93E-23	2.46E-16	2.45E-12	1.56E-09	2.71E-08
r_{76}	8.46E-25	3.08E-18	2.91E-14	1.58E-11	4.63E-10
r_{77}	2.93E-23	2.46E-16	2.45E-12	1.56E-09	2.72E-08
r_{78}	2.67E-09	1.81E-05	3.44E-03	9.97E-02	3.37E-01
r_{79}	2.67E-09	1.81E-05	3.44E-03	9.97E-02	3.37E-01
r_{80}	6.61E-27	4.87E-21	2.73E-17	1.01E-14	4.47E-13
r_{81}	-2.54E-23	-2.41E-17	-6.83E-14	-1.31E-11	-4.17E-10
r_{82}	-8.31E-28	-1.15E-15	-1.28E-12	-4.18E-11	-1.57E-08
r_{83}	9.67E-24	1.34E-18	2.72E-15	4.76E-13	1.28E-11
r_{84}	-9.66E-24	-1.34E-18	-2.70E-15	-4.66E-13	-1.23E-11
r_{85}	9.67E-24	1.34E-18	2.71E-15	4.72E-13	1.26E-11
r_{86}	2.67E-09	1.81E-05	3.44E-03	9.97E-02	3.37E-01
r_{87}	-9.85E-27	1.55E-18	-1.39E-14	-5.44E-13	-9.04E-10
r_{88}	1.91E-27	1.87E-21	1.23E-17	5.88E-15	2.77E-13
r_{89}	-7.94E-27	1.55E-18	-1.39E-14	-5.27E-13	-9.05E-10
r_{90}	2.67E-09	1.81E-05	3.44E-03	9.97E-02	3.37E-01
r_{91}	-2.92E-20	-1.36E-12	-1.07E-08	-4.04E-06	-1.39E-04
r_{92}	2.17E-19	0.00E+00	0.00E+00	-4.55E-11	-3.05E-09
r_{93}	-2.54E-23	-2.41E-17	-6.83E-14	-1.31E-11	-4.17E-10
r_{94}	2.67E-09	1.81E-05	3.44E-03	9.97E-02	3.37E-01
r_{95}	7.67E-22	6.28E-15	4.61E-11	1.60E-08	3.41E-06
r_{96}	3.80E-24	1.11E-17	1.83E-13	1.41E-10	1.36E-08

Table B.3: Rates of all the elementary reaction rates at various temperatures for two site model

Reaction step	Temperature (K)				
	323	373	423	473	523
r_1	2.23E-06	4.38E-04	1.30E-02	1.64E-02	3.23E-02
r_2	2.23E-06	4.38E-04	1.30E-02	1.64E-02	3.23E-02
r_3	2.23E-06	4.38E-04	1.30E-02	1.64E-02	3.23E-02
r_4	8.66E-17	5.00E-13	1.89E-10	1.23E-09	9.66E-09
r_5	2.42E-18	2.60E-15	1.92E-13	1.34E-12	5.69E-11
r_6	2.85E-21	3.06E-17	1.81E-14	2.01E-13	2.16E-12
r_7	6.90E-13	1.30E-09	2.28E-07	5.90E-07	2.11E-05
r_8	7.69E-16	1.06E-12	1.48E-10	1.31E-10	6.27E-10
r_9	-6.12E-19	1.05E-14	-8.81E-12	-5.13E-12	8.37E-15
r_{10}	6.82E-27	1.41E-21	9.35E-18	1.69E-16	8.37E-15
r_{11}	6.58E-27	1.03E-21	8.96E-18	1.26E-15	8.37E-15
r_{12}	6.75E-16	2.20E-12	6.05E-10	9.16E-10	6.17E-09
r_{13}	6.89E-13	1.30E-09	2.28E-07	5.89E-07	2.11E-05
r_{14}	6.89E-13	1.30E-09	2.28E-07	5.89E-07	2.11E-05
r_{15}	-2.44E-15	2.53E-09	2.63E-10	-2.06E-07	2.03E-06
r_{16}	-2.04E-15	2.69E-09	5.99E-10	-2.12E-07	2.12E-06
r_{17}	-4.40E-15	5.80E-10	-2.79E-10	2.08E-07	-2.04E-06
r_{18}	-1.97E-17	2.09E-14	-1.02E-09	4.85E-06	-1.22E-04
r_{19}	1.30E-21	9.39E-17	2.01E-13	8.68E-12	1.66E-10
r_{20}	-1.39E-20	-2.38E-16	-1.83E-13	-5.14E-12	-6.13E-11
r_{21}	-7.24E-26	4.88E-20	1.38E-19	-7.06E-18	4.49E-16
r_{22}	-9.33E-20	-1.08E-15	-6.30E-13	-9.49E-12	-1.01E-10
r_{23}	6.42E-20	7.04E-16	3.77E-13	3.71E-12	3.41E-11
r_{24}	1.52E-20	1.41E-16	7.06E-14	6.41E-13	5.52E-12
r_{25}	2.36E-17	1.87E-13	2.20E-12	-2.75E-09	-2.65E-08
r_{26}	-2.26E-17	5.48E-14	6.18E-13	-6.44E-11	-2.39E-08
r_{27}	-1.02E-18	5.24E-14	-2.81E-12	2.81E-09	5.09E-08
r_{28}	6.65E-21	-2.94E-13	-1.07E-14	7.37E-12	-5.01E-10
r_{29}	1.50E-26	2.00E-21	8.08E-18	3.98E-16	1.40E-14
r_{30}	6.77E-17	3.71E-13	1.32E-10	9.62E-10	7.23E-09
r_{31}	-2.80E-14	-4.52E-10	-1.54E-08	-8.96E-06	9.36E-05
r_{32}	2.81E-14	4.52E-10	1.54E-08	8.96E-06	-9.36E-05
r_{33}	-4.77E-16	2.51E-11	-2.40E-11	2.78E-10	1.33E-08
r_{34}	-3.86E-20	3.81E-14	9.15E-15	-7.52E-12	9.48E-11
r_{35}	4.68E-20	4.62E-16	2.40E-13	-4.79E-11	1.04E-09
r_{36}	-2.88E-17	2.17E-14	-1.12E-12	-1.45E-11	-2.49E-08
r_{37}	-5.93E-19	4.13E-14	-2.01E-12	2.08E-09	3.27E-08
r_{38}	-4.18E-19	1.12E-14	-7.94E-13	7.15E-10	1.56E-08
r_{39}	-4.27E-21	2.10E-18	2.69E-15	1.47E-11	2.66E-09
r_{40}	4.20E-21	1.02E-18	-2.49E-16	-1.18E-11	-8.40E-10

r_{41}	6.34E-23	-1.66E-18	1.86E-16	-3.87E-13	-1.05E-11
r_{42}	-2.80E-14	-4.52E-10	-1.54E-08	-8.96E-06	9.36E-05
r_{43}	-2.91E-17	2.95E-11	1.24E-11	-5.90E-09	5.54E-08
r_{44}	-4.65E-16	7.78E-11	-1.21E-10	7.23E-09	-1.51E-08
r_{45}	-1.19E-16	9.57E-11	1.38E-10	-1.89E-09	2.67E-08
r_{46}	-5.17E-29	-3.49E-23	-2.12E-19	7.05E-16	1.96E-13
r_{47}	-3.80E-14	-5.52E-10	-2.77E-08	8.44E-06	-9.36E-05
r_{48}	2.37E-15	5.89E-10	-4.37E-10	4.78E-06	-1.42E-04
r_{49}	-2.39E-15	-5.89E-10	4.35E-10	-4.78E-06	1.42E-04
r_{50}	-5.93E-25	6.08E-20	1.51E-17	6.23E-13	-1.51E-11
r_{51}	-6.74E-23	3.16E-18	2.51E-15	2.23E-12	1.83E-09
r_{52}	-3.98E-24	1.49E-18	2.69E-15	1.84E-12	1.82E-09
r_{53}	-4.83E-26	-7.62E-21	-3.07E-17	-1.27E-15	-3.99E-12
r_{54}	-1.17E-15	-7.99E-11	-5.91E-11	4.96E-08	3.41E-06
r_{55}	-6.88E-13	-4.07E-09	-2.29E-07	4.53E-06	-1.42E-04
r_{56}	-1.64E-15	-2.09E-12	-1.80E-10	5.68E-08	3.39E-06
r_{57}	2.43E-18	3.18E-15	1.99E-13	-1.79E-12	2.35E-11
r_{58}	-1.19E-18	3.13E-13	2.06E-14	-9.67E-12	8.35E-11
r_{59}	-4.77E-16	2.52E-11	-2.40E-11	2.70E-10	1.34E-08
r_{60}	4.80E-16	6.18E-11	3.66E-11	-2.62E-10	4.23E-08
r_{61}	-1.86E-16	9.53E-11	5.70E-12	-2.84E-09	1.94E-08
r_{62}	1.85E-16	-9.48E-11	-5.63E-12	2.82E-09	-1.92E-08
r_{63}	-7.80E-15	3.20E-09	-1.58E-10	-1.14E-09	1.53E-08
r_{64}	-1.74E-17	8.22E-11	-8.41E-11	1.06E-09	2.69E-08
r_{65}	-6.82E-15	-9.41E-12	-8.62E-10	2.85E-07	1.78E-05
r_{66}	1.77E-17	1.23E-13	5.42E-11	2.52E-10	2.26E-09
r_{67}	6.78E-17	3.72E-13	1.33E-10	9.71E-10	7.33E-09
r_{68}	1.08E-18	4.58E-15	1.34E-12	8.55E-12	5.93E-11
r_{69}	1.56E-22	2.33E-18	1.78E-15	2.43E-14	3.11E-13
r_{70}	6.29E-22	2.06E-17	2.90E-14	6.30E-13	1.19E-11
r_{71}	5.21E-24	9.40E-20	8.12E-17	1.21E-15	1.66E-14
r_{72}	1.77E-17	1.23E-13	5.42E-11	2.52E-10	2.26E-09
r_{73}	2.36E-18	1.08E-14	3.34E-12	1.14E-11	7.84E-11
r_{74}	-1.77E-17	-1.23E-13	-5.40E-11	-2.43E-10	-2.09E-09
r_{75}	1.53E-17	1.12E-13	5.07E-11	2.32E-10	2.02E-09
r_{76}	1.30E-21	9.39E-17	2.01E-13	8.68E-12	1.70E-10
r_{77}	1.53E-17	1.12E-13	5.07E-11	2.32E-10	2.03E-09
r_{78}	2.23E-06	4.38E-04	1.30E-02	1.64E-02	3.23E-02
r_{79}	2.23E-06	4.38E-04	1.30E-02	1.64E-02	3.23E-02
r_{80}	2.72E-24	-3.68E-16	-7.12E-18	7.30E-16	2.27E-15
r_{81}	-1.06E-17	-8.41E-15	-4.19E-13	-1.19E-11	-3.52E-10
r_{82}	4.88E-23	-8.73E-11	-1.24E-11	4.76E-13	-5.57E-08
r_{83}	1.46E-19	-1.55E-14	4.73E-15	1.18E-13	2.21E-12
r_{84}	-1.46E-19	1.52E-14	-4.74E-15	-1.18E-13	-2.21E-12
r_{85}	1.47E-19	-1.53E-14	4.78E-15	1.18E-13	2.22E-12

r_{86}	2.23E-06	4.38E-04	1.30E-02	1.64E-02	3.23E-02
r_{87}	-3.28E-21	1.93E-13	1.05E-14	-1.92E-11	-3.40E-10
r_{88}	8.32E-22	-1.03E-16	3.78E-17	4.82E-16	9.42E-15
r_{89}	-2.44E-21	2.94E-13	1.05E-14	-1.92E-11	-3.40E-10
r_{90}	2.23E-06	4.38E-04	1.30E-02	1.64E-02	3.23E-02
r_{91}	-6.76E-13	-1.04E-09	-2.15E-07	-7.38E-08	-3.52E-10
r_{92}	-1.21E-17	-1.20E-14	-1.32E-12	-1.21E-11	-3.52E-10
r_{93}	-1.06E-17	-8.41E-15	-4.19E-13	-1.19E-11	-3.52E-10
r_{94}	2.23E-06	4.38E-04	1.30E-02	1.64E-02	3.23E-02
r_{95}	-1.50E-16	-3.64E-13	-1.59E-10	-8.69E-10	-2.78E-17
r_{96}	1.57E-21	5.03E-17	1.94E-13	8.47E-12	9.69E-11

B.5 Reaction rates computed at different la conc., i.e. at 0.025 m LA and 1.5 m LA, at varying temperature and hydrogen partial pressures

Table B.4: Computed turnover frequencies at various reaction temperatures, hydrogen partial pressures, and 0.025 M LA solution

a) 1 site model

TOF (s^{-1})		**Hydrogen partial pressure (bar)**			
		4	**10**	**20**	**40**
Temperature (K)	**323**	3.67×10^{-10}	1.47×10^{-10}	7.35×10^{-11}	3.67×10^{-11}
	373	2.52×10^{-6}	1.09×10^{-6}	5.54×10^{-7}	2.78×10^{-7}
	423	6.70×10^{-4}	4.13×10^{-4}	2.38×10^{-4}	1.24×10^{-4}
	473	2.13×10^{-2}	1.60×10^{-2}	1.10×10^{-2}	6.43×10^{-3}
	523	7.79×10^{-2}	7.85×10^{-2}	7.27×10^{-2}	5.90×10^{-2}

b) 2 site model

TOF (s^{-1})		**Hydrogen partial pressure (bar)**			
		4	**10**	**20**	**40**
Temperature (K)	**323**	6.18×10^{-7}	8.39×10^{-7}	1.06×10^{-6}	1.33×10^{-6}
	373	1.21×10^{-4}	1.65×10^{-4}	2.07×10^{-4}	2.61×10^{-4}
	423	3.53×10^{-3}	4.80×10^{-3}	6.06×10^{-3}	7.65×10^{-3}
	473	2.90×10^{-3}	4.42×10^{-3}	6.07×10^{-3}	8.31×10^{-3}
	523	5.29×10^{-3}	8.25×10^{-3}	1.15×10^{-2}	1.60×10^{-2}

Table B.5: Computed turnover frequencies at various reaction temperatures, hydrogen partial pressures, and 1.5 M LA solution

a) 1 site model

TOF (s^{-1})		**Hydrogen partial pressure (bar)**			
		4	**10**	**20**	**40**
Temperature (K)	**323**	2.20×10^{-8}	8.88×10^{-9}	4.45×10^{-9}	2.22×10^{-9}
	373	5.48×10^{-5}	4.12×10^{-5}	2.78×10^{-5}	1.58×10^{-5}
	423	7.99×10^{-3}	7.18×10^{-3}	6.15×10^{-3}	4.76×10^{-3}
	473	1.95×10^{-1}	1.93×10^{-1}	1.80×10^{-1}	1.57×10^{-1}
	523	5.05×10^{-1}	5.95×10^{-1}	6.42×10^{-1}	6.65×10^{-1}

b) 2 site model

TOF (s^{-1})		**Hydrogen partial pressure (bar)**			
		4	**10**	**20**	**40**
Temperature (K)	**323**	2.45×10^{-6}	3.33×10^{-6}	4.19×10^{-6}	5.28×10^{-6}
	373	4.82×10^{-4}	6.54×10^{-4}	8.24×10^{-4}	1.04×10^{-3}
	423	1.43×10^{-2}	1.96×10^{-2}	2.48×10^{-2}	3.14×10^{-2}
	473	1.85×10^{-2}	2.79×10^{-2}	3.77×10^{-2}	5.07×10^{-2}
	523	3.62×10^{-2}	5.59×10^{-2}	7.69×10^{-2}	1.05×10^{-1}

B.6 Surface coverage of all adsorbed surface species at various reaction temperatures

(reported values are from simulation results obtained using 0.45 m LA and 10 bar

hydrogen pressure)

Table B.6: Surface coverage of all the surface species at various temperatures for one site model

Adsorbed species	Temperature (K)				
	323	373	423	473	523
I-1	3.17E-16	1.46E-12	1.13E-10	1.88E-09	2.18E-09
I-2	3.17E-13	2.94E-09	1.99E-07	3.46E-06	2.32E-06
I-3	7.60E-18	6.07E-14	5.76E-12	8.23E-11	1.36E-10
I-4	2.12E-23	4.56E-19	1.24E-16	3.76E-15	1.44E-14
I-5	1.86E-20	1.43E-16	2.49E-14	7.59E-13	1.32E-11
I-6	2.31E-13	2.99E-07	2.06E-05	2.53E-05	6.71E-04
I-7	6.50E-19	1.52E-12	2.33E-10	4.92E-10	2.56E-08
I-8	6.60E-21	1.66E-14	3.42E-12	8.44E-12	7.16E-10
I-9	9.23E-25	1.19E-20	3.27E-18	9.49E-17	4.79E-16
I-10	4.20E-18	1.77E-12	1.04E-10	8.06E-11	4.24E-09

I-11	9.98E-22	1.21E-17	2.41E-15	5.98E-14	2.11E-13
I-12	5.04E-19	1.72E-12	2.05E-10	3.27E-10	1.71E-08
I-13	1.73E-20	2.96E-14	4.81E-12	9.87E-12	6.31E-10
I-14	1.04E-14	3.75E-09	1.61E-07	1.15E-07	3.10E-06
I-15	3.77E-20	7.50E-14	1.07E-11	1.85E-11	1.47E-09
I-16	6.79E-23	9.66E-17	1.42E-14	2.29E-14	2.16E-12
I-17	3.09E-19	3.17E-12	6.59E-10	1.78E-09	1.14E-07
I-18	3.06E-21	1.56E-14	4.29E-12	1.44E-11	1.09E-09
I-19	1.16E-17	2.19E-11	2.72E-09	4.94E-09	2.28E-07
I-20	1.28E-09	2.89E-04	4.68E-03	1.57E-03	2.61E-02
I-21	4.75E-15	4.13E-09	2.60E-07	2.72E-07	8.04E-06
I-22	1.72E-23	6.42E-17	1.48E-14	3.70E-14	3.99E-12
I-23	4.09E-23	3.13E-16	9.37E-14	3.15E-13	3.42E-11
I-24	1.88E-23	7.68E-17	2.44E-14	8.49E-14	9.43E-12
I-25	1.05E-09	3.79E-04	9.10E-03	4.86E-03	6.60E-02
I-26	6.29E-19	3.41E-13	3.08E-11	3.65E-11	1.89E-09
I-27	6.12E-14	6.98E-09	2.07E-07	1.03E-07	3.02E-06
I-28	1.66E-11	1.65E-06	2.99E-05	1.08E-05	1.68E-04
I-29	1.91E-26	8.05E-18	1.41E-14	9.39E-14	3.07E-12
I-30	3.40E-22	1.18E-18	1.29E-16	1.89E-15	5.64E-15
I-31	6.89E-23	1.78E-18	4.52E-16	1.35E-14	4.09E-14
I-32	1.88E-18	6.47E-15	5.12E-13	5.70E-12	1.09E-11
LA	2.24E-11	5.68E-09	9.39E-08	3.97E-07	3.16E-07
Al	1.67E-11	2.39E-09	1.95E-08	4.45E-08	3.36E-08
Hy	1.10E-20	3.81E-17	4.23E-15	6.36E-14	1.95E-13
HPA	1.10E-23	5.52E-20	7.33E-18	1.32E-16	6.20E-16
AGL	2.12E-21	1.19E-14	3.42E-12	1.20E-11	1.06E-09
GVL	6.55E-12	3.15E-10	1.42E-09	2.25E-09	7.55E-10
H	1.00E+00	9.90E-01	9.07E-01	8.41E-01	7.04E-01
OH	2.17E-06	8.87E-05	4.96E-04	8.26E-04	3.94E-04
Free sites	1.47E-06	2.03E-05	1.03E-04	4.00E-04	8.37E-04
I-42	3.76E-30	1.52E-19	7.87E-18	8.31E-18	1.23E-16
I-43	2.99E-18	5.59E-10	1.46E-09	3.45E-10	4.88E-09
I-44	2.03E-22	3.63E-19	2.79E-17	3.49E-16	1.33E-15
I-45	6.60E-23	1.88E-13	2.71E-12	2.89E-12	7.73E-11
I-46	1.35E-05	2.66E-03	1.85E-02	4.61E-02	1.33E-02
I-47	9.33E-13	1.45E-09	4.49E-08	3.57E-07	2.32E-07
I-48	7.91E-22	5.33E-18	6.09E-16	1.21E-14	4.17E-14
I-49	2.21E-09	6.22E-08	2.13E-07	2.29E-07	1.34E-07
H_2O	1.45E-12	4.88E-11	2.98E-10	9.00E-10	1.55E-09
O	1.94E-06	7.38E-05	4.93E-04	1.16E-03	2.12E-03

Note: All reported numbers are the surface coverage over the number of adsorption sites.

Table B.7: Surface coverage of all the surface species at various temperatures for two site model

Adsorbed species	Temperature (K)				
	323	373	423	473	523
I-1	7.67E-12	1.81E-10	1.10E-09	1.81E-10	1.13E-10
I-2	2.22E-07	1.89E-06	5.56E-06	2.32E-07	8.58E-08
I-3	4.09E-16	3.95E-13	3.10E-11	2.17E-10	5.25E-10
I-4	1.14E-21	2.82E-18	4.50E-16	5.51E-15	2.08E-14
I-5	1.56E-17	3.59E-15	1.31E-13	3.20E-13	2.81E-12
I-6	9.96E-07	1.69E-06	3.05E-04	1.30E-03	2.45E-03
I-7	2.60E-12	6.49E-11	2.33E-09	1.41E-08	3.50E-08
I-8	1.08E-15	1.13E-14	1.78E-11	6.26E-10	3.65E-09
I-9	4.74E-22	2.04E-19	9.89E-18	3.02E-17	5.85E-17
I-10	1.29E-12	1.22E-12	2.45E-10	1.85E-09	3.03E-09
I-11	7.08E-19	2.42E-16	1.08E-14	3.17E-14	6.18E-14
I-12	5.97E-12	5.44E-12	1.38E-09	5.21E-09	8.74E-09
I-13	6.79E-14	1.20E-12	3.24E-11	1.57E-10	3.23E-10
I-14	4.91E-08	1.20E-08	1.09E-06	1.82E-06	1.59E-06
I-15	1.16E-14	5.42E-14	3.76E-11	7.63E-10	2.80E-09
I-16	2.09E-17	6.65E-17	3.36E-14	5.24E-13	1.54E-12
I-17	3.66E-12	1.05E-11	6.59E-09	5.10E-08	1.56E-07
I-18	1.23E-14	6.35E-13	4.29E-11	4.12E-10	1.49E-09
I-19	4.99E-11	1.18E-10	2.72E-08	1.41E-07	3.12E-07
I-20	5.28E-04	1.86E-04	2.43E-02	1.16E-01	1.33E-01
I-21	2.26E-08	1.39E-08	2.60E-06	7.80E-06	1.10E-05
I-22	5.31E-18	4.64E-17	5.18E-14	1.53E-12	7.60E-12
I-23	1.27E-17	2.38E-16	4.87E-13	2.34E-11	1.74E-10
I-24	2.86E-18	5.49E-17	1.27E-13	6.29E-12	4.80E-11
I-25	5.02E-03	1.34E-03	1.35E-01	2.50E-01	2.41E-01
I-26	2.46E-12	1.32E-11	1.40E-10	3.23E-10	3.62E-10
I-27	8.62E-09	7.41E-09	7.24E-07	4.25E-06	5.76E-06
I-28	6.61E-05	6.73E-05	2.02E-04	1.71E-04	8.58E-05
I-29	7.36E-17	6.50E-16	4.83E-13	3.72E-13	2.85E-13
I-30	2.28E-19	2.20E-17	3.34E-16	4.55E-16	4.93E-16
I-31	1.24E-18	1.55E-16	2.97E-15	2.50E-15	3.04E-15
I-32	1.18E-15	1.15E-13	1.76E-12	2.73E-12	3.03E-12
LA	1.87E-08	1.36E-07	3.22E-07	5.52E-08	2.18E-08
Al	2.54E-07	1.80E-07	5.86E-08	1.69E-08	1.18E-08
Hy	7.40E-18	7.12E-16	1.10E-14	1.52E-14	1.69E-14
HPA	4.53E-21	2.50E-19	7.77E-18	7.92E-18	4.41E-18
AGL	3.48E-16	8.61E-15	2.64E-11	1.60E-09	1.44E-08
GVL	5.46E-09	7.64E-09	5.37E-09	3.71E-10	7.24E-11
H	1.00E+00	1.00E+00	1.00E+00	9.99E-01	9.97E-01
OH	1.80E-03	2.02E-03	1.15E-03	6.37E-05	1.00E-05

Free sites (*)	4.25E-05	1.00E-04	1.99E-04	1.54E-04	2.24E-04
I-42	2.98E-28	5.05E-14	5.59E-17	4.97E-24	1.09E-17
I-43	0.00E+00	8.11E-06	4.49E-09	0.00E+00	1.70E-08
I-44	3.08E-18	3.28E-17	5.67E-17	7.36E-17	1.75E-16
I-45	7.20E-18	1.41E-08	2.38E-11	2.42E-13	1.89E-10
I-46	3.27E-01	3.31E-01	1.81E-01	4.45E-03	6.55E-04
I-47	6.49E-07	8.43E-07	5.69E-07	7.39E-09	1.15E-09
I-48	1.20E-17	4.22E-16	2.72E-15	8.28E-15	3.94E-14
I-49	1.16E-06	9.49E-07	3.32E-07	2.25E-07	1.78E-07
H_2O	4.25E-11	2.47E-10	5.89E-10	3.36E-10	4.08E-10
O	2.27E-04	3.84E-04	4.32E-04	1.21E-04	4.42E-05
Free sites (Δ)	1.48E-06	2.16E-05	1.69E-04	8.54E-04	3.17E-03

B.7 Kinetic degree of rate control of key transition states at 423 k (reported values are from simulation results obtained using 0.45 m LA and 10 bar hydrogen pressure)

Table B.8: Kinetic rate control of key reaction steps for both one and two site model

Step	**KRC** (1 site microkinetic model)	**KRC** (2 site microkinetic model)
r_1	5.22E-01	2.64E-01
r_2	-2.50E-05	-3.30E-05
r_3	4.76E-01	7.37E-01
r_{79}	2.42E-03	3.87E-03
r_{80}	2.62E-12	-1.16E-09
r_{87}	-8.06E-14	-9.83E-10
r_{91}	4.48E-06	2.20E-05
r_{95}	-1.02E-10	-6.96E-10

APPENDIX C: SUPPORTING INFORMATION FOR INVESTIGATION OF SOLVENT EFFECTS ON THE HYDRODEOXYGENATION OF LEVULINIC ACID OVER Ru(0001)

Mamun, O.; Saleheen, M.; Bond, J.Q.; Heyden, A.

To be submitted

C.1 Eckart tunneling correction

Here, we briefly discuss the mathematical procedure used to calculate Eckart tunneling correction in our rate constant computation. First we calculate parameters, α_1, α_2, and u^*, used by Johnston and Heicklen[1].

$$\alpha_1 = \frac{2\pi E_{for}^{\ddagger}}{hc\nu_{im}} \tag{C1}$$

$$\alpha_2 = \frac{2\pi E_{rev}^{\ddagger}}{hc\nu_{im}} \tag{C2}$$

$$u^* = \frac{hc\nu_{im}}{k_B T} \tag{C3}$$

Where, $E_{for}^{\ddagger}$, $E_{rev}^{\ddagger}$, and ν_{im} are forward barrier, reverse barrier, and imaginary frequency, respectively. Then, We calculate c_{eckart}, ε_0, d, and D using the following formulas,

$$c_{eckart} = \frac{\pi u^* (\alpha_1^{-0.5} + \alpha_2^{-0.5})^2}{8} \tag{C4}$$

$$\varepsilon_0 = -\frac{E_{for}^{\ddagger}}{k_B T} \tag{C5}$$

$$d = \frac{(4\alpha_1\alpha_2 - \pi^2)^{0.5}}{2\pi} \tag{C6}$$

$$D = \begin{cases} \cosh(|2\pi d|) & if \text{ d is real} \\ \cos(|2\pi d|) & if \text{ d is imaginary} \end{cases} \tag{C7}$$

Next, we evaluate K as a function of ε,

$$K(\varepsilon) = \frac{(t_1(\varepsilon) - t_2(\varepsilon))}{t_1(\varepsilon) + D} \exp(-\varepsilon) \tag{C8}$$

Where, $t_1(\varepsilon)$ and $t_2(\varepsilon)$ are computed as,

$$t_1(\varepsilon) = \cosh\left(\left(\frac{\pi \times \left(\varepsilon + \frac{E^{\ddagger}_{for}}{k_B T}\right)}{c_{eckart}}\right)^{0.5} + \left(\frac{\pi \times \left(\varepsilon + \frac{E^{\ddagger}_{rev}}{k_B T}\right)}{c_{eckart}}\right)^{0.5}\right) \quad \text{(C9)}$$

$$t_2(\varepsilon) = \cosh\left(\left(\frac{\pi \times \left(\varepsilon + \frac{E^{\ddagger}_{for}}{k_B T}\right)}{c_{eckart}}\right)^{0.5} - \left(\frac{\pi \times \left(\varepsilon + \frac{E^{\ddagger}_{rev}}{k_B T}\right)}{c_{eckart}}\right)^{0.5}\right) \quad \text{(C10)}$$

Finally, we compute transmission coefficient κ,

$$\kappa = \int_{\varepsilon_0}^{\infty} K(\varepsilon) d\varepsilon \quad \text{(C11)}$$

Table C.1: Eckart tunneling correction, κ (dimensionless), for all the surface reaction processes at different temperatures. For adsorption/desorption, and reaction processes where we don't have a transition state, we write N/A to denote that the transmission coefficient is not available for those steps.

Step	Reaction	Temperature			
		323	373	423	473
$\boldsymbol{r_1}$	$LA(g) + 2* \rightarrow LA*$	N/A	N/A	N/A	N/A
$\boldsymbol{r_2}$	$H_2(g) + 2* \rightarrow 2H*$	N/A	N/A	N/A	N/A
$\boldsymbol{r_3}$	$LA* + H* \rightarrow Al* + *$	1.86	1.58	1.42	1.32
$\boldsymbol{r_4}$	$LA* + H* \rightarrow Hy* + *$	4.77	3.04	2.32	1.93
$\boldsymbol{r_5}$	$Al* + H* \rightarrow HPA*$	4.19	2.77	2.16	1.83
$\boldsymbol{r_6}$	$Hy* + H* \rightarrow HPA*$	2.45	1.92	1.64	1.48
$\boldsymbol{r_7}$	$LA* + 2* \rightarrow I - 1* + H*$	1.71	1.49	1.37	1.29
$\boldsymbol{r_8}$	$LA* + 2* \rightarrow I - 7* + OH*$	1.06	1.00	1.00	1.00
$\boldsymbol{r_9}$	$I - 1* + 2* \rightarrow I - 2* + H*$	2.97	2.22	1.84	1.62
$\boldsymbol{r_{10}}$	$I - 2* \rightarrow I - 3* + 2*$	1.13	1.09	1.07	1.00
$\boldsymbol{r_{11}}$	$I - 3* + H* \rightarrow I - 4* + *$	3.38	2.53	2.08	1.81
$\boldsymbol{r_{12}}$	$I - 1* + * \rightarrow I - 6* + OH*$	1.10	1.07	1.06	1.05
$\boldsymbol{r_{13}}$	$I - 1* \rightarrow I - 5* + *$	N/A	N/A	N/A	N/A
$\boldsymbol{r_{14}}$	$I - 5* + * \rightarrow AGL* + OH*$	1.00	1.00	1.00	1.00
$\boldsymbol{r_{15}}$	$I - 7* + * \rightarrow I - 6* + H*$	1.78	1.53	1.39	1.30
$\boldsymbol{r_{16}}$	$I - 6* \rightarrow AGL* + *$	1.00	1.00	1.00	1.00
$\boldsymbol{r_{17}}$	$I - 7* \rightarrow I - 8* + *$	1.00	1.00	1.00	1.00
$\boldsymbol{r_{18}}$	$AGL* + H* \rightarrow I - 8* + *$	2.17	1.78	1.56	1.43
$\boldsymbol{r_{19}}$	$I - 4* + * \rightarrow AGL* + OH*$	1.00	1.00	1.00	1.00
$\boldsymbol{r_{20}}$	$HPA* + * \rightarrow I - 9* + H*$	1.85	1.57	1.42	1.32
$\boldsymbol{r_{21}}$	$HPA*** \rightarrow I - 10** + OH*$	1.00	1.00	1.00	1.00
$\boldsymbol{r_{22}}$	$I - 9* + * \rightarrow I - 11* + H*$	2.08	1.72	1.52	1.40
$\boldsymbol{r_{23}}$	$I - 9* + * \rightarrow I - 12* + OH*$	1.00	1.00	1.00	1.00
$\boldsymbol{r_{24}}$	$I - 9* + * \rightarrow I - 13* + OH*$	1.00	1.00	1.00	1.00

r_{25}	$I-10*+2*\rightarrow I-12*+H*$	2.21	1.79	1.57	1.43
r_{26}	$I-10*+2*\rightarrow I-14*+H*$	4.60	3.03	2.33	1.95
r_{27}	$I-10*+*\rightarrow I-15*+H*$	1.54	1.40	1.32	1.25
r_{28}	$I-10*\rightarrow I-16*$	N/A	N/A	N/A	N/A
r_{29}	$I-11*+*\rightarrow I-17*+OH*$	1.16	1.12	1.09	1.07
r_{30}	$I-11*+*\rightarrow I-19*+OH*$	1.00	1.00	1.00	1.00
r_{31}	$I-12*+*\rightarrow I-17*+H*$	1.80	1.55	1.41	1.32
r_{32}	$I-12*\rightarrow I-20*+H*$	5.66	3.48	2.57	2.11
r_{33}	$I-13*+*\rightarrow I-18*+H*$	3.36	2.41	1.96	1.70
r_{34}	$I-13*+*\rightarrow I-19*+H*$	2.07	1.70	1.50	1.38
r_{35}	$I-14*\rightarrow I-20*+H*$	5.40	1.99	1.51	1.38
r_{36}	$I-14*+*\rightarrow I-21*+H*$	1.77	1.54	1.40	1.31
r_{37}	$I-15*+2*\rightarrow I-17*+H*$	2.14	1.76	1.55	1.42
r_{38}	$I-15*+2*\rightarrow I-21***+H*$	2.53	1.98	1.70	1.52
r_{39}	$I-15**\rightarrow I-22**$	1.00	1.00	1.00	1.00
r_{40}	$I-16**+*\rightarrow I-22*+H*$	1.88	1.59	1.43	1.33
r_{41}	$I-17*\rightarrow I-23*+*$	1.16	1.12	1.09	1.00
r_{42}	$I-17*+*\rightarrow I-25*+H*$	3.24	2.36	1.93	1.69
r_{43}	$I-18*+*\rightarrow I-6*+H*$	1.32	1.23	1.17	1.00
r_{44}	$I-18*\rightarrow I-24*+*$	1.00	1.00	1.00	1.00
r_{45}	$I-19*+*\rightarrow I-6*+H*$	4.62	3.06	2.36	1.97
r_{46}	$I-20*\rightarrow I-24*$	1.47	1.15	1.11	1.09
r_{47}	$I-20*+2*\rightarrow I-25*+H*$	1.76	1.52	1.38	1.29
r_{48}	$I-21*+*\rightarrow I-25*+H*$	2.31	1.86	1.61	1.46
r_{49}	$I-21*\rightarrow I-8*+*$	1.06	1.04	1.03	1.03
r_{50}	$I-22*+*\rightarrow I-8*+H*$	4.74	2.98	2.26	1.89
r_{51}	$I-22*+*\rightarrow I-23*+H*$	1.60	1.42	1.31	1.24
r_{52}	$I-23*+*\rightarrow AGL*+H*$	4.60	2.92	2.24	1.88
r_{53}	$I-29*\rightarrow I-4*+2*$	N/A	N/A	N/A	N/A
r_{54}	$AGL*+H*\rightarrow I-24*+*$	1.42	1.31	1.24	1.19
r_{55}	$I-25*\rightarrow AGL*+*$	1.08	1.05	1.04	1.03
r_{56}	$I-24*+H*\rightarrow GVL*+*$	2.26	1.81	1.57	1.43
r_{57}	$HPA*+*\rightarrow I-26*+OH*$	1.00	1.00	1.00	1.00
r_{58}	$I-26*\rightarrow I-27*+H*$	2.44	1.91	1.64	1.48
r_{59}	$I-26*+*\rightarrow I-13*+H*$	1.96	1.64	1.47	1.36
r_{60}	$I-26*+*\rightarrow I-28*+H*$	4.27	2.86	2.23	1.88
r_{61}	$I-27*+2*\rightarrow I-19*+H*$	1.18	1.13	1.10	1.00
r_{62}	$I-27*+2*\rightarrow I-7*+H*$	5.14	3.20	2.41	1.99
r_{63}	$I-28*+*\rightarrow I-7*+H*$	1.64	1.44	1.33	1.25
r_{64}	$I-28*+*\rightarrow I-18*+H*$	1.99	1.65	1.47	1.36
r_{65}	$I-8*+H*\rightarrow GVL*+*$	1.60	1.41	1.30	1.24
r_{66}	$Hy*\rightarrow I-30*$	N/A	N/A	N/A	N/A
r_{67}	$Hy*+2*\rightarrow I-11*+H*$	1.82	1.58	1.43	1.34
r_{68}	$Hy*+*\rightarrow I-27*+OH*$	1.09	1.00	1.00	1.00
r_{69}	$Hy*+*\rightarrow I-15*+OH*$	1.14	1.10	1.08	1.06
r_{70}	$Hy*+2*\rightarrow I-31*+H*$	2.33	1.86	1.61	1.46
r_{71}	$I-30*+*\rightarrow I-22*+OH*$	1.00	1.00	1.00	1.00
r_{72}	$I-30*+*\rightarrow I-32*+H*$	4.37	2.98	2.33	1.97
r_{73}	$I-31*+*\rightarrow I-21*+OH*$	1.15	1.00	1.00	1.00
r_{74}	$I-31*\rightarrow I-32*+*$	N/A	N/A	N/A	N/A
r_{75}	$I-31*+2*\rightarrow I-29*+H*$	1.84	1.59	1.44	1.35
r_{76}	$I-32*+*\rightarrow I-4*+H*$	2.07	1.70	1.50	1.38

r_{77}	$I-29*\rightarrow I-25*+OH*$	1.00	1.00	1.00	1.00
r_{78}	$GVL*\rightarrow GVL(g)+2*$	N/A	N/A	N/A	N/A
r_{79}	$OH*+H*\rightarrow H_2O**$	3.36	2.38	1.93	1.68
r_{80}	$HPA*+H*\rightarrow I-33*+2*$	5.72	3.46	2.55	2.08
r_{81}	$I-39*+H*\rightarrow I-40*+2*$	4.00	2.79	2.22	1.89
r_{82}	$I-26*+H*\rightarrow I-34*+3*$	1.95	1.63	1.46	1.35
r_{83}	$I-33*\rightarrow I-34*+OH*$	1.00	1.00	1.00	1.00
r_{84}	$I-33**\rightarrow I-35*+H*$	2.15	1.75	1.54	1.41
r_{85}	$Al*+H*\rightarrow I-35**$	5.54	3.45	2.57	2.11
r_{86}	$Al*\rightarrow I-40**$	1.00	1.00	1.00	1.00
r_{87}	$I-34*+2*\rightarrow I-36*+H*$	5.52	3.33	2.47	2.03
r_{88}	$I-35**\rightarrow I-36*+OH*$	1.25	1.18	1.14	1.00
r_{89}	$I-36*\rightarrow I-16*$	1.08	1.06	1.00	1.00
r_{90}	$I-40*+2*\rightarrow GVL*+OH*$	1.05	1.04	1.03	1.03
r_{91}	$LA*+2*\rightarrow I-37*+H*$	1.70	1.51	1.38	1.30
r_{92}	$I-37*+H*\rightarrow I-38*$	1.23	1.17	1.13	1.10
r_{93}	$I-38*\rightarrow I-39**$	N/A	N/A	N/A	N/A
r_{94}	$H_2O*\rightarrow H_2O(g)+*$	N/A	N/A	N/A	N/A
r_{95}	$OH**\rightarrow H*+O*$	6.35	3.61	2.60	2.10
r_{96}	$HPA*\rightarrow HPA(g)+*$	N/A	N/A	N/A	N/A

C.2 Enthalpic and entropic contribution of solvation on the adsorption strength

To compare the relative contribution of the enthalpic and the entropic term in the free energy of solvation, we use the Van't Hoff equation to compute $\Delta\Delta H$ and $\Delta\Delta S$ from the calculated $\Delta\Delta G$ for each adsorbed thermodynamic and kinetic state of the reaction system. Below, we briefly discuss the procedure we use to calculate $\Delta\Delta H$ and $\Delta\Delta S$. The Van't Hoff equation for any adsorbed intermediate can be written as:

$$\frac{\mathrm{d}\ln K_{eq}}{dT}=\frac{\Delta H}{RT^2} \tag{C12}$$

$$-\frac{\Delta G}{RT}=-\frac{\Delta H}{RT}+\frac{\Delta S}{R} \tag{C13}$$

$$-\frac{(\Delta G_{gas}+\Delta\Delta G)}{RT}=-\frac{(\Delta H_{gas}+\Delta\Delta H)}{RT}+\frac{(\Delta S_{gas}+\Delta\Delta S)}{R} \tag{C14}$$

Separating the gas phase and solvent phase contribution,

$$-\frac{\Delta\Delta G}{RT}=-\frac{\Delta\Delta H}{RT}+\frac{\Delta\Delta S}{R} \tag{C15}$$

In the above equation, $\Delta\Delta H$ is a weak function of temperature while $\Delta\Delta S$ is a strong function. In our calculation, we assume that within a temperature range of ±5 K both the terms are constant. Then, using interpolation formula, specifically, we use linregress function from scipy module, between a temperature range of 318-328 K and 418-428 K, we calculate both $\Delta\Delta H$ and $\Delta\Delta S$ at a temperature of 323 K and 423 K, respectively. In the table below, we list computed $\Delta\Delta H$ and $\Delta\Delta S$ value for all the adsorbed intermediates and transition states. From our analysis, we see that for some species the enthalpic term is the major contributing term while for some other species, the entropic term dominates over the enthalpic term.

Table C.2: Enthalpic and entropic contribution to the adosrption strength of various surface intermediates and transition state structures at 323 K and 423 K

a) Water

Species	T=323 K				T=423K			
	$\Delta\Delta H$ (eV)	$\Delta\Delta S$ (eV/K)	$-T\Delta\Delta S$ (eV)	$\Delta\Delta G$ (eV)	$\Delta\Delta H$ (eV)	$\Delta\Delta S$ (eV/K)	$-T\Delta\Delta S$ (eV)	$\Delta\Delta G$ (eV)
I-1	3.42E-02	-4.00E-04	1.29E-01	1.63E-01	1.98E-01	3.44E-05	-1.45E-02	1.83E-01
I-2	7.31E-02	-1.73E-04	5.59E-02	1.29E-01	2.02E-01	1.71E-04	-7.25E-02	1.29E-01
I-3	5.40E-03	-1.39E-04	4.49E-02	5.03E-02	1.41E-01	2.26E-04	-9.57E-02	4.51E-02
I-4	-1.11E-01	-3.69E-04	1.19E-01	8.35E-03	5.60E-02	8.00E-05	-3.38E-02	2.22E-02
I-5	-4.08E-02	-3.60E-04	1.16E-01	7.54E-02	1.29E-01	9.43E-05	-3.99E-02	8.87E-02
I-6	1.82E-01	-5.22E-05	1.69E-02	1.99E-01	2.91E-01	2.41E-04	-1.02E-01	1.89E-01
I-7	1.92E-01	-1.26E-04	4.07E-02	2.33E-01	3.05E-01	1.77E-04	-7.47E-02	2.31E-01
I-8	1.87E-01	-2.87E-06	9.25E-04	1.87E-01	2.88E-01	2.69E-04	-1.14E-01	1.74E-01
I-9	-1.34E-01	-3.89E-04	1.26E-01	-8.70E-03	2.39E-02	3.41E-05	-1.44E-02	9.50E-03
I-10	-2.00E-01	-4.60E-04	1.49E-01	-5.12E-02	-3.58E-02	-2.12E-05	8.97E-03	-2.68E-02
I-11	6.33E-02	-1.85E-04	5.97E-02	1.23E-01	1.90E-01	1.54E-04	-6.51E-02	1.25E-01
I-12	-1.88E-01	-5.29E-04	1.71E-01	-1.67E-02	-1.25E-02	-6.17E-05	2.61E-02	1.37E-02
I-13	1.24E-01	-2.63E-04	8.50E-02	2.09E-01	2.56E-01	8.60E-05	-3.64E-02	2.19E-01
I-14	8.99E-02	-1.46E-04	4.71E-02	1.37E-01	2.14E-01	1.86E-04	-7.86E-02	1.35E-01
I-15	-1.11E-01	-5.16E-04	1.67E-01	5.60E-02	6.74E-02	-4.02E-05	1.70E-02	8.44E-02
I-16	1.75E-01	-1.61E-04	5.21E-02	2.27E-01	3.00E-01	1.72E-04	-7.28E-02	2.27E-01
I-17	1.12E-01	-1.53E-04	4.96E-02	1.62E-01	2.37E-01	1.80E-04	-7.60E-02	1.61E-01
I-18	1.47E-01	-3.50E-04	1.13E-01	2.60E-01	3.02E-01	6.35E-05	-2.68E-02	2.75E-01
I-19	-4.81E-02	-3.08E-04	9.96E-02	5.15E-02	8.94E-02	5.85E-05	-2.47E-02	6.47E-02
I-20	1.08E-01	-1.39E-04	4.50E-02	1.52E-01	2.47E-01	2.36E-04	-9.98E-02	1.47E-01

I-21	2.15E-01	-1.42E-04	4.59E-02	2.61E-01	3.37E-01	1.82E-04	-7.68E-02	2.60E-01
I-22	1.41E-01	-1.36E-04	4.41E-02	1.85E-01	2.53E-01	1.63E-04	-6.88E-02	1.85E-01
I-23	4.32E-02	-2.42E-04	7.81E-02	1.21E-01	1.77E-01	1.13E-04	-4.77E-02	1.29E-01
I-24	7.19E-02	-8.40E-06	2.71E-03	7.46E-02	1.71E-01	2.60E-04	-1.10E-01	6.17E-02
I-25	1.65E-01	-8.78E-05	2.84E-02	1.93E-01	2.76E-01	2.07E-04	-8.77E-02	1.88E-01
I-26	-8.04E-02	-2.28E-04	7.36E-02	-6.74E-03	4.41E-02	1.06E-04	-4.47E-02	-5.22E-04
I-27	1.32E-01	-2.69E-04	8.69E-02	2.19E-01	2.65E-01	8.33E-05	-3.52E-02	2.30E-01
I-28	2.40E-01	-9.07E-05	2.93E-02	2.69E-01	3.51E-01	2.06E-04	-8.72E-02	2.64E-01
I-29	1.51E-01	-2.64E-04	8.52E-02	2.36E-01	2.94E-01	1.16E-04	-4.92E-02	2.44E-01
I-30	7.95E-02	-1.89E-04	6.09E-02	1.40E-01	2.11E-01	1.61E-04	-6.82E-02	1.42E-01
I-31	-1.48E-01	-2.66E-04	8.60E-02	-6.21E-02	-4.82E-03	1.18E-04	-5.00E-02	-5.48E-02
I-32	-8.37E-02	-3.30E-04	1.07E-01	2.30E-02	8.18E-02	1.15E-04	-4.85E-02	3.34E-02
I-33	2.46E-02	-3.39E-04	1.09E-01	1.34E-01	1.74E-01	5.83E-05	-2.47E-02	1.49E-01
I-34	1.78E-01	-1.15E-04	3.73E-02	2.16E-01	2.94E-01	1.93E-04	-8.15E-02	2.13E-01
I-35	-3.54E-02	-4.06E-04	1.31E-01	9.58E-02	1.12E-01	-1.42E-05	6.00E-03	1.18E-01
I-36	3.33E-01	-8.18E-05	2.64E-02	3.60E-01	4.48E-01	2.24E-04	-9.48E-02	3.54E-01
I-37	5.64E-02	-1.20E-04	3.89E-02	9.53E-02	1.83E-01	2.20E-04	-9.32E-02	8.98E-02
I-38	5.39E-02	-3.66E-04	1.18E-01	1.72E-01	2.19E-01	7.45E-05	-3.15E-02	1.87E-01
I-39	-2.07E-01	-6.50E-04	2.10E-01	3.38E-03	1.47E-02	-5.47E-05	2.31E-02	3.78E-02
I-40	-1.07E-01	-3.82E-04	1.23E-01	1.64E-02	5.62E-02	5.52E-05	-2.33E-02	3.29E-02
LA	1.36E-01	-1.99E-06	6.43E-04	1.37E-01	2.44E-01	2.88E-04	-1.22E-01	1.22E-01
Al	-8.69E-02	-5.20E-04	1.68E-01	8.10E-02	8.73E-02	-5.50E-05	2.32E-02	1.11E-01
Hy	-2.29E-01	-7.60E-04	2.45E-01	1.68E-02	-1.96E-02	-2.01E-04	8.52E-02	6.57E-02
HPA	-1.87E-02	-4.70E-04	1.52E-01	1.33E-01	1.45E-01	-3.50E-05	1.48E-02	1.60E-01
AGL	1.32E-01	-1.27E-04	4.09E-02	1.72E-01	2.60E-01	2.16E-04	-9.13E-02	1.68E-01
GVL	1.71E-01	-1.91E-04	6.18E-02	2.33E-01	3.05E-01	1.66E-04	-7.03E-02	2.34E-01
H	6.25E-02	-1.66E-04	5.35E-02	1.16E-01	1.00E-01	-6.77E-05	2.86E-02	1.29E-01
OH	7.16E-03	-5.31E-04	1.72E-01	1.79E-01	9.83E-02	-2.92E-04	1.23E-01	2.22E-01
H2O	-6.84E-03	-3.90E-04	1.26E-01	1.19E-01	6.61E-02	-1.99E-04	8.43E-02	1.50E-01
O	-2.84E-02	-1.96E-04	6.31E-02	3.47E-02	2.67E-02	-4.97E-05	2.10E-02	4.78E-02
TS-3	-2.16E-01	-7.69E-04	2.48E-01	3.29E-02	-1.20E-02	-2.25E-04	9.52E-02	8.32E-02
TS-4	-2.35E-02	-5.60E-04	1.81E-01	1.57E-01	1.71E-01	-4.12E-05	1.74E-02	1.88E-01
TS-5	2.33E-01	-8.52E-05	2.75E-02	2.60E-01	3.51E-01	2.29E-04	-9.69E-02	2.54E-01
TS-6	-1.06E-01	-4.94E-04	1.60E-01	5.34E-02	6.14E-02	-4.83E-05	2.04E-02	8.19E-02
TS-7	2.26E-02	-2.01E-04	6.50E-02	8.76E-02	1.49E-01	1.36E-04	-5.77E-02	9.14E-02
TS-8	-5.06E-02	-2.41E-04	7.78E-02	2.72E-02	8.51E-02	1.22E-04	-5.17E-02	3.34E-02
TS-9	1.92E-01	-2.61E-05	8.42E-03	2.01E-01	3.04E-01	2.73E-04	-1.16E-01	1.89E-01
TS-10	1.28E-01	4.72E-05	-1.52E-02	1.13E-01	2.30E-01	3.22E-04	-1.36E-01	9.40E-02
TS-11	1.08E-01	-4.28E-05	1.38E-02	1.22E-01	2.18E-01	2.52E-04	-1.07E-01	1.11E-01
TS-12	1.52E-01	-1.46E-04	4.72E-02	1.99E-01	2.82E-01	2.02E-04	-8.56E-02	1.97E-01
TS-14	-4.93E-02	-1.57E-04	5.06E-02	1.34E-03	9.00E-02	2.18E-04	-9.24E-02	-2.40E-03
TS-15	1.74E-01	-1.31E-04	4.24E-02	2.16E-01	2.90E-01	1.79E-04	-7.58E-02	2.14E-01
TS-16	1.90E-01	-4.68E-05	1.51E-02	2.06E-01	2.95E-01	2.32E-04	-9.80E-02	1.97E-01
TS-17	1.72E-01	-8.76E-05	2.83E-02	2.00E-01	2.86E-01	2.19E-04	-9.25E-02	1.94E-01

TS-18	1.53E-01	-6.73E-05	2.17E-02	1.75E-01	2.60E-01	2.20E-04	-9.30E-02	1.68E-01
TS-19	1.01E-01	-6.50E-05	2.10E-02	1.22E-01	2.19E-01	2.50E-04	-1.06E-01	1.13E-01
TS-20	2.08E-02	-3.53E-04	1.14E-01	1.35E-01	1.78E-01	6.58E-05	-2.78E-02	1.50E-01
TS-21	1.94E-02	-3.27E-04	1.06E-01	1.25E-01	1.55E-01	3.40E-05	-1.44E-02	1.41E-01
TS-22	1.10E-01	-2.21E-04	7.14E-02	1.82E-01	2.40E-01	1.23E-04	-5.21E-02	1.88E-01
TS-23	-3.10E-01	-6.18E-04	2.00E-01	-1.10E-01	-1.12E-01	-8.88E-05	3.76E-02	-7.42E-02
TS-24	-1.11E-01	-4.47E-04	1.44E-01	3.38E-02	5.11E-02	-1.60E-05	6.78E-03	5.79E-02
TS-25	2.40E-01	-1.38E-04	4.45E-02	2.84E-01	3.53E-01	1.64E-04	-6.92E-02	2.84E-01
TS-26	2.67E-01	-1.33E-05	4.30E-03	2.72E-01	3.68E-01	2.55E-04	-1.08E-01	2.60E-01
TS-27	2.32E-01	5.62E-06	-1.81E-03	2.30E-01	3.28E-01	2.62E-04	-1.11E-01	2.17E-01
TS-29	-1.76E-01	-5.37E-04	1.73E-01	-2.31E-03	-3.80E-03	-7.93E-05	3.35E-02	2.98E-02
TS-30	-4.99E-02	-1.92E-04	6.20E-02	1.22E-02	7.31E-02	1.36E-04	-5.77E-02	1.54E-02
TS-31	2.43E-02	-2.43E-04	7.84E-02	1.03E-01	1.53E-01	1.00E-04	-4.24E-02	1.11E-01
TS-32	2.60E-01	-8.15E-06	2.63E-03	2.63E-01	3.53E-01	2.39E-04	-1.01E-01	2.52E-01
TS-33	1.52E-01	-1.92E-04	6.20E-02	2.14E-01	2.73E-01	1.29E-04	-5.48E-02	2.18E-01
TS-34	-1.50E-01	-4.20E-04	1.36E-01	-1.43E-02	2.67E-03	-1.18E-05	4.97E-03	7.67E-03
TS-35	1.17E-01	-3.54E-04	1.14E-01	2.32E-01	2.71E-01	5.50E-05	-2.33E-02	2.47E-01
TS-36	1.75E-01	-1.61E-04	5.21E-02	2.27E-01	2.99E-01	1.67E-04	-7.07E-02	2.28E-01
TS-37	8.29E-02	-8.26E-05	2.67E-02	1.10E-01	1.90E-01	2.04E-04	-8.64E-02	1.04E-01
TS-38	2.93E-01	2.82E-05	-9.11E-03	2.84E-01	3.85E-01	2.75E-04	-1.16E-01	2.69E-01
TS-39	1.75E-01	-2.28E-04	7.37E-02	2.49E-01	2.97E-01	9.38E-05	-3.97E-02	2.57E-01
TS-40	1.21E-01	-2.12E-04	6.84E-02	1.89E-01	2.47E-01	1.22E-04	-5.18E-02	1.95E-01
TS-41	1.29E-01	-1.53E-04	4.93E-02	1.79E-01	2.49E-01	1.66E-04	-7.03E-02	1.79E-01
TS-42	2.22E-01	6.66E-05	-2.15E-02	2.00E-01	3.03E-01	2.84E-04	-1.20E-01	1.83E-01
TS-43	8.33E-02	-2.98E-04	9.62E-02	1.80E-01	2.34E-01	1.06E-04	-4.47E-02	1.90E-01
TS-44	1.63E-01	-8.49E-05	2.74E-02	1.91E-01	2.71E-01	2.04E-04	-8.63E-02	1.85E-01
TS-45	2.47E-01	-6.34E-05	2.05E-02	2.68E-01	3.55E-01	2.22E-04	-9.40E-02	2.61E-01
TS-46	1.18E-01	1.84E-06	-5.94E-04	1.18E-01	2.23E-01	2.83E-04	-1.20E-01	1.03E-01
TS-47	2.11E-01	-1.02E-04	3.30E-02	2.44E-01	3.29E-01	2.13E-04	-9.02E-02	2.39E-01
TS-48	2.12E-01	-1.01E-04	3.26E-02	2.45E-01	3.28E-01	2.09E-04	-8.84E-02	2.40E-01
TS-49	1.11E-01	-3.28E-05	1.06E-02	1.21E-01	2.09E-01	2.30E-04	-9.75E-02	1.11E-01
TS-50	1.88E-01	1.81E-05	-5.84E-03	1.82E-01	2.87E-01	2.84E-04	-1.20E-01	1.67E-01
TS-51	-3.56E-02	-2.64E-04	8.54E-02	4.99E-02	8.40E-02	5.36E-05	-2.27E-02	6.13E-02
TS-52	1.36E-01	-1.10E-04	3.54E-02	1.72E-01	2.58E-01	2.16E-04	-9.16E-02	1.67E-01
TS-54	-6.85E-03	-8.12E-05	2.62E-02	1.94E-02	1.02E-01	2.10E-04	-8.90E-02	1.26E-02
TS-55	2.42E-01	-2.45E-05	7.92E-03	2.50E-01	3.40E-01	2.38E-04	-1.01E-01	2.40E-01
TS-56	7.80E-02	-7.42E-05	2.40E-02	1.02E-01	1.77E-01	1.91E-04	-8.07E-02	9.63E-02
TS-57	-5.96E-03	-3.76E-04	1.21E-01	1.15E-01	1.48E-01	3.42E-05	-1.44E-02	1.33E-01
TS-58	1.01E-02	-3.16E-04	1.02E-01	1.12E-01	1.45E-01	4.40E-05	-1.86E-02	1.27E-01
TS-59	5.79E-02	-2.25E-04	7.27E-02	1.31E-01	1.87E-01	1.20E-04	-5.08E-02	1.36E-01
TS-60	2.08E-01	-1.89E-04	6.10E-02	2.69E-01	3.31E-01	1.38E-04	-5.85E-02	2.73E-01
TS-61	1.72E-01	-5.63E-05	1.82E-02	1.90E-01	2.67E-01	1.96E-04	-8.30E-02	1.84E-01
TS-62	1.83E-01	-2.08E-04	6.71E-02	2.50E-01	3.14E-01	1.41E-04	-5.96E-02	2.54E-01
TS-63	1.72E-01	-7.36E-05	2.38E-02	1.95E-01	2.75E-01	2.03E-04	-8.61E-02	1.89E-01

TS-64	7.40E-02	-2.50E-04	8.09E-02	1.55E-01	2.17E-01	1.33E-04	-5.62E-02	1.61E-01
TS-65	1.64E-01	-2.43E-05	7.84E-03	1.72E-01	2.61E-01	2.34E-04	-9.90E-02	1.62E-01
TS-67	1.24E-01	-1.81E-04	5.83E-02	1.83E-01	2.49E-01	1.50E-04	-6.36E-02	1.85E-01
TS-68	1.71E-01	-9.82E-05	3.17E-02	2.03E-01	2.77E-01	1.86E-04	-7.85E-02	1.99E-01
TS-69	-3.67E-02	-3.84E-04	1.24E-01	8.75E-02	1.16E-01	2.32E-05	-9.81E-03	1.06E-01
TS-70	6.72E-02	-2.14E-04	6.92E-02	1.36E-01	1.96E-01	1.32E-04	-5.57E-02	1.41E-01
TS-71	1.65E-02	-1.10E-04	3.56E-02	5.21E-02	1.29E-01	1.92E-04	-8.11E-02	4.82E-02
TS-72	1.15E-01	-1.59E-04	5.15E-02	1.67E-01	2.44E-01	1.86E-04	-7.86E-02	1.66E-01
TS-73	-8.66E-03	-2.58E-04	8.34E-02	7.48E-02	1.29E-01	1.10E-04	-4.65E-02	8.27E-02
TS-75	1.23E-01	-1.95E-04	6.30E-02	1.86E-01	2.53E-01	1.52E-04	-6.43E-02	1.88E-01
TS-76	-1.13E-01	-3.58E-04	1.16E-01	2.75E-03	4.42E-02	6.51E-05	-2.75E-02	1.67E-02
TS-77	2.96E-02	-3.07E-04	9.90E-02	1.29E-01	1.78E-01	9.05E-05	-3.83E-02	1.40E-01
TS-78	-8.26E-02	-3.42E-04	1.10E-01	2.79E-02	-8.74E-03	-1.48E-04	6.24E-02	5.37E-02
TS-80	9.66E-02	-2.38E-04	7.67E-02	1.73E-01	2.39E-01	1.44E-04	-6.07E-02	1.79E-01
TS-81	5.36E-03	-3.15E-04	1.02E-01	1.07E-01	1.57E-01	9.29E-05	-3.93E-02	1.18E-01
TS-82	1.30E-01	-1.97E-04	6.35E-02	1.94E-01	2.57E-01	1.42E-04	-6.02E-02	1.97E-01
TS-83	-1.49E-01	-4.84E-04	1.56E-01	7.22E-03	1.89E-02	-3.60E-05	1.52E-02	3.41E-02
TS-84	-2.25E-02	-4.86E-04	1.57E-01	1.35E-01	1.48E-01	-3.09E-05	1.31E-02	1.61E-01
TS-85	1.64E-01	-2.39E-04	7.73E-02	2.41E-01	2.92E-01	9.98E-05	-4.22E-02	2.49E-01
TS-86	2.40E-01	-6.03E-05	1.95E-02	2.59E-01	3.57E-01	2.52E-04	-1.07E-01	2.50E-01
TS-87	3.03E-01	-3.71E-05	1.20E-02	3.15E-01	4.05E-01	2.33E-04	-9.87E-02	3.06E-01
TS-88	-1.05E-01	-4.58E-04	1.48E-01	4.27E-02	4.40E-02	-6.20E-05	2.62E-02	7.02E-02
TS-89	-2.37E-01	-6.75E-04	2.18E-01	-1.94E-02	-4.54E-02	-1.63E-04	6.90E-02	2.36E-02
TS-90	6.58E-02	-2.03E-04	6.54E-02	1.31E-01	2.05E-01	1.71E-04	-7.23E-02	1.33E-01
TS-91	3.56E-02	-1.14E-04	3.69E-02	7.25E-02	1.59E-01	2.18E-04	-9.22E-02	6.66E-02
TS-92	6.08E-02	-1.81E-04	5.86E-02	1.19E-01	1.99E-01	1.89E-04	-7.98E-02	1.19E-01
TS-95	-5.30E-01	-8.83E-04	2.85E-01	-2.45E-01	-3.56E-01	-4.16E-04	1.76E-01	-1.80E-01

b) Methanol

Species	T=323 K				T=423K			
	$\Delta\Delta H$	$\Delta\Delta S$	$-T\Delta\Delta S$	$\Delta\Delta G$	$\Delta\Delta H$	$\Delta\Delta S$	$-T\Delta\Delta S$	$\Delta\Delta G$
I-1	-1.03E-01	-5.10E-04	1.65E-01	6.15E-02	3.90E-02	-1.30E-04	5.51E-02	9.42E-02
I-2	2.05E-01	2.26E-04	-7.29E-02	1.32E-01	2.01E-01	2.14E-04	-9.06E-02	1.11E-01
I-3	8.30E-02	1.77E-04	-5.73E-02	2.57E-02	8.57E-02	1.83E-04	-7.76E-02	8.17E-03
I-4	-1.10E-01	-3.05E-04	9.87E-02	-1.17E-02	-1.43E-02	-4.81E-05	2.03E-02	6.02E-03
I-5	-8.26E-02	-2.50E-04	8.07E-02	-1.80E-03	1.27E-02	5.22E-06	-2.21E-03	1.05E-02
I-6	2.38E-01	1.98E-04	-6.40E-02	1.74E-01	2.44E-01	2.13E-04	-9.00E-02	1.54E-01
I-7	2.14E-01	1.28E-04	-4.13E-02	1.72E-01	2.28E-01	1.66E-04	-7.02E-02	1.58E-01
I-8	1.90E-01	1.83E-04	-5.92E-02	1.31E-01	2.03E-01	2.17E-04	-9.20E-02	1.11E-01
I-9	-1.03E-01	-2.25E-04	7.28E-02	-3.05E-02	-2.16E-02	-7.69E-06	3.25E-03	-1.83E-02
I-10	-3.24E-01	-6.13E-04	1.98E-01	-1.26E-01	-1.73E-01	-2.08E-04	8.81E-02	-8.51E-02
I-11	-6.73E-02	-3.37E-04	1.09E-01	4.15E-02	5.52E-02	-7.62E-06	3.22E-03	5.84E-02
I-12	-3.13E-01	-6.93E-04	2.24E-01	-8.87E-02	-1.48E-01	-2.52E-04	1.07E-01	-4.11E-02

I-13	9.88E-02	-1.71E-04	5.51E-02	1.54E-01	1.75E-01	3.26E-05	-1.38E-02	1.61E-01
I-14	1.39E-01	1.64E-04	-5.30E-02	8.63E-02	1.52E-01	1.96E-04	-8.27E-02	6.90E-02
I-15	-2.01E-01	-5.77E-04	1.86E-01	-1.45E-02	-5.40E-02	-1.84E-04	7.78E-02	2.38E-02
I-16	1.26E-01	-3.31E-05	1.07E-02	1.37E-01	1.87E-01	1.30E-04	-5.51E-02	1.32E-01
I-17	-3.25E-03	-2.39E-04	7.72E-02	7.39E-02	9.58E-02	2.62E-05	-1.11E-02	8.47E-02
I-18	2.14E-01	4.71E-05	-1.52E-02	1.99E-01	2.45E-01	1.28E-04	-5.40E-02	1.91E-01
I-19	-6.95E-02	-2.51E-04	8.12E-02	1.17E-02	1.81E-02	-1.75E-05	7.41E-03	2.56E-02
I-20	1.04E-01	9.85E-05	-3.18E-02	7.21E-02	1.29E-01	1.66E-04	-7.03E-02	5.92E-02
I-21	2.58E-01	1.64E-04	-5.30E-02	2.05E-01	2.70E-01	1.95E-04	-8.23E-02	1.88E-01
I-22	8.71E-02	-8.52E-05	2.75E-02	1.15E-01	1.54E-01	9.20E-05	-3.89E-02	1.15E-01
I-23	-7.54E-02	-3.47E-04	1.12E-01	3.68E-02	3.95E-02	-4.00E-05	1.69E-02	5.64E-02
I-24	1.17E-01	1.90E-04	-6.13E-02	5.61E-02	1.23E-01	2.04E-04	-8.64E-02	3.67E-02
I-25	2.29E-01	1.97E-04	-6.35E-02	1.66E-01	2.36E-01	2.12E-04	-8.98E-02	1.46E-01
I-26	-1.01E-01	-1.60E-04	5.16E-02	-4.94E-02	-3.00E-02	3.03E-05	-1.28E-02	-4.28E-02
I-27	1.07E-01	-1.60E-04	5.18E-02	1.59E-01	1.83E-01	4.13E-05	-1.75E-02	1.66E-01
I-28	2.50E-01	1.54E-04	-4.97E-02	2.00E-01	2.66E-01	1.94E-04	-8.20E-02	1.84E-01
I-29	1.49E-01	-7.53E-05	2.43E-02	1.74E-01	2.14E-01	9.66E-05	-4.09E-02	1.73E-01
I-30	5.62E-02	-7.78E-05	2.51E-02	8.14E-02	1.26E-01	1.10E-04	-4.66E-02	7.97E-02
I-31	-1.29E-01	-1.31E-04	4.25E-02	-8.62E-02	-5.99E-02	5.25E-05	-2.22E-02	-8.21E-02
I-32	2.31E-02	5.55E-05	-1.79E-02	5.15E-03	5.08E-02	1.28E-04	-5.44E-02	-3.56E-03
I-33	-1.75E-02	-2.62E-04	8.45E-02	6.71E-02	7.80E-02	-6.83E-06	2.89E-03	8.09E-02
I-34	1.50E-01	2.16E-05	-6.98E-03	1.43E-01	1.98E-01	1.51E-04	-6.37E-02	1.34E-01
I-35	-1.40E-01	-5.04E-04	1.63E-01	2.24E-02	3.37E-03	-1.19E-04	5.02E-02	5.36E-02
I-36	2.76E-01	1.07E-04	-3.44E-02	2.42E-01	3.07E-01	1.86E-04	-7.87E-02	2.28E-01
I-37	1.27E-01	1.74E-04	-5.61E-02	7.09E-02	1.37E-01	1.99E-04	-8.41E-02	5.27E-02
I-38	1.92E-01	9.29E-05	-3.00E-02	1.62E-01	2.17E-01	1.58E-04	-6.67E-02	1.50E-01
I-39	-1.19E-01	-2.50E-04	8.06E-02	-3.86E-02	-4.12E-02	-4.18E-05	1.77E-02	-2.35E-02
I-40	-8.64E-02	-2.00E-04	6.46E-02	-2.18E-02	-3.26E-03	2.26E-05	-9.58E-03	-1.28E-02
LA	1.17E-01	1.41E-04	-4.56E-02	7.11E-02	1.37E-01	1.95E-04	-8.24E-02	5.43E-02
Al	-2.15E-01	-6.49E-04	2.10E-01	-5.18E-03	-5.78E-02	-2.29E-04	9.67E-02	3.89E-02
Hy	-2.51E-01	-7.21E-04	2.33E-01	-1.82E-02	-8.56E-02	-2.78E-04	1.18E-01	3.21E-02
HPA	-3.99E-02	-3.73E-04	1.21E-01	8.07E-02	7.71E-02	-6.04E-05	2.55E-02	1.03E-01
AGL	1.96E-01	1.79E-04	-5.78E-02	1.38E-01	2.05E-01	2.01E-04	-8.51E-02	1.20E-01
GVL	2.00E-01	1.19E-04	-3.84E-02	1.62E-01	2.21E-01	1.72E-04	-7.28E-02	1.48E-01
H	5.13E-02	-4.27E-05	1.38E-02	6.51E-02	6.38E-02	-1.09E-05	4.59E-03	6.84E-02
OH	-1.07E-01	-6.72E-04	2.17E-01	1.11E-01	2.17E-02	-3.30E-04	1.39E-01	1.61E-01
H2O	-1.05E-01	-4.94E-04	1.60E-01	5.46E-02	-1.07E-03	-2.17E-04	9.18E-02	9.07E-02
O	2.18E-02	2.51E-05	-8.11E-03	1.37E-02	2.49E-02	3.16E-05	-1.34E-02	1.15E-02
TS-3	-1.91E-01	-6.12E-04	1.98E-01	6.92E-03	-5.80E-02	-2.58E-04	1.09E-01	5.12E-02
TS-4	-2.01E-02	-3.41E-04	1.10E-01	8.99E-02	8.26E-02	-6.69E-05	2.83E-02	1.11E-01
TS-5	1.83E-01	5.19E-05	-1.68E-02	1.67E-01	2.29E-01	1.75E-04	-7.39E-02	1.56E-01
TS-6	-2.50E-01	-7.01E-04	2.26E-01	-2.36E-02	-7.01E-02	-2.18E-04	9.24E-02	2.23E-02
TS-7	2.11E-03	-1.35E-04	4.36E-02	4.58E-02	7.66E-02	6.41E-05	-2.71E-02	4.95E-02
TS-8	-3.93E-02	-1.02E-04	3.29E-02	-6.38E-03	2.49E-02	7.00E-05	-2.96E-02	-4.64E-03

TS-9	1.86E-01	1.61E-04	-5.19E-02	1.34E-01	2.03E-01	2.05E-04	-8.67E-02	1.16E-01
TS-10	1.09E-01	1.81E-04	-5.84E-02	5.07E-02	1.25E-01	2.23E-04	-9.44E-02	3.08E-02
TS-11	1.50E-01	1.69E-04	-5.47E-02	9.49E-02	1.60E-01	1.96E-04	-8.30E-02	7.70E-02
TS-12	9.56E-02	-3.48E-05	1.12E-02	1.07E-01	1.55E-01	1.25E-04	-5.27E-02	1.03E-01
TS-14	-6.30E-02	-1.32E-05	4.27E-03	-5.87E-02	-1.29E-02	1.22E-04	-5.15E-02	-6.43E-02
TS-15	2.28E-01	1.76E-04	-5.70E-02	1.71E-01	2.38E-01	2.01E-04	-8.49E-02	1.53E-01
TS-16	2.28E-01	2.08E-04	-6.73E-02	1.60E-01	2.32E-01	2.18E-04	-9.23E-02	1.40E-01
TS-17	2.29E-01	2.04E-04	-6.58E-02	1.63E-01	2.35E-01	2.17E-04	-9.18E-02	1.43E-01
TS-18	2.05E-01	1.85E-04	-5.99E-02	1.45E-01	2.10E-01	1.96E-04	-8.30E-02	1.27E-01
TS-19	4.79E-02	-5.05E-05	1.63E-02	6.42E-02	1.13E-01	1.25E-04	-5.27E-02	6.04E-02
TS-20	1.92E-03	-2.45E-04	7.91E-02	8.10E-02	9.46E-02	2.55E-06	-1.08E-03	9.35E-02
TS-21	-3.99E-03	-2.87E-04	9.26E-02	8.87E-02	9.70E-02	-1.67E-05	7.05E-03	1.04E-01
TS-22	-1.74E-02	-3.47E-04	1.12E-01	9.46E-02	1.08E-01	-1.06E-05	4.49E-03	1.12E-01
TS-23	-4.59E-01	-7.96E-04	2.57E-01	-2.02E-01	-2.70E-01	-2.87E-04	1.21E-01	-1.48E-01
TS-24	-1.47E-01	-4.28E-04	1.38E-01	-8.49E-03	-2.17E-02	-9.34E-05	3.95E-02	1.78E-02
TS-25	1.84E-01	-4.72E-05	1.52E-02	1.99E-01	2.45E-01	1.14E-04	-4.84E-02	1.96E-01
TS-26	2.44E-01	1.73E-04	-5.58E-02	1.88E-01	2.62E-01	2.19E-04	-9.25E-02	1.70E-01
TS-27	1.71E-01	6.92E-05	-2.23E-02	1.48E-01	2.07E-01	1.67E-04	-7.08E-02	1.37E-01
TS-29	-3.25E-01	-7.65E-04	2.47E-01	-7.81E-02	-1.40E-01	-2.68E-04	1.13E-01	-2.64E-02
TS-30	-7.78E-02	-1.61E-04	5.21E-02	-2.57E-02	3.71E-03	5.79E-05	-2.45E-02	-2.08E-02
TS-31	-7.35E-02	-3.42E-04	1.11E-01	3.71E-02	3.85E-02	-4.25E-05	1.80E-02	5.65E-02
TS-32	2.69E-01	2.02E-04	-6.51E-02	2.03E-01	2.78E-01	2.24E-04	-9.46E-02	1.83E-01
TS-33	2.01E-01	1.26E-04	-4.07E-02	1.60E-01	2.15E-01	1.61E-04	-6.80E-02	1.47E-01
TS-34	-1.26E-01	-2.94E-04	9.49E-02	-3.13E-02	-3.93E-02	-6.23E-05	2.64E-02	-1.29E-02
TS-35	2.44E-01	1.22E-04	-3.93E-02	2.05E-01	2.52E-01	1.38E-04	-5.84E-02	1.93E-01
TS-36	2.38E-01	1.78E-04	-5.76E-02	1.80E-01	2.48E-01	2.02E-04	-8.52E-02	1.62E-01
TS-37	-1.28E-02	-1.28E-04	4.13E-02	2.86E-02	6.32E-02	7.56E-05	-3.20E-02	3.12E-02
TS-38	2.75E-01	1.86E-04	-5.99E-02	2.15E-01	2.90E-01	2.24E-04	-9.47E-02	1.95E-01
TS-39	1.81E-01	-3.27E-05	1.06E-02	1.92E-01	2.32E-01	1.02E-04	-4.34E-02	1.89E-01
TS-40	7.07E-02	-1.27E-04	4.09E-02	1.12E-01	1.47E-01	7.62E-05	-3.22E-02	1.15E-01
TS-41	2.01E-01	1.63E-04	-5.26E-02	1.48E-01	2.09E-01	1.83E-04	-7.73E-02	1.32E-01
TS-42	2.25E-01	2.16E-04	-6.98E-02	1.55E-01	2.33E-01	2.35E-04	-9.94E-02	1.33E-01
TS-43	2.02E-01	1.59E-04	-5.14E-02	1.51E-01	2.07E-01	1.70E-04	-7.17E-02	1.36E-01
TS-44	2.28E-01	1.95E-04	-6.31E-02	1.65E-01	2.34E-01	2.08E-04	-8.78E-02	1.46E-01
TS-45	2.73E-01	1.92E-04	-6.21E-02	2.11E-01	2.81E-01	2.13E-04	-9.02E-02	1.91E-01
TS-46	1.00E-01	1.61E-04	-5.19E-02	4.86E-02	1.17E-01	2.05E-04	-8.67E-02	3.07E-02
TS-47	2.15E-01	1.54E-04	-4.99E-02	1.65E-01	2.33E-01	2.01E-04	-8.49E-02	1.49E-01
TS-48	2.49E-01	1.71E-04	-5.52E-02	1.94E-01	2.61E-01	2.00E-04	-8.45E-02	1.77E-01
TS-49	1.55E-01	1.83E-04	-5.90E-02	9.62E-02	1.60E-01	1.94E-04	-8.19E-02	7.78E-02
TS-50	1.70E-01	1.87E-04	-6.05E-02	1.10E-01	1.86E-01	2.27E-04	-9.62E-02	8.93E-02
TS-51	-1.34E-01	-3.98E-04	1.28E-01	-5.79E-03	-1.95E-02	-9.02E-05	3.82E-02	1.87E-02
TS-52	1.68E-01	1.51E-04	-4.88E-02	1.19E-01	1.82E-01	1.87E-04	-7.92E-02	1.03E-01
TS-54	5.26E-02	1.56E-04	-5.05E-02	2.14E-03	5.78E-02	1.69E-04	-7.14E-02	-1.36E-02
TS-55	2.55E-01	1.76E-04	-5.67E-02	1.98E-01	2.65E-01	2.02E-04	-8.53E-02	1.80E-01

TS-56	1.70E-01	1.86E-04	-6.01E-02	1.10E-01	1.69E-01	1.83E-04	-7.74E-02	9.17E-02
TS-57	1.73E-02	-1.92E-04	6.19E-02	7.93E-02	9.97E-02	2.84E-05	-1.20E-02	8.77E-02
TS-58	6.96E-03	-2.21E-04	7.13E-02	7.82E-02	8.73E-02	-6.46E-06	2.73E-03	9.01E-02
TS-59	2.53E-02	-1.54E-04	4.98E-02	7.51E-02	1.02E-01	5.00E-05	-2.12E-02	8.05E-02
TS-60	2.66E-01	1.60E-04	-5.16E-02	2.15E-01	2.77E-01	1.85E-04	-7.84E-02	1.98E-01
TS-61	1.46E-01	2.17E-05	-7.00E-03	1.39E-01	1.88E-01	1.34E-04	-5.68E-02	1.32E-01
TS-62	2.50E-01	1.44E-04	-4.65E-02	2.04E-01	2.62E-01	1.73E-04	-7.31E-02	1.89E-01
TS-63	2.29E-01	1.98E-04	-6.41E-02	1.65E-01	2.33E-01	2.07E-04	-8.75E-02	1.45E-01
TS-64	1.43E-01	9.13E-05	-2.95E-02	1.14E-01	1.65E-01	1.47E-04	-6.22E-02	1.03E-01
TS-65	1.85E-01	1.75E-04	-5.67E-02	1.28E-01	1.94E-01	1.97E-04	-8.33E-02	1.10E-01
TS-67	5.00E-02	-1.52E-04	4.92E-02	9.92E-02	1.37E-01	8.16E-05	-3.45E-02	1.03E-01
TS-68	1.45E-01	4.35E-06	-1.41E-03	1.44E-01	1.90E-01	1.25E-04	-5.30E-02	1.37E-01
TS-69	-9.19E-02	-3.91E-04	1.26E-01	3.45E-02	2.85E-02	-6.79E-05	2.87E-02	5.73E-02
TS-70	-1.53E-02	-2.77E-04	8.94E-02	7.41E-02	7.96E-02	-2.24E-05	9.48E-03	8.91E-02
TS-71	-1.71E-02	-4.96E-05	1.60E-02	-1.08E-03	4.29E-02	1.12E-04	-4.75E-02	-4.54E-03
TS-72	1.53E-01	1.06E-04	-3.44E-02	1.19E-01	1.80E-01	1.78E-04	-7.54E-02	1.05E-01
TS-73	5.02E-02	-1.96E-05	6.33E-03	5.66E-02	9.84E-02	1.08E-04	-4.58E-02	5.26E-02
TS-75	1.53E-01	3.25E-05	-1.05E-02	1.43E-01	1.95E-01	1.43E-04	-6.05E-02	1.35E-01
TS-76	-1.24E-01	-3.20E-04	1.03E-01	-2.03E-02	-2.75E-02	-6.17E-05	2.61E-02	-1.38E-03
TS-77	1.30E-01	6.57E-05	-2.12E-02	1.08E-01	1.60E-01	1.45E-04	-6.13E-02	9.87E-02
TS-78	-4.36E-02	-1.60E-04	5.16E-02	7.99E-03	-6.79E-03	-6.31E-05	2.67E-02	1.99E-02
TS-80	1.73E-01	1.49E-04	-4.80E-02	1.25E-01	1.88E-01	1.86E-04	-7.85E-02	1.09E-01
TS-81	1.17E-01	1.01E-04	-3.25E-02	8.45E-02	1.36E-01	1.49E-04	-6.29E-02	7.27E-02
TS-82	1.68E-01	8.07E-05	-2.61E-02	1.41E-01	1.97E-01	1.57E-04	-6.64E-02	1.30E-01
TS-83	-1.41E-01	-3.69E-04	1.19E-01	-2.20E-02	-2.80E-02	-6.63E-05	2.81E-02	1.02E-04
TS-84	4.50E-02	-1.83E-04	5.92E-02	1.04E-01	1.17E-01	7.16E-06	-3.03E-03	1.14E-01
TS-85	1.84E-01	3.07E-05	-9.91E-03	1.74E-01	2.24E-01	1.36E-04	-5.77E-02	1.67E-01
TS-86	1.98E-01	1.14E-04	-3.67E-02	1.61E-01	2.28E-01	1.94E-04	-8.20E-02	1.46E-01
TS-87	2.67E-01	1.50E-04	-4.86E-02	2.18E-01	2.89E-01	2.07E-04	-8.77E-02	2.01E-01
TS-88	-2.37E-01	-6.23E-04	2.01E-01	-3.52E-02	-7.54E-02	-1.91E-04	8.09E-02	5.57E-03
TS-89	-3.70E-01	-8.07E-04	2.61E-01	-1.09E-01	-1.92E-01	-3.33E-04	1.41E-01	-5.16E-02
TS-90	7.73E-02	3.00E-05	-9.69E-03	6.76E-02	1.22E-01	1.48E-04	-6.28E-02	5.88E-02
TS-91	9.62E-02	1.54E-04	-4.99E-02	4.63E-02	1.06E-01	1.79E-04	-7.59E-02	2.98E-02
TS-92	1.25E-01	1.56E-04	-5.03E-02	7.47E-02	1.39E-01	1.91E-04	-8.07E-02	5.78E-02
TS-95	-3.63E-01	-5.22E-04	1.69E-01	-1.95E-01	-2.79E-01	-2.99E-04	1.27E-01	-1.53E-01

a) 1,4-dioxane

Species	T=323 K				T=423K			
	$\Delta\Delta H$	$\Delta\Delta S$	$-T\Delta\Delta S$	$\Delta\Delta G$	$\Delta\Delta H$	$\Delta\Delta S$	$-T\Delta\Delta S$	$\Delta\Delta G$
I-1	-4.71E-02	-3.96E-04	1.28E-01	8.10E-02	6.95E-02	-8.28E-05	3.50E-02	1.05E-01
I-2	2.50E-01	2.99E-04	-9.66E-02	1.53E-01	2.26E-01	2.34E-04	-9.91E-02	1.27E-01
I-3	1.05E-01	2.01E-04	-6.50E-02	3.97E-02	8.94E-02	1.60E-04	-6.77E-02	2.17E-02
I-4	-1.06E-01	-3.56E-04	1.15E-01	8.98E-03	-8.86E-03	-9.41E-05	3.98E-02	3.10E-02

I-5	-4.90E-02	-1.80E-04	5.83E-02	9.34E-03	2.04E-02	7.00E-06	-2.96E-03	1.75E-02
I-6	2.75E-01	2.69E-04	-8.70E-02	1.88E-01	2.53E-01	2.11E-04	-8.92E-02	1.64E-01
I-7	2.48E-01	2.26E-04	-7.30E-02	1.75E-01	2.31E-01	1.80E-04	-7.63E-02	1.55E-01
I-8	2.28E-01	2.83E-04	-9.15E-02	1.37E-01	2.07E-01	2.24E-04	-9.48E-02	1.12E-01
I-9	-5.96E-02	-1.75E-04	5.66E-02	-2.97E-03	1.02E-02	1.29E-05	-5.44E-03	4.74E-03
I-10	-3.16E-01	-6.30E-04	2.03E-01	-1.12E-01	-1.70E-01	-2.38E-04	1.01E-01	-6.93E-02
I-11	-4.95E-02	-3.20E-04	1.03E-01	5.38E-02	6.39E-02	-1.25E-05	5.29E-03	6.92E-02
I-12	-2.83E-01	-6.69E-04	2.16E-01	-6.73E-02	-1.29E-01	-2.53E-04	1.07E-01	-2.16E-02
I-13	1.45E-01	-8.61E-05	2.78E-02	1.73E-01	2.04E-01	7.47E-05	-3.16E-02	1.73E-01
I-14	1.88E-01	2.81E-04	-9.07E-02	9.71E-02	1.63E-01	2.14E-04	-9.05E-02	7.26E-02
I-15	-1.60E-01	-5.23E-04	1.69E-01	8.79E-03	-2.75E-02	-1.66E-04	7.01E-02	4.26E-02
I-16	1.80E-01	1.07E-04	-3.47E-02	1.46E-01	2.04E-01	1.70E-04	-7.21E-02	1.31E-01
I-17	2.96E-02	-1.69E-04	5.45E-02	8.42E-02	1.04E-01	3.18E-05	-1.35E-02	9.06E-02
I-18	3.22E-01	3.12E-04	-1.01E-01	2.21E-01	2.95E-01	2.39E-04	-1.01E-01	1.94E-01
I-19	-3.52E-02	-2.08E-04	6.72E-02	3.20E-02	4.32E-02	3.38E-06	-1.43E-03	4.18E-02
I-20	1.37E-01	1.84E-04	-5.93E-02	7.73E-02	1.23E-01	1.47E-04	-6.20E-02	6.09E-02
I-21	3.19E-01	3.14E-04	-1.02E-01	2.18E-01	2.93E-01	2.42E-04	-1.03E-01	1.90E-01
I-22	1.28E-01	6.31E-06	-2.04E-03	1.26E-01	1.70E-01	1.22E-04	-5.16E-02	1.19E-01
I-23	-3.92E-02	-2.82E-04	9.11E-02	5.19E-02	5.73E-02	-2.13E-05	9.00E-03	6.64E-02
I-24	1.31E-01	2.02E-04	-6.52E-02	6.57E-02	1.19E-01	1.70E-04	-7.21E-02	4.71E-02
I-25	2.80E-01	3.09E-04	-9.98E-02	1.80E-01	2.54E-01	2.38E-04	-1.01E-01	1.53E-01
I-26	-8.92E-02	-1.51E-04	4.87E-02	-4.05E-02	-3.07E-02	6.95E-06	-2.94E-03	-3.37E-02
I-27	1.61E-01	-5.41E-05	1.75E-02	1.78E-01	2.16E-01	9.56E-05	-4.04E-02	1.75E-01
I-28	3.02E-01	2.88E-04	-9.32E-02	2.08E-01	2.78E-01	2.24E-04	-9.46E-02	1.83E-01
I-29	2.11E-01	5.43E-05	-1.76E-02	1.93E-01	2.47E-01	1.54E-04	-6.52E-02	1.82E-01
I-30	9.00E-02	-1.00E-05	3.25E-03	9.32E-02	1.37E-01	1.18E-04	-5.01E-02	8.70E-02
I-31	-1.13E-01	-1.33E-04	4.28E-02	-7.06E-02	-5.59E-02	2.25E-05	-9.54E-03	-6.54E-02
I-32	8.14E-02	1.54E-04	-4.98E-02	3.16E-02	8.03E-02	1.52E-04	-6.42E-02	1.61E-02
I-33	2.08E-02	-1.98E-04	6.40E-02	8.49E-02	9.93E-02	1.36E-05	-5.75E-03	9.36E-02
I-34	1.93E-01	1.19E-04	-3.85E-02	1.54E-01	2.12E-01	1.72E-04	-7.28E-02	1.39E-01
I-35	-1.08E-01	-4.65E-04	1.50E-01	4.22E-02	3.18E-02	-8.67E-05	3.67E-02	6.85E-02
I-36	3.48E-01	3.11E-04	-1.00E-01	2.48E-01	3.25E-01	2.49E-04	-1.05E-01	2.20E-01
I-37	1.49E-01	2.10E-04	-6.77E-02	8.12E-02	1.33E-01	1.67E-04	-7.06E-02	6.25E-02
I-38	2.96E-01	3.13E-04	-1.01E-01	1.95E-01	2.68E-01	2.38E-04	-1.01E-01	1.68E-01
I-39	5.34E-02	1.27E-04	-4.09E-02	1.25E-02	4.24E-02	9.68E-05	-4.10E-02	1.47E-03
I-40	-4.62E-02	-1.32E-04	4.28E-02	-3.42E-03	1.37E-02	2.93E-05	-1.24E-02	1.29E-03
LA	1.24E-01	1.60E-04	-5.17E-02	7.25E-02	1.18E-01	1.45E-04	-6.12E-02	5.72E-02
Al	-1.90E-01	-6.22E-04	2.01E-01	1.09E-02	-4.47E-02	-2.31E-04	9.79E-02	5.32E-02
Hy	-1.90E-01	-6.60E-04	2.13E-01	2.34E-02	-2.41E-02	-2.12E-04	8.98E-02	6.58E-02
HPA	1.45E-02	-2.85E-04	9.20E-02	1.07E-01	1.19E-01	-2.83E-06	1.20E-03	1.20E-01
AGL	2.61E-01	3.14E-04	-1.02E-01	1.60E-01	2.36E-01	2.45E-04	-1.04E-01	1.32E-01
GVL	2.61E-01	2.78E-04	-8.99E-02	1.71E-01	2.37E-01	2.13E-04	-9.02E-02	1.47E-01
H	8.96E-02	6.93E-05	-2.24E-02	6.72E-02	8.25E-02	4.98E-05	-2.11E-02	6.14E-02
OH	-7.29E-02	-6.05E-04	1.96E-01	1.23E-01	5.57E-02	-2.59E-04	5.41E-02	1.65E-01

H2O	-6.30E-02	-4.07E-04	1.31E-01	6.85E-02	4.04E-02	-1.28E-04	-3.71E-02	9.44E-02
O	6.24E-02	1.25E-04	-4.03E-02	2.21E-02	4.88E-02	8.78E-05	7.83E-02	1.17E-02
TS-3	-1.34E-01	-5.54E-04	1.79E-01	4.45E-02	2.37E-03	-1.85E-04	1.07E-02	8.07E-02
TS-4	2.71E-02	-2.67E-04	8.62E-02	1.13E-01	1.16E-01	-2.53E-05	-8.23E-02	1.27E-01
TS-5	2.29E-01	1.70E-04	-5.48E-02	1.74E-01	2.38E-01	1.95E-04	8.67E-02	1.56E-01
TS-6	-2.30E-01	-7.07E-04	2.28E-01	-1.15E-03	-4.37E-02	-2.05E-04	-2.90E-02	4.31E-02
TS-7	3.09E-02	-9.77E-05	3.16E-02	6.25E-02	9.24E-02	6.86E-05	-2.33E-02	6.34E-02
TS-8	-2.09E-02	-9.24E-05	2.99E-02	8.93E-03	3.35E-02	5.51E-05	-8.21E-02	1.02E-02
TS-9	2.18E-01	2.39E-04	-7.72E-02	1.41E-01	2.01E-01	1.94E-04	-8.57E-02	1.19E-01
TS-10	1.37E-01	2.52E-04	-8.14E-02	5.57E-02	1.19E-01	2.03E-04	-7.11E-02	3.31E-02
TS-11	1.66E-01	1.91E-04	-6.18E-02	1.05E-01	1.58E-01	1.68E-04	-6.40E-02	8.66E-02
TS-12	1.43E-01	8.39E-05	-2.71E-02	1.16E-01	1.68E-01	1.51E-04	-3.37E-02	1.04E-01
TS-14	-4.45E-02	1.94E-05	-6.26E-03	-5.07E-02	-2.24E-02	7.97E-05	-1.02E-01	-5.61E-02
TS-15	2.86E-01	3.17E-04	-1.02E-01	1.83E-01	2.57E-01	2.41E-04	-1.10E-01	1.56E-01
TS-16	2.82E-01	3.37E-04	-1.09E-01	1.73E-01	2.53E-01	2.60E-04	-1.09E-01	1.44E-01
TS-17	2.88E-01	3.33E-04	-1.07E-01	1.81E-01	2.60E-01	2.57E-04	-8.98E-02	1.51E-01
TS-18	2.44E-01	2.65E-04	-8.55E-02	1.58E-01	2.24E-01	2.12E-04	-3.86E-02	1.35E-01
TS-19	6.14E-02	-3.25E-05	1.05E-02	7.19E-02	1.07E-01	9.11E-05	-6.74E-03	6.84E-02
TS-20	3.70E-02	-1.97E-04	6.37E-02	1.01E-01	1.16E-01	1.59E-05	-8.11E-03	1.09E-01
TS-21	3.35E-02	-2.47E-04	7.99E-02	1.13E-01	1.32E-01	1.92E-05	-5.28E-03	1.24E-01
TS-22	1.50E-02	-2.91E-04	9.40E-02	1.09E-01	1.27E-01	1.25E-05	1.30E-01	1.22E-01
TS-23	-4.43E-01	-8.03E-04	2.59E-01	-1.84E-01	-2.60E-01	-3.08E-04	3.15E-02	-1.29E-01
TS-24	-1.17E-01	-4.09E-04	1.32E-01	1.55E-02	7.16E-03	-7.44E-05	-6.66E-02	3.86E-02
TS-25	2.30E-01	6.69E-05	-2.16E-02	2.08E-01	2.63E-01	1.57E-04	-1.08E-01	1.96E-01
TS-26	3.03E-01	3.26E-04	-1.05E-01	1.97E-01	2.77E-01	2.56E-04	-6.93E-02	1.69E-01
TS-27	1.97E-01	1.36E-04	-4.38E-02	1.53E-01	2.07E-01	1.64E-04	1.10E-01	1.38E-01
TS-29	-3.04E-01	-7.67E-04	2.48E-01	-5.60E-02	-1.15E-01	-2.59E-04	-1.96E-02	-5.77E-03
TS-30	-6.65E-02	-1.72E-04	5.55E-02	-1.09E-02	1.38E-02	4.63E-05	1.67E-02	-5.78E-03
TS-31	-4.85E-02	-3.13E-04	1.01E-01	5.26E-02	5.29E-02	-3.95E-05	-1.11E-01	6.96E-02
TS-32	3.23E-01	3.35E-04	-1.08E-01	2.15E-01	2.97E-01	2.64E-04	-9.36E-02	1.85E-01
TS-33	2.66E-01	2.88E-04	-9.31E-02	1.73E-01	2.41E-01	2.21E-04	1.90E-02	1.48E-01
TS-34	-9.52E-02	-2.78E-04	8.97E-02	-5.43E-03	-8.76E-03	-4.49E-05	-9.79E-02	1.03E-02
TS-35	3.35E-01	3.02E-04	-9.75E-02	2.37E-01	3.09E-01	2.31E-04	-1.05E-01	2.11E-01
TS-36	3.01E-01	3.25E-04	-1.05E-01	1.96E-01	2.73E-01	2.49E-04	-3.15E-02	1.67E-01
TS-37	1.21E-02	-6.94E-05	2.24E-02	3.45E-02	6.52E-02	7.44E-05	-1.02E-01	3.37E-02
TS-38	3.20E-01	3.07E-04	-9.91E-02	2.21E-01	2.96E-01	2.42E-04	-7.47E-02	1.94E-01
TS-39	2.45E-01	1.09E-04	-3.51E-02	2.09E-01	2.69E-01	1.77E-04	-5.28E-02	1.95E-01
TS-40	1.24E-01	-2.11E-06	6.81E-04	1.25E-01	1.71E-01	1.25E-04	-9.72E-02	1.18E-01
TS-41	2.59E-01	2.83E-04	-9.13E-02	1.68E-01	2.40E-01	2.30E-04	-1.05E-01	1.42E-01
TS-42	2.66E-01	3.16E-04	-1.02E-01	1.63E-01	2.40E-01	2.47E-04	-9.53E-02	1.35E-01
TS-43	2.69E-01	2.95E-04	-9.54E-02	1.74E-01	2.44E-01	2.25E-04	-9.61E-02	1.48E-01
TS-44	2.75E-01	2.91E-04	-9.40E-02	1.81E-01	2.51E-01	2.27E-04	-1.11E-01	1.55E-01
TS-45	3.33E-01	3.36E-04	-1.08E-01	2.24E-01	3.06E-01	2.62E-04	-8.18E-02	1.95E-01
TS-46	1.32E-01	2.47E-04	-7.98E-02	5.18E-02	1.12E-01	1.93E-04	-1.02E-01	2.99E-02

TS-47	2.75E-01	3.15E-04	-1.02E-01	1.73E-01	2.48E-01	2.42E-04	-9.75E-02	1.46E-01
TS-48	3.02E-01	2.94E-04	-9.49E-02	2.07E-01	2.78E-01	2.30E-04	-7.27E-02	1.81E-01
TS-49	1.74E-01	2.14E-04	-6.91E-02	1.05E-01	1.59E-01	1.72E-04	-1.03E-01	8.59E-02
TS-50	2.18E-01	3.16E-04	-1.02E-01	1.16E-01	1.91E-01	2.44E-04	3.71E-02	8.79E-02
TS-51	-1.18E-01	-3.90E-04	1.26E-01	7.81E-03	-6.14E-03	-8.77E-05	-9.05E-02	3.10E-02
TS-52	2.21E-01	2.75E-04	-8.88E-02	1.32E-01	1.99E-01	2.14E-04	-6.53E-02	1.08E-01
TS-54	7.06E-02	1.65E-04	-5.34E-02	1.73E-02	6.65E-02	1.54E-04	-9.09E-02	1.19E-03
TS-55	2.93E-01	2.73E-04	-8.83E-02	2.05E-01	2.72E-01	2.15E-04	-7.52E-02	1.81E-01
TS-56	1.92E-01	1.97E-04	-6.36E-02	1.29E-01	1.85E-01	1.78E-04	-3.11E-02	1.10E-01
TS-57	7.42E-02	-9.67E-05	3.12E-02	1.05E-01	1.37E-01	7.35E-05	-5.58E-03	1.06E-01
TS-58	3.80E-02	-1.88E-04	6.07E-02	9.87E-02	1.13E-01	1.32E-05	-2.08E-02	1.07E-01
TS-59	5.33E-02	-1.07E-04	3.44E-02	8.77E-02	1.11E-01	4.93E-05	-1.05E-01	9.01E-02
TS-60	3.34E-01	3.25E-04	-1.05E-01	2.29E-01	3.05E-01	2.48E-04	-6.14E-02	2.00E-01
TS-61	1.72E-01	6.68E-05	-2.16E-02	1.50E-01	2.00E-01	1.45E-04	-1.01E-01	1.39E-01
TS-62	3.23E-01	3.06E-04	-9.89E-02	2.24E-01	2.99E-01	2.39E-04	-9.39E-02	1.97E-01
TS-63	2.70E-01	2.87E-04	-9.26E-02	1.77E-01	2.46E-01	2.22E-04	-7.55E-02	1.52E-01
TS-64	2.05E-01	2.26E-04	-7.31E-02	1.32E-01	1.87E-01	1.78E-04	-8.24E-02	1.11E-01
TS-65	2.13E-01	2.40E-04	-7.74E-02	1.35E-01	1.96E-01	1.95E-04	-4.56E-02	1.13E-01
TS-67	8.50E-02	-7.73E-05	2.50E-02	1.10E-01	1.53E-01	1.08E-04	-5.87E-02	1.07E-01
TS-68	1.71E-01	5.36E-05	-1.73E-02	1.54E-01	2.02E-01	1.39E-04	3.18E-02	1.44E-01
TS-69	-8.21E-02	-4.10E-04	1.32E-01	5.04E-02	4.18E-02	-7.51E-05	2.27E-02	7.35E-02
TS-70	-1.27E-02	-3.05E-04	9.84E-02	8.58E-02	8.03E-02	-5.37E-05	-3.59E-02	1.03E-01
TS-71	-1.05E-02	-4.98E-05	1.61E-02	5.61E-03	3.87E-02	8.49E-05	-8.72E-02	2.80E-03
TS-72	2.08E-01	2.28E-04	-7.36E-02	1.34E-01	2.00E-01	2.06E-04	-5.34E-02	1.12E-01
TS-73	8.97E-02	3.76E-05	-1.21E-02	7.76E-02	1.22E-01	1.26E-04	-7.25E-02	6.90E-02
TS-75	1.98E-01	1.17E-04	-3.78E-02	1.60E-01	2.18E-01	1.71E-04	5.01E-02	1.45E-01
TS-76	-1.34E-01	-3.96E-04	1.28E-01	-5.50E-03	-3.06E-02	-1.18E-04	-9.51E-02	1.96E-02
TS-77	2.18E-01	2.43E-04	-7.87E-02	1.40E-01	2.11E-01	2.25E-04	-2.70E-02	1.16E-01
TS-78	4.69E-02	3.35E-05	-1.08E-02	3.61E-02	5.80E-02	6.39E-05	-1.01E-01	3.10E-02
TS-80	2.46E-01	3.06E-04	-9.88E-02	1.48E-01	2.22E-01	2.40E-04	-8.16E-02	1.21E-01
TS-81	1.88E-01	2.55E-04	-8.23E-02	1.06E-01	1.65E-01	1.93E-04	-9.19E-02	8.35E-02
TS-82	2.50E-01	2.71E-04	-8.76E-02	1.62E-01	2.30E-01	2.17E-04	-1.14E-02	1.38E-01
TS-83	-4.15E-02	-1.98E-04	6.39E-02	2.25E-02	4.14E-02	2.69E-05	-2.78E-02	3.00E-02
TS-84	1.06E-01	-8.26E-05	2.67E-02	1.33E-01	1.61E-01	6.58E-05	-8.51E-02	1.34E-01
TS-85	2.44E-01	1.72E-04	-5.56E-02	1.89E-01	2.55E-01	2.01E-04	-8.65E-02	1.70E-01
TS-86	2.43E-01	2.44E-04	-7.87E-02	1.65E-01	2.29E-01	2.04E-04	-1.14E-01	1.42E-01
TS-87	3.37E-01	3.40E-04	-1.10E-01	2.27E-01	3.11E-01	2.70E-04	6.77E-02	1.97E-01
TS-88	-2.11E-01	-5.97E-04	1.93E-01	-1.77E-02	-4.88E-02	-1.60E-04	1.39E-01	1.89E-02
TS-89	-3.40E-01	-7.72E-04	2.49E-01	-9.10E-02	-1.75E-01	-3.28E-04	-5.98E-02	-3.64E-02
TS-90	1.08E-01	1.04E-04	-3.37E-02	7.45E-02	1.22E-01	1.41E-04	-5.43E-02	6.19E-02
TS-91	1.04E-01	1.52E-04	-4.90E-02	5.50E-02	9.54E-02	1.28E-04	-7.50E-02	4.10E-02
TS-92	1.57E-01	2.32E-04	-7.49E-02	8.21E-02	1.37E-01	1.77E-04	2.08E-03	6.18E-02
TS-95	-9.82E-02	-3.76E-06	1.21E-03	-9.70E-02	-9.86E-02	-4.92E-06	5.41E-02	-9.65E-02

C.3 Equilibrium and reaction rate constants in different solvents for all reaction steps considered in the reaction mechanism for the HDO of LA

Table C.3: Equilibrium and reaction rate constants, at 323 K and 423 K, for all the elementary reaction steps considered in the development of the microkinetic model

*All rate constants are in units of inverse seconds and bar.

Step	Constant	Solvent					
		Water		1,4-dioxane		Methanol	
		323 K	423 K	323 K	423 K	323 K	423 K
$\boldsymbol{r_1}$	K_1	5.07E+06	2.83E+02	5.17E+07	1.69E+03	5.44E+07	1.83E+03
	k_1^+	8.62E+07	7.53E+07	8.62E+07	7.53E+07	8.62E+07	7.53E+07
$\boldsymbol{r_2}$	K_2	1.95E+11	5.28E+06	6.47E+12	2.12E+08	7.55E+12	1.44E+08
	k_2^+	6.57E+08	5.74E+08	6.57E+08	5.74E+08	6.57E+08	5.74E+08
$\boldsymbol{r_3}$	K_3	2.82E+01	4.05E+00	5.96E+00	5.18E-01	9.34E+00	8.56E-01
	k_3^+	6.03E+05	5.73E+06	6.76E+03	1.63E+05	2.29E+04	4.09E+05
$\boldsymbol{r_4}$	K_4	1.18E-10	6.74E-09	1.58E-12	1.78E-10	6.19E-12	5.01E-10
	k_4^+	7.03E-07	8.83E-03	5.84E-08	1.25E-03	1.19E-07	2.18E-03
$\boldsymbol{r_5}$	K_5	7.58E-12	4.74E-09	2.75E-13	4.64E-10	3.62E-13	6.07E-10
	k_5^+	9.65E-08	3.01E-02	2.98E-08	1.47E-02	2.03E-08	1.20E-02
$\boldsymbol{r_6}$	K_6	1.81E+00	2.85E+00	1.04E+00	1.35E+00	5.46E-01	1.04E+00
	k_6^+	3.84E+02	2.97E+05	6.01E+02	1.36E+05	2.80E+02	1.16E+05
$\boldsymbol{r_7}$	K_7	3.93E+04	5.67E+02	4.30E+05	5.19E+03	8.87E+05	5.26E+03
	k_7^+	4.96E+09	1.08E+10	1.20E+09	3.93E+09	2.08E+09	5.30E+09
$\boldsymbol{r_8}$	K_8	2.55E+04	3.23E+02	1.52E+05	2.05E+03	2.45E+05	1.94E+03
	k_8^+	1.25E+03	1.33E+05	2.37E+02	4.22E+04	3.90E+02	5.86E+04
$\boldsymbol{r_9}$	K_9	2.45E+13	1.92E+10	3.09E+12	1.52E+10	3.56E+12	1.46E+10
	k_9^+	1.05E+08	4.57E+09	4.72E+07	3.57E+09	3.00E+07	2.92E+09
$\boldsymbol{r_{10}}$	K_{10}	6.98E-13	4.67E-10	2.42E-12	8.21E-10	1.86E-12	7.70E-10
	k_{10}^+	6.26E-20	4.79E-12	1.14E-18	2.36E-11	6.36E-19	1.62E-11
$\boldsymbol{r_{11}}$	K_{11}	1.20E-09	1.57E-07	1.39E-10	1.03E-08	1.63E-10	1.70E-08
	k_{11}^+	5.37E-01	9.78E+02	1.20E-01	1.61E+02	9.53E-02	1.75E+02
$\boldsymbol{r_{12}}$	K_{12}	8.98E+09	4.06E+07	5.05E+09	4.38E+07	6.37E+09	4.87E+07
	k_{12}^+	6.34E-01	2.00E+03	6.48E-01	2.98E+03	4.48E-01	2.31E+03
$\boldsymbol{r_{13}}$	K_{13}	1.82E-05	3.23E-04	1.01E-05	2.65E-04	7.50E-06	2.41E-04
	k_{13}^+	6.56E-02	1.59E+02	6.95E-02	1.63E+02	7.16E-02	1.64E+02
$\boldsymbol{r_{14}}$	K_{14}	1.87E+01	3.81E+00	2.05E+01	6.89E+00	4.67E+01	8.94E+00
	k_{14}^+	1.49E+10	1.15E+11	8.99E+09	7.12E+10	8.02E+09	7.37E+10
$\boldsymbol{r_{15}}$	K_{15}	1.39E+10	7.14E+07	1.43E+10	1.11E+08	2.31E+10	1.32E+08
	k_{15}^+	4.12E+05	3.92E+07	1.65E+05	2.42E+07	2.33E+05	2.87E+07
$\boldsymbol{r_{16}}$	K_{16}	3.78E-14	3.03E-11	4.11E-14	4.16E-11	5.51E-14	4.43E-11
	k_{16}^+	1.80E-05	1.83E-01	3.97E-05	4.02E-01	3.82E-05	3.37E-01
$\boldsymbol{r_{17}}$	K_{17}	9.08E-08	7.12E-06	6.87E-08	4.93E-06	7.87E-08	5.52E-06
	k_{17}^+	4.63E-01	6.74E+02	1.15E-01	2.70E+02	1.92E-01	3.69E+02
$\boldsymbol{r_{18}}$	K_{18}	1.73E-04	3.29E-03	1.17E-04	1.07E-03	6.19E-05	9.44E-04

	k_{18}^{+}	1.75E+04	3.95E+06	3.49E+03	5.65E+05	2.38E+03	6.10E+05
$\boldsymbol{r_{19}}$	K_{19}	1.66E+04	8.76E+02	2.00E+05	1.42E+04	3.25E+05	1.13E+04
	k_{19}^{+}	4.54E+02	1.90E+05	2.83E+03	8.19E+05	1.77E+03	5.14E+05
$\boldsymbol{r_{20}}$	K_{20}	9.13E+03	1.01E+03	1.65E+04	2.44E+03	1.89E+04	2.37E+03
	k_{20}^{+}	1.94E+05	2.08E+07	2.54E+05	2.12E+07	2.04E+05	2.04E+07
$\boldsymbol{r_{21}}$	K_{21}	6.22E+05	1.37E+04	1.59E+07	6.91E+04	1.62E+07	7.51E+04
	k_{21}^{+}	2.10E-03	1.55E+01	1.22E-03	8.33E+00	1.18E-03	8.93E+00
$\boldsymbol{r_{22}}$	K_{22}	9.21E+04	7.29E+03	7.81E+06	1.88E+05	4.89E+06	1.11E+05
	k_{22}^{+}	5.88E+05	4.92E+07	9.88E+06	2.65E+08	6.17E+06	1.82E+08
$\boldsymbol{r_{23}}$	K_{23}	2.24E+10	2.20E+07	1.27E+12	2.39E+08	1.58E+12	2.44E+08
	k_{23}^{+}	1.29E+08	2.05E+09	2.24E+09	8.18E+09	1.61E+09	7.34E+09
$\boldsymbol{r_{24}}$	K_{24}	7.66E+04	1.83E+03	2.64E+06	2.73E+04	2.97E+06	2.21E+04
	k_{24}^{+}	1.72E+05	1.03E+07	4.08E+05	1.53E+07	3.59E+05	1.44E+07
$\boldsymbol{r_{25}}$	K_{25}	3.29E+08	1.62E+06	1.31E+09	8.43E+06	1.84E+09	7.71E+06
	k_{25}^{+}	1.61E+03	6.90E+05	2.80E+03	2.40E+06	2.31E+03	1.54E+06
$\boldsymbol{r_{26}}$	K_{26}	1.08E+10	4.52E+07	2.92E+10	5.00E+08	2.81E+10	2.95E+08
	k_{26}^{+}	1.49E+03	7.19E+05	2.40E+03	2.79E+06	2.00E+03	1.75E+06
$\boldsymbol{r_{27}}$	K_{27}	2.01E+00	1.26E+00	7.07E+00	7.85E+00	1.06E+01	7.02E+00
	k_{27}^{+}	2.61E+07	1.34E+09	4.59E+07	3.65E+09	3.32E+07	2.45E+09
$\boldsymbol{r_{28}}$	K_{1}	7.40E-10	1.28E-07	1.53E-09	5.58E-07	1.28E-09	3.54E-07
	k_{28}^{+}	6.32E+00	2.74E+03	5.88E+00	2.37E+03	5.98E+00	2.48E+03
$\boldsymbol{r_{29}}$	K_{29}	2.58E+06	4.39E+04	2.60E+07	3.07E+05	3.73E+07	3.01E+05
	k_{29}^{+}	5.40E-02	6.02E+01	3.10E-02	3.44E+01	4.41E-02	4.51E+01
$\boldsymbol{r_{30}}$	K_{30}	1.85E+09	2.54E+06	2.32E+09	4.84E+06	4.79E+09	6.30E+06
	k_{30}^{+}	1.25E+08	1.34E+09	2.39E+07	5.17E+08	2.61E+07	5.80E+08
$\boldsymbol{r_{31}}$	K_{31}	1.06E+01	1.45E+01	1.60E+02	2.41E+02	1.16E+02	1.37E+02
	k_{31}^{+}	2.21E+08	6.17E+09	2.16E+08	7.24E+09	1.75E+08	6.06E+09
$\boldsymbol{r_{32}}$	K_{32}	9.06E+04	1.56E+04	1.26E+06	3.99E+05	7.62E+05	2.02E+05
	k_{32}^{+}	2.59E+03	1.65E+06	2.35E+03	3.96E+06	1.64E+03	2.45E+06
$\boldsymbol{r_{33}}$	K_{33}	3.07E+02	4.94E+01	1.89E+03	8.08E+02	2.36E+03	5.33E+02
	k_{33}^{+}	6.64E+06	2.34E+08	7.75E+06	4.45E+08	6.31E+06	3.38E+08
$\boldsymbol{r_{34}}$	K_{34}	2.22E+09	1.01E+07	6.85E+09	3.34E+07	7.87E+09	3.16E+07
	k_{34}^{+}	2.41E+05	1.56E+07	4.66E+04	4.03E+06	6.03E+04	5.61E+06
$\boldsymbol{r_{35}}$	K_{35}	2.77E+03	5.59E+02	5.66E+04	6.73E+03	5.00E+04	5.28E+03
	k_{35}^{+}	2.57E-04	1.46E-01	5.01E-05	7.14E-02	1.08E-04	1.04E-01
$\boldsymbol{r_{36}}$	K_{36}	5.54E+01	1.35E+01	3.67E+02	1.05E+02	4.28E+02	8.37E+01
	k_{36}^{+}	2.40E+08	2.70E+09	1.78E+08	2.55E+09	2.10E+08	2.64E+09
$\boldsymbol{r_{37}}$	K_{37}	1.74E+09	1.87E+07	2.97E+10	2.59E+08	2.00E+10	1.50E+08
	k_{37}^{+}	3.10E+08	6.91E+09	8.45E+08	1.50E+10	4.52E+08	9.60E+09
$\boldsymbol{r_{38}}$	K_{38}	2.97E+11	4.86E+08	1.52E+12	6.70E+09	1.13E+12	3.52E+09
	k_{38}^{+}	1.75E+05	2.83E+07	3.01E+05	7.02E+07	1.65E+05	4.11E+07
$\boldsymbol{r_{39}}$	K_{39}	4.46E-06	8.83E-05	6.90E-06	1.71E-04	4.41E-06	1.14E-04
	k_{39}^{+}	1.28E+01	5.83E+03	9.81E+00	1.03E+04	7.98E+00	7.17E+03
$\boldsymbol{r_{40}}$	K_{40}	1.21E+04	8.66E+02	3.20E+04	2.41E+03	3.66E+04	2.26E+03

	k_{40}^{+}	2.25E+05	1.14E+07	1.25E+05	6.79E+06	1.43E+05	7.57E+06
$\boldsymbol{r_{41}}$	K_{41}	6.28E-10	3.53E-08	4.72E-10	2.86E-08	5.62E-10	3.19E-08
	k_{41}^{+}	1.59E-09	9.16E-05	1.45E-10	3.59E-05	2.05E-10	4.10E-05
$\boldsymbol{r_{42}}$	K_{42}	4.58E+12	1.69E+09	2.61E+12	4.02E+09	3.30E+12	3.45E+09
	k_{42}^{+}	2.55E+07	5.21E+08	5.99E+06	2.82E+08	5.57E+06	2.56E+08
$\boldsymbol{r_{43}}$	K_{43}	7.70E+12	1.31E+10	1.60E+13	1.76E+10	1.26E+13	1.76E+10
	k_{43}^{+}	4.30E+06	2.28E+08	1.30E+06	7.63E+07	1.33E+06	9.97E+07
$\boldsymbol{r_{44}}$	K_{44}	7.67E-06	2.05E-04	2.63E-06	3.29E-05	1.64E-06	4.04E-05
	k_{44}^{+}	3.76E+01	2.80E+04	1.34E+01	6.91E+03	1.03E+01	8.18E+03
$\boldsymbol{r_{45}}$	K_{45}	1.06E+06	6.42E+04	4.43E+06	4.27E+05	3.78E+06	2.97E+05
	k_{45}^{+}	2.48E+05	2.58E+07	5.87E+05	8.42E+07	4.64E+05	5.93E+07
$\boldsymbol{r_{46}}$	K_{46}	8.87E-14	5.43E-11	8.21E-15	7.61E-12	9.59E-15	9.65E-12
	k_{46}^{+}	1.69E-22	2.81E-14	1.21E-22	1.97E-14	1.12E-22	1.84E-14
$\boldsymbol{r_{47}}$	K_{47}	5.36E+08	1.58E+06	3.31E+08	2.43E+06	5.02E+08	2.33E+06
	k_{47}^{+}	9.69E+01	2.13E+04	8.08E+01	2.56E+04	8.92E+01	2.27E+04
$\boldsymbol{r_{48}}$	K_{48}	2.68E+10	6.53E+07	5.10E+10	1.56E+08	5.87E+10	1.47E+08
	k_{48}^{+}	1.25E+09	1.21E+10	1.01E+09	8.94E+09	1.00E+09	9.44E+09
$\boldsymbol{r_{49}}$	K_{49}	2.92E-11	1.43E-08	3.71E-11	1.16E-08	2.94E-11	1.11E-08
	k_{49}^{+}	2.25E+02	8.46E+04	8.32E+01	2.46E+04	7.19E+01	2.89E+04
$\boldsymbol{r_{50}}$	K_{50}	1.95E+06	7.86E+04	8.16E+06	4.54E+05	7.52E+06	3.43E+05
	k_{50}^{+}	8.11E+01	3.65E+04	1.04E+02	5.26E+04	8.77E+01	4.54E+04
$\boldsymbol{r_{51}}$	K_{51}	2.45E+05	7.49E+03	2.03E+06	4.32E+04	2.55E+06	4.21E+04
	k_{51}^{+}	3.29E+10	9.41E+10	1.76E+10	3.54E+10	1.94E+10	4.44E+10
$\boldsymbol{r_{52}}$	K_{52}	4.58E+04	3.19E+03	3.44E+04	9.83E+03	4.76E+04	8.65E+03
	k_{52}^{+}	5.76E+01	3.69E+04	1.96E+01	3.30E+04	1.85E+01	2.92E+04
$\boldsymbol{r_{53}}$	K_{53}	3.50E-13	2.61E-10	7.29E-14	3.70E-11	7.68E-14	5.78E-11
	k_{53}^{+}	1.02E-12	5.59E-07	1.20E-12	6.79E-07	1.19E-12	6.50E-07
$\boldsymbol{r_{54}}$	K_{54}	2.63E-05	5.17E-04	3.98E-06	4.49E-05	2.36E-06	5.17E-05
	k_{54}^{+}	2.80E+08	5.80E+09	3.32E+07	4.62E+08	2.40E+07	6.01E+08
$\boldsymbol{r_{55}}$	K_{55}	6.29E-18	6.64E-14	6.22E-18	6.98E-14	8.09E-18	8.00E-14
	k_{55}^{+}	7.29E-07	2.80E-02	2.31E-06	5.46E-02	1.77E-06	4.63E-02
$\boldsymbol{r_{56}}$	K_{56}	5.15E-01	7.37E-01	5.92E-01	8.64E-01	5.41E-01	7.57E-01
	k_{56}^{+}	2.58E+01	1.54E+04	1.25E+00	1.13E+03	1.63E+00	1.68E+03
$\boldsymbol{r_{57}}$	K_{57}	5.72E+09	1.92E+07	5.52E+10	7.49E+07	4.64E+10	6.77E+07
	k_{57}^{+}	7.30E+10	3.86E+11	4.03E+10	2.75E+11	4.08E+10	2.83E+11
$\boldsymbol{r_{58}}$	K_{58}	4.57E-01	3.20E-01	3.46E+00	3.64E+00	5.39E+00	3.06E+00
	k_{58}^{+}	1.06E+00	1.07E+03	5.13E-01	7.42E+02	7.80E-01	9.17E+02
$\boldsymbol{r_{59}}$	K_{59}	1.22E-01	9.65E-02	7.89E-01	8.87E-01	1.21E+00	7.74E-01
	k_{59}^{+}	2.58E+04	2.74E+06	3.58E+04	3.93E+06	4.09E+04	3.98E+06
$\boldsymbol{r_{60}}$	K_{60}	1.38E+07	1.75E+05	2.11E+08	4.14E+06	2.22E+08	2.61E+06
	k_{60}^{+}	2.92E+03	4.70E+05	3.72E+03	1.38E+06	4.52E+03	1.13E+06
$\boldsymbol{r_{61}}$	K_{61}	5.94E+08	3.04E+06	1.56E+09	8.14E+06	1.76E+09	7.99E+06
	k_{61}^{+}	2.23E+08	3.83E+09	2.13E+08	2.95E+09	1.60E+08	2.77E+09
$\boldsymbol{r_{62}}$	K_{62}	4.56E+04	2.74E+03	4.84E+05	3.14E+04	2.89E+05	1.80E+04

	k_{62}^{+}	1.16E+05	7.65E+06	6.64E+04	8.22E+06	7.00E+04	7.86E+06
$\boldsymbol{r_{63}}$	K_{63}	1.51E-03	5.01E-03	7.92E-03	2.76E-02	7.04E-03	2.11E-02
	k_{63}^{+}	1.27E+02	7.37E+04	2.75E+01	2.22E+04	3.18E+01	2.71E+04
$\boldsymbol{r_{64}}$	K_{64}	2.72E-06	2.72E-05	7.07E-06	1.73E-04	1.29E-05	1.58E-04
	k_{64}^{+}	1.18E+00	1.13E+03	3.07E-01	4.72E+02	4.34E-01	6.14E+02
$\boldsymbol{r_{65}}$	K_{65}	7.83E-02	1.16E-01	2.02E-02	3.63E-02	2.07E-02	4.14E-02
	k_{65}^{+}	9.31E-01	1.61E+03	9.88E-02	1.70E+02	9.22E-02	2.20E+02
$\boldsymbol{r_{66}}$	K_{66}	3.64E-04	3.73E-03	2.52E-03	1.72E-02	8.66E-04	8.30E-03
	k_{66}^{+}	1.18E+04	6.12E+05	9.73E+03	5.26E+05	1.08E+04	5.65E+05
$\boldsymbol{r_{67}}$	K_{67}	2.05E+09	2.85E+07	1.80E+11	8.41E+08	6.78E+10	3.70E+08
	k_{67}^{+}	6.80E+08	1.95E+10	1.18E+10	1.67E+11	3.91E+09	7.51E+10
$\boldsymbol{r_{68}}$	K_{68}	6.37E+09	2.38E+07	2.67E+11	5.00E+08	1.84E+11	2.92E+08
	k_{68}^{+}	4.66E+00	1.58E+04	3.43E+01	7.25E+04	1.12E+01	3.41E+04
$\boldsymbol{r_{69}}$	K_{69}	3.04E+06	6.67E+04	1.57E+08	9.95E+05	1.26E+08	7.42E+05
	k_{69}^{+}	4.48E-02	2.90E+02	2.15E-01	7.13E+02	8.56E-02	4.41E+02
$\boldsymbol{r_{70}}$	K_{70}	1.48E+10	8.14E+07	1.47E+11	6.92E+08	6.25E+10	3.58E+08
	k_{70}^{+}	4.50E+04	1.75E+07	3.53E+05	4.93E+07	1.21E+05	2.86E+07
$\boldsymbol{r_{71}}$	K_{71}	1.91E+03	1.45E+02	2.21E+04	9.12E+02	3.30E+04	9.35E+02
	k_{71}^{+}	1.28E+01	1.63E+04	1.25E+01	1.24E+04	1.04E+01	1.24E+04
$\boldsymbol{r_{72}}$	K_{72}	3.96E+09	2.08E+07	3.07E+09	4.63E+07	5.59E+09	5.37E+07
	k_{72}^{+}	1.22E+09	9.43E+09	7.17E+08	8.88E+09	8.12E+08	8.86E+09
$\boldsymbol{r_{73}}$	K_{73}	6.10E+07	3.99E+05	1.62E+09	9.64E+06	2.28E+09	7.28E+06
	k_{73}^{+}	3.76E+02	1.30E+05	2.51E+02	1.42E+05	3.05E+02	1.41E+05
$\boldsymbol{r_{74}}$	K_{74}	1.89E-03	1.04E-02	1.02E-03	1.25E-02	1.51E-03	1.35E-02
	k_{74}^{+}	1.36E+04	2.72E+06	1.45E+04	2.67E+06	1.39E+04	2.65E+06
$\boldsymbol{r_{75}}$	K_{75}	1.77E+09	7.56E+06	3.52E+10	1.99E+08	4.34E+10	1.32E+08
	k_{75}^{+}	4.92E+07	9.31E+08	8.96E+07	2.26E+09	9.62E+07	1.93E+09
$\boldsymbol{r_{76}}$	K_{76}	3.27E-01	1.90E-01	2.51E+00	5.89E-01	2.20E+00	5.62E-01
	k_{76}^{+}	3.39E+00	2.35E+03	6.20E+00	1.35E+03	4.09E+00	1.40E+03
$\boldsymbol{r_{77}}$	K_{77}	9.24E+08	3.44E+06	2.35E+09	7.54E+06	3.09E+09	8.15E+06
	k_{77}^{+}	2.83E+06	9.49E+07	4.08E+05	3.33E+07	6.28E+05	4.22E+07
$\boldsymbol{r_{78}}$	K_{78}	1.87E-02	1.85E+01	2.04E-03	1.67E+00	1.47E-03	1.73E+00
	k_{78}^{+}	1.74E+06	1.50E+09	1.90E+05	1.35E+08	1.36E+05	1.41E+08
$\boldsymbol{r_{79}}$	K_{79}	2.92E-06	2.33E-04	4.16E-07	3.63E-05	4.10E-07	4.33E-05
	k_{79}^{+}	4.53E-01	1.80E+03	7.84E-03	1.12E+02	1.29E-02	1.64E+02
$\boldsymbol{r_{80}}$	K_{80}	1.27E-07	9.16E-06	4.96E-08	2.21E-06	3.44E-08	2.37E-06
	k_{80}^{+}	5.23E-02	2.26E+02	8.80E-03	5.90E+01	7.26E-03	6.08E+01
$\boldsymbol{r_{81}}$	K_{81}	3.55E+02	2.46E+02	1.74E+02	3.41E+01	4.98E+01	3.06E+01
	k_{81}^{+}	6.50E+08	1.73E+10	1.64E+08	2.60E+09	5.17E+07	2.13E+09
$\boldsymbol{r_{82}}$	K_{82}	3.35E-15	1.75E-11	1.56E-15	8.28E-12	1.59E-15	8.91E-12
	k_{82}^{+}	1.86E-12	3.19E-06	2.99E-13	1.03E-06	4.23E-13	1.19E-06
$\boldsymbol{r_{83}}$	K_{83}	1.51E+02	3.66E+01	1.73E+03	2.80E+02	2.15E+03	2.54E+02
	k_{83}^{+}	4.66E+10	2.05E+11	4.61E+09	5.00E+10	1.20E+10	8.04E+10
$\boldsymbol{r_{84}}$	K_{84}	7.05E+02	1.04E+02	4.78E+03	5.65E+02	5.55E+03	4.96E+02

	k_{84}^{+}	1.15E+03	1.87E+05	2.08E+02	8.75E+04	3.10E+02	1.06E+05
$\boldsymbol{r_{85}}$	K_{85}	6.80E-16	4.50E-12	6.52E-17	5.80E-13	6.90E-17	7.15E-13
	k_{85}^{+}	3.73E-10	1.23E-04	3.41E-11	3.58E-05	2.97E-11	3.18E-05
$\boldsymbol{r_{86}}$	K_{86}	1.98E-03	9.51E-03	3.26E-04	4.69E-03	3.54E-04	4.68E-03
	k_{86}^{+}	3.18E+04	7.17E+06	7.69E+04	2.87E+07	4.84E+04	1.73E+07
$\boldsymbol{r_{87}}$	K_{87}	6.00E+02	9.67E+01	2.15E+04	3.24E+03	1.89E+04	1.86E+03
	k_{87}^{+}	4.88E+02	1.09E+05	1.24E+03	2.90E+05	1.13E+03	2.26E+05
$\boldsymbol{r_{88}}$	K_{88}	1.28E+02	3.41E+01	7.81E+03	1.60E+03	7.32E+03	9.55E+02
	k_{88}^{+}	5.35E+01	1.92E+04	6.81E+01	1.99E+04	6.28E+01	1.91E+04
$\boldsymbol{r_{89}}$	K_{89}	4.01E-02	5.43E-02	1.32E-02	1.92E-02	1.49E-02	2.36E-02
	k_{89}^{+}	3.51E-02	2.11E+01	8.23E-03	2.79E+00	1.27E-02	5.30E+00
$\boldsymbol{r_{90}}$	K_{90}	3.23E-03	6.90E-03	1.08E-01	1.51E-01	1.21E-01	1.11E-01
	k_{90}^{+}	2.57E+10	1.70E+11	9.67E+10	5.02E+11	6.40E+10	3.70E+11
$\boldsymbol{r_{91}}$	K_{91}	1.93E+16	1.20E+12	1.81E+16	2.69E+12	2.69E+16	2.69E+12
	k_{91}^{+}	2.09E+13	1.65E+13	3.85E+12	5.60E+12	4.99E+12	7.04E+12
$\boldsymbol{r_{92}}$	K_{92}	2.80E-07	6.32E-06	1.29E-08	8.05E-07	2.71E-08	1.20E-06
	k_{92}^{+}	2.49E+03	4.90E+05	9.94E+02	1.74E+05	8.31E+02	1.80E+05
$\boldsymbol{r_{93}}$	K_{93}	4.24E-14	3.16E-11	6.92E-14	5.03E-11	1.33E-13	6.20E-11
	k_{93}^{+}	1.27E-12	6.09E-07	1.21E-12	5.81E-07	1.13E-12	5.69E-07
$\boldsymbol{r_{94}}$	K_{94}	1.16E+00	1.32E+02	1.89E-01	2.84E+01	1.15E-01	2.56E+01
	k_{94}^{+}	2.54E+08	2.52E+10	4.14E+07	5.43E+09	2.51E+07	4.90E+09
$\boldsymbol{r_{95}}$	K_{95}	1.84E+13	1.56E+10	2.24E+13	5.64E+10	2.12E+13	4.16E+10
	k_{95}^{+}	8.40E+09	1.75E+10	5.55E+06	3.76E+08	1.20E+08	1.56E+09
$\boldsymbol{r_{96}}$	K_{96}	4.82E-07	2.68E-02	1.86E-07	8.95E-03	7.34E-08	5.60E-03
	k_{96}^{+}	4.12E+01	2.00E+06	1.59E+01	6.69E+05	6.27E+00	4.18E+05

C.4 Development of microkinetic model

Set of elementary reactions for one site model

$$r_1 = k_{1f} P_{LA} \theta_*^2 - k_{1b} \theta_{LA}$$

$$r_2 = k_{2f} P_{H_2} \theta_*^2 - k_{2b} {\theta_H}^2$$

$$r_3 = k_{3f} \theta_{LA} \theta_H - k_{3b} \theta_{Al} \theta_*$$

$$r_4 = k_{4f} \theta_{LA} \theta_H - k_{4b} \theta_{Hy} \theta_*$$

$$r_5 = k_{5f} \theta_{Al} \theta_H - k_{5b} \theta_{HPA}$$

$$r_6 = k_{6f} \theta_{Hy} \theta_H - k_{6b} \theta_{HPA}$$

$$r_7 = k_{7f} \theta_{LA} \theta_*^2 - k_{7b} \theta_{01} \theta_H$$

$$r_8 = k_{8f} \theta_{LA} \theta_*^2 - k_{8b} \theta_{07} \theta_{OH}$$

$$r_9 = k_{9f} \theta_{01} {\theta_*}^2 - k_{9b} \theta_{02} \theta_H$$

$$r_{10} = k_{10f} \theta_{02} - k_{10b} \theta_{03} {\theta_*}^2$$

$$r_{11} = k_{11f} \theta_{03} \theta_H - k_{11b} \theta_{04} \theta_*$$

$$r_{12} = k_{12f} \theta_{01} \theta_* - k_{12b} \theta_{06} \theta_{OH}$$

$$r_{13} = k_{13f} \theta_{01} - k_{13b} \theta_{05} \theta_*$$

$$r_{14} = k_{14f} \theta_{05} \theta_* - k_{14b} \theta_{AGL} \theta_{OH}$$

$$r_{15} = k_{15f} \theta_{07} \theta_* - k_{15b} \theta_{06} \theta_H$$

$$r_{16} = k_{16f} \theta_{06} - k_{16b} \theta_{AGL} \theta_*$$

$$r_{17} = k_{17f} \theta_{07} - k_{17b} \theta_{08} \theta_*$$

$$r_{18} = k_{18f} \theta_{AGL} \theta_H - k_{18b} \theta_{08} \theta_*$$

$$r_{19} = k_{19f} \theta_{04} \theta_* - k_{19b} \theta_{AGL} \theta_{OH}$$

$$r_{20} = k_{20f}\theta_{HPA}\theta_* - k_{20b}\theta_{09}\theta_H$$

$$r_{21} = k_{21f}\theta_{HPA} - k_{21b}\theta_{10}\theta_{OH}$$

$$r_{22} = k_{22f}\theta_{09}\theta_* - k_{22b}\theta_{11}\theta_H$$

$$r_{23} = k_{23f}\theta_{09}\theta_* - k_{23b}\theta_{12}\theta_{OH}$$

$$r_{24} = k_{24f}\theta_{09}\theta_* - k_{24b}\theta_{13}\theta_{OH}$$

$$r_{25} = k_{25f}\theta_{10}\theta_*^{\,2} - k_{25b}\theta_{12}\theta_H$$

$$r_{26} = k_{26f}\theta_{10}\theta_*^{\,2} - k_{26b}\theta_{14}\theta_H$$

$$r_{27} = k_{27f}\theta_{10}\theta_* - k_{27b}\theta_{15}\theta_H$$

$$r_{28} = k_{28f}\theta_{10} - k_{28b}\theta_{16}$$

$$r_{29} = k_{29f}\theta_{11}\theta_* - k_{29b}\theta_{17}\theta_{OH}$$

$$r_{30} = k_{30f}\theta_{11}\theta_* - k_{30b}\theta_{19}\theta_{OH}$$

$$r_{31} = k_{31f}\theta_{12}\theta_* - k_{31b}\theta_{17}\theta_H$$

$$r_{32} = k_{32f}\theta_{12} - k_{32b}\theta_{20}\theta_H$$

$$r_{33} = k_{33f}\theta_{13}\theta_* - k_{33b}\theta_{18}\theta_H$$

$$r_{34} = k_{34f}\theta_{13}\theta_* - k_{34b}\theta_{19}\theta_H$$

$$r_{35} = k_{35f}\theta_{14} - k_{35b}\theta_{20}\theta_H$$

$$r_{36} = k_{36f}\theta_{14}\theta_* - k_{36b}\theta_{21}\theta_H$$

$$r_{37} = k_{37f}\theta_{15}\theta_*^{\,2} - k_{37b}\theta_{17}\theta_H$$

$$r_{38} = k_{38f}\theta_{15}\theta_*^{\,2} - k_{38b}\theta_{21}\theta_H$$

$$r_{39} = k_{39f}\theta_{15} - k_{39b}\theta_{22}$$

$$r_{40} = k_{40f}\theta_{16}\theta_* - k_{40b}\theta_{22}\theta_H$$

$$r_{41} = k_{41f}\theta_{17} - k_{41b}\theta_{23}\theta_*$$

$$r_{42} = k_{42f}\theta_{17}\theta_* - k_{42b}\theta_{25}\theta_H$$

$$r_{43} = k_{43f}\theta_{18}\theta_* - k_{43b}\theta_{06}\theta_H$$

$$r_{44} = k_{44f}\theta_{18} - k_{44b}\theta_{24}\theta_*$$

$$r_{45} = k_{45f}\theta_{19}\theta_* - k_{45b}\theta_{06}\theta_H$$

$$r_{46} = k_{46f}\theta_{20} - k_{46b}\theta_{24}$$

$$r_{47} = k_{47f}\theta_{20}{\theta_*}^2 - k_{47b}\theta_{25}\theta_H$$

$$r_{48} = k_{48f}\theta_{21}\theta_* - k_{48b}\theta_{25}\theta_H$$

$$r_{49} = k_{49f}\theta_{21} - k_{49b}\theta_{08}\theta_*$$

$$r_{50} = k_{50f}\theta_{22}\theta_* - k_{50b}\theta_{08}\theta_H$$

$$r_{51} = k_{51f}\theta_{22}\theta_* - k_{51b}\theta_{23}\theta_H$$

$$r_{52} = k_{52f}\theta_{23}\theta_* - k_{52b}\theta_{AGL}\theta_H$$

$$r_{53} = k_{53f}\theta_{29} - k_{53b}\theta_{04}{\theta_*}^2$$

$$r_{54} = k_{54f}\theta_{AGL}\theta_H - k_{54b}\theta_{24}\theta_*$$

$$r_{55} = k_{55f}\theta_{25} - k_{55b}\theta_{AGL}\theta_H$$

$$r_{56} = k_{56f}\theta_{24}\theta_H - k_{56b}\theta_{GVL}\theta_*$$

$$r_{57} = k_{57f}\theta_{HPA}\theta_* - k_{57b}\theta_{26}\theta_{OH}$$

$$r_{58} = k_{58f}\theta_{26} - k_{58b}\theta_{27}\theta_H$$

$$r_{59} = k_{59f}\theta_{26}\theta_* - k_{59b}\theta_{13}\theta_H$$

$$r_{60} = k_{60f}\theta_{26}\theta_* - k_{60b}\theta_{28}\theta_H$$

$$r_{61} = k_{61f}\theta_{27}{\theta_*}^2 - k_{61b}\theta_{19}\theta_H$$

$$r_{62} = k_{62f}\theta_{27}{\theta_*}^2 - k_{62b}\theta_{07}\theta_H$$

$$r_{63} = k_{63f}\theta_{28}\theta_* - k_{63b}\theta_{07}\theta_H$$

$$r_{64} = k_{64f}\theta_{28}\theta_* - k_{64b}\theta_{18}\theta_H$$

$$r_{65} = k_{65f}\theta_{08}\theta_H - k_{65b}\theta_{GVL}\theta_*$$

$$r_{66} = k_{66f}\theta_{Hy} - k_{66b}\theta_{30}$$

$$r_{67} = k_{67f}\theta_{Hy}{\theta_*}^2 - k_{67b}\theta_{11}\theta_H$$

$$r_{68} = k_{68f}\theta_{Hy}\theta_* - k_{68b}\theta_{27}\theta_{OH}$$

$$r_{69} = k_{69f}\theta_{Hy}\theta_* - k_{69b}\theta_{15}\theta_{OH}$$

$$r_{70} = k_{70f}\theta_{Hy}{\theta_*}^2 - k_{70b}\theta_{31}\theta_H$$

$$r_{71} = k_{71f}\theta_{30}\theta_* - k_{71b}\theta_{22}\theta_{OH}$$

$$r_{72} = k_{72f}\theta_{30}\theta_* - k_{72b}\theta_{32}\theta_H$$

$$r_{73} = k_{73f}\theta_{31}\theta_* - k_{73b}\theta_{21}\theta_{OH}$$

$$r_{74} = k_{74f}\theta_{31} - k_{74b}\theta_{32}\theta_*$$

$$r_{75} = k_{75f}\theta_{31}{\theta_*}^2 - k_{75b}\theta_{29}\theta_H$$

$$r_{76} = k_{76f}\theta_{32}\theta_* - k_{76b}\theta_{04}\theta_H$$

$$r_{77} = k_{77f}\theta_{29} - k_{77b}\theta_{25}\theta_{OH}$$

$$r_{78} = k_{78f}\theta_{GVL} - k_{78b}P_{GVL}{\theta_*}^2$$

$$r_{79} = k_{79f}\theta_H\theta_{OH} - k_{79b}\theta_{H_2O}\theta_*$$

$$r_{80} = k_{80f}\theta_{HPA}\theta_H - k_{80b}\theta_{33}{\theta_*}^2$$

$$r_{81} = k_{81f}\theta_{39}\theta_H - k_{81b}\theta_{40}{\theta_*}^2$$

$$r_{82} = k_{82f}\theta_{26}\theta_H - k_{82b}\theta_{34}{\theta_*}^2$$

$$r_{83} = k_{83f}\theta_{33} - k_{83b}\theta_{34}\theta_{OH}$$

$$r_{84} = k_{84f}\theta_{33}\theta_{*} - k_{84b}\theta_{35}\theta_{H}$$

$$r_{85} = k_{85f}\theta_{Al}\theta_{H} - k_{85b}\theta_{35}\theta_{*}$$

$$r_{86} = k_{86f}\theta_{Al} - k_{86b}\theta_{40}\theta_{*}$$

$$r_{87} = k_{87f}\theta_{34}\theta_{*}^{2} - k_{87b}\theta_{36}\theta_{H}$$

$$r_{88} = k_{88f}\theta_{35}\theta_{*} - k_{88b}\theta_{36}\theta_{OH}$$

$$r_{89} = k_{89f}\theta_{36} - k_{89b}\theta_{16}$$

$$r_{90} = k_{90f}\theta_{40}\theta_{*}^{2} - k_{90b}\theta_{GVL}\theta_{OH}$$

$$r_{91} = k_{91f}\theta_{LA}\theta_{*}^{2} - k_{91b}\theta_{37}\theta_{H}$$

$$r_{92} = k_{92f}\theta_{37}\theta_{H} - k_{92b}\theta_{38}$$

$$r_{93} = k_{93f}\theta_{38} - k_{93b}\theta_{39}\theta_{*}$$

$$r_{94} = k_{94f}\theta_{H_2O} - k_{94b}P_{H_2O}\theta_{*}$$

$$r_{95} = k_{95f}\theta_{OH}\theta_{*} - k_{95b}\theta_{O}\theta_{H}$$

$$r_{96} = k_{96f}\theta_{HPA} - k_{96b}P_{HPA}\theta_{*}^{3}$$

Steady state species balance and the overall site balance for 1 site model:

$$\frac{d\theta_{LA}}{dt} = r_1 - r_3 - r_4 - r_7 - r_8 - r_{91}$$

$$\frac{d\theta_{Al}}{dt} = r_3 - r_5 - r_{85} - r_{86}$$

$$\frac{d\theta_{Hy}}{dt} = r_4 - r_6 - r_{66} - r_{67} - r_{68} - r_{69} - r_{70}$$

$$\frac{d\theta_{HPA}}{dt} = r_5 + r_6 - r_{20} - r_{21} - r_{57} - r_{80} - r_{96}$$

$$\frac{d\theta_{01}}{dt} = r_7 - r_9 - r_{12} - r_{13}$$

$$\frac{d\theta_{02}}{dt} = r_9 - r_{10}$$

$$\frac{d\theta_{03}}{dt} = r_{10} - r_{11}$$

$$\frac{d\theta_{04}}{dt} = r_{11} - r_{19} + r_{76} + r_{53}$$

$$\frac{d\theta_{05}}{dt} = r_{13} - r_{14}$$

$$\frac{d\theta_{06}}{dt} = r_{12} + r_{15} - r_{16} + r_{43} + r_{45}$$

$$\frac{d\theta_{07}}{dt} = r_8 - r_{15} - r_{17} + r_{62} + r_{63}$$

$$\frac{d\theta_{08}}{dt} = r_{17} + r_{18} + r_{49} + r_{50} - r_{65}$$

$$\frac{d\theta_{09}}{dt} = r_{20} - r_{22} - r_{23} - r_{24}$$

$$\frac{d\theta_{10}}{dt} = r_{21} - r_{25} - r_{26} - r_{27} - r_{28}$$

$$\frac{d\theta_{11}}{dt} = r_{22} - r_{29} - r_{30} + r_{67}$$

$$\frac{d\theta_{12}}{dt} = r_{23} + r_{25} - r_{31} - r_{32}$$

$$\frac{d\theta_{13}}{dt} = r_{24} - r_{33} - r_{34} + r_{59}$$

$$\frac{d\theta_{14}}{dt} = r_{26} - r_{35} - r_{36}$$

$$\frac{d\theta_{15}}{dt} = r_{27} - r_{37} - r_{38} - r_{39} + r_{69}$$

$$\frac{d\theta_{16}}{dt} = r_{28} - r_{40} + r_{89}$$

$$\frac{d\theta_{17}}{dt} = r_{29} + r_{31} + r_{37} - r_{41} - r_{42}$$

$$\frac{d\theta_{18}}{dt} = r_{33} - r_{43} - r_{44} + r_{64}$$

$$\frac{d\theta_{19}}{dt} = r_{30} + r_{34} - r_{45} + r_{61}$$

$$\frac{d\theta_{20}}{dt} = r_{32} + r_{35} - r_{46} - r_{47}$$

$$\frac{d\theta_{21}}{dt} = r_{36} + r_{38} - r_{48} - r_{49} + r_{73}$$

$$\frac{d\theta_{22}}{dt} = r_{39} + r_{40} - r_{50} - r_{51} + r_{71}$$

$$\frac{d\theta_{23}}{dt} = r_{41} + r_{51} - r_{52}$$

$$\frac{d\theta_{24}}{dt} = r_{44} + r_{46} + r_{54} - r_{56}$$

$$\frac{d\theta_{25}}{dt} = r_{42} + r_{47} + r_{48} - r_{55} + r_{77}$$

$$\frac{d\theta_{26}}{dt} = r_{57} - r_{58} - r_{59} - r_{60} - r_{82}$$

$$\frac{d\theta_{27}}{dt} = r_{58} - r_{61} - r_{62} + r_{68}$$

$$\frac{d\theta_{28}}{dt} = r_{60} - r_{63} - r_{64}$$

$$\frac{d\theta_{29}}{dt} = r_{75} - r_{77} - r_{53}$$

$$\frac{d\theta_{30}}{dt} = r_{66} - r_{71} - r_{72}$$

$$\frac{d\theta_{31}}{dt} = r_{70} - r_{73} - r_{74} - r_{75}$$

$$\frac{d\theta_{32}}{dt} = r_{72} - r_{76} + r_{74}$$

$$\frac{d\theta_{33}}{dt} = r_{80} - r_{83} - r_{84}$$

$$\frac{d\theta_{34}}{dt} = r_{82} + r_{43} - r_{87}$$

$$\frac{d\theta_{35}}{dt} = r_{84} + r_{85} - r_{88}$$

$$\frac{d\theta_{36}}{dt} = r_{87} + r_{88} - r_{89}$$

$$\frac{d\theta_{37}}{dt} = r_{91} - r_{92}$$

$$\frac{d\theta_{38}}{dt} = r_{92} - r_{93}$$

$$\frac{d\theta_{39}}{dt} = r_{93} - r_{81}$$

$$\frac{d\theta_{40}}{dt} = r_{81} + r_{86} - r_{90}$$

$$\frac{d\theta_{AGL}}{dt} = r_{14} + r_{16} - r_{18} + r_{19} + r_{52} - r_{54} + r_{55}$$

$$\frac{d\theta_{GVL}}{dt} = r_{56} + r_{65} - r_{78} + r_{90}$$

$$\frac{d\theta_H}{dt} = 2r_2 - r_3 - r_4 - r_5 - r_6 + r_7 + r_9 - r_{11} + r_{15} - r_{18} + r_{20}$$
$$+ r_{22} + r_{25} + r_{26} + r_{27} + r_{31} + r_{32} + r_{33} + r_{34} + r_{35}$$
$$+ r_{36} + r_{37} + r_{38} + r_{40} + r_{42} + r_{43} + r_{45} + r_{47} + r_{48}$$
$$+ r_{50} + r_{51} + r_{52} - r_{54} - r_{56} + r_{58} + r_{59} + r_{60} + r_{61}$$
$$+ r_{62} + r_{63} + r_{64} - r_{65} + r_{67} + r_{70} + r_{72} + r_{75} + r_{76}$$
$$- r_{79} - r_{80} - r_{81} - r_{82} + r_{84} - r_{85} + r_{87} + r_{91} - r_{92}$$
$$+ r_{95}$$

$$\frac{d\theta_{OH}}{dt} = r_8 + r_{12} + r_{14} + r_{19} + r_{21} + r_{23} + r_{24} + r_{29} + r_{30} + r_{57}$$
$$+ r_{68} + r_{69} + r_{71} + r_{73} + r_{77} - r_{79} + r_{83} + r_{88} + r_{90}$$
$$- r_{95}$$

$$\frac{d\theta_{H_2O}}{dt} = r_{79} - r_{94}$$

$$\frac{d\theta_O}{dt} = r_{95}$$

and $$2\theta_{LA} + 3\theta_{HPA} + 2\theta_{Al} + 2\theta_{Hy} + 3\theta_{01} + 4\theta_{02} + 2\theta_{03} +$$
$$2\theta_{04} + 2\theta_{05} + 3\theta_{06} + 3\theta_{07} + 2\theta_{08} + 3\theta_{09} + 2\theta_{10} + 3\theta_{11} +$$
$$3\theta_{12} + 3\theta_{13} + 3\theta_{14} + 2\theta_{15} + 2\theta_{16} + 3\theta_{17} + 3\theta_{18} + 3\theta_{19} + 2\theta_{20} +$$
$$3\theta_{21} + 2\theta_{22} + 2\theta_{23} + 2\theta_{24} + 3\theta_{25} + 3\theta_{26} + 2\theta_{27} + 3\theta_{28} +$$
$$4\theta_{29} + 2\theta_{30} + 3\theta_{31} + 3\theta_{32} + 2\theta_{33} + \theta_{34} + 2\theta_{35} + 2\theta_{36} + 3\theta_{37} +$$
$$3\theta_{38} + 2\theta_{39} + \theta_{40} + 2\theta_{AGL} + 2\theta_{GVL} + \theta_H + \theta_{OH} + \theta_* = 1.00$$

Set of elementary reactions for two site model

$$r_1 = k_{1f}P_{LA}\theta_*^2 - k_{1b}\theta_{LA}$$

$$r_2 = k_{2f}P_{H_2}\theta_\Delta^2 - k_{2b}{\theta_H}^2$$

$$r_3 = k_{3f}\theta_{LA}\theta_H - k_{3b}\theta_{Al}\theta_\Delta$$

$$r_4 = k_{4f}\theta_{LA}\theta_H - k_{4b}\theta_{Hy}\theta_\Delta$$

$$r_5 = k_{5f}\theta_{Al}\theta_H\theta_* - k_{5b}\theta_{HPA}\theta_\Delta$$

$$r_6 = k_{6f}\theta_{Hy}\theta_H\theta_* - k_{6b}\theta_{HPA}\theta_\Delta$$

$$r_7 = k_{7f}\theta_{LA}\theta_*\theta_\Delta - k_{7b}\theta_{01}\theta_H$$

$$r_8 = k_{8f}\theta_{LA}\theta_*^2 - k_{8b}\theta_{07}\theta_{OH}$$

$$r_9 = k_{9f}\theta_{01}\theta_*\theta_\Delta - k_{9b}\theta_{02}\theta_H$$

$$r_{10} = k_{10f}\theta_{02} - k_{10b}\theta_{03}{\theta_*}^2$$

$$r_{11} = k_{11f}\theta_{03}\theta_H - k_{11b}\theta_{04}\theta_\Delta$$

$$r_{12} = k_{12f}\theta_{01}\theta_* - k_{12b}\theta_{06}\theta_{OH}$$

$$r_{13} = k_{13f}\theta_{01} - k_{13b}\theta_{05}\theta_*$$

$$r_{14} = k_{14f}\theta_{05}\theta_* - k_{14b}\theta_{AGL}\theta_{OH}$$

$$r_{15} = k_{15f}\theta_{07}\theta_\Delta - k_{15b}\theta_{06}\theta_H$$

$$r_{16} = k_{16f}\theta_{06} - k_{16b}\theta_{AGL}\theta_*$$

$$r_{17} = k_{17f}\theta_{07} - k_{17b}\theta_{08}\theta_*$$

$$r_{18} = k_{18f}\theta_{AGL}\theta_H - k_{18b}\theta_{08}\theta_\Delta$$

$$r_{19} = k_{19f}\theta_{04}\theta_* - k_{19b}\theta_{AGL}\theta_{OH}$$

$$r_{20} = k_{20f}\theta_{HPA}\theta_\Delta - k_{20b}\theta_{09}\theta_H$$

$$r_{21} = k_{21f}\theta_{HPA} - k_{21b}\theta_{10}\theta_{OH}$$

$$r_{22} = k_{22f}\theta_{09}\theta_{\Delta} - k_{22b}\theta_{11}\theta_{H}$$

$$r_{23} = k_{23f}\theta_{09}\theta_{*} - k_{23b}\theta_{12}\theta_{OH}$$

$$r_{24} = k_{24f}\theta_{09}\theta_{*} - k_{24b}\theta_{13}\theta_{OH}$$

$$r_{25} = k_{25f}\theta_{10}\theta_{*}\theta_{\Delta} - k_{25b}\theta_{12}\theta_{H}$$

$$r_{26} = k_{26f}\theta_{10}\theta_{*}\theta_{\Delta} - k_{26b}\theta_{14}\theta_{H}$$

$$r_{27} = k_{27f}\theta_{10}\theta_{\Delta} - k_{27b}\theta_{15}\theta_{H}$$

$$r_{28} = k_{28f}\theta_{10} - k_{28b}\theta_{16}$$

$$r_{29} = k_{29f}\theta_{11}\theta_{*} - k_{29b}\theta_{17}\theta_{OH}$$

$$r_{30} = k_{30f}\theta_{11}\theta_{*} - k_{30b}\theta_{19}\theta_{OH}$$

$$r_{31} = k_{31f}\theta_{12}\theta_{\Delta} - k_{31b}\theta_{17}\theta_{H}$$

$$r_{32} = k_{32f}\theta_{12}\theta_{\Delta} - k_{32b}\theta_{20}\theta_{H}\theta_{*}$$

$$r_{33} = k_{33f}\theta_{13}\theta_{\Delta} - k_{33b}\theta_{18}\theta_{H}$$

$$r_{34} = k_{34f}\theta_{13}\theta_{\Delta} - k_{34b}\theta_{19}\theta_{H}$$

$$r_{35} = k_{35f}\theta_{14}\theta_{\Delta} - k_{35b}\theta_{20}\theta_{H}\theta_{*}$$

$$r_{36} = k_{36f}\theta_{14}\theta_{\Delta} - k_{36b}\theta_{21}\theta_{H}$$

$$r_{37} = k_{37f}\theta_{15}\theta_{*}\theta_{\Delta} - k_{37b}\theta_{17}\theta_{H}$$

$$r_{38} = k_{38f}\theta_{15}\theta_{*}\theta_{\Delta} - k_{38b}\theta_{21}\theta_{H}$$

$$r_{39} = k_{39f}\theta_{15} - k_{39b}\theta_{22}$$

$$r_{40} = k_{40f}\theta_{16}\theta_{\Delta} - k_{40b}\theta_{22}\theta_{H}$$

$$r_{41} = k_{41f}\theta_{17} - k_{41b}\theta_{23}\theta_{*}$$

$$r_{42} = k_{42f}\theta_{17}\theta_{\Delta} - k_{42b}\theta_{25}\theta_{H}$$

$$r_{43} = k_{43f}\theta_{18}\theta_{\Delta} - k_{43b}\theta_{06}\theta_{H}$$

$$r_{44} = k_{44f}\theta_{18} - k_{44b}\theta_{24}\theta_{*}$$

$$r_{45} = k_{45f}\theta_{19}\theta_{\Delta} - k_{45b}\theta_{06}\theta_{H}$$

$$r_{46} = k_{46f}\theta_{20} - k_{46b}\theta_{24}$$

$$r_{47} = k_{47f}\theta_{20}\theta_{*}\theta_{\Delta} - k_{47b}\theta_{25}\theta_{H}$$

$$r_{48} = k_{48f}\theta_{21}\theta_{\Delta} - k_{48b}\theta_{25}\theta_{H}$$

$$r_{49} = k_{49f}\theta_{21} - k_{49b}\theta_{08}\theta_{*}$$

$$r_{50} = k_{50f}\theta_{22}\theta_{\Delta} - k_{50b}\theta_{08}\theta_{H}$$

$$r_{51} = k_{51f}\theta_{22}\theta_{\Delta} - k_{51b}\theta_{23}\theta_{H}$$

$$r_{52} = k_{52f}\theta_{23}\theta_{\Delta} - k_{52b}\theta_{AGL}\theta_{H}$$

$$r_{53} = k_{53f}\theta_{29} - k_{53b}\theta_{04}\theta_{*}^{\ 2}$$

$$r_{54} = k_{54f}\theta_{AGL}\theta_{H} - k_{54b}\theta_{24}\theta_{\Delta}$$

$$r_{55} = k_{55f}\theta_{25}\theta_{\Delta} - k_{55b}\theta_{AGL}\theta_{H}\theta_{*}$$

$$r_{56} = k_{56f}\theta_{24}\theta_{H} - k_{56b}\theta_{GVL}\theta_{\Delta}$$

$$r_{57} = k_{57f}\theta_{HPA}\theta_{*} - k_{57b}\theta_{26}\theta_{OH}$$

$$r_{58} = k_{58f}\theta_{26}\theta_{\Delta} - k_{58b}\theta_{27}\theta_{H}\theta_{*}$$

$$r_{59} = k_{59f}\theta_{26}\theta_{\Delta} - k_{59b}\theta_{13}\theta_{H}$$

$$r_{60} = k_{60f}\theta_{26}\theta_{\Delta} - k_{60b}\theta_{28}\theta_{H}$$

$$r_{61} = k_{61f}\theta_{27}\theta_{*}\theta_{\Delta} - k_{61b}\theta_{19}\theta_{H}$$

$$r_{62} = k_{62f}\theta_{27}\theta_{*}\theta_{\Delta} - k_{62b}\theta_{07}\theta_{H}$$

$$r_{63} = k_{63f}\theta_{28}\theta_{\Delta} - k_{63b}\theta_{07}\theta_{H}$$

$$r_{64} = k_{64f}\theta_{28}\theta_{\Delta} - k_{64b}\theta_{18}\theta_{H}$$

$$r_{65} = k_{65f}\theta_{08}\theta_{H} - k_{65b}\theta_{GVL}\theta_{\Delta}$$

$$r_{66} = k_{66f}\theta_{Hy} - k_{66b}\theta_{30}$$

$$r_{67} = k_{67f}\theta_{Hy}\theta_{*}\theta_{\Delta} - k_{67b}\theta_{11}\theta_{H}$$

$$r_{68} = k_{68f}\theta_{Hy}\theta_{*} - k_{68b}\theta_{27}\theta_{OH}$$

$$r_{69} = k_{69f}\theta_{Hy}\theta_{*} - k_{69b}\theta_{15}\theta_{OH}$$

$$r_{70} = k_{70f}\theta_{Hy}\theta_{*}\theta_{\Delta} - k_{70b}\theta_{31}\theta_{H}$$

$$r_{71} = k_{71f}\theta_{30}\theta_{*} - k_{71b}\theta_{22}\theta_{OH}$$

$$r_{72} = k_{72f}\theta_{30}\theta_{\Delta} - k_{72b}\theta_{32}\theta_{H}$$

$$r_{73} = k_{73f}\theta_{31}\theta_{*} - k_{73b}\theta_{21}\theta_{OH}$$

$$r_{74} = k_{74f}\theta_{31} - k_{74b}\theta_{32}\theta_{*}$$

$$r_{75} = k_{75f}\theta_{31}\theta_{*}\theta_{\Delta} - k_{75b}\theta_{29}\theta_{H}$$

$$r_{76} = k_{76f}\theta_{32}\theta_{\Delta} - k_{76b}\theta_{04}\theta_{H}$$

$$r_{77} = k_{77f}\theta_{29} - k_{77b}\theta_{25}\theta_{OH}$$

$$r_{78} = k_{78f}\theta_{GVL} - k_{78b}P_{GVL}{\theta_{*}}^{2}$$

$$r_{79} = k_{79f}\theta_{H}\theta_{OH} - k_{79b}\theta_{H_2O}\theta_{\Delta}$$

$$r_{80} = k_{80f}\theta_{HPA}\theta_{H} - k_{80b}\theta_{33}\theta_{*}\theta_{\Delta}$$

$$r_{81} = k_{81f}\theta_{39}\theta_{H} - k_{81b}\theta_{40}\theta_{*}\theta_{\Delta}$$

$$r_{82} = k_{82f}\theta_{26}\theta_{H} - k_{82b}\theta_{34}\theta_{*}\theta_{\Delta}$$

$$r_{83} = k_{83f}\theta_{33} - k_{83b}\theta_{34}\theta_{OH}$$

$$r_{84} = k_{84f}\theta_{33}\theta_{\Delta} - k_{84b}\theta_{35}\theta_{H}$$

$$r_{85} = k_{85f}\theta_{Al}\theta_{H} - k_{85b}\theta_{35}\theta_{\Delta}$$

$$r_{86} = k_{86f}\theta_{Al} - k_{86b}\theta_{40}\theta_{*}$$

$$r_{87} = k_{87f}\theta_{34}\theta_{*}\theta_{\Delta} - k_{87b}\theta_{36}\theta_{H}$$

$$r_{88} = k_{88f}\theta_{35}\theta_{*} - k_{88b}\theta_{36}\theta_{OH}$$

$$r_{89} = k_{89f}\theta_{36} - k_{89b}\theta_{16}$$

$$r_{90} = k_{90f}\theta_{40}\theta_{*}^{\,2} - k_{90b}\theta_{GVL}\theta_{OH}$$

$$r_{91} = k_{91f}\theta_{LA}\theta_{*}\theta_{\Delta} - k_{91b}\theta_{37}\theta_{H}$$

$$r_{92} = k_{92f}\theta_{37}\theta_{H}\theta_{*} - k_{92b}\theta_{38}\theta_{\Delta}$$

$$r_{93} = k_{93f}\theta_{38} - k_{93b}\theta_{39}\theta_{*}$$

$$r_{94} = k_{94f}\theta_{H_2O} - k_{94b}P_{H_2O}\theta_{*}$$

$$r_{95} = k_{95f}\theta_{OH}\theta_{\Delta} - k_{95b}\theta_{O}\theta_{H}$$

$$r_{96} = k_{96f}\theta_{HPA} - k_{96b}P_{HPA}\theta_{*}^{\,3}$$

Steady state species balance and the overall site balance for 2 site model:

$$\frac{d\theta_{LA}}{dt} = r_1 - r_3 - r_4 - r_7 - r_8 - r_{91}$$

$$\frac{d\theta_{Al}}{dt} = r_3 - r_5 - r_{85} - r_{86}$$

$$\frac{d\theta_{Hy}}{dt} = r_4 - r_6 - r_{66} - r_{67} - r_{68} - r_{69} - r_{70}$$

$$\frac{d\theta_{HPA}}{dt} = r_5 + r_6 - r_{20} - r_{21} - r_{57} - r_{80} - r_{96}$$

$$\frac{d\theta_{01}}{dt} = r_7 - r_9 - r_{12} - r_{13}$$

$$\frac{d\theta_{02}}{dt} = r_9 - r_{10}$$

$$\frac{d\theta_{03}}{dt} = r_{10} - r_{11}$$

$$\frac{d\theta_{04}}{dt} = r_{11} - r_{19} + r_{76} + r_{53}$$

$$\frac{d\theta_{05}}{dt} = r_{13} - r_{14}$$

$$\frac{d\theta_{06}}{dt} = r_{12} + r_{15} - r_{16} + r_{43} + r_{45}$$

$$\frac{d\theta_{07}}{dt} = r_8 - r_{15} - r_{17} + r_{62} + r_{63}$$

$$\frac{d\theta_{08}}{dt} = r_{17} + r_{18} + r_{49} + r_{50} - r_{65}$$

$$\frac{d\theta_{09}}{dt} = r_{20} - r_{22} - r_{23} - r_{24}$$

$$\frac{d\theta_{10}}{dt} = r_{21} - r_{25} - r_{26} - r_{27} - r_{28}$$

$$\frac{d\theta_{11}}{dt} = r_{22} - r_{29} - r_{30} + r_{67}$$

$$\frac{d\theta_{12}}{dt} = r_{23} + r_{25} - r_{31} - r_{32}$$

$$\frac{d\theta_{13}}{dt} = r_{24} - r_{33} - r_{34} + r_{59}$$

$$\frac{d\theta_{14}}{dt} = r_{26} - r_{35} - r_{36}$$

$$\frac{d\theta_{15}}{dt} = r_{27} - r_{37} - r_{38} - r_{39} + r_{69}$$

$$\frac{d\theta_{16}}{dt} = r_{28} - r_{40} + r_{89}$$

$$\frac{d\theta_{17}}{dt} = r_{29} + r_{31} + r_{37} - r_{41} - r_{42}$$

$$\frac{d\theta_{18}}{dt} = r_{33} - r_{43} - r_{44} + r_{64}$$

$$\frac{d\theta_{19}}{dt} = r_{30} + r_{34} - r_{45} + r_{61}$$

$$\frac{d\theta_{20}}{dt} = r_{32} + r_{35} - r_{46} - r_{47}$$

$$\frac{d\theta_{21}}{dt} = r_{36} + r_{38} - r_{48} - r_{49} + r_{73}$$

$$\frac{d\theta_{22}}{dt} = r_{39} + r_{40} - r_{50} - r_{51} + r_{71}$$

$$\frac{d\theta_{23}}{dt} = r_{41} + r_{51} - r_{52}$$

$$\frac{d\theta_{24}}{dt} = r_{44} + r_{46} + r_{54} - r_{56}$$

$$\frac{d\theta_{25}}{dt} = r_{42} + r_{47} + r_{48} - r_{55} + r_{77}$$

$$\frac{d\theta_{26}}{dt} = r_{57} - r_{58} - r_{59} - r_{60} - r_{82}$$

$$\frac{d\theta_{27}}{dt} = r_{58} - r_{61} - r_{62} + r_{68}$$

$$\frac{d\theta_{28}}{dt} = r_{60} - r_{63} - r_{64}$$

$$\frac{d\theta_{29}}{dt} = r_{75} - r_{77} - r_{53}$$

$$\frac{d\theta_{30}}{dt} = r_{66} - r_{71} - r_{72}$$

$$\frac{d\theta_{31}}{dt} = r_{70} - r_{73} - r_{74} - r_{75}$$

$$\frac{d\theta_{32}}{dt} = r_{72} - r_{76} + r_{74}$$

$$\frac{d\theta_{33}}{dt} = r_{80} - r_{83} - r_{84}$$

$$\frac{d\theta_{34}}{dt} = r_{82} + r_{43} - r_{87}$$

$$\frac{d\theta_{35}}{dt} = r_{84} + r_{85} - r_{88}$$

$$\frac{d\theta_{36}}{dt} = r_{87} + r_{88} - r_{89}$$

$$\frac{d\theta_{37}}{dt} = r_{91} - r_{92}$$

$$\frac{d\theta_{38}}{dt} = r_{92} - r_{93}$$

$$\frac{d\theta_{39}}{dt} = r_{93} - r_{81}$$

$$\frac{d\theta_{40}}{dt} = r_{81} + r_{86} - r_{90}$$

$$\frac{d\theta_{AGL}}{dt} = r_{14} + r_{16} - r_{18} + r_{19} + r_{52} - r_{54} + r_{55}$$

$$\frac{d\theta_{GVL}}{dt} = r_{56} + r_{65} - r_{78} + r_{90}$$

$$\frac{d\theta_H}{dt} = 2r_2 - r_3 - r_4 - r_5 - r_6 + r_7 + r_9 - r_{11} + r_{15} - r_{18} + r_{20}$$
$$+ r_{22} + r_{25} + r_{26} + r_{27} + r_{31} + r_{32} + r_{33} + r_{34} + r_{35}$$
$$+ r_{36} + r_{37} + r_{38} + r_{40} + r_{42} + r_{43} + r_{45} + r_{47} + r_{48}$$
$$+ r_{50} + r_{51} + r_{52} - r_{54} - r_{56} + r_{58} + r_{59} + r_{60} + r_{61}$$
$$+ r_{62} + r_{63} + r_{64} - r_{65} + r_{67} + r_{70} + r_{72} + r_{75} + r_{76}$$
$$- r_{79} - r_{80} - r_{81} - r_{82} + r_{84} - r_{85} + r_{87} + r_{91} - r_{92}$$
$$+ r_{95}$$

$$\frac{d\theta_{OH}}{dt} = r_8 + r_{12} + r_{14} + r_{19} + r_{21} + r_{23} + r_{24} + r_{29} + r_{30} + r_{57}$$
$$+ r_{68} + r_{69} + r_{71} + r_{73} + r_{77} - r_{79} + r_{83} + r_{88} + r_{90}$$
$$- r_{95}$$

$$\frac{d\theta_{H_2O}}{dt} = r_{79} - r_{94}$$

$$\frac{d\theta_O}{dt} = r_{95}$$

$$2\theta_{LA} + 3\theta_{HPA} + 2\theta_{Al} + 2\theta_{Hy} + 3\theta_{01} + 4\theta_{02} + 2\theta_{03} +$$
$$2\theta_{04} + 2\theta_{05} + 3\theta_{06} + 3\theta_{07} + 2\theta_{08} + 3\theta_{09} + 2\theta_{10} + 3\theta_{11} +$$
$$3\theta_{12} + 3\theta_{13} + 3\theta_{14} + 2\theta_{15} + 2\theta_{16} + 3\theta_{17} + 3\theta_{18} + 3\theta_{19} + 2\theta_{20} +$$
$$3\theta_{21} + 2\theta_{22} + 2\theta_{23} + 2\theta_{24} + 3\theta_{25} + 3\theta_{26} + 2\theta_{27} + 3\theta_{28} +$$
$$4\theta_{29} + 2\theta_{30} + 3\theta_{31} + 3\theta_{32} + 2\theta_{33} + \theta_{34} + 2\theta_{35} + 2\theta_{36} + 3\theta_{37} +$$
$$3\theta_{38} + 2\theta_{39} + \theta_{40} + 2\theta_{AGL} + 2\theta_{GVL} + \theta_{OH} + \theta_* = 1.00$$

and

$$\theta_H + \theta_\Delta = 1.00$$

In 1,4-dioxane and methanol simulations, we include solvent adsorption process with an extra balance equation.

For 1,4-dioxane:

$$r_{97} = k_{97f}\theta_{14DO} - k_{97b}P_{14DO}\theta_*$$

$$\frac{d\theta_{14DO}}{dt} = -r_{97}$$

For methanol:

$$r_{97} = k_{97f}\theta_{mtOH} - k_{97b}P_{mtOH}\theta_*$$

$$\frac{d\theta_{mtOH}}{dt} = -r_{97}$$

C.5 Rates of all elementary reaction (s^{-1}) at 323 and 423 k in different solvent environment

Table C.4: Rates of all the elementary reaction rates at 323 K and 423 K for one site model

Reaction step	Solvent					
	Water		1,4-dioxane		Methanol	
	323 K	423 K	323 K	423 K	323 K	423 K
r_1	1.00E-05	2.39E-01	2.83E-07	1.03E-02	2.86E-07	2.03E-02
r_2	1.00E-05	2.39E-01	2.83E-07	1.03E-02	2.86E-07	2.03E-02
r_3	1.00E-05	2.39E-01	2.83E-07	1.03E-02	2.86E-07	2.03E-02
r_4	1.17E-17	3.66E-10	2.45E-18	7.80E-11	1.49E-18	1.07E-10
r_5	2.65E-15	-1.68E-09	3.52E-17	-1.16E-09	2.56E-17	-1.18E-09
r_6	1.15E-17	3.54E-10	2.44E-18	7.34E-11	1.48E-18	1.01E-10
r_7	3.57E-16	6.20E-09	2.96E-16	3.82E-09	1.85E-16	4.80E-09
r_8	1.71E-16	5.66E-09	2.31E-18	1.34E-10	1.13E-18	2.33E-10
r_9	-3.32E-21	2.13E-18	-1.04E-25	-1.81E-18	-7.37E-26	5.75E-17
r_{10}	6.83E-29	3.63E-18	3.48E-30	4.23E-19	1.36E-30	5.53E-19
r_{11}	4.96E-29	3.63E-18	3.53E-30	4.23E-19	1.38E-30	5.52E-19
r_{12}	3.11E-19	6.16E-11	4.18E-20	1.31E-11	1.76E-20	1.61E-11
r_{13}	3.57E-16	6.14E-09	2.96E-16	3.81E-09	1.85E-16	4.78E-09
r_{14}	3.57E-16	6.14E-09	2.96E-16	3.81E-09	1.85E-16	4.78E-09
r_{15}	1.73E-16	1.81E-07	2.56E-19	-1.54E-08	3.30E-19	7.63E-09
r_{16}	2.89E-15	2.05E-09	3.92E-17	2.34E-10	3.03E-17	-4.63E-10
r_{17}	6.36E-17	2.41E-09	5.39E-19	-1.10E-09	4.65E-19	-1.92E-10
r_{18}	4.40E-17	-1.03E-08	2.10E-19	-3.98E-09	2.31E-19	1.21E-09
r_{19}	4.47E-24	-9.40E-15	8.01E-25	1.11E-15	3.52E-25	6.36E-16
r_{20}	7.12E-21	-1.13E-13	2.37E-22	-8.64E-14	1.35E-22	-7.99E-14

r_{21}	8.57E-25	-1.29E-16	7.51E-26	-1.82E-16	5.13E-26	-1.51E-16
r_{22}	-2.29E-22	-3.20E-13	-3.76E-23	-4.90E-14	-1.49E-23	-6.41E-14
r_{23}	7.39E-21	2.12E-13	2.75E-22	-3.78E-14	1.50E-22	-1.55E-14
r_{24}	-4.06E-23	-4.82E-15	4.33E-26	3.79E-16	3.08E-26	-3.33E-16
r_{25}	1.35E-19	-7.13E-10	1.72E-22	9.35E-11	6.51E-20	2.52E-11
r_{26}	8.29E-20	-1.15E-09	-3.36E-21	9.30E-11	5.35E-20	-2.11E-10
r_{27}	5.89E-18	1.90E-09	5.74E-21	-2.14E-10	2.06E-18	1.41E-10
r_{28}	-6.13E-18	-3.64E-11	-3.74E-21	2.77E-11	-2.19E-18	4.42E-11
r_{29}	2.02E-28	6.71E-18	1.47E-29	3.12E-19	8.23E-30	4.85E-19
r_{30}	1.68E-19	2.57E-11	1.13E-20	4.45E-12	4.86E-21	5.25E-12
r_{31}	-4.62E-15	7.49E-07	-4.10E-16	-3.80E-07	-3.67E-16	-1.85E-07
r_{32}	4.62E-15	-7.50E-07	4.10E-16	3.80E-07	3.67E-16	1.85E-07
r_{33}	-7.05E-17	-1.48E-08	-3.84E-20	-6.07E-09	-7.76E-21	9.57E-09
r_{34}	1.07E-18	4.48E-09	2.47E-21	-4.11E-11	3.69E-21	-2.94E-11
r_{35}	2.17E-16	8.72E-09	2.33E-18	-1.20E-09	4.08E-18	2.40E-09
r_{36}	-2.19E-16	-9.87E-09	-2.34E-18	1.29E-09	-4.03E-18	-2.61E-09
r_{37}	5.89E-18	1.95E-09	5.79E-21	-2.06E-10	2.06E-18	1.47E-10
r_{38}	1.84E-21	-4.92E-11	-4.61E-23	-8.34E-12	7.17E-22	-5.48E-12
r_{39}	4.76E-23	9.91E-13	7.83E-25	6.48E-14	3.35E-24	-8.13E-13
r_{40}	-5.08E-23	-1.11E-12	-8.71E-25	-7.32E-14	-2.35E-24	7.60E-13
r_{41}	-5.92E-26	4.05E-15	-4.83E-29	-1.17E-15	-1.87E-26	5.14E-15
r_{42}	-4.62E-15	7.51E-07	-4.10E-16	-3.80E-07	-3.65E-16	-1.85E-07
r_{43}	1.85E-18	3.29E-09	1.56E-21	3.86E-11	2.82E-21	-4.51E-10
$\boldsymbol{r_{44}}$	8.81E-18	6.75E-10	5.49E-20	-3.44E-11	4.42E-20	-2.09E-10
r_{45}	2.72E-15	-1.82E-07	3.89E-17	1.56E-08	2.99E-17	-7.66E-09
r_{46}	-2.27E-30	-1.44E-18	-5.62E-31	2.80E-18	-3.83E-31	-7.45E-18
r_{47}	-1.73E-15	-7.41E-07	-4.65E-17	3.79E-07	-3.81E-17	1.88E-07
r_{48}	6.07E-15	-2.23E-08	1.09E-16	-6.05E-09	1.40E-16	-4.22E-09
r_{49}	-6.29E-15	1.24E-08	-1.12E-16	7.33E-09	-1.44E-16	1.61E-09
r_{50}	1.50E-26	-4.01E-15	-7.12E-27	-5.60E-15	1.10E-25	1.33E-15
r_{51}	-3.25E-24	-1.17E-13	-7.89E-26	-2.81E-15	8.83E-25	-5.45E-14
r_{52}	-3.30E-24	-1.13E-13	-7.90E-26	-3.98E-15	8.64E-25	-4.94E-14
r_{53}	-2.60E-30	8.40E-20	-7.04E-32	-4.67E-21	-4.70E-32	-3.28E-21
$\boldsymbol{r_{54}}$	-2.61E-14	6.11E-09	-4.78E-17	6.60E-10	-9.66E-17	1.31E-09
r_{55}	-2.93E-14	-1.24E-08	-3.82E-16	-7.36E-09	-3.11E-16	-1.79E-09
r_{56}	-2.60E-14	6.79E-09	-4.78E-17	6.26E-10	-9.66E-17	1.10E-09
r_{57}	2.66E-15	-3.86E-09	3.76E-17	-1.12E-09	2.70E-17	-1.12E-09
r_{58}	2.71E-15	-1.90E-07	3.89E-17	1.56E-08	2.99E-17	-6.93E-09
r_{59}	-6.94E-17	-1.03E-08	-3.60E-20	-6.11E-09	-4.06E-21	9.54E-09
r_{60}	1.84E-16	1.99E-07	-1.22E-18	-1.06E-08	5.56E-20	-3.73E-09
r_{61}	2.72E-15	-1.87E-07	3.89E-17	1.56E-08	2.99E-17	-7.63E-09
r_{62}	-5.81E-18	-3.04E-09	-2.80E-21	3.62E-11	-4.92E-21	7.07E-10
r_{63}	7.08E-17	1.81E-07	-1.52E-18	-1.66E-08	-3.31E-19	6.50E-09
$\boldsymbol{r_{64}}$	8.11E-17	1.87E-08	9.49E-20	6.08E-09	5.48E-20	-1.02E-08
r_{65}	-6.19E-15	4.52E-09	-1.11E-16	2.25E-09	-1.43E-16	2.63E-09

r_{66}	7.68E-20	-1.39E-11	1.79E-22	7.92E-14	1.08E-22	7.40E-14
r_{67}	1.68E-19	2.60E-11	1.13E-20	4.50E-12	4.87E-21	5.31E-12
r_{68}	1.28E-23	2.64E-14	2.17E-24	1.04E-14	9.16E-25	1.01E-14
r_{69}	1.23E-25	4.85E-16	1.36E-26	1.02E-16	7.00E-27	1.30E-16
r_{70}	1.06E-23	2.60E-14	3.21E-25	1.29E-15	1.43E-25	2.00E-15
r_{71}	1.27E-26	-1.49E-16	1.99E-27	9.62E-18	7.35E-28	4.93E-18
r_{72}	7.68E-20	-1.39E-11	1.79E-22	7.92E-14	1.08E-22	7.40E-14
r_{73}	6.00E-21	-2.09E-12	2.79E-23	1.97E-14	1.86E-23	1.75E-14
$\boldsymbol{r_{74}}$	-7.68E-20	1.39E-11	-1.78E-22	-7.81E-14	-1.08E-22	-7.34E-14
r_{75}	7.08E-20	-1.18E-11	1.51E-22	5.96E-14	8.92E-23	5.78E-14
r_{76}	4.47E-24	-9.40E-15	8.01E-25	1.11E-15	3.52E-25	6.35E-16
r_{77}	7.08E-20	-1.18E-11	1.51E-22	5.96E-14	8.92E-23	5.78E-14
r_{78}	1.00E-05	2.39E-01	2.83E-07	1.03E-02	2.86E-07	2.03E-02
r_{79}	1.00E-05	2.39E-01	2.83E-07	1.03E-02	2.86E-07	2.03E-02
r_{80}	-2.07E-21	-3.00E-13	5.34E-25	1.39E-15	1.33E-25	3.83E-15
r_{81}	-3.68E-20	-3.63E-14	-8.05E-24	1.66E-15	-1.70E-23	4.64E-17
r_{82}	-1.68E-16	-3.25E-09	-4.67E-21	-6.64E-11	-2.94E-18	1.07E-13
r_{83}	2.61E-19	-3.34E-12	2.58E-22	-9.36E-16	3.29E-22	2.50E-14
$\boldsymbol{r_{84}}$	-2.64E-19	3.04E-12	-2.58E-22	2.33E-15	-3.29E-22	-2.12E-14
$\boldsymbol{r_{85}}$	2.64E-19	-3.08E-12	2.64E-22	-2.47E-15	3.35E-22	2.17E-14
$\boldsymbol{r_{86}}$	1.00E-05	2.39E-01	2.83E-07	1.03E-02	2.86E-07	2.03E-02
$\boldsymbol{r_{87}}$	6.13E-18	3.54E-11	3.74E-21	-2.78E-11	2.19E-18	-4.35E-11
$\boldsymbol{r_{88}}$	7.88E-22	-4.01E-14	6.20E-24	-1.37E-16	5.68E-24	4.97E-16
$\boldsymbol{r_{89}}$	6.13E-18	3.53E-11	3.74E-21	-2.78E-11	2.19E-18	-4.35E-11
r_{90}	1.00E-05	2.39E-01	2.83E-07	1.03E-02	2.86E-07	2.03E-02
r_{91}	-5.43E-15	-1.44E-13	-4.09E-18	-1.01E-12	-1.80E-18	1.67E-11
$\boldsymbol{r_{92}}$	4.44E-15	3.64E-12	0.00E+00	2.27E-13	0.00E+00	2.27E-13
$\boldsymbol{r_{93}}$	-3.68E-20	-3.63E-14	-8.04E-24	1.66E-15	-1.70E-23	4.64E-17
$\boldsymbol{r_{94}}$	1.00E-05	2.39E-01	2.83E-07	1.03E-02	2.86E-07	2.03E-02
$\boldsymbol{r_{95}}$	0.00E+00	-7.96E-13	5.42E-20	2.63E-14	-5.42E-20	-3.93E-13
$\boldsymbol{r_{96}}$	1.71E-20	2.53E-09	9.79E-22	3.10E-11	2.73E-22	3.69E-11

Table C.5: Rates of all the elementary reaction rates at 323 K and 423 K for two site model

Reaction step	Solvent					
	Water		1,4-dioxane		Methanol	
	323 K	423 K	323 K	423 K	323 K	423 K
r_1	2.43E-04	3.09E-01	3.73E-05	5.35E-02	7.43E-05	9.14E-02
r_2	2.43E-04	3.09E-01	3.73E-05	5.35E-02	7.43E-05	9.14E-02
r_3	2.43E-04	3.09E-01	3.73E-05	5.35E-02	7.43E-05	9.14E-02
r_4	2.83E-16	4.62E-10	3.18E-16	3.80E-10	3.81E-16	4.50E-10
r_5	3.37E-17	9.07E-12	5.98E-18	4.38E-13	1.13E-17	8.64E-13
r_6	8.67E-19	6.76E-13	8.45E-19	2.65E-13	1.43E-18	4.57E-13

r_7	4.46E-14	2.53E-08	4.75E-13	1.05E-07	7.79E-13	1.06E-07
r_8	1.00E-13	5.85E-09	3.96E-14	2.35E-09	7.64E-14	3.27E-09
r_9	-2.70E-18	-4.27E-12	-1.19E-19	-1.32E-12	-4.80E-19	-2.05E-12
r_{10}	4.39E-26	7.32E-17	6.88E-26	8.51E-17	9.23E-26	8.30E-17
r_{11}	4.20E-26	6.93E-17	6.89E-26	8.95E-17	9.20E-26	8.65E-17
r_{12}	1.91E-16	2.82E-10	7.69E-16	7.81E-10	1.19E-15	7.44E-10
r_{13}	4.44E-14	2.50E-08	4.74E-13	1.04E-07	7.77E-13	1.06E-07
r_{14}	4.44E-14	2.50E-08	4.74E-13	1.04E-07	7.77E-13	1.06E-07
r_{15}	8.68E-14	5.68E-09	2.84E-14	2.21E-09	6.47E-14	3.14E-09
r_{16}	9.77E-14	6.27E-09	3.14E-14	3.27E-09	7.00E-14	4.14E-09
r_{17}	2.99E-15	7.67E-11	1.60E-15	5.78E-11	5.28E-15	6.84E-11
r_{18}	2.11E-16	3.59E-10	2.61E-17	1.81E-10	8.29E-16	2.79E-10
r_{19}	1.57E-21	9.15E-14	1.43E-20	4.48E-13	1.22E-20	4.31E-13
r_{20}	3.92E-21	-9.62E-15	4.78E-22	-4.54E-15	1.03E-21	-3.81E-15
r_{21}	4.41E-25	5.08E-19	1.39E-25	5.89E-20	3.34E-25	8.84E-20
r_{22}	-2.36E-20	-1.22E-12	-8.41E-20	-1.81E-12	-6.47E-20	-1.73E-12
r_{23}	4.15E-20	1.21E-12	8.67E-20	1.81E-12	7.42E-20	1.73E-12
r_{24}	-1.39E-20	5.81E-15	-2.18E-21	3.37E-15	-8.52E-21	3.36E-15
r_{25}	-5.70E-19	-8.43E-13	2.22E-18	9.75E-14	3.17E-16	1.83E-13
r_{26}	-2.54E-18	-1.34E-12	7.41E-19	1.67E-14	2.94E-18	-1.65E-12
r_{27}	5.70E-17	3.49E-12	7.80E-17	2.78E-12	-1.44E-16	3.09E-12
r_{28}	-5.40E-17	-1.32E-12	-8.16E-17	-2.91E-12	-1.77E-16	-1.65E-12
r_{29}	8.90E-26	1.13E-17	3.60E-25	1.95E-17	5.58E-25	2.51E-17
r_{30}	1.46E-16	2.50E-10	2.73E-16	2.93E-10	3.06E-16	3.23E-10
r_{31}	5.29E-14	3.81E-09	-1.47E-13	-1.68E-08	-4.57E-13	-2.13E-08
r_{32}	-5.29E-14	-3.81E-09	1.47E-13	1.68E-08	4.57E-13	2.13E-08
r_{33}	-4.40E-15	-7.41E-11	-1.34E-17	6.66E-12	-5.05E-15	2.06E-10
r_{34}	2.80E-15	3.43E-11	2.30E-16	3.27E-12	5.85E-16	4.70E-12
r_{35}	1.03E-18	2.49E-14	8.30E-20	1.89E-14	1.60E-18	4.96E-14
r_{36}	-7.28E-17	-3.62E-12	-5.07E-17	-3.86E-12	-1.01E-16	-6.06E-12
r_{37}	5.70E-17	3.76E-12	7.80E-17	2.79E-12	-1.45E-16	3.24E-12
r_{38}	-5.27E-20	-2.62E-13	1.06E-20	-1.12E-14	1.45E-18	-1.45E-13
r_{39}	6.23E-22	-3.04E-15	1.01E-23	-1.54E-15	7.11E-20	-6.54E-15
r_{40}	-6.64E-22	-1.06E-15	-5.73E-23	-6.37E-18	-7.11E-20	2.78E-15
r_{41}	-9.24E-25	1.34E-17	-4.12E-25	-2.76E-18	-2.82E-23	9.21E-17
r_{42}	5.30E-14	3.81E-09	-1.47E-13	-1.68E-08	-4.57E-13	-2.13E-08
r_{43}	1.54E-15	1.22E-10	2.00E-16	4.45E-11	4.22E-16	2.54E-11
$\boldsymbol{r_{44}}$	4.19E-16	1.60E-11	1.65E-16	7.92E-12	5.30E-16	6.14E-12
r_{45}	9.35E-15	3.20E-10	2.13E-15	3.24E-10	3.71E-15	3.45E-10
r_{46}	-1.75E-29	-9.93E-21	-9.25E-29	-1.28E-19	-5.14E-30	-1.65E-19
r_{47}	-9.39E-14	-1.18E-08	-1.23E-13	-4.05E-08	1.38E-13	-2.93E-08
r_{48}	1.62E-13	1.66E-08	1.74E-14	1.92E-09	4.33E-14	4.10E-09
r_{49}	-1.62E-13	-1.66E-08	-1.75E-14	-1.92E-09	-4.34E-14	-4.09E-09
r_{50}	-6.14E-25	-2.21E-17	1.55E-25	-3.70E-18	-6.40E-24	1.36E-17
r_{51}	-2.98E-23	-3.96E-15	-3.06E-24	-1.14E-15	1.38E-23	-3.38E-15

r_{52}	-3.08E-23	-3.95E-15	-3.49E-24	-1.14E-15	-1.44E-23	-3.29E-15
r_{53}	-4.50E-27	-9.28E-19	-1.45E-26	-4.12E-18	-2.63E-26	-4.69E-18
$\boldsymbol{r_{54}}$	-6.69E-13	-2.43E-08	-7.01E-15	-4.79E-10	-2.57E-14	-1.58E-09
r_{55}	-8.11E-13	-5.52E-08	-5.12E-13	-1.07E-07	-8.72E-13	-1.11E-07
r_{56}	-6.69E-13	-2.43E-08	-6.84E-15	-4.71E-10	-2.52E-14	-1.57E-09
r_{57}	3.46E-17	9.50E-12	6.82E-18	7.02E-13	1.27E-17	1.29E-12
r_{58}	1.06E-15	1.19E-12	1.94E-16	7.63E-13	2.57E-16	1.04E-12
r_{59}	-1.60E-15	-3.98E-11	2.16E-16	9.93E-12	-4.46E-15	2.11E-10
r_{60}	2.06E-15	1.69E-10	-3.04E-16	3.16E-11	4.46E-15	-1.87E-10
r_{61}	6.41E-15	3.58E-11	1.62E-15	2.79E-11	2.82E-15	1.74E-11
r_{62}	-5.34E-15	-3.46E-11	-1.43E-15	-2.71E-11	-2.57E-15	-1.63E-11
r_{63}	-5.11E-15	-5.56E-11	-8.19E-15	-4.90E-11	-3.85E-15	-4.68E-11
$\boldsymbol{r_{64}}$	6.37E-15	2.12E-10	3.78E-16	4.58E-11	6.00E-15	-1.74E-10
r_{65}	-1.59E-13	-1.61E-08	-1.59E-14	-1.68E-09	-3.73E-14	-3.75E-09
r_{66}	1.35E-16	2.10E-10	4.32E-17	8.47E-11	7.34E-17	1.25E-10
r_{67}	1.46E-16	2.51E-10	2.73E-16	2.95E-10	3.06E-16	3.25E-10
r_{68}	1.05E-20	3.62E-14	4.82E-20	1.41E-13	5.72E-20	1.35E-13
r_{69}	1.01E-22	6.64E-16	3.02E-22	1.39E-15	4.37E-22	1.74E-15
r_{70}	9.51E-21	2.16E-13	7.84E-21	8.05E-14	9.14E-21	1.15E-13
r_{71}	1.05E-23	1.21E-16	4.43E-23	4.00E-16	4.58E-23	3.94E-16
r_{72}	1.35E-16	2.10E-10	4.32E-17	8.47E-11	7.34E-17	1.25E-10
r_{73}	1.00E-17	5.08E-12	6.28E-18	5.47E-12	1.26E-17	7.76E-12
$\boldsymbol{r_{74}}$	-1.35E-16	-2.10E-10	-4.32E-17	-8.43E-11	-7.34E-17	-1.24E-10
r_{75}	1.25E-16	2.05E-10	3.70E-17	7.89E-11	6.08E-17	1.16E-10
r_{76}	1.57E-21	9.14E-14	1.43E-20	4.48E-13	1.22E-20	4.31E-13
r_{77}	1.25E-16	2.05E-10	3.70E-17	7.89E-11	6.08E-17	1.16E-10
r_{78}	2.43E-04	3.09E-01	3.73E-05	5.35E-02	7.43E-05	9.14E-02
r_{79}	2.43E-04	3.09E-01	3.73E-05	5.35E-02	7.43E-05	9.14E-02
r_{80}	-1.15E-19	-1.03E-14	-1.94E-21	-3.63E-16	-3.81E-21	-2.33E-16
r_{81}	-4.98E-18	-9.09E-13	-6.09E-20	2.79E-14	-3.59E-19	-4.24E-15
r_{82}	-1.49E-15	-1.21E-10	-1.01E-16	-4.16E-11	-2.45E-16	-2.38E-11
r_{83}	8.09E-18	3.79E-13	1.82E-19	3.90E-15	5.41E-19	1.79E-14
$\boldsymbol{r_{84}}$	-8.21E-18	-3.90E-13	-1.84E-19	-4.26E-15	-5.45E-19	-1.81E-14
$\boldsymbol{r_{85}}$	8.32E-18	3.93E-13	2.35E-19	4.49E-15	6.96E-19	1.89E-14
$\boldsymbol{r_{86}}$	2.43E-04	3.09E-01	3.73E-05	5.35E-02	7.43E-05	9.14E-02
$\boldsymbol{r_{87}}$	5.39E-17	1.32E-12	8.16E-17	2.91E-12	1.77E-16	1.65E-12
$\boldsymbol{r_{88}}$	1.19E-19	3.77E-15	5.06E-20	2.30E-16	1.51E-19	8.11E-16
$\boldsymbol{r_{89}}$	5.40E-17	1.32E-12	8.16E-17	2.91E-12	1.77E-16	1.65E-12
r_{90}	2.43E-04	3.09E-01	3.73E-05	5.35E-02	7.43E-05	9.14E-02
r_{91}	-9.60E-13	-6.94E-08	-4.25E-13	-9.02E-08	-8.12E-13	-9.86E-08
$\boldsymbol{r_{92}}$	-1.11E-16	-1.11E-12	-1.39E-17	-1.42E-14	-1.39E-17	-7.82E-14
$\boldsymbol{r_{93}}$	-4.98E-18	-9.09E-13	-6.09E-20	2.79E-14	-3.59E-19	-4.24E-15
$\boldsymbol{r_{94}}$	2.43E-04	3.09E-01	3.73E-05	5.35E-02	7.43E-05	9.14E-02
$\boldsymbol{r_{95}}$	-2.13E-14	-2.14E-11	-1.02E-16	-3.20E-11	-6.94E-17	-3.55E-11
$\boldsymbol{r_{96}}$	2.93E-20	2.67E-13	1.97E-21	6.20E-15	1.00E-19	3.86E-14

C.6 Surface coverage of all adsorbed surface species at 323 k and 423 k at different reaction medium

Table C.6: Surface coverage of all the surface species at 323 K and 423 K for one site model

Adsorbed species	Solvent					
	Water		1,4-dioxane		Methanol	
	323 K	423 K	323 K	423 K	323 K	423 K
I-1	5.44E-15	3.87E-11	4.25E-15	2.34E-11	2.58E-15	2.92E-11
I-2	1.09E-09	7.59E-07	3.06E-12	1.79E-08	2.13E-12	3.42E-08
I-3	8.32E-18	6.28E-13	2.07E-18	6.80E-13	1.22E-18	7.34E-13
I-4	1.09E-22	7.70E-17	1.87E-23	2.63E-17	1.31E-23	3.72E-17
I-5	4.52E-22	3.20E-14	2.17E-21	3.95E-14	1.51E-21	4.06E-14
I-6	4.56E-10	6.41E-05	1.36E-12	2.17E-05	1.26E-12	3.43E-05
I-7	3.66E-16	7.07E-10	6.28E-18	7.33E-10	3.69E-18	7.76E-10
I-8	2.31E-19	6.27E-12	7.23E-21	1.93E-11	6.54E-21	1.79E-11
I-9	6.03E-24	1.65E-15	8.41E-27	4.42E-17	6.33E-27	8.31E-17
I-10	1.61E-12	4.34E-07	7.07E-14	4.43E-07	1.95E-13	5.81E-07
I-11	8.67E-23	1.54E-14	3.12E-23	2.27E-15	1.23E-23	3.14E-15
I-12	4.30E-12	7.23E-07	2.15E-14	1.88E-07	3.17E-14	3.59E-07
I-13	2.35E-17	6.06E-11	1.93E-19	2.14E-11	1.87E-19	3.25E-11
I-14	1.42E-10	2.02E-05	5.23E-13	1.11E-05	5.21E-13	1.38E-05
I-15	2.93E-16	7.03E-10	7.66E-18	9.28E-10	3.16E-17	1.37E-09
I-16	1.19E-21	5.56E-14	1.08E-22	2.47E-13	2.50E-22	2.06E-13
I-17	4.15E-15	1.34E-08	5.27E-17	1.21E-08	5.59E-17	1.64E-08
I-18	6.56E-19	3.84E-12	5.61E-21	4.62E-12	6.75E-21	5.79E-12
I-19	4.71E-12	7.82E-07	1.99E-14	1.90E-07	2.20E-14	3.46E-07
I-20	3.92E-07	1.81E-02	2.73E-08	1.06E-01	2.42E-08	1.02E-01
I-21	7.13E-13	3.50E-07	2.95E-15	3.13E-07	3.39E-15	3.86E-07
I-22	1.30E-21	6.21E-14	5.29E-23	1.59E-13	1.40E-22	1.56E-13
I-23	2.91E-20	5.93E-13	1.65E-21	1.83E-12	5.41E-21	2.18E-12
I-24	3.59E-20	9.84E-13	2.63E-22	8.08E-13	2.64E-22	9.84E-13
I-25	1.73E-06	2.92E-02	2.30E-09	1.30E-02	3.02E-09	1.90E-02
I-26	2.11E-12	4.91E-07	1.59E-14	9.02E-08	1.02E-14	1.25E-07
I-27	9.67E-13	2.52E-07	5.54E-14	4.65E-07	5.46E-14	5.38E-07
I-28	2.66E-09	1.10E-04	5.16E-11	9.99E-05	3.44E-11	1.09E-04
I-29	4.77E-21	3.39E-13	2.88E-25	1.83E-14	1.64E-25	3.17E-14
I-30	1.10E-23	9.87E-18	1.05E-23	1.39E-17	4.64E-24	1.11E-17
I-31	1.77E-19	2.39E-14	7.32E-21	2.58E-15	3.99E-21	3.51E-15
I-32	3.71E-18	3.12E-13	4.93E-19	1.71E-13	3.95E-19	1.99E-13
LA	1.68E-11	6.70E-08	4.25E-11	8.96E-08	1.25E-11	6.93E-08
Al	2.77E-08	3.40E-07	1.42E-09	2.96E-08	1.38E-09	6.58E-08
Hy	3.04E-20	2.62E-15	4.16E-21	8.13E-16	5.37E-21	1.34E-15
HPA	4.14E-22	1.27E-15	6.16E-23	4.64E-17	4.35E-23	8.82E-17
AGL	1.23E-19	2.43E-12	1.01E-21	4.81E-12	1.71E-21	6.36E-12
GVL	5.77E-12	1.59E-10	1.49E-12	7.65E-11	2.11E-12	1.44E-10
H	9.92E-01	6.23E-01	9.88E-01	7.06E-01	1.00E+00	7.14E-01

OH	2.54E-06	3.99E-05	2.96E-07	1.06E-05	1.68E-07	1.36E-05
Free sites	9.02E-05	7.98E-04	1.52E-05	1.88E-04	1.52E-05	2.39E-04
I-42	1.25E-18	3.05E-14	1.80E-23	5.69E-16	3.72E-21	3.11E-25
I-43	3.71E-11	2.79E-08	1.06E-13	1.50E-08	4.78E-11	0.00E+00
I-44	4.04E-19	1.34E-15	6.00E-21	6.45E-17	6.20E-21	1.39E-16
I-45	3.50E-16	2.70E-12	4.63E-19	2.88E-12	1.72E-16	5.03E-13
I-46	8.02E-03	8.18E-02	1.80E-04	1.21E-02	7.79E-05	1.50E-02
I-47	2.23E-09	3.22E-07	2.28E-12	6.86E-09	2.11E-12	1.29E-08
I-48	2.79E-17	1.52E-14	4.07E-20	1.08E-15	1.49E-19	3.31E-15
I-49	6.04E-07	3.65E-06	3.05E-08	7.30E-07	3.18E-08	1.26E-06
H_2O	9.64E-06	2.88E-05	1.28E-12	4.13E-11	2.12E-12	5.97E-11
O	1.16E-04	6.17E-03	8.99E-06	1.90E-03	4.40E-06	1.90E-03

Note: All reported numbers are the surface coverage over the number of adsorption sites.

Table C.7: Surface coverage of all the surface species at various temperatures for two site model

Adsorbed species	Solvent					
	Water		1,4-dioxane		Methanol	
	323 K	423 K	323 K	423 K	323 K	423 K
I-1	6.77E-13	1.57E-10	6.82E-12	6.37E-10	1.09E-11	6.44E-10
I-2	7.02E-07	1.53E-05	6.04E-08	3.63E-06	1.45E-07	5.16E-06
I-3	6.21E-16	1.94E-11	3.46E-15	1.17E-10	2.65E-15	1.08E-10
I-4	7.79E-21	5.38E-16	2.91E-20	1.33E-15	2.82E-20	1.68E-15
I-5	1.00E-20	4.38E-16	3.04E-19	3.57E-15	8.48E-19	3.41E-15
I-6	2.60E-08	8.83E-07	1.09E-09	6.72E-08	5.37E-07	2.03E-06
I-7	2.19E-14	2.21E-12	1.51E-14	7.71E-13	1.54E-12	1.41E-11
I-8	3.15E-18	1.66E-14	4.52E-19	6.67E-15	4.84E-16	1.53E-13
I-9	4.35E-22	1.23E-18	2.65E-24	5.42E-19	4.53E-21	6.84E-19
I-10	1.98E-11	5.88E-11	4.27E-12	1.32E-11	5.87E-09	4.63E-10
I-11	7.53E-21	2.33E-16	6.71E-20	1.38E-15	3.91E-19	1.14E-15
I-12	2.76E-10	4.87E-10	1.50E-11	4.14E-11	4.05E-08	1.96E-09
I-13	1.34E-15	4.28E-14	4.31E-16	6.63E-15	7.78E-14	1.80E-13
I-14	9.09E-09	1.36E-08	3.50E-10	2.47E-09	6.19E-07	7.52E-08
I-15	3.80E-15	4.21E-13	4.98E-16	9.43E-14	9.56E-13	3.57E-12
I-16	1.47E-20	7.53E-18	6.53E-21	7.38E-18	7.51E-18	1.64E-16
I-17	2.80E-13	4.00E-11	3.96E-14	9.07E-12	7.19E-11	2.94E-10
I-18	3.92E-17	1.20E-14	1.35E-17	4.85E-15	2.82E-15	1.05E-13
I-19	2.56E-10	2.44E-09	1.49E-11	1.73E-10	9.30E-09	6.23E-09
I-20	5.37E-06	4.79E-05	1.34E-06	3.24E-05	1.93E-03	8.67E-04
I-21	4.81E-11	1.04E-09	2.12E-12	2.36E-10	4.05E-09	6.90E-09
I-22	1.69E-20	3.72E-17	3.44E-21	1.61E-17	4.21E-18	4.07E-16
I-23	3.95E-19	1.57E-15	1.15E-19	6.34E-16	1.64E-16	1.87E-14
I-24	4.85E-19	2.62E-15	1.73E-20	2.96E-16	1.84E-17	8.44E-15
I-25	1.22E-04	3.85E-04	1.77E-06	3.34E-05	3.63E-03	1.11E-03
I-26	1.15E-10	7.84E-11	3.30E-11	8.23E-12	4.21E-09	2.11E-10
I-27	1.02E-11	1.58E-10	3.32E-12	5.70E-11	1.40E-09	1.42E-09
I-28	1.51E-07	7.78E-08	1.15E-07	3.09E-08	1.43E-05	6.05E-07
I-29	2.08E-18	2.61E-15	2.70E-20	5.29E-17	5.08E-17	1.83E-15
I-30	1.84E-21	8.26E-18	2.03E-20	7.85E-17	1.80E-20	6.37E-17

I-31	6.01E-17	4.36E-14	1.44E-16	9.36E-14	1.68E-16	1.10E-13
I-32	2.55E-16	5.08E-13	8.43E-16	2.85E-12	1.03E-15	3.00E-12
LA	4.06E-10	5.48E-08	5.52E-09	3.29E-07	3.25E-09	2.24E-07
Al	7.86E-07	3.38E-07	1.15E-06	7.26E-08	2.28E-06	1.45E-07
Hy	5.08E-18	2.56E-15	8.08E-18	4.74E-15	2.08E-17	7.90E-15
HPA	7.11E-22	1.34E-19	1.24E-22	9.27E-21	1.60E-20	9.24E-20
AGL	1.75E-18	2.87E-14	7.14E-20	5.99E-15	1.20E-16	1.79E-13
GVL	1.40E-10	2.06E-10	1.97E-10	3.97E-10	5.47E-10	6.49E-10
H	1.00E+00	9.94E-01	1.00E+00	9.99E-01	1.00E+00	9.99E-01
OH	1.57E-05	2.33E-05	3.58E-05	1.14E-05	4.33E-05	1.34E-05
Free sites (*)	4.44E-04	8.96E-04	1.74E-04	4.11E-04	2.46E-04	5.00E-04
I-42	6.57E-18	8.32E-17	3.80E-18	3.65E-17	4.95E-18	1.70E-17
I-43	6.33E-11	1.31E-10	1.84E-10	8.92E-10	2.46E-10	3.24E-10
I-44	5.44E-18	2.67E-16	4.53E-18	4.63E-17	1.02E-17	9.39E-17
I-45	1.54E-15	6.28E-14	9.92E-15	1.04E-12	1.44E-14	3.18E-13
I-46	3.33E-01	3.32E-01	2.88E-01	3.30E-01	3.28E-01	3.31E-01
I-47	4.35E-07	3.32E-07	3.91E-08	1.20E-07	1.42E-07	1.81E-07
I-48	4.15E-16	6.46E-14	3.55E-17	8.84E-15	2.48E-16	2.34E-14
I-49	3.48E-06	3.13E-06	2.16E-06	8.08E-07	3.27E-06	1.30E-06
H_2O	4.75E-05	3.23E-05	1.55E-11	9.59E-11	3.70E-11	1.35E-10
O	2.77E-04	6.56E-04	1.95E-04	3.60E-04	2.01E-04	3.67E-04
Free sites (Δ)	9.53E-05	5.63E-03	1.65E-05	9.07E-04	1.53E-05	1.10E-03

C.7 Bibliography

1. Johnston, H. S.; Heicklen, J., *The Journal of Physical Chemistry* **1962,** *66*, 532-533.

APPENDIX D: COPYRIGHT PERMISSIONS

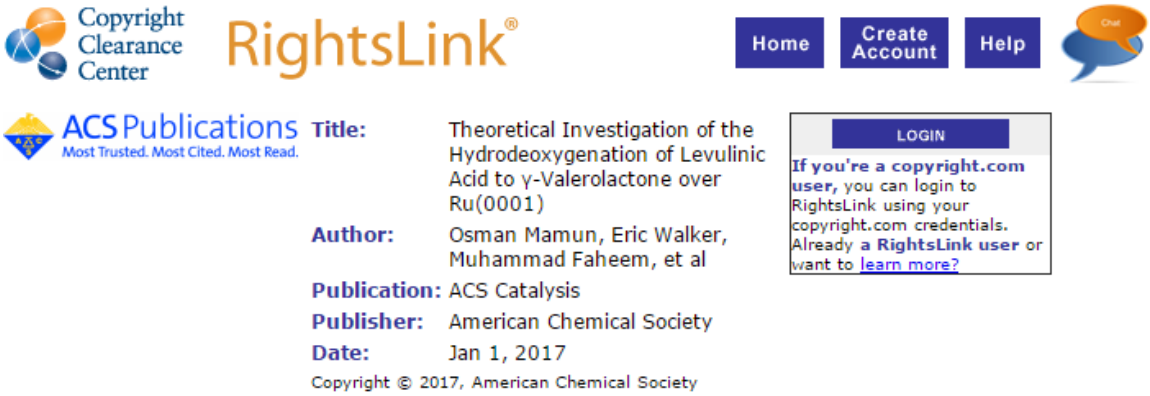

Copyright Clearance Center RightsLink®

Home | Create Account | Help

ACS Publications
Most Trusted. Most Cited. Most Read.

Title: Theoretical Investigation of the Hydrodeoxygenation of Levulinic Acid to γ-Valerolactone over Ru(0001)

Author: Osman Mamun, Eric Walker, Muhammad Faheem, et al

Publication: ACS Catalysis

Publisher: American Chemical Society

Date: Jan 1, 2017

Copyright © 2017, American Chemical Society

LOGIN

If you're a copyright.com user, you can login to RightsLink using your copyright.com credentials. Already **a RightsLink user** or want to learn more?

PERMISSION/LICENSE IS GRANTED FOR YOUR ORDER AT NO CHARGE

This type of permission/license, instead of the standard Terms & Conditions, is sent to you because no fee is being charged for your order. Please note the following:

- Permission is granted for your request in both print and electronic formats, and translations.
- If figures and/or tables were requested, they may be adapted or used in part.
- Please print this page for your records and send a copy of it to your publisher/graduate school.
- Appropriate credit for the requested material should be given as follows: "Reprinted (adapted) with permission from (COMPLETE REFERENCE CITATION). Copyright (YEAR) American Chemical Society." Insert appropriate information in place of the capitalized words.
- One-time permission is granted only for the use specified in your request. No additional uses are granted (such as derivative works or other editions). For any other uses, please submit a new request.

BACK | CLOSE WINDOW